

ABSTRACT

PALAGUMMI, SRI VIKRAM. Low Frequency Vibration Energy Harvesting using Diamagnetically Stabilized Magnet Levitation. (Under the direction of Dr. Fuh-Gwo Yuan).

Over the last decade, vibration-based energy harvesting has provided a technology push on the feasibility of self-powered portable small electronic devices and wireless sensor nodes. Vibration energy harvesters in general transduce energy by damping out the environmentally induced relative motion through either a cantilever beam or an equivalent suspension mechanism with one of the transduction mechanisms, like, piezoelectric, electrostatic, electromagnetic or magnetostrictive. Two major challenges face the present harvesters in literature, one, they suffer from the unavoidable mechanical damping due to internal friction present in the systems, second, they cannot operate efficiently in the low frequency range (< 10 Hz), when most of the ambient vibrational energy is in this low frequency broadband range. Passive and friction free diamagnetically stabilized magnet levitation mechanisms which can work efficiently as a vibration energy harvester in the low frequency range are discussed in this work.

First, a mono-stable vertical diamagnetic levitation (VDL) based vibration energy harvester (VEH) is discussed. The harvester consists of a lifting magnet (LM), a floating magnet (FM) and two diamagnetic plates (DPs). The LM balances out the weight of the FM and stability is brought about by the repulsive effect of the DPs, made of pyrolytic graphite. Two thick cylindrical coils, placed in grooves which are engraved in the DPs, are used to convert the mechanical energy into electrical energy. Experimental frequency response of the system is validated by the theoretical analysis which showed that the VEH works in a low frequency range but sufficient levitation gap was not achieved and the frequency response

characteristic of the system was effectively linear. To overcome these challenges, the influence of the geometry of the FM, the LM, and the DP were parametrically studied to assess their effects on the levitation gap, size of the system and the natural frequency. For efficient vibration energy harvesting using the VDL system, ways to mitigate eddy current damping and a coil geometry for transduction were critically discussed. With the optimized parameters, an experimental system was realized which showed a hardening type nonlinearity and an improved efficiency from the initial study.

Even after the optimization study, several challenges still hindered the VDL system from being an efficient system. The main challenges faced were the strict stability conditions and the limitations of the maximum amplitude of the FM, which was inherently limited by the distance between the DPs which in turn was coupled back with the stabilization condition. To overcome these challenges, an alternative configuration called as a horizontal diamagnetic levitation (HDL) system was investigated.

In the HDL configuration, two magnets, alias LMs, are arranged co-axially at a distance such that in between them a third smaller magnet, alias FM, is passively levitated at a laterally offset equilibrium position. The levitation is stabilized in the horizontal direction by two DPs placed on each side of the FM. This HDL configuration mitigates the limitation on the amplitude of the FM imposed in the VDL configuration. The parameters of the HDL system were characterized to understand the key factors that affect the static levitation, stability, frequency response and the power density of the HDL energy harvester. As a result of the analysis an efficient low resonant frequency vibration energy harvester was experimentally validated.

Finally, a bi-stable system based on HDL is proposed to take advantage of the broad frequency bandwidth response inherent in a bi-stable system. From initial conceptual design which involves multiple lifting magnets to a final robust frequency tunable design involving multiple lifting magnets and repelling magnets are discussed. Experimental and theoretical results of this low frequency wideband vibration energy harvester are presented.

© Copyright 2015 Sri Vikram Palagummi

All Rights Reserved

Low Frequency Vibration Energy Harvesting using Diamagnetically Stabilized Magnet
Levitation

by
Sri Vikram Palagummi

A dissertation submitted to the Graduate Faculty of
North Carolina State University
in partial fulfillment of the
requirements for the degree of
Doctor of Philosophy

Mechanical Engineering

Raleigh, North Carolina

2015

APPROVED BY:

Dr. Fuh-Gwo Yuan
Committee Chair

Dr. Gregory D. Buckner

Dr. Xiaoning Jiang

Dr. Chih-Hao Chang

Dr. Yuan-Shin Lee

DEDICATION

To my parents, my sister, my brother-in law and my niece.

BIOGRAPHY

Sri Vikram Palagummi was born on May 6, 1988 in New Delhi, Delhi, India. He graduated from BITS-Pilani (Goa campus) in 2009 with a Bachelor's in Mechanical Engineering. Immediately after a six months intern at TATA motors he decided to pursue his graduate studies in Mechanical Engineering at North Carolina State University (NCSU). He graduated with a Master's degree in 2012 and continued his graduate studies at NCSU in pursuit of a Doctoral degree. During this time at NCSU, Sri Vikram worked with Dr. Fuh-Gwo Yuan on experimentally and theoretical validating the potential uses of diamagnetically stabilized magnet levitation mechanism for vibration energy harvesting. Following this, he with the help of Dr. Fuh-Gwo Yuan was able to successfully acquire National Science Foundation funding to further investigate this levitation mechanism and its use in vibration energy harvesting in depth which has eventually led to the core of his dissertation work. He plans to finish his doctoral studies by end of the summer of 2015.

Sri Vikram Palagummi is a member of American Society of Mechanical Engineering (ASME), the Society of Photo-optical Instrumentation Engineers (SPIE) and the Golden Key International Honor Society. He has been awarded the 3rd Best Student Paper award at SPIE/Smart Structures and NDE 2013 conference at San Diego, California.

ACKNOWLEDGMENTS

I would like to express my deepest gratitude to my advisor and committee chair, Dr. Fuh-Gwo Yuan, for his time, patience and efforts. For teaching me to be critical in my thought process and for imbuing in me the thrust to work harder, for which I will be always in debt to him. I would like to thank Dr. Gregory D. Buckner, Dr. Xiaoning Jaing, Dr. Chih-Hao Chang and Dr. Yuan-Shin Lee for serving on my committee and giving me invaluable suggestions for my dissertation.

Over the course of 5 years that I have been in the Smarts Structures and Materials Lab at NCSU, I have met some amazing individuals who I have shared some memorable times with. I would like to thank Dr. Lei Liu, Dr. Xiying Wang, Dr. Xiang Yan, Mr. Junchao Zou, Mr. Patrick Leser, Mr. Donato Girolamo. Mr. Tyler Hudson and Dr. Rui Zhu. Special thanks to Mr. Mohammad Harb for his help inside and outside the lab throughout my graduate studies. Also, thanks to Dr. Shaorui Yang for sharing all the funny, yet insightful, stories about the world politics with me and for showing me some of his amazing photography skills around the campus.

I am thankful to my parents, my sister and my brother-in law: Uma Maheshwar Rao Palagummi, Annapurna Palagummi, Swetha Pooja Palagummi and Ravi Vemaraju, for their unconditional love, support and patience. I have made many friends over the course of six years at NCSU and the memories will live for a lifetime. I would like to mention some of them here: Lionel Ernest Edwin, Siva Sandeep Chintamaneni, Suraj Chanda, Varun Chinta, Suhas

Bhat, Suguna Jairam, Aditya Srinivas Balu, Sameer Suresh, Amarnath Sarma and Raviteja Manda.

I would like to thank Miss Annie White for being extremely patient with all my queries and for helping me getting done with all the paper work that was needed.

Finally, I would like to thank the National Science Foundation (CMMI-1300684) and the Department of Transportation for funding this work.

TABLE OF CONTENTS

| | |
|--|------|
| LIST OF TABLES | xi |
| LIST OF FIGURES | xii |
| LIST OF SYMBOLS AND ABBREVIATIONS | xxii |
| 1 Introduction | 1 |
| 1.1 Vibration Energy Harvesting | 4 |
| <i>1.1.1 Transduction mechanism</i> | 5 |
| <i>1.1.2 Mechanical subsystem</i> | 8 |
| 1.2 Literature review | 13 |
| <i>1.2.1 Mono-stable linear</i> | 13 |
| <i>1.2.2 Mono-stable hardening and softening</i> | 20 |
| <i>1.2.3 Bi-stable systems</i> | 21 |
| <i>1.2.4 Frequency-up conversion techniques</i> | 23 |
| <i>1.2.5 Direct force generators</i> | 23 |
| 1.3 Challenges | 24 |
| 1.4 Objective and Scope | 26 |
| 2 Magnetic materials | 30 |
| 2.1 Magnetism..... | 31 |

| | |
|--|-----------|
| 2.2 Magnetic materials..... | 34 |
| 2.2.1 <i>Diamagnetism</i> | 35 |
| 2.2.2 <i>Paramagnetism</i> | 36 |
| 2.2.3 <i>Ferromagnetism</i> | 38 |
| 2.2.4 <i>Antiferromagnetism</i> | 41 |
| 2.2.5 <i>Ferrimagnetism</i> | 42 |
| 2.3 Diamagnetic levitation and diamagnetically stabilized magnet levitation | 43 |
| 3 A Vertical Diamagnetic Levitation (VDL) based Vibration Energy Harvester..... | 49 |
| 3.1 Conceptual design of VDL | 50 |
| 3.2 Modelling tools for the VDL system | 54 |
| 3.2.1 <i>Modeling the magnetic field of a cylindrical magnet</i> | 54 |
| 3.2.2 <i>Modeling of force between two magnets</i> | 58 |
| 3.2.3 <i>Modeling of repulsive force from a diamagnetic material</i> | 60 |
| 3.3 Modified design of VDL..... | 63 |
| 3.4 Equations of motion..... | 68 |
| 3.5 Experimental studies on VDL..... | 72 |
| 3.5.1 <i>Experimental apparatus and instrumentation</i> | 72 |
| 3.5.2 <i>Comparisons between analytical prediction and experimental results</i> | 74 |
| 3.6 Conclusions..... | 77 |

| | |
|---|------------|
| 4 An optimal design of a mono-stable vertical diamagnetic levitation (VDL) based vibration energy harvester | 78 |
| 4.1 Mono-stable VDL system | 79 |
| 4.1.1 Parametric studies on the VDL system | 81 |
| 4.1.2 Design of the VDL system | 85 |
| 4.2 Damping due to eddy currents in the DP and a copper coil for transduction ... | 89 |
| 4.3 Experimental setup | 93 |
| 4.4 Conclusions | 100 |
| 5 A horizontal diamagnetic levitation (HDL) based vibration energy harvester | 102 |
| 5.1 A HDL system | 103 |
| 5.2 Theoretical modeling | 105 |
| 5.3 Eddy current damping and coil geometry | 117 |
| 5.4 Equations of motion | 119 |
| 5.5 Experimental validation | 123 |
| 5.6 Discussion | 128 |
| 5.7 Conclusions | 130 |
| 6 An efficient low resonant frequency horizontal diamagnetic levitation (HDL) based vibration energy harvester | 132 |

| | |
|---|-----|
| 6.1 Parametric studies on the HDL system..... | 133 |
| 6.1.1 Aspect ratio of the FM (β_{FM})..... | 136 |
| 6.1.2 Relative ratio of the DPs ($r_{DP/FM}, t_{DP/FM}$)..... | 136 |
| 6.1.3 Aspect ratio of the LMs (β_{LM})..... | 137 |
| 6.1.4 Stability of the FM..... | 138 |
| 6.1.5 Volume of the LM and natural frequency (V_{LM}, f_n)..... | 140 |
| 6.2 Electromagnetic coupling characteristics | 143 |
| 6.3 Experimental validation..... | 149 |
| 6.4 Improving stability of diamagnetically stabilized magnet levitation systems | 156 |
| 6.5 Conclusions..... | 159 |

| | |
|---|------------|
| 7 A bi-stable horizontal diamagnetic levitation (BHDL) based low frequency wideband vibration energy harvester | 161 |
| 7.1 Conceptual design of a BHDL system..... | 162 |
| 7.2 Theoretical modeling of the BHDL..... | 163 |
| 7.3 Proposed BHDL system..... | 170 |
| 7.4 Electromagnetic coupling characteristics | 175 |
| 7.4.1 Equivalent mechanical damping..... | 176 |
| 7.4.2 Electromagnetic transduction and electrical damping..... | 179 |
| 7.5 Experimental validation..... | 181 |

| | |
|---|------------|
| 7.6 Conclusions..... | 188 |
| 8 Conclusions and future work..... | 189 |
| 8.1 Conclusions..... | 189 |
| 8.2 Future Work..... | 191 |
| 9 References..... | 194 |

LIST OF TABLES

| | |
|--|-----|
| Table 1.1 Power source comparisons (Roundy et al.[8, 10])..... | 4 |
| Table 2.1 Summary of magnetic materials [100-102] | 42 |
| Table 3.1 The model parameters for the experimental system | 74 |
| Table 4.1 Mechanical damping co-efficient for the fundamental vibration mode for different reported VEHs | 92 |
| Table 4.2 Model parameters for experimental setup | 100 |
| Table 5.1 Model parameters for the experimental system | 124 |
| Table 6.1 Model parameters for the experimental system | 155 |
| Table 7.1 Parameters of the experimental setup of the BHDL system | 174 |

LIST OF FIGURES

| | |
|---|----|
| Figure 1.1 Schematic of wireless sensor networks in SHM systems..... | 1 |
| Figure 1.2 The d_{31} and the d_{33} mode of a piezoelectric material..... | 5 |
| Figure 1.3 Schematic of an electromagnetic harvester | 6 |
| Figure 1.4 Schematic of an axially loaded magnetostrictive energy harvesters | 7 |
| Figure 1.5 Schematic of an electrostatic VEH..... | 7 |
| Figure 1.6 Schematic of a generic inertial VEH | 9 |
| Figure 1.7 (a) Inductive circuit and (b) capacitive circuit coupled with the mechanical sub- system of a VEH | 10 |
| Figure 1.8 (a) Potential energy and (b) restoring force depending on the value of k_1 and k_3 define mono-stable linear, mono-stable hardening, mono-stable softening and bi-stable systems | 11 |
| Figure 1.9 FRCs for mono-stable linear, hardening and softening mechanisms | 12 |
| Figure 1.10 FRCs for bi-stable mechanisms with different excitation levels (a) low level of excitation ($A < A_T$) (b) high level of excitation ($A > A_T$)..... | 13 |
| Figure 1.11 Piezoelectric unimorph (left), bimorph (right) | 16 |

| | |
|---|----|
| Figure 1.12 Magnetostrictive energy harvesters (a) proposed by Wang and Yuan [43] (b) Moss et al. [44]. | 18 |
| Figure 1.13 A hardening type pseudo magnetic levitation based VEH [61]. | 20 |
| Figure 1.14 Bi-stable mechanism proposed by (a) Baker et al. [66] and Mansana and Daqaq [69] and (b) Erturk et al. [68]. | 22 |
| Figure 1.15 (a) Acceleration time history of a bridge (b) Frequency content of acceleration on a bridge [89]. | 25 |
| Figure 2.1 (a) Orbital magnetic moment (μ_o) and (b) spin magnetic moment (μ_s) | 35 |
| Figure 2.2 Schematic showing precession of orbital magnetic moment in diamagnetic materials due to an external magnetic field \mathbf{H} . | 36 |
| Figure 2.3 Schematic of orientation of magnetic dipoles in paramagnetic materials | 38 |
| Figure 2.4 Division into magnetic domains to decrease the magnetostatic energy [99] | 39 |
| Figure 2.5 (a) Levitation of a frog stabilized by the diamagnetic water in the frog (b) Levitation of a magnet stabilized by the diamagnetism of fingers (weight balanced by unseen solenoid in both cases) [108, 109]. | 46 |
| Figure 2.6 (a) Force balanced, unstable bottom magnet (b) Stabilized vertical magnetic levitation | 48 |

| | |
|---|----|
| Figure 3.1 (a) Schematic of the proposed VEH and (b) simplified modeling of the harvester | 52 |
| Figure 3.2 Amplitude-frequency responses of the FM under various nonlinear factors [125]..... | 53 |
| Figure 3.3 Schematic showing the dipole model and the thin coil model | 57 |
| Figure 3.4 Normalized magnetic field values using thin coil model (*) and dipole model (-) for different aspect ratios β | 57 |
| Figure 3.5 Two magnets with their equivalent thin coil model representations for determining the force between them. | 58 |
| Figure 3.6 Schematic of the force calculation using the image method and the discrete volume method..... | 62 |
| Figure 3.7 Normalized force between a magnet and a diamagnetic object with different approximations for different β | 63 |
| Figure 3.8 Schematic of modified design of VDL based VEH | 64 |
| Figure 3.9 Force balance between the weight of the FM ($m_{FM}g$) and the attractive force of the LM (F_{LM}). | 66 |
| Figure 3.10 Radial magnetic flux density for the FM vs the radial distance at various axial distances, measured from the center of the FM. | 67 |

| | |
|--|----|
| Figure 3.11 (a) Schematic of the restoring forces acting on the FM (b) Restoring force as a function of displacement..... | 69 |
| Figure 3.12 (a) Schematic of the VDL based VEH and (b) single-degree of freedom equivalent of the VEH | 71 |
| Figure 3.13 The experimental prototype of the VDL based VEH..... | 73 |
| Figure 3.14 (a) Experimental and theoretical predictions of relative amplitude of the FM (b) Experimental and theoretical predictions of the RMS voltage (c) Experimental and theoretical predictions of Power (d) Experimental and theoretical predictions of the efficiency..... | 76 |
| Figure 4.1. A two-dimensional view of the VDL system. | 80 |
| Figure 4.2. (a) Force per unit V_{FM} (F_{DP}/V_{FM}) versus β_{FM} , (b) force per unit volume (F_{DP}/V_{FM}) versus $\beta_{DP}^d = d_{DP}/d_{FM}$ and (c) $\beta_{DP}^t = t_{DP}/t_{FM}$ respectively. | 82 |
| Figure 4.3. Variation of the normalized diamagnetic repulsive force (F_1/V_{FM}) vs h/t_{FM} | 82 |
| Figure 4.4. Force F_2 and L varies with β_{LM} (aspect ratio of the LM) in (a) and (b) for a fixed V_{LM} and V_{FM} , in (c) and (d) force F_2 and L varies with V_{LM} for a fixed V_{FM} and fixed β_{LM} ($\eta = V_{LM}/V_{FM}$). | 84 |

Figure 4.5. (a) Variation of minimum V_{LM} with V_{FM} and (b) variation of maximum h with V_{FM} 86

Figure 4.6. (a) Variation in f_n with normalized h for a fixed $\eta = 100$ with V_{FM} varying from 0.1 cm^3 to 1 cm^3 and (b) variation in f_n with normalized h for a fixed $V_{FM} = 1 \text{ cm}^3$ for η varying from 10 to 100.87

Figure 4.7. Flowchart for tuning f_n of a VDL system with the dominant f_{ambient} 88

Figure 4.8. Cylindrically symmetric eddy current density profile in the DP.....90

Figure 4.9. (a) A two dimensional model of the VDL energy harvester with the copper coils and (b) an equivalent 1 degree of freedom (1-DOF) model of the VDL energy harvester.....93

Figure 4.10. (a) Restoring force and (b) ring down of the FM, to determine open-loop Q factor.....96

Figure 4.11. Experimental setup of the VDL based VEH98

Figure 4.12. Close-up of the VDL based VEH.....99

Figure 4.13. Experimental results and theoretical predictions of (a) RMS voltage across the load resistance, (b) RMS power in the load resistance, (c) peak relative displacement of the FM and (d) overall efficiency of the VDL based VEH system.99

Figure 5.1 Schematic of a HDL system104

Figure 5.2 A schematic of the HDL based vibration energy harvester system (a) front view (b) side section view with the lifting magnets (LM_1 and LM_2), the diamagnetic plates (DP_1 and DP_2), the floating magnet (FM) and the copper coil. The lighter colored FM shows its static equilibrium position whereas the darker colored FM shows its perturbed dynamic position.106

Figure 5.3 Thin coil (TC) model for estimating the force between laterally and axially offset magnets109

Figure 5.4 Error estimates between the thin coil model and the dipole model for estimating the lateral and axial force between two magnets.111

Figure 5.5 (a) Weight balance positions d_z of the FM with the LM at the respective d_x , (b) restoring force in the x -direction for the d_x values taken from (a), (c) zoomed section of (b) at which static levitation is permissible (d) restoring force in the y -direction for the d_x values taken from (c).113

Figure 5.6 (a) Amplitude of FM in the z -direction (z_{max}) for different d_x (b) Restoring force in the z -direction for varying d_x 115

Figure 5.7 Restoring force in the x -direction at different z amplitudes.115

| | |
|---|-----|
| Figure 5.8 (a) Restoring force in the x -direction, (b) in the y -direction, (c) in the z -direction. | 117 |
| Figure 5.9 (a) Ring-down of the FM using a high speed camera. (b) Parametric sweep to determine coil_{out} | 119 |
| Figure 5.10 An equivalent one degree-of-freedom (1-DOF) model of the HDL based VEH. | 120 |
| Figure 5.11 Schematic of the coil geometry for (a) voltage induced calculation for each loop of the coil ($V(z, \dot{z})$ in equation(5.9)) (b) Lorentz force calculation from each loop of the coil ($F_L(i, z)$) in equation (5.10)). | 122 |
| Figure 5.12 Experimental system for HDL based VEH. | 124 |
| Figure 5.13 Close-up of the HDL based VEH showing the FM (covered with a green tape), the LMs and the pyrolytic graphite with the copper coil. | 126 |
| Figure 5.14 Experimental and theoretical predictions (a) relative amplitude of the FM (b) RMS voltage across the load (c) RMS power and (d) average efficiency of the system. (RMS excitation acceleration varied from 0.028 m/s^2 to 0.0678 m/s^2 as the frequency was varied from 0.5 Hz to 3 Hz) | 127 |

Figure 6.1 Schematic of the HDL vibration energy harvester system with the floating magnet (FM), the lifting magnets (LMs) and the diamagnetic plates (DPs) (a) 3D view (b) front view (c) side view.134

Figure 6.2 (a) Force per unit V_{FM} (F_x^{DP} / V_{FM}) versus β_{FM} (b) Force per unit V_{FM} (F_x^{DP} / V_{FM}) versus $r_{DP/FM} = r_{DP} / r_{FM}$ and (c) Force per unit volume (F_x^{DP} / V_{FM}) versus $t_{DP/FM} = t_{DP} / t_{FM}$ 137

Figure 6.3 Normalized (a) maximum d_x (b) minimum d_x with β_{LM} 138

Figure 6.4 Normalized amplitude in the negative z -direction with the (a) aspect ratio of LM (β_{LM}) (b) volume ratio ($\eta = V_{LM} / V_{FM}$) and (c) normalized d_x 139

Figure 6.5 Flowchart for tuning f_n of a HDL system with the dominant $f_{ambient}$ 141

Figure 6.6 (a) Natural frequency range for V_{FM} ranging from 0.1 cm^3 to 1 cm^3 ($\eta = 10$) (b) Natural frequency range for a fixed $V_{FM} = 1 \text{ cm}^3$ with η from 1 to 10.....142

Figure 6.7 Schematic of the (a) front view and (b) side view showing the incorporation of a coil in the HDL system.144

Figure 6.8 Voltage induced variation with $coil_{out}$ of the copper coil for different A_{FM} 146

| | |
|---|-----|
| Figure 6.9 Schematic of coil geometry along with representation of terms used for calculation of (a) voltage in equation (6.2) and (b) the electromechanical coupling coefficient for equation (6.3). | 147 |
| Figure 6.10 Normalized force F_x^{FM} between the DP and the FM for varying z - displacement of the FM. | 149 |
| Figure 6.11 Restoring forces for the HDL system in the (a) x -direction (b) y -direction and (c) z -direction with system parameters given in Table 6.1. | 151 |
| Figure 6.12 Experimental setup of the HDL vibration energy harvester. | 152 |
| Figure 6.13 Close up of the HDL vibration energy harvester. | 153 |
| Figure 6.14 Theoretical predictions and experimental measurements of the (a) average amplitude of the FM (b) the RMS voltage (c) the RMS power and (d) the efficiency. | 154 |
| Figure 6.15 Schematic of HDL system with repulsive magnet for enhanced levitation gap. | 157 |
| Figure 6.16 Schematic of VDL system with repulsive magnets for enhanced levitation gap. | 158 |
| Figure 7.1 Possible BHDL system with (a) four LMs (LM_4) (b) four LMs and two RMs (LM_4RM_2). | 163 |

| | |
|---|-----|
| Figure 7.2 A general double-well potential system using HDL | 170 |
| Figure 7.3 Proposed BHDL design with four LMs and eight RMs (LM_4RM_8) | 171 |
| Figure 7.4 (a) Side view and (b) cut-section view of the proposed BHDL system | 173 |
| Figure 7.5 (a) Restoring force and (b) potential energy plot of the BHDL system | 175 |
| Figure 7.6 Schematic showing a cut-section (view along Y -axis) of the BHDL based VEH alongside with the actual copper coil assembled DP | 178 |
| Figure 7.7 Schematic of the VEH with the coil geometry (cut-section view along X -axis) for (a) voltage induced calculation for each loop of the coil ($V(z, \dot{z})$ in equation (7.15)) (b) Lorentz force calculation from each loop of the coil ($F_L(i, z)$ in equation (7.16)). | 180 |
| Figure 7.8 Experimental setup of the BHDL based VEH..... | 183 |
| Figure 7.9 Close-up of the BHDL based VEH | 183 |
| Figure 7.10 Amplitude-frequency response curves with excitation amplitudes (a) of 0.5 mm, (b) 1 mm and (c) 1.5 mm | 185 |
| Figure 7.11 (a) Peak voltage frequency response curves with excitation amplitude of 1.5 mm (b) Peak efficiency of the BHDL based vibration energy harvester | 187 |

LIST OF SYMBOLS AND ABBREVIATIONS

Roman symbols

| | |
|-----------|--|
| B | Magnetic flux density |
| Br | Residual magnetic flux density |
| d_x | Center to center axial distance between lifting magnet and floating magnet |
| d_z | Center to center lateral distance between lifting magnet and floating magnet |
| d_{DP} | Diameter of diamagnetic plate |
| d_{FM} | Diameter of floating magnet |
| d_{LM} | Diameter of lifting magnet |
| \hat{x} | Unit vector in the x-direction |
| \hat{y} | Unit vector in the y-direction |
| \hat{z} | Unit vector in the z-direction |
| f_n | Natural frequency |
| H | Magnetic field intensity |
| I | Electrical current |
| L | Inductance |
| M_{FM} | Magnetization of floating magnet |
| M_{LM} | Magnetization of lifting magnet |
| R | Electrical resistance |
| r_{FM} | Radius of floating magnet |

| | |
|-------------|---|
| r_{LM} | Radius of lifting magnet |
| r_{DP} | Radius of diamagnetic plate |
| $r_{DP/FM}$ | Ratio of radius of diamagnetic plate to floating magnet |
| t | Time variable |
| t_{DP} | Thickness of diamagnetic plate |
| t_{FM} | Thickness of floating magnet |
| t_{LM} | Thickness of lifting magnet |
| U | Potential energy |
| V_{FM} | Volume of floating magnet |
| V_{LM} | Volume of lifting magnet |
| v | Electrical voltage |
| X | x -axis notation |
| Y | y -axis notation |
| Z | z -axis notation |

Greek symbols

| | |
|----------------|---|
| β_{FM} | Aspect ratio of floating magnet |
| β_{LM} | Aspect ratio of lifting magnet |
| β_{DP}^d | Diametric ratio of diamagnetic plate to floating magnet |
| β_{DP}^t | Thickness of diamagnetic plate to floating magnet |

ω Angular frequency

Abbreviations

| | |
|------|---|
| AC | Alternating Current |
| BHDL | Bi-stable Horizontal Diamagnetic Levitation |
| DP | Diamagnetic Plate |
| DL | Diamagnetic Levitation |
| EM | Electro-Magnetic |
| FM | Floating Magnet |
| FRC | Frequency Response Curve |
| HDL | Horizontal Diamagnetic Levitation |
| LM | Lifting Magnet |
| PZT | Lead Zirconate Titanate |
| RM | Repelling magnet |
| SHM | Structural Health Monitoring |
| VEH | Vibration Energy Harvesting |
| VDL | Vertical Diamagnetic Levitation |
| WSN | Wireless Sensor Networks |

“We are at the very beginning of time for the human race. It is not unreasonable that we grapple with problems. But there are tens of thousands of years in the future. Our responsibility is to do what we can, learn what we can, improve the solutions, and pass them on”

-Richard P. Feynman

1 Introduction

Recent research and development efforts have led to an increasing deployment of wireless sensors and networks in the area of Structural Health Monitoring (SHM). The Wireless Sensor Networks (WSN) can remotely access the health status of structures, simplify the configuration by eliminating wire connections, and also reduce the maintenance and life-cycle costs. Furthermore, the advantages of WSN over traditional wired sensors include sensor node communication, network scalability, and significantly increasing deployability of the sensors under a wide range of environmental conditions. Therefore, it holds the promise in the future for monitoring the integrity of critical structural components (Figure 1.1).

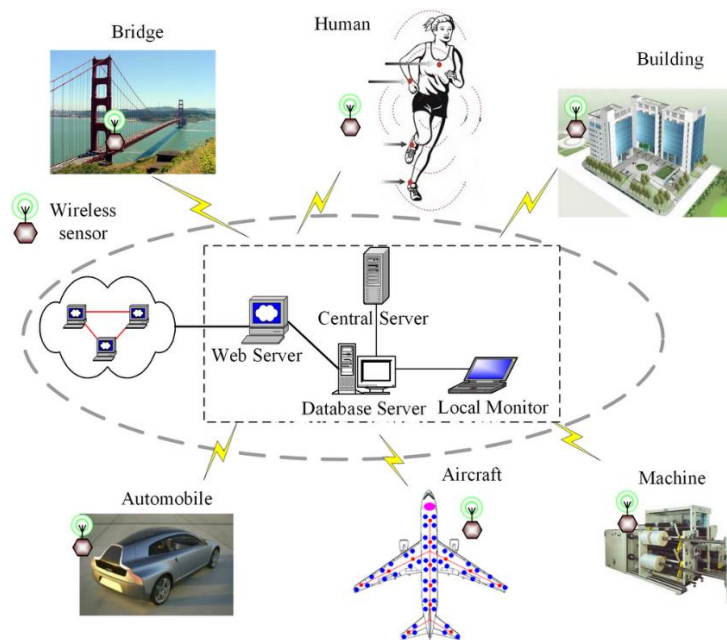


Figure 1.1 Schematic of wireless sensor networks in SHM systems

Wireless sensor nodes are tiny computers with sensors and radios capable of measuring physical parameters such as strain, acceleration, temperature, humidity, etc. of their environment. These devices transmit this data to either a central aggregation point or other peer nodes on the network that can act on this data. These networks can form intricate topologies, and there are multiple routing protocols and standards, which attempt to minimize power consumption while maintaining data latency and integrity. For communication distances over 10 meters, the energy to transmit data rapidly dominates the system [1], hence a re-configurable sensor network (ad hoc) is used in which the distance is reduced and the data is transmitted through multiple sensors and therefore creating low power, low cost nodes.

The powering of a large number of nodes in a sensor network becomes problematic if we consider the wiring and battery replacement cost. There are two solutions to this problem: one is to improve the energy density of the storage systems so that their lifetime is greatly increased; the other is to develop new technologies so that each node can generate their own power to recharge their batteries.

Although advances in low-power Very Large Scale Integration (VLSI) design along with the low duty cycles of wireless sensors have reduced power requirements of 100s – 1000s of μW (e.g., MICA) with projections into 10s of μW , such rapid improvements by Moore's law have not been matched by similar advances in battery technology. At the same time, owing to shrinking chip sizes and the ever-increasing integration of more functionalities, the expectation for powering wireless sensors continue to outpace conventional batteries energy storage capabilities. Such trend for low-power consumption of wireless sensors gives rise to the development of energy harvesting (energy scavenging) techniques, which aims at powering

the wireless sensors by scavenging ambient energy from the environment, supplementing and even entirely replacing the battery energy. Such self-powered wireless sensors could be employed potentially in hostile or inaccessible areas with little or no maintenance [2-4].

However, this is a difficult option to exploit as there is no one device that fits for all or even a majority of the applications. Hence, for WSN to achieve full potential, self-powering these autonomous sensors needs to be developed depending on its specific application. Various researchers have looked into using the different sources of ambient energy such as solar, thermal, wind and vibration to power the wireless sensors [3]. For example, Jiang et al. [5] have used solar energy to power wireless sensors and Park and Chou [6] have used wind and solar energy to power a wireless sensor. However, in the past decade there has been a surging growth in the investigation of vibration energy harvesters as a potential source to powering wireless sensor nodes [7]. Roundy et al. [8, 9] have studied the approximate power densities of the available power sources (Table 1), it can be seen that vibration as a power source fairs well when compared with other power sources. Also, the general consensus from the literature is that vibrational energy is the most versatile and ubiquitous of the ambient energy forms.

Table 1.1 Power source comparisons (Roundy et al.[8, 10])

| Power Source | Power ($\mu\text{W}/\text{cm}^3$) |
|---------------------|-------------------------------------|
| Solar (outside) | 15,000* |
| Solar (inside) | 10* |
| Temperature | 40*¶ |
| Human power | 330 |
| Air flow | 380† |
| Pressure variations | 17‡ |
| Vibrations | 375 |

* Measure in power per square centimeter, rather than power per cubic centimeter, ¶ Demonstrated from a 5°C temperature differential, † Assumes an air velocity of 5 m/s and 5 percent conversion efficiency, ‡ Based on 1cm³ closed volume of helium undergoing a 10°C change once a day.

1.1 Vibration Energy Harvesting

Vibration energy harvesters (VEHs) require a transduction mechanism coupled with a mechanical system that can be used to convert the ambient vibratory energy into useful electric energy. The transduction mechanisms most popularly investigated involve mainly, not limited to, piezoelectric, electromagnetic, electrostatic and magnetostrictive materials [2, 11, 12]. First a brief overview will be presented on the different kinds of transduction mechanisms followed by some theoretical framework on the mechanism systems that these transducers are generally coupled with.

1.1.1 Transduction mechanism

Piezoelectric materials exhibit physical deformation in the presence of an electric field or conversely produce an electric charge when deformed mechanically, the later phenomena is called the piezoelectric effect. Ceramic and polymer materials which exhibit piezoelectricity are most widely used for energy harvesting applications. The most popular engineering piezoceramic is lead zirconate titanate (PZT) of whose derivatives PZT-5A and PZT-5H have been widely implemented for energy harvesting [3]. There are typically two modes of operation of piezoelectric materials that are useful for energy harvesting, the d_{33} and the d_{31} mode. When a compressive strain is applied perpendicular to the electrodes the material induces dipoles whose collective charge depend on the d_{33} coefficient, whereas when a transverse strain is applied parallel to the electrodes the material induces dipoles whose collective charge depend on the d_{31} coefficient (Figure 1.2).

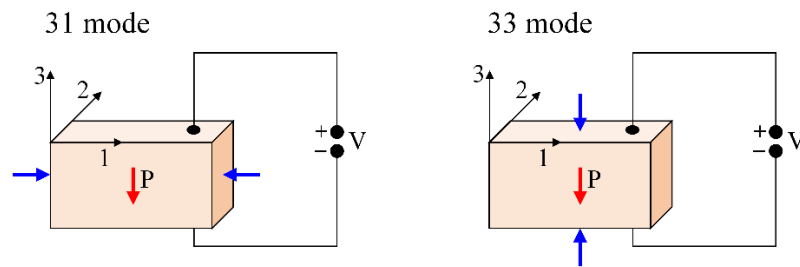


Figure 1.2 The d_{31} and the d_{33} mode of a piezoelectric material

Electromagnetic transduction is probably the oldest type of transduction known. It involves the induction of a voltage by Faraday's law when a magnet moves past a conductor.

When a load is connected to this conductor, current passes through it and can power the load. A schematic of such a system is shown in Figure 1.3.

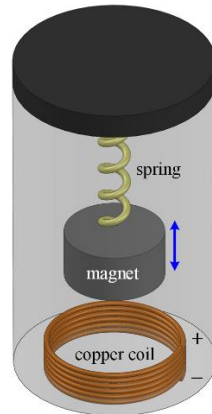


Figure 1.3 Schematic of an electromagnetic harvester

Magnetostrictive materials (MsM) have a bi-directional coupling between their mechanical and magnetic states. The magnetostrictive materials change their magnetic state when subjected to deformation, this phenomena is called as the Villari effect. Terfenol-D, a crystalline alloy and Metglass 2605SC, a metallic amorphous material are two commercially available magnetostrictive materials which have high coupling coefficients, hence suitable for energy harvesting. A schematic of a axially loaded magnetostrictive energy harvester is shown in Figure 1.4.

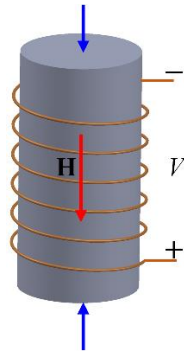


Figure 1.4 Schematic of an axially loaded magnetostrictive energy harvesters

Electrostatic VEH relies on the changing of capacitance between two charged surfaces like the one shown in Figure 1.5. When one comb finger moves relative to the other, the energy in the capacitor changes and can be used to drive current in a load. There are different forms by which this can be achieved, one of the types being a voltage constrained electrostatic VEH and the other being a charge constrained electrostatic VEH.

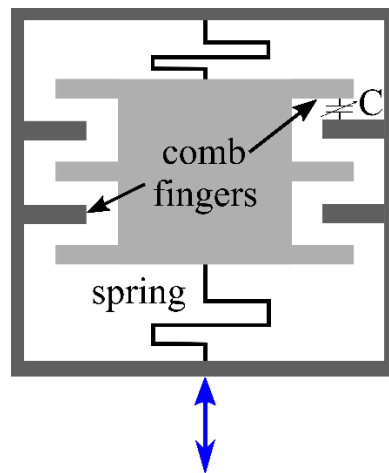


Figure 1.5 Schematic of an electrostatic VEH

1.1.2 Mechanical subsystem

The mechanical systems to which the transducers, mentioned in sub section 1.1.1, are coupled with can be broadly classified into two categories; one is the direct force system and the other is the inertial system. The direct force VEHs can be further subdivided into impact based VEHs and human powered VEHs whereas the inertial VEHs can be further subdivided into linear and nonlinear VEHs. The impact based VEHs involve usually transduction from impacts of a ball or similar objects whereas the human powered VEHs involved directly straining or impacting on the transduction material due to human motion. The transduction mechanism of the inertial VEHs uses the relative motion of a mass to convert one energy form to the other. There have been significantly less work reported on direct force generators when compared to the inertial type generators.

Due to the extensive study of inertial VEHs in literature, it is necessary to look into the mechanism before presenting the state of the art. The mechanical system of an inertial VEH can be simply modeled as a lumped mass oscillator coupled with an electric circuit which depends on the type of transduction. A simplified inertial mechanical system is shown in Figure 1.6 and its associated electrical circuit depending on the transduction mechanism used is shown in Figure 1.7.

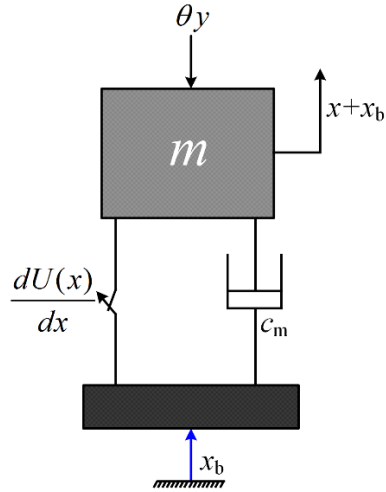


Figure 1.6 Schematic of a generic inertial VEH

where x is the relative displacement of the lumped mass m , c_m is the mechanical damping modeled as a linear viscous damper, x_b is the base displacement, $U(x)$ is a function that represents the potential energy stored in the mechanical subsystem as a function of its relative displacement, θ is a linear electromechanical coupling coefficient and y represents either voltage or current depending on either capacitive or inductive transducer used (Figure 1.7).

The mechanical equation of motion can be written as

$$m\ddot{x} + c_m\dot{x} + \frac{dU(x)}{dx} + \theta y = -m\ddot{x}_b \quad (1.1)$$

The relevant electrical equations for each case shown in Figure 1.7 are

$$\begin{aligned} \text{(a)} \quad L\dot{y} + Ry &= \theta\dot{x} \quad (\text{electromagnetic or magnetostrictive}) \\ \text{(b)} \quad C_p\dot{y} + \frac{y}{R} &= \theta\dot{x} \quad (\text{piezoelectric}) \end{aligned} \quad (1.2)$$

where C_p is the capacitance of the piezoelectric element, L is the inductance of the coil and R is the resistance of the load.

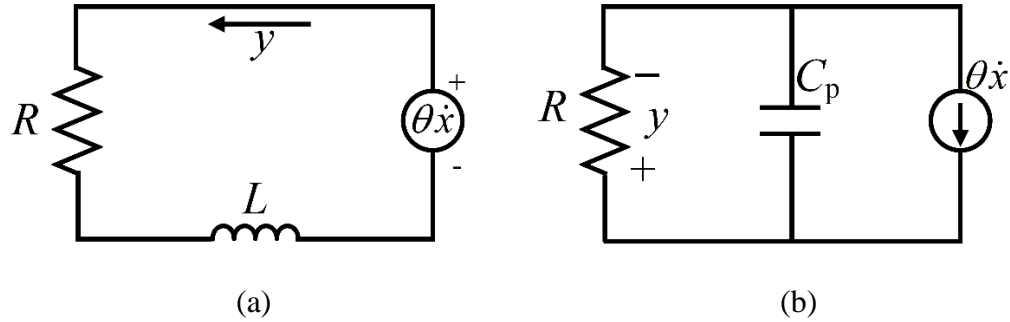


Figure 1.7 (a) Inductive circuit and (b) capacitive circuit coupled with the mechanical subsystem of a VEH

The function $U(x)$ in general can be represented by equation (1.3), however, it depends on the specific harvester. Here, k_1 represents the linear stiffness coefficient and k_3 represents the nonlinear stiffness coefficient.

$$U(x) = \frac{1}{2}k_1x^2 + \frac{1}{4}k_3x^4, \quad \frac{dU(x)}{dx} = k_1x + k_3x^3 \quad (1.3)$$

Depending on the values of k_1 and k_3 the shape of the potential functions can be very different as seen in Figure 1.8(a). When $k_1 > 0, k_3 = 0$, the restoring force is a linear function of the displacement, when $k_1 > 0, k_3 > 0$, the restoring force is said to be nonlinear hardening type mechanism as the stiffness becomes larger for larger displacements, when $k_1 > 0, k_3 < 0$, the restoring force is said to be nonlinear softening type mechanism as the stiffness becomes

smaller for larger displacements, and finally when $k_1 < 0$, $k_3 > 0$, the restoring force is said to be a nonlinear bi-stable mechanism due to the presence of two potential energy wells rather than one like the rest of the cases (shown in Figure 1.8(b))

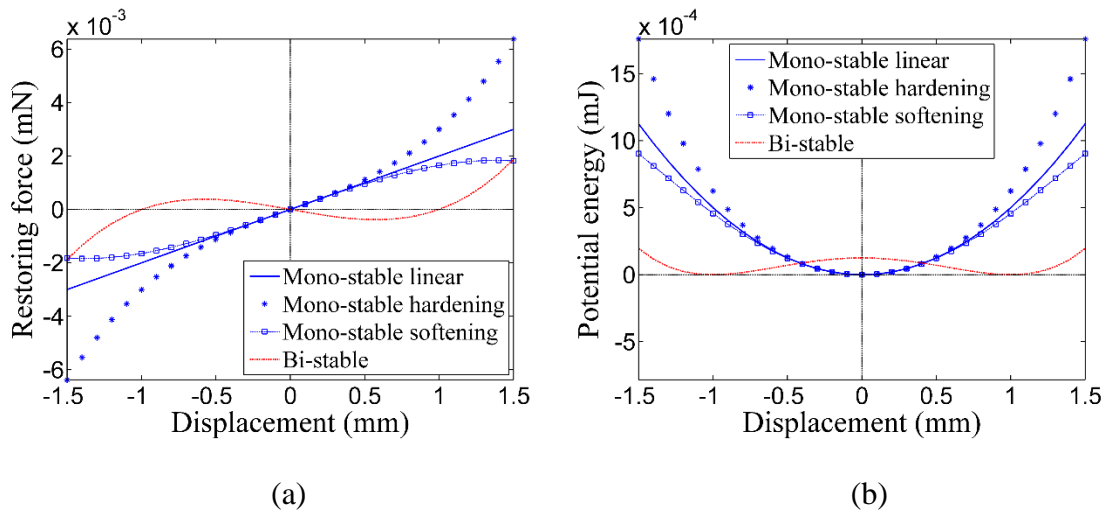


Figure 1.8 (a) Potential energy and (b) restoring force depending on the value of k_1 and k_3 define mono-stable linear, mono-stable hardening, mono-stable softening and bi-stable systems

Assuming that the system is under a harmonic base excitation (\ddot{x}_b of equation (1.1)) with frequency Ω and the system has a linear resonant frequency of ω_n . The frequency response curves (FRCs) of the mono-stable mechanisms are shown in Figure 1.9. It can be seen that the FRC for the hardening mechanism bends towards the right and the FRC for the softening mechanism bends towards the left. This bending of the amplitude-frequency response curves was the motivating result for researchers to further look into nonlinear systems

due to their wider frequency bandwidth of operation. This bend of the FRC results in non-unique solutions for a set of frequency ranges near the resonant frequency.

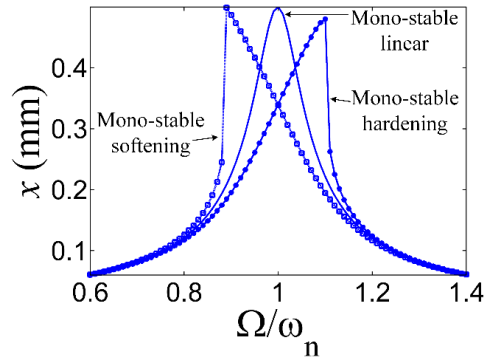


Figure 1.9 FRCs for mono-stable linear, hardening and softening mechanisms

In a bi-stable system depending on initial conditions, the magnitude, and frequency of the excitation the vibrating mass can be confined in a single potential well or move chaotically between the two potential wells or undergo large period inter-well oscillations. Figure 1.10 shows two frequency response curves with two different input excitation amplitude, low level and high levels of excitations. In general the FRC's under low level excitations are similar to the softening type mono-stable system as shown in Figure 1.9. When the amplitude of excitation is increased beyond a certain threshold (A_T) the dynamics become complicated involving from inter-well, chaotic and intra-well oscillations (Figure 1.10(b), the red lines show the stable points). These FRC's are shown for a single set of initial conditions (zero initial conditions about one of the stable points) and can be very different depending on the initial

conditions. Further analysis and details on the frequency response characteristics of bi-stable systems can be found in many advanced books on nonlinear vibrations such as Refs. [13, 14].

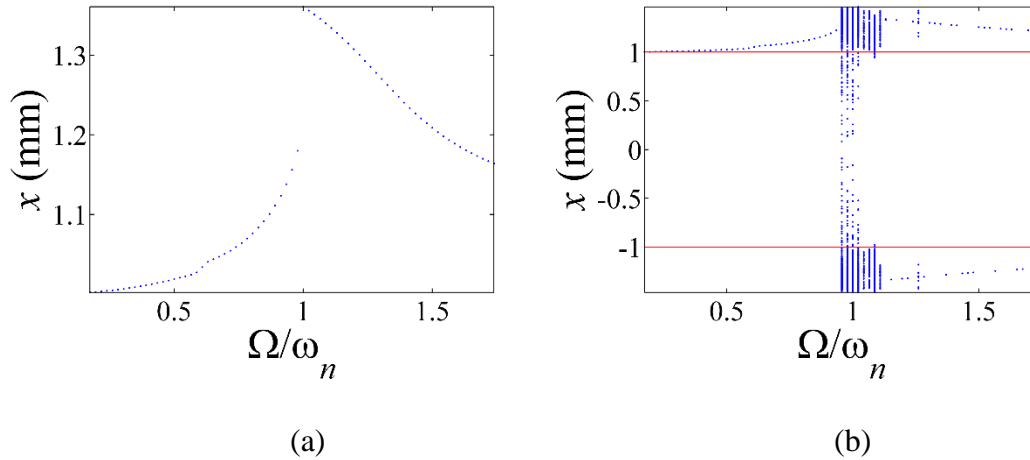


Figure 1.10 FRCs for bi-stable mechanisms with different excitation levels (a) low level of excitation ($A < A_T$) (b) high level of excitation ($A > A_T$)

1.2 Literature review

A brief literature review on VEHs is presented in this section and the discussion is primarily divided based on the type of mechanical subsystem the transducer is integrated with.

1.2.1 Mono-stable linear

From the late 1990's till 2008 most of the literature focused on mono-stable linear harvesters. Due to the simple designs it allowed researchers in understanding of the various parameters that influence the conversion of the vibration energy into useful electrical energy.

The discussion on these linear harvesters in this sub-section will be divided based on the transduction mechanism used.

One of the first investigations on VEHs was an analytical model of an electromagnetic harvester which was established by William and Yates [15]. Their analysis predicted powers of $1 \mu\text{W}$ at 70 Hz and a voltage of 0.1 mV at 330 Hz, with a deflection of around 50 μm . The first prototype of an electromagnetic harvester was by Amirtharajah and Chandrakasan [16]. In theory, they predicted that the average output power can reach $400 \mu\text{W}$ at resonance frequency 2 Hz with amplitude of 2 cm by ignoring mechanical damping. At the micro-scale, Mizuno and Chetwynd [17] proposed a microgenerator which had a resonant frequency of 700 Hz and an output power of 0.4 nW at an input vibration of 0.64 μm . Scherrer et al. [18] discussed the potential of using low-temperature co-fired ceramics to fabricate a multi-layer screen printed coil. A compact package of LTCC coil was made with 96 layers with 6 turns each. The LTCC coil is located between two springs which enable it to cut its flux across the externally placed magnets. The model had a theoretical maximum of 7 mW at a resonant frequency of 35 Hz. Beeby et al. [19] fabricated a silicon based generator which comprised of a micromachined paddle, four NdFeB magnets and a wire-wound coil. The device had a resonant frequency of 9.5 kHz and generated a power of 21 nW at an acceleration level of 1.92 m/s^2 . A review on microscale electromagnetic power generation is discussed by Arnold [20] in which practical limitations of electromagnetic harvesters at the micro scale is discussed with possible improvements.

At the macro-scale, El-Hami et al. [21] proposed a cantilever beam which had a pair of NdFeB magnets on a c-shaped core at the free end with the coil fixed in position in between

the poles of the magnets. The device had a power generation of 0.53 mW at a vibration frequency of 322 Hz. Following the work of El-Hami et al., Glynne-Jones et al. [22] assessed two prototypes, based on a cantilever structure, but with different magnet configurations. The device had a resonant frequency of around 106 Hz, and was mounted on an engine block of a car and was found to have an average power output of 157 μ W. Marin et al. [23] presented a slightly altered design by Glynne-Jones which further improved the performance. Cheng and Arnold [24] investigated the use of a multi-pole magnet array as a way to increase the frequency and amplitude of the output voltage, which addressed the general low voltage outputs of the electromagnetic based harvesters. For low frequency applications, a repulsively stacked magnets configuration was used to harvest energy from traffic-induced bridge vibration by Kwon et al. [25]. Field tests were done on a bridge in South Korea where the designed harvester worked efficiently at frequencies as low as 4.1 Hz. Also, to bridge the gap in understanding of the performance of the electromagnetic harvesters at the micro and macro scale a review focused on this issue on electromagnetic VEHs was presented by Moss et al. [26]. Scaling laws were discussed and an upper limit on the power density of these devices based on their volume and resonant frequency was formulated. Another helpful review on electromagnetic harvesters was by Cepnik et al. [27]; in this review the extensive literature was divided based on key characteristics such as based on design, based on how they were fabricated, based on the kind of input excitation they were tested with, etc.

For piezoelectric based energy harvesting, generators consisting of a cantilever type mechanism were, and still are, the most attractive ones for harvesting energy from vibration by using the d_{31} piezoelectric effect. A first prototype was a tapered cantilever beam developed

by White et al. [28] to ensure a constant strain in the piezoelectric for a given displacement. A power output of around $3 \mu\text{W}$ were generated at around 80 Hz. Later, one of the first most promising tests were conducted by Roundy and Wright [4, 9] who tested a composite piezoelectric cantilever beam generator which was fabricated by attaching a PZT-5A shim to each side of a steel center beam. A mass was attached to the end to tune the generator to resonate at 120 Hz. The prototype produced a maximum power output of $80 \mu\text{W}$ into a $250 \text{ k}\Omega$ load at 2.5ms^{-2} . The final optimized design produced $375 \mu\text{W}$ with an input acceleration of 2.5ms^{-2} at 120 Hz.

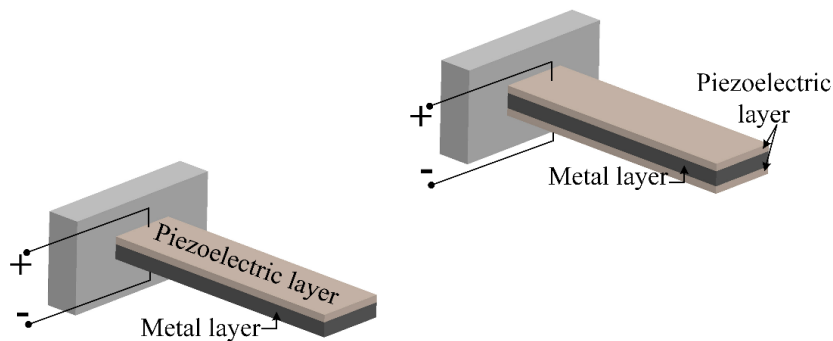


Figure 1.11 Piezoelectric unimorph (left), bimorph (right)

The most commonly used geometrical configuration is the rectangular cantilever beam for piezoelectric energy harvesting but however several errors have propagated in literature in the mathematical modeling of these devices [29]. Erturk and Inman experimentally validated unimorph and bimorph piezoelectric structures (Figure 1.11) by modeling exact analytical solutions with Euler-Bernoulli beam assumptions [30-32]. Over the last decade there have been several review articles on piezoelectric energy harvesting, notable mentions goes to the reviews

by Anton and Sodano [11] and Cook-Chennault et al. [12]. Recently, the flexoelectric phenomena has caught the attention of several researchers for their viable use as a replacement to piezoelectric based VEHs especially at the micro and nano scale due to the favorable scaling of this phenomena [33, 34]. Also, flexoelectric materials are abundant in nature in contrast to piezoelectric materials and is seen as a huge potential area of interest in the future.

The first group to investigate electrostatic transduction method for VEHs was by Chandrakasan's group at MIT [35, 36]. The papers discuss both the methods of operation of electrostatic VEHs, that is, the constant charge and the constant voltage cycles. Later, Roundy et al. [10, 37] further worked on the design, optimization of the comb-drive electrostatic VEH initiated by the Chandrakasan's group. Three different topologies of the comb-drive actuator were analyzed and an 'in-plane gap closing' topology was deemed as the highest power density device of the rest. A prototype device of this topology estimated to generate $100 \mu\text{W}/\text{cm}^3$ from a vibration source of 2.25 m/s^2 at 120 Hz. Later, an electret based electrostatic generator was introduced and working prototypes were developed by Sterken et al. [38]. A recent review on electrostatic energy harvesters by Boisseau et al. [39] and Suzuki [40] discusses the state of the art in vibration energy harvesting with this transduction mechanism.

A slightly related transduction mechanism known as the triboelectric phenomena has been used to develop nanogenerators by Wang et al. [41, 42] at Georgia Tech. This transduction mechanism works by coupling triboelectric effect and the electrostatic induction effect, cumulatively called as the triboelectric phenomena. It is a contact-induced electrification where a material gets electrically charged due to friction. Generators with this phenomena have the advantage of being developed with the use of common organic materials.

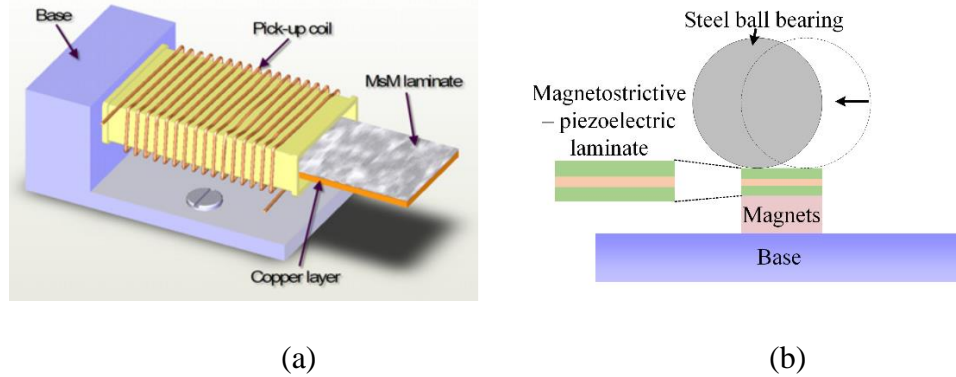


Figure 1.12 Magnetostrictive energy harvesters (a) proposed by Wang and Yuan [43] (b) Moss et al. [44].

Magnetostrictive materials as a transduction material for vibration energy harvesting made a late entry into literature because of the infancy of research in these types of materials. Probably the first investigation in magnetostrictive materials for energy harvesting was by Lundgren et al. [45] where longitudinal oscillations of a Terfenol-D rod were used to harvest energy. After a decade, Huang et al. [46] developed a Terfenol-D/PZT/Terfenol-D composite harvester which induced large strains than conventional PZT's in the traditional d31 bending mode due to their large magnetostriction properties. It achieved a power of 1.2 mW at a resonant frequency of 30Hz and at an acceleration of 5m/s^2 . Bayrashev et al.[47] fabricated a similar composite which yielded a power out in the range of 10 to 80 microwatts at frequencies below 100 Hz. Staley and Flatau [48] were the first to attempt to harvest energy by the Villari effect, Terfenol-D and Galfenol were used in the axial mode with bulk pick up coils and actuation coils for generating bias magnetic fields. Zhao and Lord [49] compared the output electrical powers of Terfenol-D and Galfenol magnetostrictive materials with longitudinal

excitation and concluded Terfenol-D as a superior material for energy harvesting. Wang and Yuan [43] were the first to investigate the feasibility of using amorphous metallic glass 2605SC for harvesting energy from vibrations by operating the material in a flexural bending mode (Figure 1.12(a)). Later Hu et al. [50] optimized factors such as number of MsM layers, coil design and load matching to improve the performance of the MsM energy harvester. Broadband magnetoelectric transducers investigated in [51-53] used multiple cantilever beams tuned to different frequencies to increase the bandwidth of the ME harvester. For energy harvesting from low frequencies a bi-axial magnetoelectric VEH was proposed by Moss et al. [44] which used a permanent magnet on a ME transducer to effectively harvest energy (Figure 1.12(b)). Recently even micro-scale size ME structures have been manufactured on Si cantilevers [54]. These devices consisted of a magnetostrictive $\text{Fe}_{0.7}\text{Ga}_{0.3}$ thin film on a piezoelectric thin film and harvested a power of 0.7 mW/cm^3 at a resonant frequency of 3.8 kHz.

A comparative study on the VEHs using the different transduction mechanisms and on their benefits at each scale is discussed in Mitcheson et al. [55] and Roundy [56]. The VEHs based on magnetostrictive transduction have not been included in these articles (due to the infancy of research on this transduction mechanism at that time), however, due to the mathematical similarity to electromagnetic transduction mechanism reasonable conclusions can be drawn for it as well. There have been several books reviewing mainly the state of the art in linear mono-stable VEHs. Notable mention goes to the book on piezoelectric energy harvesting by Erturk and Inman [57], the book on energy harvesting and their integration with

wireless sensors by Beeby and White [58], and the book on electromagnetic energy harvesting by Spreeman and Manoli [59].

1.2.2 Mono-stable hardening and softening

Burrow and Clare [60] were the first to investigate an intentionally introduced nonlinearity (hardening type) into a VEH. The generator consisted of a cantilever with a set of magnets mounted on its tip which are in close proximity to a laminated iron stator. The magnets are arranged with opposite polarities such that they form a closed magnetic circuit with the stator, the coil is placed in between the iron stator which magnified the flux through it. This arrangement of magnets and the iron stator introduced hardening type nonlinearity into the system and it was found that the response of the system was wider than a linear resonant system under harmonic excitations.

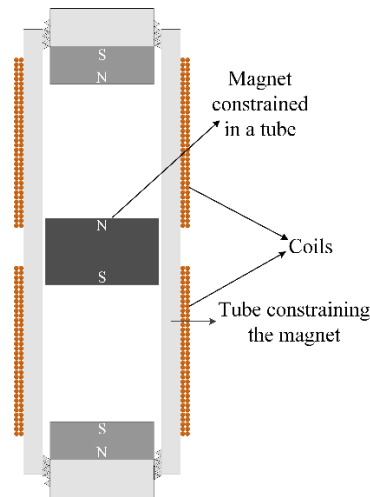


Figure 1.13 A hardening type pseudo magnetic levitation based VEH [61].

Mann and Sims [61] reported a novel hardening type nonlinear mono-stable magnetic levitating harvester which also was found to perform in a wider bandwidth than a linear resonant system under harmonic excitations (Figure 1.13). In a later study, Barton et al. [62] studied the response of the prototype proposed in Burrow and Clare [60] under random excitations as well and concluded that there appears to be no particular benefit over linear resonant type harvesters due to the existence of a low-energy state and a high-energy state, mentioned previously in sub-Section 1.1.2. Zhu and Zu [63] used the nonlinear vibration of magnetic levitation proposed by Mann and Sims [61] to harvest energy from the changing magnetic field in ME material placed in the center. Xianzhi Dai et al. [64] investigated the use of different poling directions of the piezoelectric and magnetostrictive material in the composite to yield higher ME voltage coefficient hence higher power output. The same research group investigated a similar design with multiple magnetostrictive/piezoelectric composite transducers and showed a softening response which yielded more enhanced characteristics [65].

1.2.3 Bi-stable systems

The literature on bi-stable VEH can be divided into how the bi-stability is achieved. The methods of achieving them can be broadly divided into two means, one is by using magnets and the other is by a mechanical load. The first bi-stable system investigated for vibration energy harvesting was by Baker et al. [66] who used a mechanical load to achieve bi-stability. Their system consisted of a post-buckled cantilever beam which was under an axial mechanical load and snapped from one equilibrium position to the other when excited

under harmonic excitations (Figure 1.14 (a)). This study on using bi-stable mechanism for broad bandwidth operation went largely unnoticed for a few years when it later got attention from works by Cottone et al. [67] and Erturk et al. [68] (Figure 1.14 (b)). Both of these works used an arrangement of magnets to achieve magnetoelastic buckling.

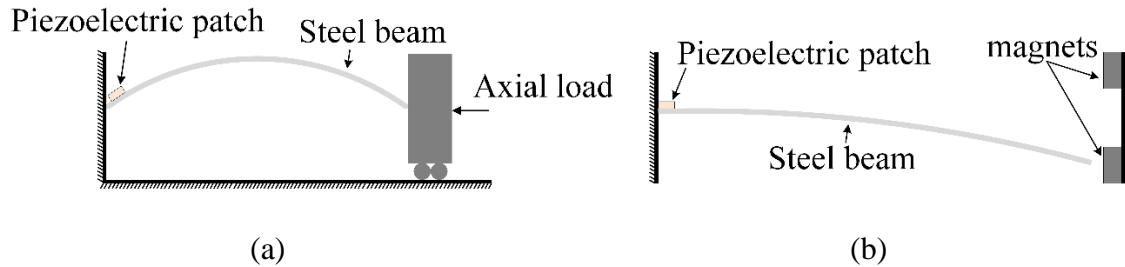


Figure 1.14 Bi-stable mechanism proposed by (a) Baker et al. [66] and Mansana and Daqaq [69] and (b) Erturk et al. [68].

Mann and Owens [70] were probably the first to demonstrate a bi-stable electromagnetic harvester with an additional set of magnets arranged over their initial design [61] which promoted bi-stability. Ramlan et al. [71] altered the geometry of the mechanism proposed in Burrow and Clare [60] to make it a bi-stable system. They found that the response of the device was insensitive to a range of excitation frequencies and hence had the benefit of operating over a wider frequency bandwidth of operation. Nguyen et al. [72] investigated a bi-stable mechanism achieved by curved springs and showed substantial enhancement in the frequency bandwidth of operation. They used the electrostatic transduction technique to achieve vibration energy harvesting.

Recently there have been some review articles discussing the benefits of bi-stable mechanisms over other mechanisms present in literature. Notable mention goes to two comprehensive reviews by Daqaq et al. [73] and Harne and Wang [74] which can be referred for further discussion on this mechanism.

1.2.4 Frequency-up conversion techniques

The frequency-up conversion type VEHs consist of converting the low frequency type vibration into high frequency resonant vibrations which are then used to transduce into electrical energy. Kulah and Najafi [75] were among the first to introduce the concept of frequency-up conversion based vibration energy harvesting. They discussed the major drawbacks of linear resonant type VEHs to harvest efficiently at low frequencies and proposed a magnetically buckled frequency up converted harvester using piezoelectric [76] or electromagnetic transduction [77]. Several other researchers implemented the frequency-up conversion by contact and non-contact based methods to show superiority over frequency bandwidth of operation and power output levels [78-81].

1.2.5 Direct force generators

The first examples of piezoelectric energy harvesting was by using an impact method for energy extraction. Umeda et al. [82] were the first group to investigate the energy transfer to a load when a steel ball impacted on to a plate bonded with PZT. Later they also explored the feasibility of storing the charge on a capacitor and a battery after rectifying it [83]. Recently

there have been fewer studies on these impact based energy harvesting [84, 85] as the application for such devices are still unclear.

Clark and Ramsay [86] considered piezoelectric energy harvesting for medical applications by harvesting energy from fluctuations of pressure in blood vessels. However, the study showed power levels of only one microwatt and suggested that the power can be supplied to load electronics of a low duty cycle. Donelan et al. [87] suggested the possibility of harvesting energy from the bending of a knee, unlike the shoe inserts this mechanism assists the leg motion in decelerating the swing motion of the stride, output powers of up to 7 W were generated. Two review papers aptly describe the challenges that are yet to be overcome for harvesting energy from human motion such as increased power output levels, rectification, manufacturing and lowering the resistance to motion [7, 88].

1.3 Challenges

Most of the VEHs discussed to date are more suited to aerospace and mechanical applications. The performance of similar devices in harvesting energy from civil infrastructures and human motion is severely limited due to the unique challenges in these applications. Some of the challenges faced that will be addressed are:

Challenge 1: High operating frequency

The ambient vibration of civil structures and human motion is concentrated on relatively low frequencies [89] ($< 10\text{Hz}$), Figure 1.15, especially the long-span suspension and long-span cable-stayed bridges ($< 1\text{Hz}$) [90-93]. Most of the current VEHs, which operate on

designs which consist of a cantilever beam with an end mass, operate at a much higher operating frequency. Due to the limitation of the maximum mass attached to the tip, high stiffness of the cantilever beam and the brittleness of the PZT transducer, it is difficult to achieve low resonance frequencies with this type of design. A new VEH design is needed which can work at such low frequencies.

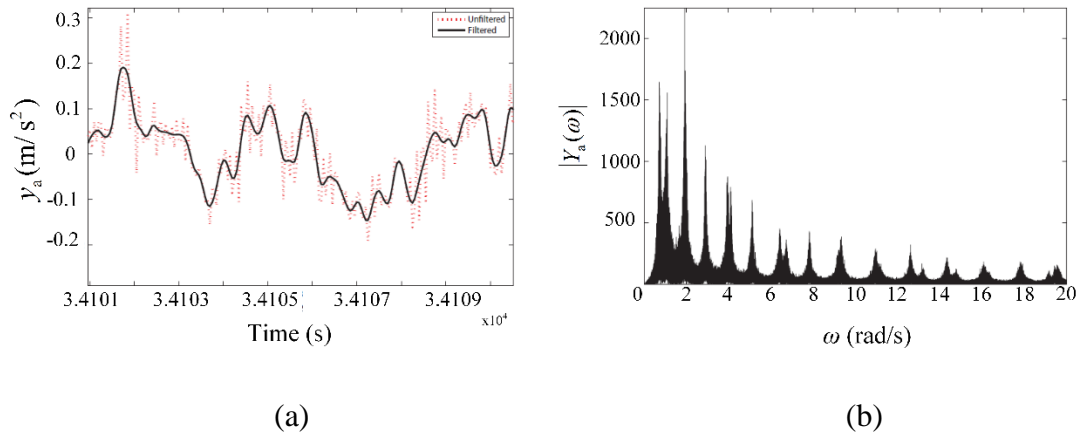


Figure 1.15 (a) Acceleration time history of a bridge (b) Frequency content of acceleration on a bridge [89].

Challenge 2: High level of mechanical damping

Most of the energy that flows into the harvester is not completely converted into useful electrical energy. Portion of it is lost in mechanical damping, another portion of it is lost due to the resistance of the transduction mechanism (electrical damping) and the remaining part is the useful energy used to power the sensor. In many cases, the resistance of the transduction mechanism is usually unavoidable. The acceleration levels available are rather low for civil

structures [94, 95] unlike for other vibration energy harvesting applications; hence efficiency becomes an important criterion. A new VEH needs to be developed in which mechanical damping can be greatly reduced or even completely eliminated.

Challenge 3: Narrow operating frequency range

Ambient vibrations usually are wideband in nature, yet current linear VEHs are limited to design around the lowest natural frequency. However, few nonlinear VEH designs with softening, hardening or bi-stable structures which operate in a wider frequency bandwidth have been suggested [61, 67, 70, 96-98]. Most of these VEHs need at least an order higher acceleration than those available in ambient environments, like civil infrastructures, to unlock their nonlinearity and showcase their wide frequency operation. A new VEH is needed which can showcase the wide frequency operation under really low excitations.

1.4 Objective and Scope

The objective of this work is to address the challenges described in Section 1.3 by exploring the possibility of novel diamagnetically stabilized magnet levitation systems as viable mechanisms for vibration energy harvesting. To meet this end, the discussion in the following chapters is divided as follows.

In Chapter 2, magnetism and magnetic materials are introduced with a brief description about their underlying mechanism. Earnshaw's theorem and its shortcoming are discussed which allow for passive stable levitation with the use of diamagnetic materials. Also, the

different forms of levitation using diamagnetism namely, diamagnetic levitation and diamagnetically stabilized magnet levitation are introduced.

In Chapter 3, a novel electromagnetic VEH that uses a vertical diamagnetic levitation (VDL) system is conceptualized, designed, fabricated, and tested. The harvester consists of a lifting magnet (LM), a floating magnet (FM) and two diamagnetic plates (DPs). The LM balances out the weight of the FM and stability is brought about by the repulsive effect of the pyrolytic graphite plates which serve as the DPs. Two thick cylindrical coils, placed in grooves which are engraved in the pyrolytic graphite plates, are used to convert the mechanical energy into electrical energy efficiently. Initial studies showed that simple analytical techniques such as the dipole model and the image method provide useful guideline for understanding the potential of a diamagnetic levitation system, however, it is discussed here that the more accurate semi-analytical techniques such as the thin coil model and the discrete volume method are needed for a practical design of the VDL system. A thorough theoretical analysis is carried out to compare with experimental results.

In Chapter 4, a detailed analysis of a mono-stable VDL system for optimal vibration energy harvesting is presented. The influence of the cylindrical geometry of the FM, the LM and the DP are parametrically studied to assess their effects on the levitation gap, size of the system and the natural frequency. For efficient vibration energy harvesting using the VDL system, ways to mitigate eddy current damping and a coil geometry for transduction are critically discussed. With the optimized parameters, an experimental system is realized which showed a hardening type nonlinearity. The main challenges the authors faced in designing an efficient VEH were the strict stability conditions and the limitations of the maximum amplitude

of the FM in the vertical direction, which was inherently limited by the distance between the DPs which in turn was coupled back with the stabilization condition.

To overcome the challenges mentioned in Chapter 4, the authors explored another possible configuration of the diamagnetic levitation mechanism for vibration energy harvesting in Chapter 5. A horizontal diamagnetic levitation (HDL) system for vibration energy harvesting in contrast to the VDL system is proposed. In this configuration, two large magnets, alias LMs, are arranged co-axially at a distance such that in between them a magnet, alias FM, is passively levitated at a laterally offset equilibrium position. The levitation is stabilized in the horizontal direction by two DPs made of pyrolytic graphite placed on each side of the floating magnet. This HDL configuration mitigates the limitation on the amplitude of the FM imposed in the VDL configuration and exploits the ability to tailor the geometry to meet specific applications due to its frequency tuning capability. A simple circular coil geometry is designed to replace a portion of the pyrolytic graphite plate without sacrificing the stability of the levitation for transduction. An experimental setup exhibited a weak softening frequency response and validated the theoretical findings.

Due to the potential advantages of the HDL configuration over the VDL configuration, Chapter 6 identifies and studies the parameters that characterize a HDL system for use as a VEH. The influence of the geometry of the FM, the LM and the DP are parametrically studied to quantify their effects on the size of the system, the stability of the levitation and the resonant frequency of the system. For vibration energy harvesting using the HDL system, a coil geometry and eddy current damping are critically discussed. Based on the analysis, an efficient experimental system is setup which showed an improvement in the performance from the state

of the art VEHs in the low frequency range (< 5 Hz). Also, the use of repelling magnets is theorized to increase the stability range in the HDL and VDL configurations.

Chapter 7 introduces a bi-stable HDL (BHDL) system from an initial concept to an experimental prototype and discusses the use of repelling magnets to achieve this. Design constraints are discussed with respect to stability of the FM in a range of different dynamics and equality of both the potential energy wells of the system. A prototype is setup with a priority given to stability over having an ideal equal potential energy well system. A system is theoretically modelled and the dynamics of the FM are experimentally validated with three different frequency sweeps each at a different constant excitation amplitude. It was observed that larger the amplitude of excitation, larger is the bandwidth of operation, consistent with literature. Next, a simple coil geometry is discussed that was incorporated into the DP without affecting the stability of the FM at both of the stably levitation positions. Finally, experimental voltage FRCs measured across a resistive load are validated from theoretical simulations for a constant input amplitude excitation.

Chapter 8 discusses the major conclusions of this work and proposes future research directions to improve the efficiency and the frequency bandwidth of operation of the BHDL system based VEH. Also, suggestions are given on reducing the overall size by using two-dimensional magnet array configurations for diamagnetic levitation based VEHs and on exploring the possibility of a bi-stable VDL system based VEH.

2 Magnetic materials

In this chapter, the fundamentals of magnetism will be introduced along with the underlying mechanism of magnetic behavior in materials. Materials are divided into five major categories based on their magnetic behavior, they are, diamagnetic, paramagnetic, ferromagnetic, ferrimagnetic and antiferromagnetic. There are two forms of magnetic moments at the atomic level which contribute to magnetism in materials, they are, the orbital magnetic moment and the spin magnetic moment. These two magnetic moments along with the laws of quantum physics dictate the macroscopic behavior of the materials to external magnetic fields.

Special focus is then laid on how Earnshaw's theorem prohibits magnetic levitation and how levitation using diamagnetic materials is possible despite the theorem. Following this, a brief literature review on the levitation mechanisms using diamagnetism and its possible applications are presented. Finally, the diamagnetically stabilized magnet levitation mechanisms which form the core of this dissertation will be introduced.

2.1 Magnetism

In lay man terms the word ‘magnetism’ is associated with the notion of a magnet getting attracted to something made of iron. This attraction force not only varies between the magnet and different materials but would also seem to be absent with some materials. Based on how materials responds when an external magnetic field is applied, such as the action of bringing a magnet in its vicinity, they can be classified into different categories which will be discussed in this section. Before one can study the response of materials to magnetic field, the fundamental parameters associated with magnetism (**B**, **H** and **M**) need to be understood first.

The term magnetic field is conventionally referred to by the symbol **H**. It is generated whenever there is a motion of an electrical charge. Alternatively, this field intensity **H** is defined so that the line integral of **H** along a closed curve (**I**) is equal to the total current enclosed (*I*). That is,

$$\oint \mathbf{H} \cdot d\mathbf{l} = I \quad (2.1)$$

When a material is introduced in this magnetic field, the response of this material is called as magnetic induction, denoted by **B**. When this material is free space or vacuum they simply defer by a constant μ_0 .

$$\mathbf{B} = \mu_0 \mathbf{H} \quad (2.2)$$

When mentioning magnetic fields in free space or vacuum, one may be referring to **B** or **H** as both just defer by a constant.

For a given surface (**S**), the magnetic induction passing through that area is termed as magnetic flux, ϕ . Thus,

$$\phi = \iint_S \mathbf{B} \cdot d\mathbf{S} \quad (2.3)$$

for this reason \mathbf{B} is also called as the magnetic flux density. As discussed, a magnetic field arises only because of the motion of an electric charge. By this definition one can consider a simple loop of a conductor carrying current to be a fundamental unit for magnetism. If such a current loop has an area A and carries a current I , a term known as magnetic moment, $\boldsymbol{\mu}$, is defined by their product

$$\boldsymbol{\mu} = \hat{\mathbf{n}}IA \quad (2.4)$$

where $\hat{\mathbf{n}}$ is the unit vector in a direction normal to the loop. As an equivalence to electricity, where its fundamental unit is an electric dipole, this circular loop of current is called as a magnetic dipole. Also, the field produced by this loop is identical to the one produced by two imaginary magnetic poles of strength p and separated by a distance of l . Hence, the magnetic dipole moment, similar to the electric dipole moment, is defined alternatively as $\boldsymbol{\mu} = \hat{\mathbf{n}}pl$. This pole strength is similar to the flux term defined earlier, only in a different unit system, that is, $p = \phi / \mu_0$. Hence the magnetic moment can be also written as

$$\boldsymbol{\mu} = \phi l / \mu_0 \quad (2.5)$$

This dipole moment per unit volume is defined as magnetization, \mathbf{M} . So, if we consider a simple bar magnet with a flux ϕ at the center of the magnet, its magnetization if it has a dipole of length l and a cross-sectional area A is given by

$$\mathbf{M} = \frac{\boldsymbol{\mu}}{Al} = \frac{\hat{\mathbf{n}}\phi}{\mu_0 A} = \frac{\mathbf{B}}{\mu_0} \quad (2.6)$$

In this case of the simple bar magnet when there is no external magnetic field (\mathbf{H}) the magnetic induction, \mathbf{B} , is equal to $\mu_0\mathbf{M}$. Hence, the magnetic induction in a more general case is the sum of the magnetic induction in free space due to the external magnetic field and the induction from the magnetization of the material, from equation (2.2) and (2.6),

$$\mathbf{B} = \mu_0(\mathbf{H} + \mathbf{M}) \quad (2.7)$$

This equation can be rewritten to $\mathbf{H} = 1/\mu_0 \mathbf{B} - \mathbf{M}$ which is analogous to $\mathbf{D} = \epsilon_0 \mathbf{E} + \mathbf{P}$ as in both cases the auxiliary fields relates to the fundamental fields and the contribution from the material. The magnetization is related to the external magnetic field, linearly for some materials, by the following relation,

$$\chi = \frac{\mathbf{M}}{\mathbf{H}} \quad (2.8)$$

where χ is called the magnetic susceptibility of the material. The magnetic susceptibility (χ) expresses the responsiveness of a material to the applied magnetic field and is related to the permeability of the material (μ) by

$$\begin{aligned} \mu &= \mu_0\mu_r \\ \mu_r &= 1 + \chi \end{aligned} \quad (2.9)$$

where μ_r is called the relative permeability. More details on how and why materials respond differently with applied magnetic fields along with how they are classified based on these underlying mechanisms will be discussed in the next section.

2.2 Magnetic materials

The various types of materials can be broadly classified based on their magnetic susceptibility amongst other things. Materials with their susceptibility slightly less than zero are known as diamagnetic materials. Materials with susceptibility slightly greater than zero can be paramagnetic or antiferromagnetic materials and if their susceptibilities are large and positive they can be ferromagnetic or ferrimagnetic materials. This sign of the susceptibility leads to the material being attracted or repelled in an external non-uniform magnetic field, which can be understood by looking at the magnetic potential energy of the material. Consider the net magnetic potential energy (U) of a material with magnetization \mathbf{M} placed in a magnetic field \mathbf{B} ,

$$U = -\frac{1}{2} \int \mathbf{M} \cdot \mathbf{B} dV \quad (2.10)$$

Even though equation (2.8) holds only for linear materials, a qualitative understanding of the general material response can be understood by using that in equation (2.10),

$$U = -\frac{\chi}{2} \int \mathbf{H} \cdot \mathbf{B} dV \quad (2.11)$$

It can be seen from this equation that for materials with positive susceptibility the material is pushed towards stronger magnetic fields as it tends to a lower potential energy whereas an opposite response for materials with negative susceptibility. Hence, diamagnetic materials (negative susceptibility) are repelled and pushed towards weaker magnetic fields and paramagnetic, ferromagnetic, ferrimagnetic and antiferromagnetic (positive susceptibility) are pulled towards stronger magnetic fields.

In order to understand the magnetic properties of a material the source of the susceptibility at the atomic level which differentiates these materials needs to be addressed. The magnetism in a material is associated with the magnetic moments generated due to motion of electron in its orbit and due to the spin of the electron (Figure 2.1). Diamagnetism is present to some extent in all kinds of materials, however weak and usually counteracted by other forms of magnetism, is discussed first.

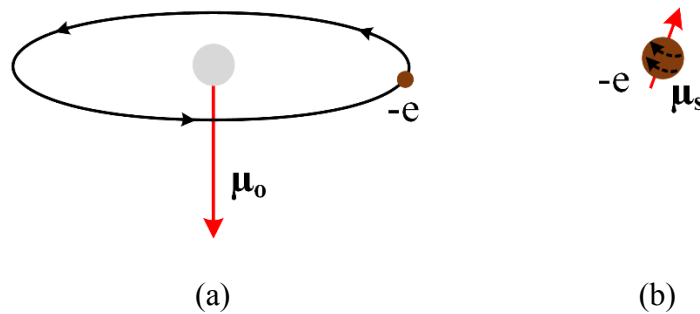


Figure 2.1 (a) Orbital magnetic moment (μ_o) and (b) spin magnetic moment (μ_s)

2.2.1 Diamagnetism

As mentioned earlier this form of magnetism represents materials which opposes the external magnetic field \mathbf{H} , that is, expel some of the magnetic field from entering into it. When an external magnetic field is applied, electrons revolving in the orbits of atoms, which represent like a current in a conductor, accelerate or decelerates in order to create an opposing magnetic moment. A more accurate explanation of the phenomena would represent the currents as precession of the electrons orbit about the magnetic field direction, also known as Larmor precession. A schematic of this precession of the orbits is shown in Figure 2.2, here, p is the

momentum vector and ω_L is the precession frequency (or also called as Larmor frequency). This is a result of the Lenz's law which causes change in the motion of the electron to oppose the external field. The force due to this change in acceleration balances the force from the external magnetic field. This phenomena is most dominant in materials in which the individual atoms have a net zero magnetic moment in the absence of an external field. This zero magnetic moment is most likely possible in materials which have only balanced electrons in there orbits.

Superconductive materials exhibit a superior form of diamagnetism, which is they completely expel magnetic fields from their interior, below a certain critical temperature and a critical magnetic field. The phenomena behind this superior diamagnetism, however, is not Lorentz's law but an effect called as the Meissner effect, description of which is out of the scope of this dissertation.

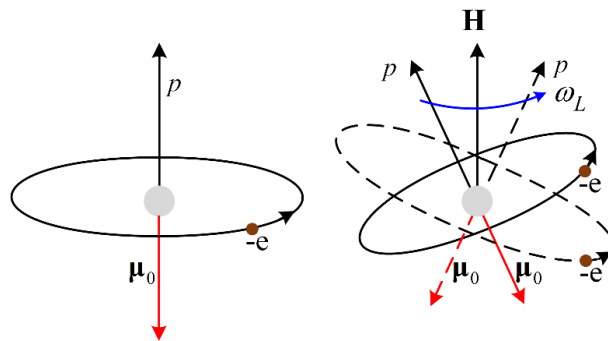


Figure 2.2 Schematic showing precession of orbital magnetic moment in diamagnetic materials due to an external magnetic field \mathbf{H} .

2.2.2 Paramagnetism

Paramagnetism is the orientation of the magnetic moments of the atoms in the direction of the applied magnetic field. Paramagnetism is a weak phenomenon and the effect of

diamagnetism in the material needs to be also considered to determine its net response to an external magnetic field. The main difference between materials which exhibit dominant paramagnetism or diamagnetism is that the individual atoms in the former have a net magnetic moment unlike the latter. Paramagnetic materials have a low positive susceptibilities of the order of 10^{-3} to 10^{-5} . The reason behind paramagnetism can be categorized mainly into two different models, one is the Langevin theory of orbital paramagnetism and the other is the Pauli paramagnetism model.

The Langevin theory applies to materials in which non interacting unbalanced orbital magnetic moments exist. Thermal energy tends to randomize these magnetic moments and hence in the absence of an external magnetic field the orbital magnetic moments result in a net zero magnetization. When an external field is applied, the individual magnetic dipoles tend to align themselves with the field direction. A schematic of the rotation of the magnetic dipoles of the paramagnetic material are shown in Figure 2.3. In most cases a fairly simple behavior is found, the susceptibility (χ) depending strongly on temperature, known by as Curie law is

$$\chi = \frac{C}{T} \quad (2.12)$$

where T is the absolute temperature and C is the ‘Curie constant’.

Metals with a few exceptions, such as the rare earth elements, do not obey the Curie law because the outermost electrons are usually not localized at the atomic core. In such metals the conduction band is identically split for both spin-up and spin-down electrons. When an external magnetic field is applied, some of the electrons in the unfavorable direction jump to the more favorable direction. The resulting net spin moment contributes to the spin

paramagnetism. Only electrons that are in the highest occupied quantum state can realign in the magnetic field direction. This form of paramagnetism is called the Pauli paramagnetism.

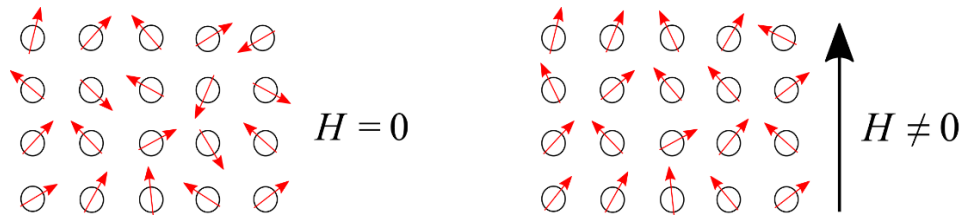


Figure 2.3 Schematic of orientation of magnetic dipoles in paramagnetic materials

2.2.3 Ferromagnetism

This magnetism can be regarded as a strong form of paramagnetism as these materials have high magnetic susceptibilities which are also due to unpaired electrons. The main difference between ferromagnetic and paramagnetic materials is that unlike the latter parallel alignment of spins occurs spontaneously in ferromagnetic materials, a certain cooperation occurs between the neighboring atoms for this phenomena to occur, which results in the formation of domains in the material. This cooperation occurs due to the quantum exchange energy interactions between the neighboring atoms. This exchange energy interactions depends, amongst other things, on the distance between the neighboring atoms which is shorter for ferromagnetic materials and hence stronger interaction energies exist.

Due to the positive interaction energy, all the electron spins in a crystal will be aligned in parallel and north, south poles will be created on opposite ends of the solid as shown in Figure 2.4(a). This will create a large magnetic field external to the material which is energetically less favorable. The magnetostatic energy of the field can be reduced if the crystal

is divided into two domains that are magnetized in opposite directions; this reduces the external magnetic field as shown in Figure 2.4(b). Further division into smaller domains will further reduce the magnetostatic energy (Figure 2.4(c)) but this division is halted at a certain point where it is no longer advantageous. The point at which this halting takes place depends on the energy stored in each domain wall. The transition of the spins from one domain to the other doesn't happen drastically but happens gradually as the exchange energy favors only parallel spins. Some amount of energy is required in making this transition wall or domain wall. Hence an optimum domain size is reached when the energy for further division into smaller domains and the exchange energy for parallel spins counteract each other. The crystal structure of ferromagnetic materials are generally either body-centered cubic (e.g. iron), face-centered cubic (e.g. nickel) or hexagonal (e.g. cobalt). Based on the crystal structure some directions of magnetization are easier than others. So this anisotropy in magnetization also plays a role in the thickness of the domain wall as it restricts magnetization in other directions.

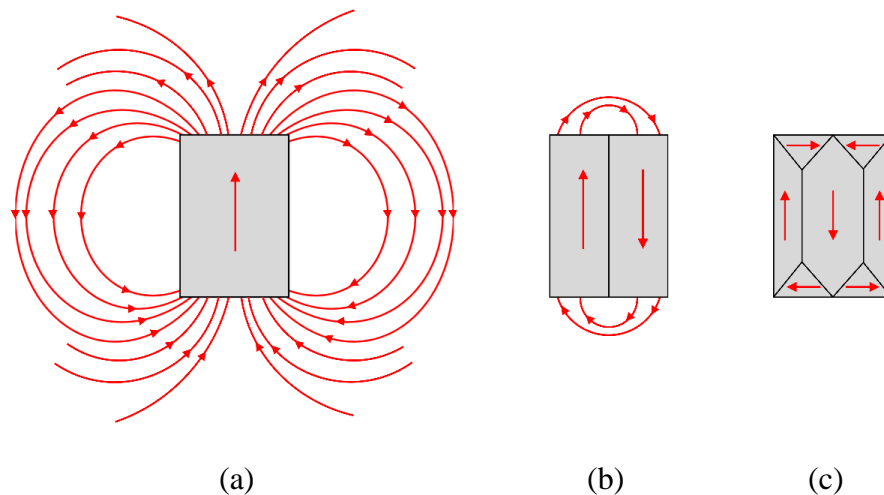


Figure 2.4 Division into magnetic domains to decrease the magnetostatic energy [99]

On a macroscopic scale, however, the net magnetization vector is zero because the domains are randomly oriented for a minimum magnetostatic energy and the magnetic moments cancel one another. When a ferromagnetic material is subjected to an applied field, the spins of the atoms start to align themselves with the magnetic field. The domains already in the direction of the magnetic field start to become larger and the ones in the opposite direction start to shrink. At full saturation almost all the magnetic domains are pointed in the direction of the magnetic field. It would seem that the domain walls move in the opposite sequence as shown in Figure 2.4, that is from (c) to (a) under an external magnetic field pointing upwards. The vector sum of all the magnetic moments and the associated vector magnetization are very large, leading to extremely large values of magnetic susceptibility χ and relative permeability μ_r as show in Table 2.1. This effect is not necessarily linear as for paramagnetic materials because it strongly depends on the structure and dimensions of the domains and their evolution and interaction. At high temperatures, thermal agitation overcomes these interaction energies and the susceptibility follows a modified form of the Curie law known as the Curie-Weiss law.

$$\chi = \frac{C}{T - T_c} \quad (2.13)$$

where C is again the Curie constant, T is the absolute temperature and T_c is the curie temperature.

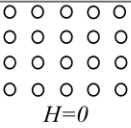
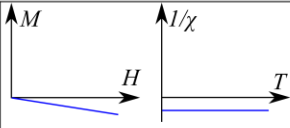
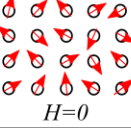
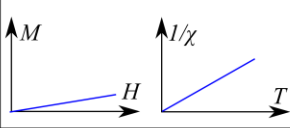
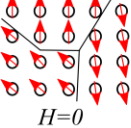
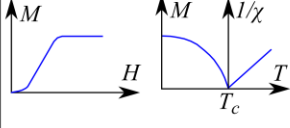
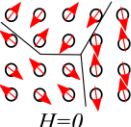
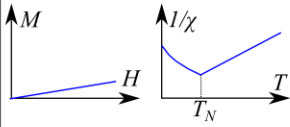
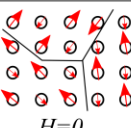
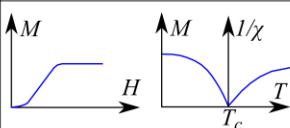
2.2.4 Antiferromagnetism

Antiferromagnetic materials are similar to ferromagnetic materials, in the sense that their magnetism also arises from the cooperative phenomena which forms domains but with a distinct difference. This form of magnetism is best understood by imagining a material with two cations which have similar magnetic moments in them but with their moment's antiparallel to each other. This antiparallel arrangement is a result of the exchange energy interactions between the neighboring atoms in the lattice. This will result in a net magnetic moment of zero and the material behaves in the same way as paramagnetic materials when an external magnetic field is applied.

They have magnetic susceptibility of the same order as paramagnetic materials. Antiferromagnetic materials can be distinguished from paramagnetic materials in that the value of χ increases with temperature, whereas χ shows no change or decreases in value as temperature rises for paramagnetic materials. However, when the temperature is increased beyond a certain temperature called as Néel temperature (T_N), the thermal agitation overcomes the interaction effects and the susceptibility varies with the temperature much similar to the paramagnetic materials as seen in Table 2.1.

$$\chi = \frac{C}{T + T_N} \quad (2.14)$$

Table 2.1 Summary of magnetic materials [100-102]

| Magnetism | Examples | Magnetic behavior | |
|--------------------|--|---|---|
| Diamagnetism | Bi, Si, Cu, inert gases Susceptibility small and negative (-10^{-6} to -10^{-5}) |  <p>Atoms have no magnetic moments.</p> <p>$H=0$</p> |  |
| Paramagnetism | Al, O ₂ , MnBi Susceptibility small and positive (10^{-5} to 10^{-3}) |  <p>Atoms have randomly oriented magnetic moments.</p> <p>$H=0$</p> |  |
| Ferromagnetism | Fe, Ni, Co, Gd Susceptibility large (generally > 100) |  <p>Atoms are organized in domains which have parallel aligned magnetic moments.</p> <p>$H=0$</p> |  |
| Antiferromagnetism | Cr, MnO, FeO Susceptibility small and positive (10^{-5} to 10^{-3}) |  <p>Atoms are organized in domains which have antiparallel aligned moments.</p> <p>$H=0$</p> |  |
| Ferrimagnetism | Fe ₃ O ₄ , MnFe ₂ O ₄ , NiFe ₂ O ₄ Susceptibility large (generally > 100) |  <p>Atoms are organized in domains which have a mixture of unequal antiparallel aligned moments.</p> <p>$H=0$</p> |  |

2.2.5 Ferrimagnetism

These materials are iron-metal oxides, also known as ferrites. They behave similarly to ferromagnetic materials by exhibiting a spontaneous magnetic moment and hysteresis below the Curie temperature. They have complex crystal structures, which result in different exchange energy interactions and lead to a mixture of parallel and antiparallel alignments in the neighboring atoms. The opposite spins are not equal in magnetic moment and hence result in a net magnetization lower than general ferromagnetic materials. A 2D schematic is shown in Table 2.1. The unequal lengths of the arrows show their difference in the magnetic moments. Attempts have been made to make ferrites with rare earth metals which have larger magnetic

moments than iron and hence then the net magnetization is similar to that of ferromagnetic materials. Ferrimagnetic materials have the added advantage of being good insulators and hence they are suitable for high frequency applications by mitigating eddy currents.

The temperature dependence of ferrimagnetics is similar to ferromagnetic material, the magnetic ordering decreases with temperature and vanishes at the Curie temperature (T_C). Above this temperature the material behaves like paramagnetic material as seen in Table 2.1.

2.3 Diamagnetic levitation and diamagnetically stabilized magnet levitation

The brief introduction to magnetism and magnetic materials in this chapter is to form a basis into the understanding of magnetic levitation possible due to diamagnetic materials. Any form of magnetic levitation shall contradict Earnshaw's theorem [103]. This theorem states that particles in ether cannot have a stable equilibrium position if interacted by forces which vary by the inverse of the square of the distance between them. Since many of the forces in nature are of the inverse square law ($1/r^2$), this theorem's implication go beyond that of ether and in our case particularly to magnetic forces.

For example, a magnetic material with a constant magnetic dipole (\mathbf{M}) when placed in an external magnetic field (\mathbf{B}), the energy of this dipole is given by

$$\mathbf{U} = -\mathbf{M} \cdot \mathbf{B} + mgz = -(M_x B_x + M_y B_y + M_z B_z) + mgz \quad (2.15)$$

$$\nabla U = -(M_x \nabla B_x + M_y \nabla B_y + M_z \nabla B_z) + mg$$

The first gradient of the potential energy can be zero, which is dependent only on the gradient of the magnetic field, but for stability the Laplace of the potential energy need to have a minimum, that is,

$$\nabla^2 U = M_x \nabla^2 B_x + M_y \nabla^2 B_y + M_z \nabla^2 B_z \quad (2.16)$$

As the divergence and curl of each of the individual components of a magnetic field are zero in the absence of any currents, hence, $\nabla^2 U = 0$. This results in no maximum or minimum of the energy, only saddle points, hence no stable point is possible for a magnetic dipole particle when interacted by magnetic and gravitational forces alone. This simple proof describes Earnshaw's theorem.

However, in materials like paramagnetic and diamagnetic materials, the magnetic dipoles align either parallel or antiparallel to the magnetic field and are proportional to the magnetic field. As Earnshaw's theorem considers only hard fixed magnets, these magnetic materials can cause exceptions to the theorem. . Assuming $\mathbf{M} = k\mathbf{B}$ such that k is a positive constant for paramagnetic materials and a negative constant for diamagnetic materials, the magnetic potential energy of such materials in an external magnetic field are,

$$\mathbf{U} = -\mathbf{M} \cdot \mathbf{B} + mgz = -k|\mathbf{B}|^2 + mgz = -k(B_x^2 + B_y^2 + B_z^2) + mgz \quad (2.17)$$

The laplacian of the potential energy needs to be a minimum for the material to have an equilibrium in this external magnetic field.

$$\nabla^2 U = -k \left(\nabla^2 |B_x|^2 + \nabla^2 |B_y|^2 + \nabla^2 |B_z|^2 + B_x \nabla^2 B_x + B_y \nabla^2 B_y + B_z \nabla^2 B_z \right) \quad (2.18)$$

but for magnetostatic fields $\nabla^2 B_x = \nabla^2 B_y = \nabla^2 B_z = 0$, hence,

$$\nabla^2 U = -k \left(\nabla^2 |B_x|^2 + \nabla^2 |B_y|^2 + \nabla^2 |B_z|^2 \right) \quad (2.19)$$

As $\nabla^2 |B_x|^2, \nabla^2 |B_y|^2, \nabla^2 |B_z|^2 > 0$, hence, for a paramagnetic material the laplacian of the potential energy can never be positive (as, $k > 0$), hence there can be only maximum energy points and no equilibrium points in space. However for a diamagnetic material, the laplacian of the potential energy is always positive (as, $k < 0$); hence, stability is possible. Overall diamagnetic materials contradict Earnshaw's theorem in two ways, one is that their magnetization is not a constant but depends on the external magnetic field and second is that its magnetic moment opposes external magnetic field. These two exclusions make it possible for diamagnetic materials to have a potential minimum.

The term 'diamagnetic' or 'diamagnetism' was first coined by Michael Faraday associating analogy with dielectrics in the year of 1845. Quickly after that, William Thomson (Lord Kelvin) theoretically showed the feasibility of diamagnetic levitation [104]. Later, in the 20th century stronger magnetic materials were available to experimentally verify William Thomson's prediction. As a result, W. Braunbeck levitated small beads of graphite with the help of an electromagnet [105]. Later, A.H. Boerdijk [106] did a similar setup as Braunbeck but he used permanent magnets instead of electromagnets and hence was able to decrease the size of his setup. Boerdijk [107] was also the first to levitate a magnet using diamagnetic materials. Only recently it has reached considerable attention after Berry and Geim [108], Geim et al. [109] and Simon et al. [110] demonstrated the mechanism by levitating a frog and by levitating a permanent magnet between two fingers (Figure 2.5). The phenomena of frog

levitation has particularly garnered large media attention as it was the first time a living object was levitated purely due to magnetic fields.

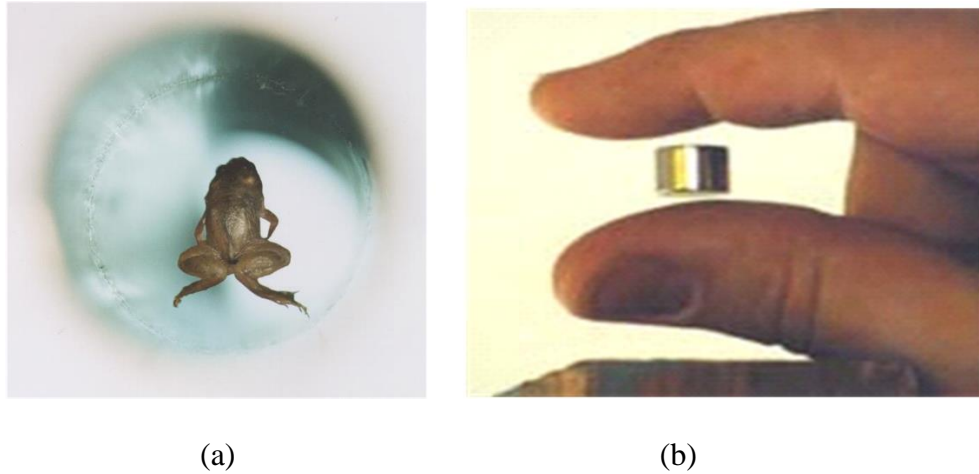


Figure 2.5 (a) Levitation of a frog stabilized by the diamagnetic water in the frog (b) Levitation of a magnet stabilized by the diamagnetism of fingers (weight balanced by unseen solenoid in both cases) [108, 109].

As diamagnetism is a property inherent in many materials including most biological materials, this form of levitation has been used by researchers to simulate microgravity environments for the study of biological processes [111-113]. Some researchers have used the diamagnetic repulsion forces for the selective manipulation of microparticles inside microfluidic devices [114, 115]. Friction and stiction are areas of major concern when it comes to microsensors and microactuators. Diamagnetic levitation offers possible solution in this area of research as the diamagnetic volume forces scale favorable at the micro and nano scale, making levitation easily achievable [116]. Such principles have been applied in the study and

development of diamagnetic bearings [117, 118], diamagnetically levitated micro robots [119, 120], in lateral-force calibration of atomic force microscopes [121], micro-nano force sensors [122] and accelerometers [123, 124]. The modern era of micro- and nano- technology will offer the opportunity for more integration of diamagnetic levitation components in real applications.

Referring back to Figure 2.5, the frog levitation and the magnet levitation although are both made possible due to diamagnetic materials, the role played in each of them is different. In the frog levitation, the frog itself is the diamagnetic material and it is also the object that is levitating. Traditionally, this form of levitation is referred to as diamagnetic levitation. In the case of the magnet levitating between the fingers, the fingers are the diamagnetic material but the levitation object is the magnet. The role of the diamagnetic material is to stabilize the magnet levitation, hence, this form of levitation is referred to as diamagnetically stabilized magnet levitation. Now consider Figure 2.6(a), in this setup two magnets are shown which are set in an attractive orientation. The distance between the two magnets can be arranged such that the weight of the bottom magnet is balanced by the attractive force from the top magnet. However, this is only pseudo-stable, that is the bottom magnet will either fall down due to gravity or move towards the top magnet. If a diamagnetic plate is placed just below the bottom magnet in close proximity, one would observe that on slightly moving the top magnet a little away one would observe the bottom magnet to float. The gap between the floating magnet and the diamagnetic plate can be increased if another plate is introduced above the floating magnet (Figure 2.6(b)). This is now a similar setup as the magnet floating between two fingers in Figure 2.5(b) and hence referred to as diamagnetically stabilized vertical magnet levitation. However, to shorten the lengthy reference to the levitation, here it will be referred to as vertical

diamagnetic levitation (VDL). This form of levitation is not possible with any set of two magnets due to limitation of the strength of diamagnetic materials currently available. Further details about this levitation mechanism and its associated configurations will be discussed in the following chapters.

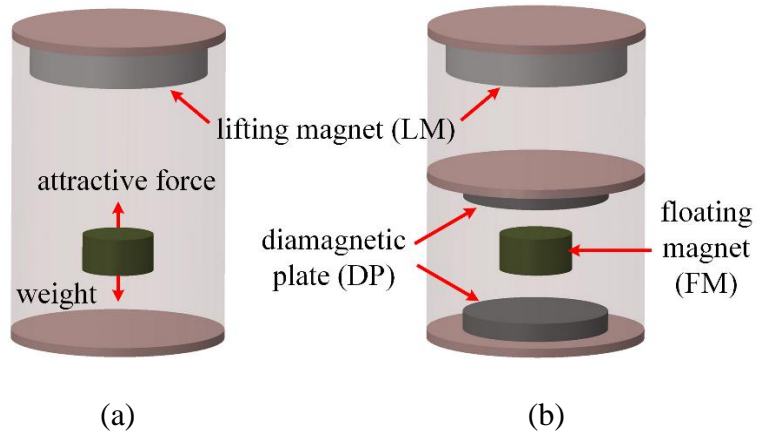


Figure 2.6 (a) Force balanced, unstable bottom magnet (b) Stabilized vertical magnetic levitation

3 A Vertical Diamagnetic Levitation (VDL) based Vibration Energy Harvester

This chapter is largely reprinted with permission from the article X.Y. Wang, S. Palagummi, L. Liu, F.G. Yuan, A magnetically levitated vibration energy harvester, *Smart Materials and Structures* 22 (2013) 055016 and partly from S. Palagummi, F.G. Yuan, An optimal design of a mono-stable vertical diamagnetic levitation based electromagnetic vibration energy harvester, 342 (2015) 330–345.

In this chapter, a detailed discussion of a mono-stable vertical diamagnetic levitation (VDL) based vibration energy harvester (VEH) from a conceptual design to an experimentally and theoretically validated design is presented. The initial conceptual design consisted of two cylindrical magnets, one as the lifting magnet (LM) on top and the other as the floating magnet (FM) between two bismuth coils. The bismuth coils served dual purpose of providing the necessary diamagnetic stabilization force for levitating the magnet and for electromagnetic transduction in order to convert the vibration energy of the FM into useful electrical energy.

On attempting to make an experimental prototype of the concept, a couple of difficulties were encountered. Firstly, due to the unfeasibility of the extrusion of bismuth wires, the design was changed from using dual purpose bismuth coils to pyrolytic graphite for diamagnetism and copper coils for energy transduction. Secondly, it is shown that although initial studies which used simple analytical techniques such as the dipole model and the image method provided useful guideline for understanding the potential of a diamagnetic levitation

system, however, the more accurate semi-analytical techniques such as the thin coil model and the discrete volume method are needed to accurately model the system. An experimental prototype is setup which uses two diamagnetic plates (DPs) made of pyrolytic graphite between which a cylindrical magnet levitates passively whose weight is balanced by a LM placed coaxially on top of it. Two thick cylindrical coils, placed in grooves which are engraved in the pyrolytic graphite plates, are used to convert the mechanical energy into electrical energy. The geometric configurations of the coils are selected based on the field distribution of the magnet to enhance the transduction. Experimental frequency response of the system is validated by the theoretical analysis which showed that the VEH works in a low frequency range (resonant frequency ≈ 2.7 Hz).

3.1 Conceptual design of VDL

VEHs in general transduce energy by damping out the environmentally induced relative motion through either a cantilever beam or an equivalent suspension mechanism with one of the transduction mechanisms (Section 1.1). Mann and Sims [61] used an alternative approach by using magnetic levitation for the spring mechanism to investigate the nonlinearity of the magnetic forces. The magnetic levitation achieved was unstable and had to be confined in a tight-fit tube, this was a consequence of Earnshaw's theorem [103], and suffered from friction which inevitably consumed useful energy. Liu and Yuan [125] introduced the novel idea of using a stable passive VDL system for vibration energy harvesting, hence overcoming the problem of stability while retaining the potential advantages of nonlinear magnetic springs. The system comprised of two cylindrical magnets, one as the LM on top and the other as the

FM between two bismuth coils (Figure 3.1(a)). The bismuth coils served dual purpose of providing the necessary diamagnetic stabilization force for levitating the magnet and for electromagnetic transduction in order to convert the vibration energy of the FM into useful electrical energy. To be consistent with the literature on the levitation mechanisms using diamagnetism, this form of levitation should be actually referred to as the diamagnetically stabilized vertical levitation rather than vertical diamagnetic levitation as the latter may refer to the levitation of the diamagnetic material as opposed to a magnet in the former. However, to shorten the lengthy reference to the levitation, here it will be referred to as vertical diamagnetic levitation or simply as VDL.

Simple analytical modeling techniques (Figure 3.1(b)) were used to develop the equations of motion and predict the frequency response characteristics of the system. The modeling techniques involved using the dipole model for the magnet, to determine its magnetic flux through the coil and to estimate the force between the LM and the FM. The image method was used for estimating the force between the FM and the bismuth coil. These analytical methods and models are described in detail in Section 3.2.

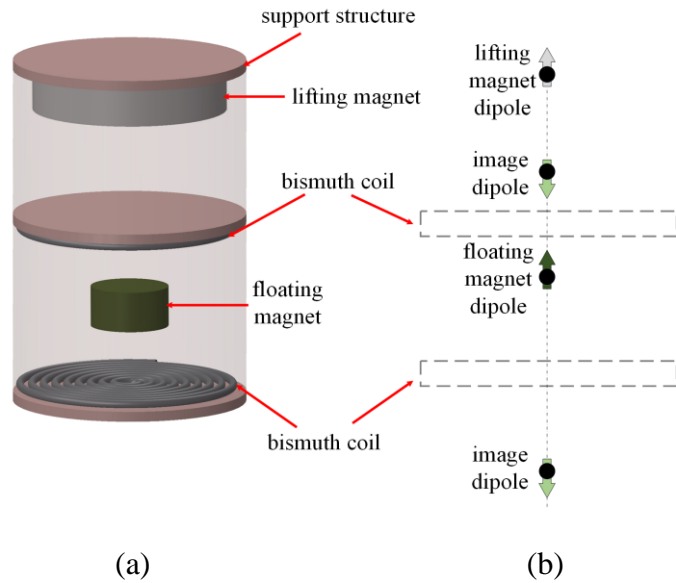


Figure 3.1 (a) Schematic of the proposed VEH and (b) simplified modeling of the harvester

The amplitude-frequency response plots are shown in Figure 3.2 for different values of the nonlinear parameter defined as β , which is equal to k_3/k_1 which are the linear and nonlinear stiffness terms defined in equation (1.3) of Chapter 1. One of the essential conclusions drawn from Figure 3.2 were that the larger the nonlinear term (β) the more bend it had in the frequency response. Other things that were noted are the favorable jump-up frequency (J1-J2) and the unfavorable drop-jump phenomena (D1-D2). More particular details about the frequency response curves shown in Figure 2 can be found in Ref. [125].

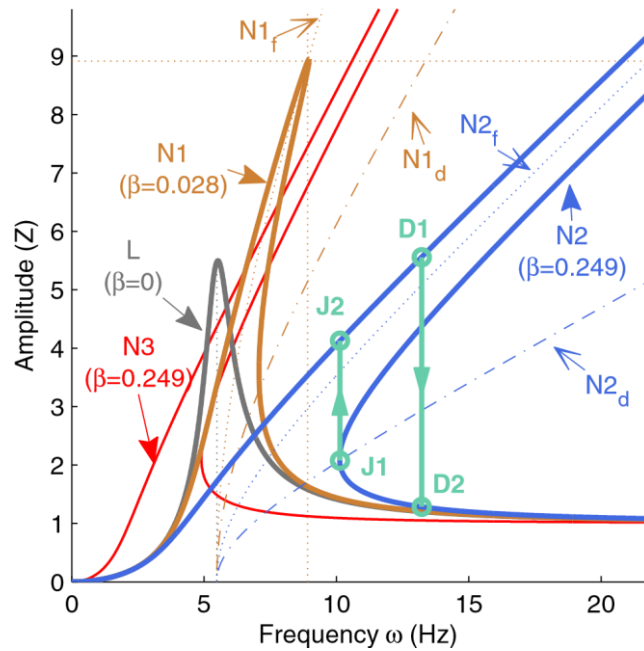


Figure 3.2 Amplitude-frequency responses of the FM under various nonlinear factors [125].

However, on attempting to make an experimental prototype of the conceptual design, which is detailed in this chapter, a couple of difficulties were encountered and necessary changes were made to the design. One important change was the replacement of dual purpose bismuth coil, due to the unfeasibility of the extrusion of bismuth wires, with pyrolytic graphite for diamagnetism and copper coils for energy transduction. As explained in Chapter 2, diamagnetism arises in atoms with paired electrons in their orbits which oppose external magnetic field due to Lenz’s law. These opposing currents in the atoms are significantly larger in pyrolytic graphite because some of its electrons effectively travel in larger than normal orbits, hence they produce a larger repulsive force than most diamagnetic materials. Due to its strong diamagnetic properties, in this dissertation whenever reference is made to a diamagnetic material it is intended to refer to pyrolytic graphite unless and otherwise mentioned. Before

dwelling into the design of the VDL based VEH, it is first necessary to discuss the modelling tools necessary for analyzing the system. These include the magnetic field models, models for estimating force between magnets and models for estimating force between a magnet and a diamagnetic material which are discussed in the following section.

3.2 Modelling tools for the VDL system

3.2.1 Modeling the magnetic field of a cylindrical magnet

In general the dipole model (analytical model) and the amperian model (semi-analytical model) are used for modelling the magnetic field of a magnet. For large distances away from the magnet the dipole model serves as a sufficiently accurate magnetic field model. The radial and axial magnetic field for the dipole, B_r^D and B_z^D , at a distance $a = \sqrt{r^2 + z^2}$ (r and z being the cylindrical co-ordinates as shown in Figure 3.3) for the magnet with dipole moment \mathbf{m} ($|\mathbf{m}|=m$) is given in an analytical form by

$$\begin{aligned} B_r^D(a) &= \frac{\mu_0}{4\pi} \left(\frac{3mrz}{a^5} \right) \\ B_z^D(a) &= \frac{\mu_0 m}{4\pi a^3} \left(\frac{3z^2}{a^2} - 1 \right) \end{aligned} \quad (3.1)$$

where the dipole moment $m = MV$, M is the magnetization of the magnet, which is generally provided by the manufacturer, V is the volume of the magnet and μ_0 ($= 4\pi \times 10^{-7} \text{ NA}^{-2}$) is the magnetic constant.

The magnet can be more accurately modeled as a thin coil [126, 127] for field calculations both at near and far distances from the magnet. The radial and axial magnetic field equations for a cylindrical magnet by approximating it as a thin coil (TC) are [127]

$$\begin{aligned} B_r^{\text{TC}}(r, z) &= B_0 [\alpha_+ C(k_+, 1, 1, -1) - \alpha_- C(k_-, 1, 1, -1)] \\ B_z^{\text{TC}}(r, z) &= \frac{B_0 d}{d + 2r} [\beta_+ C(k_+, \gamma^2, 1, \gamma) - \beta_- C(k_-, \gamma^2, 1, \gamma)] \end{aligned} \quad (3.2)$$

where $B_0 = (\mu_0 / \pi) nI$, the product nI is equal to the magnetization M , n is the number of turns in the thin coil, I is the current in the thin coil, r is the radius of the magnet, $\alpha_{\pm}, \beta_{\pm}, k_{\pm}, C(k_{\pm}, 1, 1, -1)$ and $C(k_{\pm}, \gamma^2, 1, \gamma)$ are the scalar coefficients that depend on the position of the cylindrical point (r, z) with respect to the center of the magnet. These scalar coefficients are defined below

$$\alpha_{\pm} = \frac{d}{\sqrt{4z_{\pm}^2 + (2r + d)^2}}, \beta_{\pm} = \frac{4z_{\pm}}{\sqrt{4z_{\pm}^2 + (2r + d)^2}} \quad (3.3)$$

where,

$$z_{\pm} = z \pm \frac{t}{2} \quad (3.4)$$

$$k_{\pm} = \sqrt{\frac{4z_{\pm} + (d - 2r)^2}{4z_{\pm} + (d + 2r)^2}} \quad (3.5)$$

$$\gamma = \frac{d - 2r}{d + 2r} \quad (3.6)$$

The functions $C(k_{\pm}, 1, 1, -1)$ and $C(k_{\pm}, \gamma^2, 1, \gamma)$ defined in equation (3.2) are a form of the generalized complete elliptic integral, defined as

$$C(k_{\pm}, p, c, s) = \int_0^{\pi/2} \frac{c \cos^2 \varphi + s \sin^2 \varphi}{(\cos^2 \varphi + p \sin^2 \varphi) \sqrt{\cos^2 \varphi + k_c^2 \sin^2 \varphi}} d\varphi \quad (3.7)$$

Equations (3.1) to (3.7) were implemented in a MATLAB to determine the variation in the models for various distances $a_{pp\#}$ diagonally from the tip of the magnet (Figure 3.3). Figure 3.4 shows the values of \mathbf{B} , B_r and B_z for both these models for different aspect ratios of the magnet ($\beta = t/d$, t is the thickness of the magnet and d is the diameter of the magnet). The magnetic fields were normalized with respect to the residual magnetic flux density (B_r) of the magnet which was taken to be 1T and the distance $a_{pp\#}$ was normalized with respect to the thickness t . The volume of the magnet considered for this figure was 1 cm³. It can be seen that the dipole model insufficiently models the magnetic field for distances less than the thickness t , hence, the more accurate semi-analytical thin coil model is necessary as the distances between different magnetic materials in the VDL system are in this range, such as the distance between the FM and the DP.

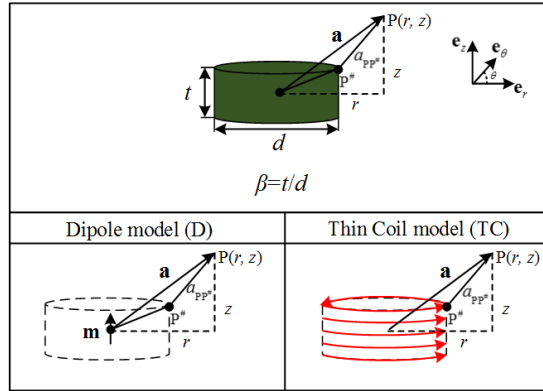


Figure 3.3 Schematic showing the dipole model and the thin coil model

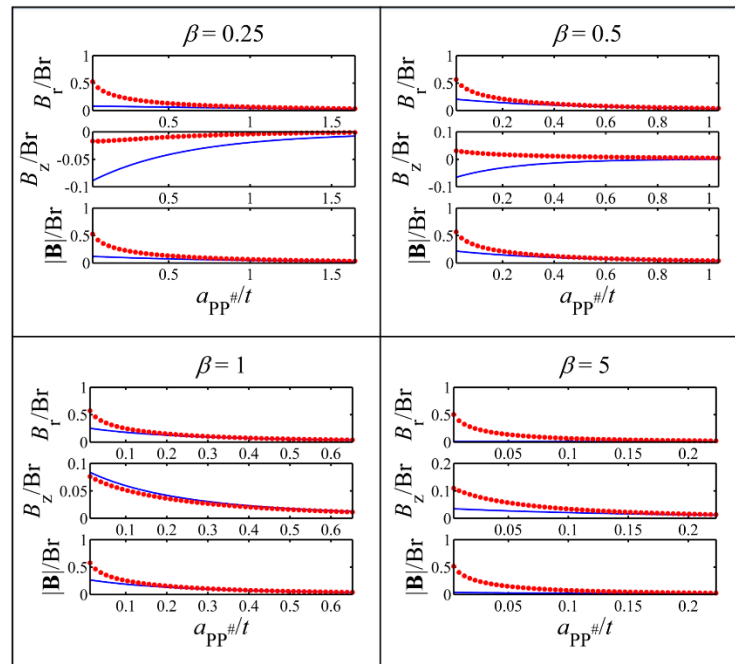


Figure 3.4 Normalized magnetic field values using thin coil model (*) and dipole model (-) for different aspect ratios β .

3.2.2 Modeling of force between two magnets

For determining the force between two magnets one can model them as two thin coils as shown in Figure 3.5. Assuming that the magnetizations of the original magnets are M_1 and M_2 , and their equivalent thin coils have I_1, N_1 and I_2, N_2 number of turns per unit length and current respectively.

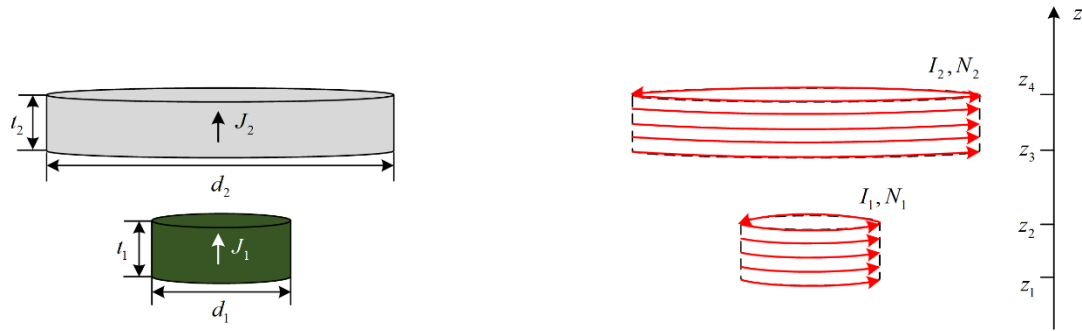


Figure 3.5 Two magnets with their equivalent thin coil model representations for determining the force between them.

Due to the equivalence between a permanent magnet and a thin coil [126], their polarizations can be equated which are represented as J_1 and J_2

$$J_1 = \mu_0 M_1 = \mu_0 N_1 I_1 / t_1 \tag{3.8}$$

$$J_2 = \mu_0 M_2 = \mu_0 N_2 I_2 / t_2$$

The force between the two magnets is calculated by using the Lorentz law, that is, by calculating the field due to every loop of current in one thin coil at every loop of current in the other coil and integrating this over each loop of current in both the magnets. This involves two

double integrals which results into a very complex expression as shown in equation (22) of Ravaud et al.[126]. However, Robertson et al. [128] has greatly simplified the equation into

$$F_z = \frac{J_1 J_2}{2\mu_0} \sum_{i=1}^2 \sum_{j=3}^4 (-1)^{i+j} a_1 a_2 a_3 f'_z \quad (3.9)$$

where,

$$f'_z = K(a_4) - \frac{1}{a_2} E(a_4) + \left(\frac{a_1^2}{a_3^2} - 1 \right) \Pi \left(\frac{a_4}{1-a_2} \middle| a_4 \right) \quad (3.10)$$

and,

$$\begin{aligned} a_1 &= z_i - z_j \\ a_2 &= \frac{(d_1 - d_2)^2}{4a_1^2} + 1 \\ a_3^2 &= \frac{(d_1 + d_2)^2}{4} + a_1^2 \\ a_4 &= \frac{d_1 d_2}{a_3^2}, \quad 0 < a_4 \leq 1 \end{aligned} \quad (3.11)$$

$$\begin{aligned} K(m) &= \int_0^{\pi/2} \frac{1}{\sqrt{1-m \sin^2 \theta}} d\theta \\ E(m) &= \int_0^{\pi/2} \sqrt{1-m \sin^2 \theta} d\theta \\ \Pi(n|m) &= \int_0^{\pi/2} \frac{1}{\sqrt{1-m \sin^2 \theta}} \frac{1}{\sqrt{1-n \sin^2 \theta}} d\theta \end{aligned}$$

The complete elliptical integrals (K , E and Π) of the three kinds can all be numerically computed with a single iteration of the arithmetic-geometric mean approach [129]. However, Robertson et al. [128] has implemented the equations and has generously made the codes

available for others at <http://github.com/wspr/magcode>. The MATLAB codes available on the link, were used to calculate the force between the magnets in this chapter.

3.2.3 Modeling of repulsive force from a diamagnetic material

With the magnetic field model and the force between two magnets determined, the force between a magnet and a diamagnetic material, such as pyrolytic graphite, need to be estimated. The diamagnetic material more often than not is in the shape of a plate, hence it will referred it as a DP in this dissertation. The force between a magnet and a DP with magnetic susceptibility χ_z in the \mathbf{e}_z direction can be calculated in two ways, one is the image method, which is an analytical method, and the other is a semi-analytical method which was first discussed by Boukallel et al. [130]. In this dissertation the author would like to address this semi-analytical technique as the discrete volume (DV) method as the method involves discretizing the diamagnetic object into unit discrete volumes and estimating the force on each of them. The simple image method was used in [110, 125, 131] to calculate the force with the dipole model and the thin coil model of the magnet. The force with the image method in the e_z direction are

$$F_{\text{TC}}^{\text{I}} = \frac{\mu_0 \chi_z M^2}{4} \sum_{i=1}^2 \sum_{j=3}^4 (-1)^{i+j} a_1 a_2 a_3 f'_z \quad (3.12)$$

where F_{TC}^{I} is the forces between the magnet and the DP using the image (I) method for the force and the thin coil (TC) model for the magnet and a is the distance between the magnet and the

DP (Figure 3.6). The parameters a_1, a_2, a_3 , and f'_z depend on the cylindrical geometry of the magnet and the distance between the magnet and the DP [128] (see section 3.2.2 for details). The image method approximates the force between the magnet and the DP as the force between the magnet and another identically sized magnet, also known as the image magnet, which is at twice the original distance between the magnet and the DP (equivalent to image of the magnet with respect to the DP)[110]. The dipole moment of the image magnet is a function of the magnetic susceptibility of the DP and the dipole moment of the magnet ($m\chi_z / 2$).

The discrete volume (DV) method considers variation of the induced magnetization (\mathbf{M}_{DP}) at different points in the DP due to the magnetic field of the magnet. This involves discretizing the DP into unit volume elements in the radial and axial direction as shown in Figure 3.6. Hence, the force expression in the e_z direction is given by

$$F^{\text{DV}} = \sum \nabla_z (\mathbf{M}_{\text{DP}} \cdot \mathbf{B}) dV = \sum \mathbf{M}_{\text{DP}} \cdot \nabla_z \mathbf{B} dV, \quad (3.13)$$

$$\mathbf{M}_{\text{DP}} = \frac{\chi_r B_r^T \mathbf{e}_r + \chi_z B_z^T \mathbf{e}_z}{\mu_0}$$

In equation (3.13), the discrete volume (DV) method is used with the magnetic field \mathbf{B} from equation (3.2), χ_r, χ_z are the anisotropic magnetic susceptibility properties of the DP and ∇_z is the gradient in the z -direction. It should be noted that the total magnetic field responsible for the induced magnetization needs to be considered. For the VDL system this includes the magnetic field from the LM and the FM. Using equations. (3.12) and (3.13), Figure 3.7 shows the force between a magnet and a DP (F_{DP}), pyrolytic graphite in this case, with the methods

and models described till now. The forces in each sub-figure of Figure 3.7 have been normalized with the contact force (F_0) between the magnet and the DP calculated using equation (3.2) and equation (3.13), and the distance a is normalized with the thickness t . It is clear from Figure 3.7 that none of the approximations can accurately model the forces in the system for distances less than the thickness t , which is the range of distances present in the VDL system. Hence, the semi-analytical techniques, the thin coil model for the modeling the magnetic field, for modeling the forces between magnets and the discrete volume method for the forces, are adapted for further analysis on the VDL system.

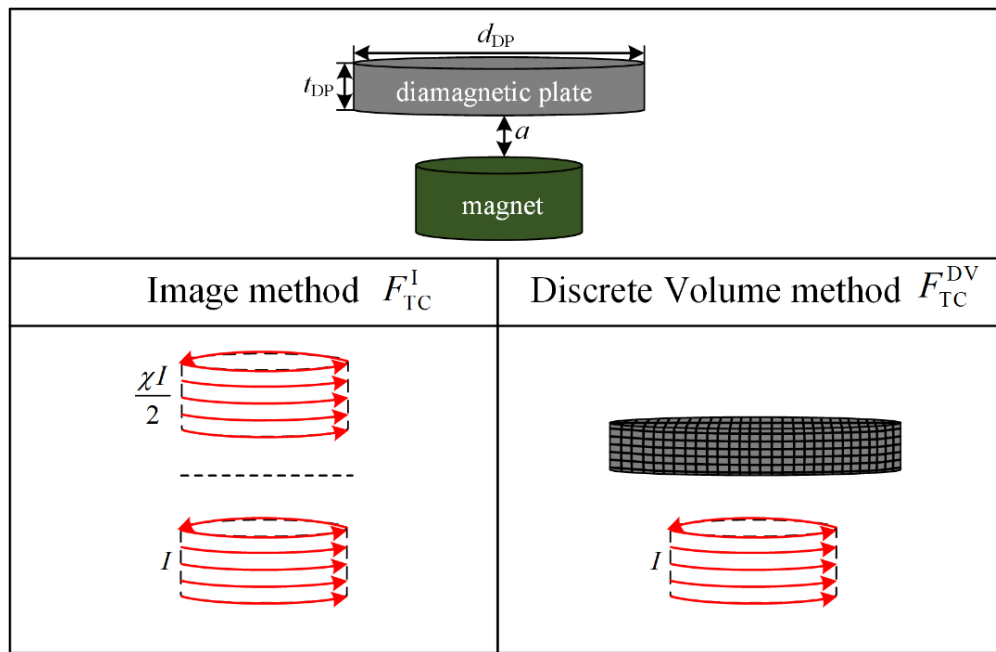


Figure 3.6 Schematic of the force calculation using the image method and the discrete volume method

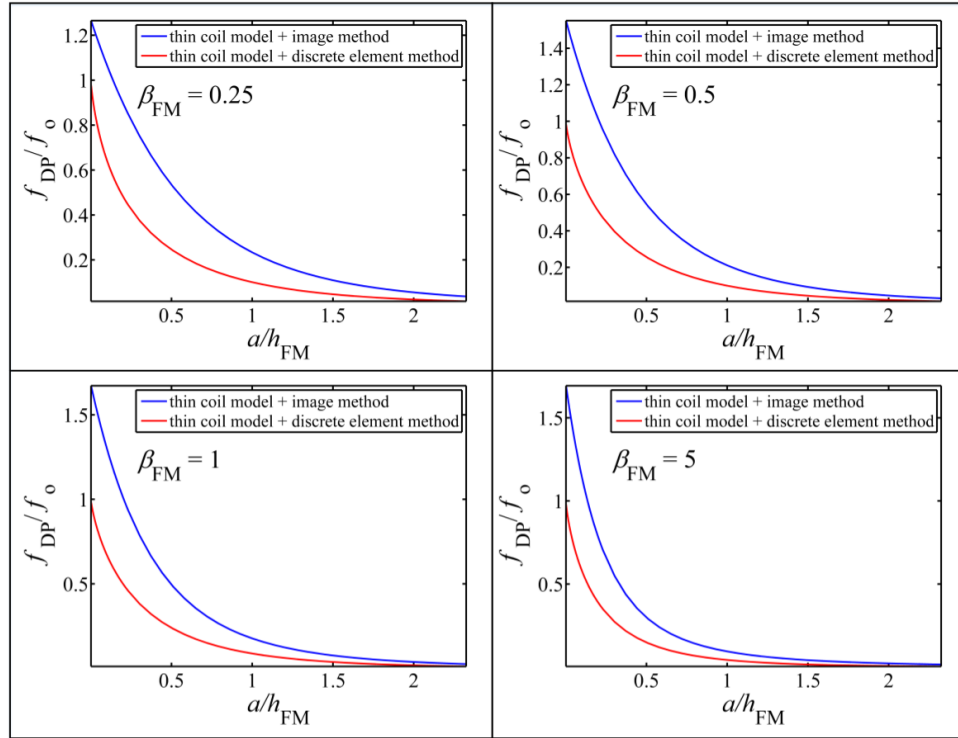


Figure 3.7 Normalized force between a magnet and a diamagnetic object with different approximations for different β .

3.3 Modified design of VDL

The proposed VDL system is illustrated in Figure 3.8. The device consists of two cylindrical magnets, one as a FM and the other as a LM of larger size. The FM is positioned between two parallel DPs (pyrolytic graphite in this case) used for providing vertical stability and a restoring force to the FM. Two thick cylindrical coils made of copper are mounted onto circular grooves which are engraved in the DPs, to convert the mechanical energy of the FM into electrical energy. The design parameters such as the dimensions of the FM, LM and DP,

the distance between the LM and the FM, the distance between the top and bottom DP and the coil geometry will be discussed in this section.

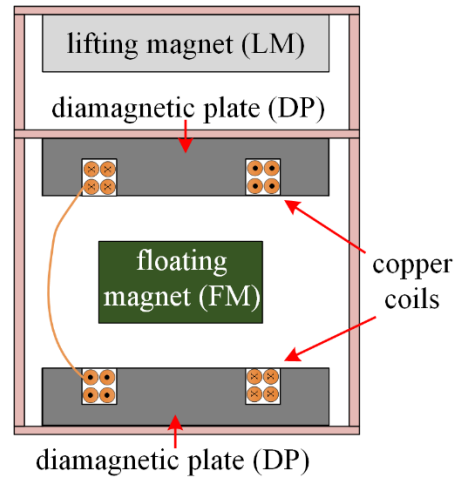


Figure 3.8 Schematic of modified design of VDL based VEH

As a preliminary test, first a VDL system without the copper coils is setup. For this, a magnet of the highest grade available in the market (grade N52 of KJ Magnetics, Inc.) of an aspect ratio close to 1 is selected for the FM. Two DPs made of pyrolytic graphite were also procured from the same vendor. Based on the selected FM and DP several LMs were tested to check the levitation of the FM with a reasonable levitation gap between the DP of at least 1mm on either side of the FM. After some trial and error a LM of dimensions give in Table 3.1 was chosen.

Ideally, at the equilibrium position of the FM the repulsive forces from both the DPs are equal and opposite in magnitude assuming the levitation gap is equal at both ends of the FM. Hence, the weight of the FM is purely balanced by the attractive force of the LM (F_{LM}),

$$F_{LM} = m_{FM}g \quad (3.14)$$

where m_{FM} is the mass of the FM and g is the acceleration due to gravity. The analytical solution for the force F_{LM} given by equation (3.9) for system parameter values given in Table 3.1 is shown in Figure 3.9. It can be seen in the figure that the attractive force from the LM is approximately equal to the weight of the FM at roughly a distance of 116.4 mm. In the experimental setup this estimated distance was validated with an error of less than 1%.

With an experimental setup of the VDL system established, one should determine the coil geometry for the energy harvesting aspect of the proposed VDL system. For an inertial vibrational energy harvester, the electrical energy which can be extracted originates from the mechanical energy of the relative motion in the harvester. The available mechanical energy is determined primarily by the frequency and amplitude of the FM in this case. The vibrational harvesting capability is in turn determined by the magnetic field gradient of the FM, the loops of coil, the impedance of the coil and the impedance of the load attached. Hence, the geometry of the coil and of the FM play a key role in generating maximum power

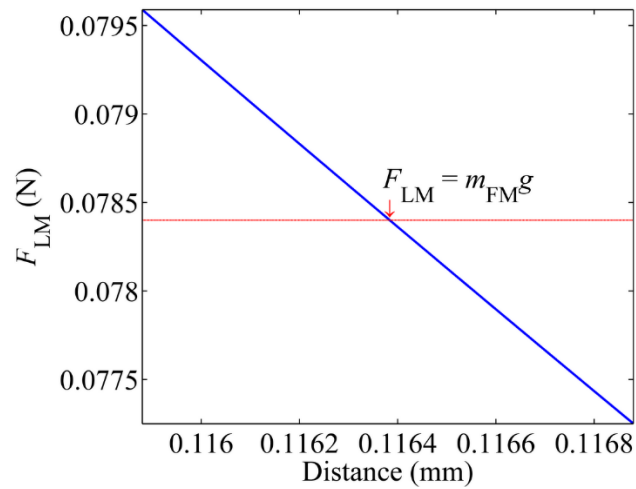


Figure 3.9 Force balance between the weight of the FM ($m_{FM}g$) and the attractive force of the LM (F_{LM}).

Using the thin coil model described in Section 3.2, a plot of the radial magnetic field distribution of the FM at various distances above the flat surface of the magnet is shown in Figure 3.10. It can be seen that the maximum radial magnetic field intensity is at the radius of the FM and decreases rapidly away from the radius location. It can also be seen that the radial magnetic field intensity decreases rapidly as the distance from the top surface of the FM increases. As the output voltage is proportional to the number of loops of the coil and the magnitude of the magnetic field intensity cutting through it, the inner and outer diameters of the coil were selected as 7.15 mm and 12.9 mm, respectively, and 1 mm as the thickness of the coils at a distance of 1mm from the FM. This coil geometry corresponds to roughly a region of 60% of the maximum magnetic field intensity available from the FM (Figure 3.10). Two coils each containing 1300 turns of AWG-48 enameled copper wire with a combined resistance

of 1870Ω were made. Due to the small levitation gap (slightly less than 1.3 mm) and possible interference of the coil with the motion of the FM, the copper coils were placed in grooves made in the DP. It was noticed that the levitation gap decreased on replacing a part of the DP with the copper coil. However, this combined DP-coil assembly made the inclusion of copper coil to the VDL system easier.

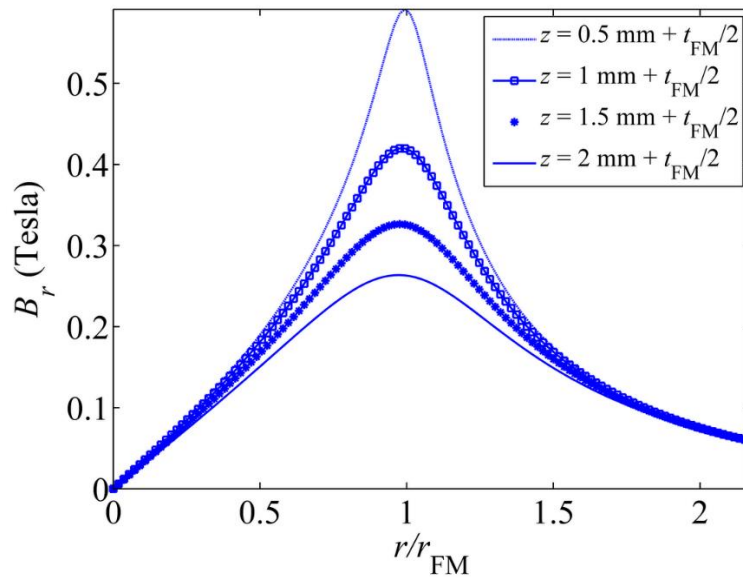


Figure 3.10 Radial magnetic flux density for the FM vs the radial distance at various axial distances, measured from the center of the FM.

With the design details of the VDL based VEH system discussed, next the electrical and mechanical equations of motion are discussed to understand the amplitude-frequency and voltage-frequency response characteristics of the system.

3.4 Equations of motion

The restoring force on the FM consists of the components shown in Figure 3.11(a). The force arrows are color coded with respect to the component which is exerting a force on the FM. Here it should be noted that a part of the DP is replaced with copper coils, and for that region the copper wire's magnetic susceptibility has to be taken into account while estimating the force using equation (3.13). The restoring force ($F_K(z)$) can be written as,

$$F_K(z) = F_{\text{weight}} + F_{\text{TDP}} + F_{\text{top coil}} - F_{\text{LM}} - F_{\text{BDP}} - F_{\text{bottom coil}} \quad (3.15)$$

where F_{TDP} , F_{BDP} are the repulsive forces from the top and bottom DP and $F_{\text{top coil}}$, $F_{\text{bottom coil}}$ are the repulsive forces from the top and bottom coil. By calculating the individual forces in equation (3.15) using equations (3.9) and (3.13), the restoring force F_K versus the displacement of the FM in between the two pyrolytic graphite plates is plotted in Figure 3.11(b).

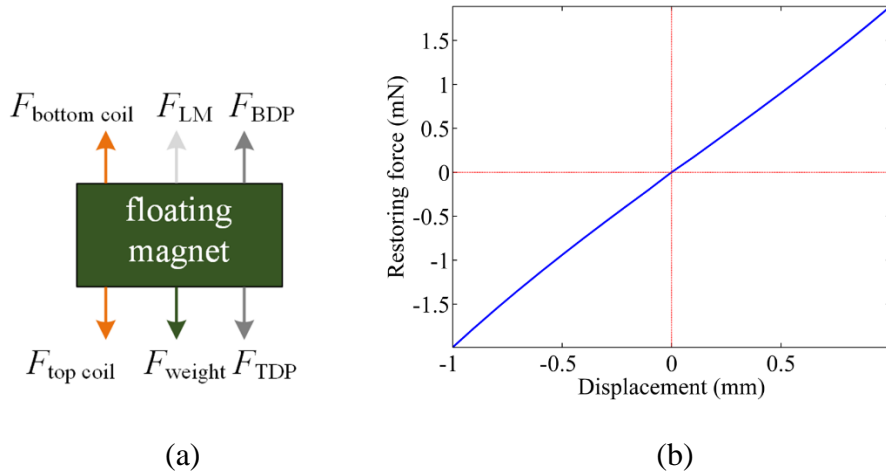


Figure 3.11 (a) Schematic of the restoring forces acting on the FM (b) Restoring force as a function of displacement

When the base of the VDL system is given an excitation there is relative motion arises between the magnet and the pyrolytic graphite plate–coil assembly. By Faraday’s law a voltage is induced in the coil and the motion of the FM is damped as a result of Lorentz law. In the proposed design, the two series-wound coils are located over the upper face and the lower face of a cylindrical magnet, respectively. The total closed loop damping force is given by

$$F_L(i, z) = F_{\text{upper coil (Lorentz)}} + F_{\text{lower coil (Lorentz)}} \quad (3.16)$$

where,

$$F_{\text{upper coil(Lorentz)}} = I_{\text{coil}} \sum_{j=1}^n \sum_{i=1}^m B_r(r_i, z_j + D/2 - z) 2\pi r_i \quad (3.17)$$

$$F_{\text{lower coil(Lorentz)}} = I_{\text{coil}} \sum_{j=1}^n \sum_{i=1}^m B_r(r_i, z_j + D/2 + z) 2\pi r_i$$

where the current in the coil by ohm’s law is,

$$I_{\text{coil}} = \frac{V_{\text{upper coil}} + V_{\text{lower coil}}}{2R_{\text{coil}} + R_{\text{load}}} \quad (3.18)$$

and the voltage in each coil by Faraday's law is,

$$\begin{aligned} V_{\text{upper coil}} &= \dot{z}(t) \sum_{j=1}^n \sum_{i=1}^m B_r(r_i, z_j + D/2 - z) 2\pi r_i \\ V_{\text{lower coil}} &= \dot{z}(t) \sum_{j=1}^n \sum_{i=1}^m B_r(r_i, z_j + D/2 + z) 2\pi r_i \end{aligned} \quad (3.19)$$

where n is the number of coil layers in the axial direction, m is the number of turns in the radial direction, r_i is the radius of each turn in the coil, and z_j is the height of each layer of the coil.

Finally, the damping force on the FM in open-circuit is measured by calculating its ring-down after giving a mechanical impulse to the system. This damping force is due to the presence of eddy currents in the pyrolytic graphite. The measured open-circuit Q factor was found to be around 20, i.e. a damping ratio of 0.025. This factor of equivalent mechanical damping has been neglected in the theoretical model as it will be discussed later to be around two orders of magnitude lower when compared with damping for closed-circuit with load (Q factor closed-circuit with load = 0.42, i.e. damping ratio of 1.18).

Finally, now that the restoring and damping forces of the VEH are discussed, one can write the equations of motion of the system (equation (3.20)). The VEH can be modeled as a one degree of freedom (1-DOF) system with a spring, a mass and a damper, excited by a harmonic sine wave $A \sin \omega t$ as shown in Figure 3.12(b). Its equation of motion is governed by the following:

$$\begin{aligned}
 m_{\text{FM}} \ddot{z} + F_{\text{K}}(z) + F_{\text{L}}(i, z) &= -m_{\text{FM}} \omega^2 A \sin \omega t \\
 iR_{\text{load}} + iR_{\text{coil}} &= V(z, \dot{z})
 \end{aligned}
 \tag{3.20}$$

here z is the relative displacement of the FM, i is the current in the coil, A is the amplitude of the sinusoidal base displacement, $F_{\text{L}}(i, z)$ is the electromagnetic (Lorentz) force as a function of the relative displacement and the current in the coil, R_{load} is the resistance of the load, R_{coil} is the resistance of the coil, $V(z, \dot{z})$ is the voltage induced in the coil which is the sum of the voltages in equation (3.19) and $F_{\text{K}}(z)$ is the restoring force as a function of the relative displacement.

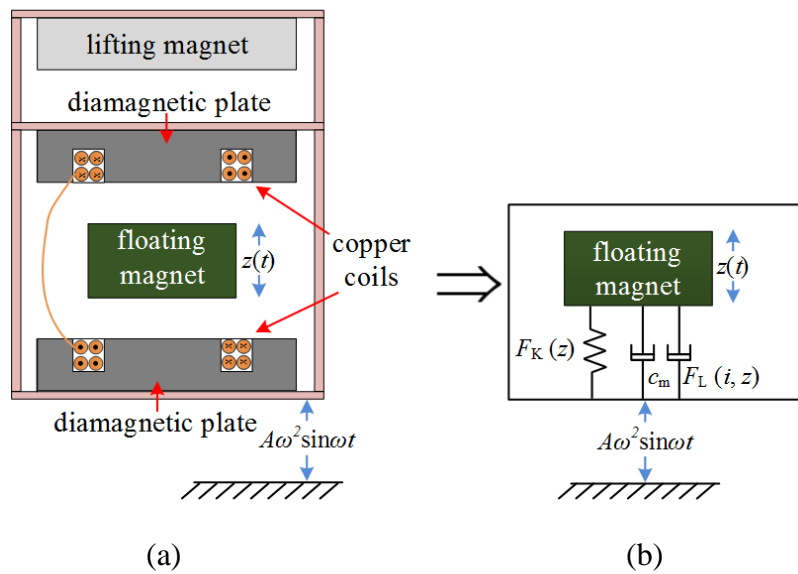


Figure 3.12 (a) Schematic of the VDL based VEH and (b) 1-DOF equivalent of the VEH

The amplitude-frequency response as well as the voltage-frequency response characteristics can be theoretically predicted from equation (3.20). The next section discusses

the experimental validation for the theoretical analysis presented for a given set of excitation conditions.

3.5 Experimental studies on VDL

This section primarily describes the experimental tests, along with a comparison of the results with theoretical predictions. The experimental tests were performed at different excitation frequencies while keeping the given input power of the energy harvester and other experimental variables constant.

3.5.1 Experimental apparatus and instrumentation

The experimental setup is shown in Figure 3.13. A plastic cylindrical extension was used to avoid magnetic field interference from the energy harvester from the electromagnetic shaker (VTS100-8, Vibration Test Systems, Inc.) which was used to base excite the system. The lower frequency excitations were performed on a servohydraulic load frame (INSTRON 8501), because of the frequency limitation of the shaker. For frequencies at which the shaker was used, a digital signal generator (DPO 2024, Tektronix) and an amplifier (7602 model, Krohn-hite) were used to control the frequency and the amplitude of the shaker, respectively. A laser displacement sensor (OptoNCDT 1607, Micro-Epsilon) and a high speed camera (MotionScope PCI 8000S, Redlake Imaging) were mounted on a base to obtain the displacement of the FM. Two tiny beams of balsa wood were glued on the FM to measure the absolute displacement of the FM via the laser displacement sensor.

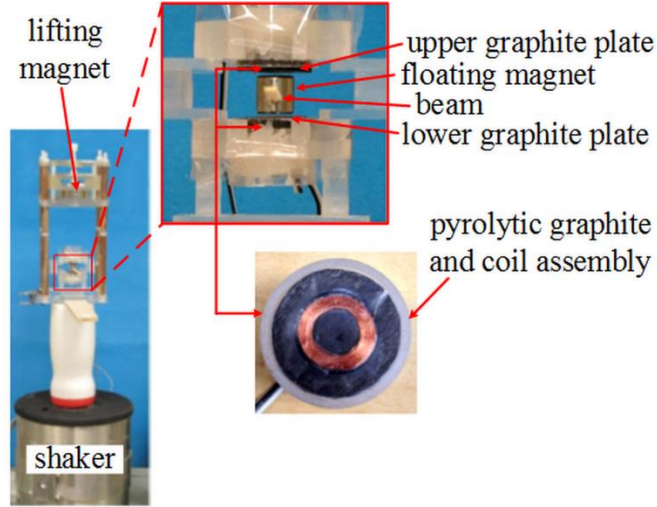


Figure 3.13 The experimental prototype of the VDL based VEH

For a system as shown in Figure 3.12(b), if the input power is held constant, it can absorb the maximum energy that will be generated around its resonance frequency. For a harmonic base excitation $A\sin\omega t$, if the mass of the vibrator (mass of FM, m_{FM} in this case) is much less than the mass of the energy harvester system, the input power of the energy harvester is approximated by:

$$\begin{aligned}\bar{P}_{input} &\approx \frac{2\omega}{\pi} \int_0^{\pi/2\omega} m_{harvester} \left| (-A\omega^2 \sin \omega t)(A\omega \cos \omega t) \right| dt \\ &\approx \frac{\omega}{\pi} \int_0^{\pi/2\omega} m_{harvester} \omega^3 A^2 \sin 2\omega t dt \approx \frac{1}{\pi} m_{harvester} \omega^3 A^2\end{aligned}\quad (3.21)$$

where $m_{harvester}$ is the mass of the energy harvester system, ω is the angular frequency of the base excitation, A is the amplitude of the base excitation, and \bar{P}_{input} is the average input power of the energy harvester system. As shown in equation (3.21), a constant input power to the energy harvester is maintained by keeping $\omega^3 A^2$ constant.

The model parameters for the experimental system are given in Table 3.1. $m_{\text{harvester}}$ is the total mass of the energy harvester, r_{FM} is the radius of the FM, t_{FM} is the thickness of the FM, r_{wire} is the radius of the wire used for making the coils, t_{coil} is the thickness of the coil, $r_{\text{coil}}^{\text{in}}$ is the inner radius of the ring-shaped coil, $r_{\text{coil}}^{\text{out}}$ is the outer radius of the ring-shaped coil (see figure 10(c)), D is the perpendicular distance between the two pyrolytic graphite plates, N is the number of turns in each coil and $A^2\omega^3$, as previously discussed, is the factor proportional to the average power input that is maintained as a constant. With these model parameters, tests are performed at different excitation frequencies by keeping the input power of the energy harvester fixed at around 103.45 μW .

Table 3.1 The model parameters for the experimental system

| | | | | | | | | |
|-----------|-------------------------------|--------------------------------|-------------------|-----------------|------------------------|-------------------|----------------------------|-------------------|
| Parameter | r_{FM} | t_{FM} | m_{FM} | d_{LM} | t_{LM} | R_{coil} | t_{DP} | r_{wire} |
| Value | 5.53 | 11.1 | 8 | 50.8 | 12.7 | 935 | 3.5 | 0.0158 |
| Unit | mm | mm | g | mm | mm | Ω | mm | mm |
| Parameter | $r_{\text{coil}}^{\text{in}}$ | $r_{\text{coil}}^{\text{out}}$ | t_{coil} | D | $m_{\text{harvester}}$ | N | $A^2\omega^3$ | R_{load} |
| Value | 3.575 | 6.45 | 1 | 13 | 650 | 1300 | 500 | 1870 |
| Unit | mm | mm | mm | mm | g | - | mm^2s^{-3} | Ω |

3.5.2 Comparisons between analytical prediction and experimental results

The experimental tests were performed for a frequency sweep of 58 points to show the response behavior of the energy harvester. The excitation frequency was varied from 0.2 Hz to 7 Hz with increments varying from 0.1 Hz to 0.4 Hz. Hence, the base accelerations were

varied from 0.025 ms^{-2} to 0.148 ms^{-2} and the input amplitudes from 15 mm to $76 \text{ }\mu\text{m}$ as the frequency was varied from 0.2 to 7 Hz to keep the input power a constant.

The voltage on the load resistance connected in series to the coils of the energy harvester was measured at each frequency. A prediction of the output voltage for the energy harvester was also made using the theoretical model via the experimentally identified parameters given in Table 3.1. The theoretical predictions are compared with the experimental results in Figure 3.14. The FM can only vibrate in a small range because of the limitations of the design of the VDL based VEH. The maximum levitation gap between the FM and the pyrolytic graphite plate was around 0.95 mm . Due to the limited range of motion of the FM, the output power of the energy harvester is relatively low. Meanwhile, at relatively low excitation levels, the frequency response behavior of the system behaves like a linear system. There are no jump response phenomena near the primary resonance frequency. For frequencies below 0.8 Hz , there is contact between the magnet and the DP and hence there is a moderate deviation between the analytical predictions and experimental results for these frequencies. This is because the input amplitude at these frequencies is much greater than the distance between the FM and the pyrolytic graphite plate. Also, one can see an increase in the effect of eddy currents on the pyrolytic graphite plates with frequencies close to 7 Hz , as the estimated theoretical value is slightly greater than the experimental value. However, there is a good match for the remaining frequencies which validates the analytical prediction.

From Figure 3.12(c), the quality factor for the harvester can be calculated by measuring the ratio of the natural frequency and the half-power bandwidth. The quality factor was found to be around 0.42 . This low quality factor is due to the selection of the load resistance, which

was not optimum, and led to the high magnitude of electrical damping in the coils. This led to a two orders of magnitude higher electrical damping in closed-circuit with load when compared with open-circuit (eddy currents in pyrolytic graphite plate). However, this large damping did restrict the FM from impacting the DP which was essential in providing a proof of concept for the theoretical and experimental investigations carried out.

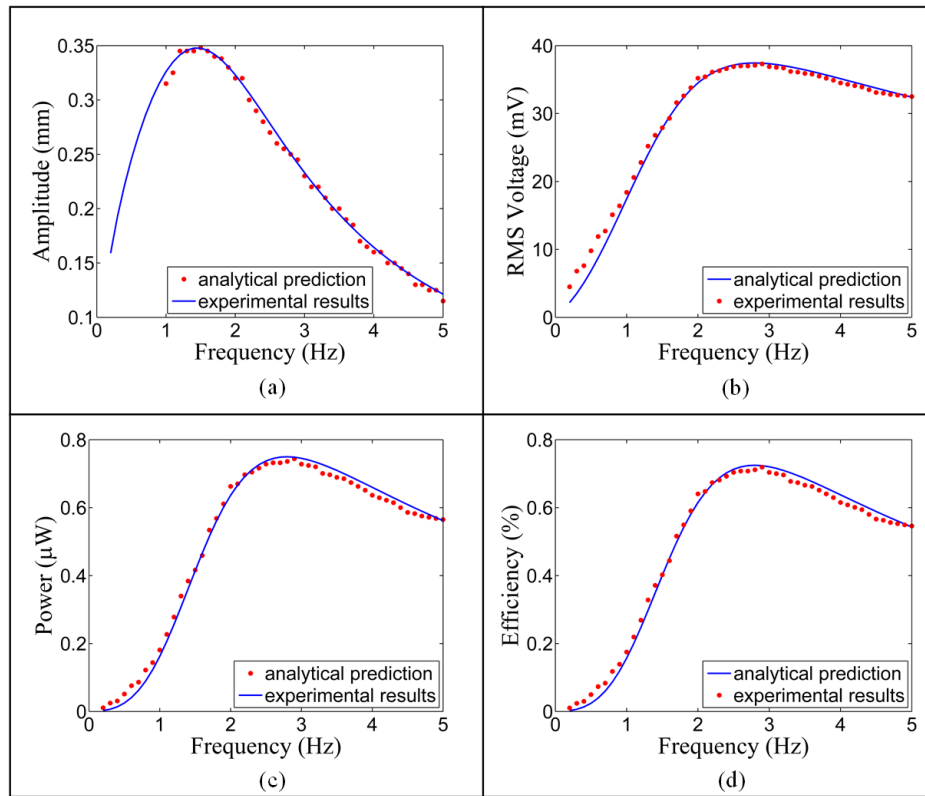


Figure 3.14 (a) Experimental and theoretical predictions of relative amplitude of the FM (b) Experimental and theoretical predictions of the RMS voltage (c) Experimental and theoretical predictions of Power (d) Experimental and theoretical predictions of the efficiency

3.6 Conclusions

This chapter theoretically and experimentally investigated a novel VDL based VEH. The VEH uses the stabilized diamagnetic levitation mechanism to passively levitate a magnet between two DPs and with a LM placed axially above it to in an attractive configuration to balance its weight. The repulsive force from the DPs and the attractive from the LM constitutes to the restoring force on the FM. For efficient energy harvesting, coils needed to be placed in a location where they can capture the maximum magnetic flux from the FM. Hence for this, circular grooves were engraved in the DPs in which the coils were incorporated. A semi-analytical model in terms of the magnetic field and the magnetic forces were discussed

Unlike energy harvesting devices that operate at a high frequency range, the energy harvester proposed in this chapter primarily works at a low frequency range (0.1–10 Hz). By changing the dimensions of the FM along with the geometry of the coil, the resonance frequency can be tuned to a certain frequency for specific applications. This low working frequency range is in the range of natural frequencies of the vibrations observed in civil infrastructures [89]. However, the work here doesn't focus on maximizing the output power or the efficiency, which would require a change in the design, such that the motion of the FM is not constrained, and also a decrease in the overall mass of the harvester. Also an optimization study can be made of the coil geometry, which is the key in capturing maximum output power. The focus of this chapter was to introduce a low resonant frequency VEH, a harvester which avoids mechanical frictions, and lastly a harvester which has the capability of being nonlinear.

4 An optimal design of a mono-stable vertical diamagnetic levitation (VDL) based vibration energy harvester

This chapter is largely reprinted with permission from the article S. Palagummi, F.G. Yuan, An optimal design of a mono-stable vertical diamagnetic levitation based electromagnetic vibration energy harvester, 342 (2015) 330–345.

A detailed analysis of a mono-stable vertical diamagnetic levitation (VDL) system for optimal vibration energy harvesting is presented in this chapter. In Chapter 3, a first demonstration of a vibration energy harvester (VEH) using diamagnetic levitation has been presented. The experimental system validated some of the claims made in [125, 131] of being a low frequency resonant system (less than 5 Hz) but sufficient levitation gap was not achieved and the frequency response characteristic of the system was effectively linear. Due to the small levitation gap, the electrical damping in the system had to be increased to avoid/reduce impact energy loss between the pyrolytic graphite and the floating magnet. Also, it was seen that although the system had no mechanical damping elements, eddy currents were generated in the pyrolytic graphite plate which served as an equivalent mechanical damping element. The goal of this chapter is to address these issues and provide an optimal design of a mono-stable VDL system.

To meet these goals, the influence of the geometry of the floating magnet (FM), the lifting magnet (LM), and the diamagnetic plate (DP) are parametrically studied to assess their effects on the levitation gap, size of the system and the natural frequency. For efficient

vibration energy harvesting using the VDL system, ways to mitigate eddy current damping and a coil geometry for transduction are critically discussed. With the optimized parameters, an experimental system is realized which showed a hardening type nonlinearity and an improved efficiency from the initial study.

4.1 Mono-stable VDL system

Consider the VDL system as discussed in Ref. [110] and as shown in Figure 4.1. The system primarily consists of a LM, a FM and two DPs. In this chapter, wherever not mentioned, a pyrolytic graphite plate is used as the DP. The LM balances out the weight of the FM and stability is brought about by the repulsive effect of the DPs [110]. In the last chapter (Chapter 3), for using this VDL system for vibration energy harvesting a part of the DP was replaced with copper coils for transduction. This increased the flux change in the copper coil but as a tradeoff it decreased the levitation gap. This decrease in the levitation gap was due to the reduction in the repulsive force from the DP because of a partial replacement of it with the copper coil. Due to the interplay between coil geometry for transduction and repulsive force from DP for levitation gap, a discussion on copper coil geometry is deliberately delayed till a later section in this chapter after addressing the influence of the individual components of the VDL system on the static and dynamics of the levitation of the FM.

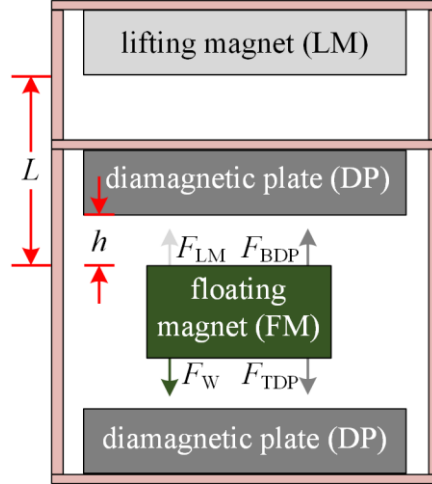


Figure 4.1. A two-dimensional view of the VDL system.

The restoring force on the FM (F_K) consists of two parts, one is the net diamagnetic repulsive force (F_1) and the other is the net gravity compensation by the LM (F_2) (equation (4.1)). The diamagnetic repulsive force comes from the bottom and top DPs (F_{BDP} and F_{TDP}) and the net gravity compensation is a resultant of the weight of the FM and the attractive force from the LM (F_w and F_{LM}), these forces are illustrated in Figure 4.1. It is the aim of this chapter to understand the geometric influence of the individual components of the VDL system on the restoring force (F_K). To meet this end, the aspect ratio of the FM, the relative size of the DP with respect to the FM, the aspect ratio of the LM are parametrically studied to estimate the minimum volume of the LM needed to levitate a given volume of the FM with a certain levitation gap in a mono-stable condition. For the parametric studies the semi-analytical techniques, that is, the thin coil model for the magnet and the discrete volume method for the force between the magnet and the diamagnetic material introduced in Chapter 3 will be used.

$$\begin{aligned}
F_K &= F_1 - F_2 \\
&= \overbrace{(F_{\text{TDP}} - F_{\text{BDP}})}^{F_1} - \overbrace{(F_{\text{LM}} - F_{\text{W}})}^{F_2}
\end{aligned} \tag{4.1}$$

4.1.1 Parametric studies on the VDL system

Firstly, an appropriate aspect ratio of the FM ($\beta_{\text{FM}} = t_{\text{FM}} / d_{\text{FM}}$, where t_{FM} and d_{FM} are the thickness and the diameter of the FM respectively) which maximizes F_1 needs to be determined. This is chosen based on the variation of the force F_{DP} with different aspect ratios. A parametric sweep of the force F_{DP} is done (shown in Figure 4.2(a)) for this purpose between a DP and FM at a distance of 0.1mm and with the size of the DP much larger than the size of the FM. It can be seen from Figure 4.2(a) that for an aspect ratio of around four-tenth for different volumes of the FM, the force F_{DP} has a maximum. For the sake of demonstration, an aspect ratio of four-tenth is taken for all further discussion on the FM from here forth.

Figure 4.2 (b) and (c) are plotted to estimate the variation of force F_{DP} with the relative dimensions of the DP with respect to the FM. It can be seen from the plot that the force reaches a maximum for a diameter of the DP (d_{DP}) slightly greater than the diameter of the FM (d_{FM}) and for a thickness of the DP (t_{DP}) around the same as the FM (t_{FM}). For further discussion a $\beta'_{\text{DP}} = t_{\text{DP}} / t_{\text{FM}} = 2$ and $\beta^d_{\text{DP}} = d_{\text{DP}} / d_{\text{FM}} = 2$ are considered as they provide close to the maximum repulsive force possible. With $\beta_{\text{FM}} = 0.4$ and for a $V_{\text{FM}} = 1 \text{ cm}^3$ the variation of the net repulsive force from the DPs (F_1) with different levitation gap (h) is shown in

Figure 4.3. It can be seen that the force variation with displacement changes from linear to nonlinear with an increase in h .

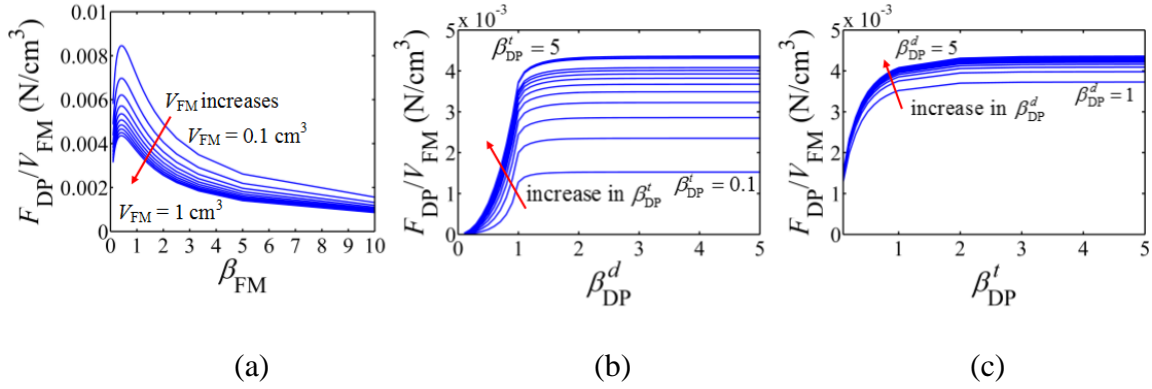


Figure 4.2. (a) Force per unit V_{FM} (F_{DP}/V_{FM}) versus β_{FM} , (b) force per unit volume (F_{DP}/V_{FM}) versus $\beta_{DP}^d = d_{DP}/d_{FM}$ and (c) $\beta_{DP}^t = t_{DP}/t_{FM}$ respectively.

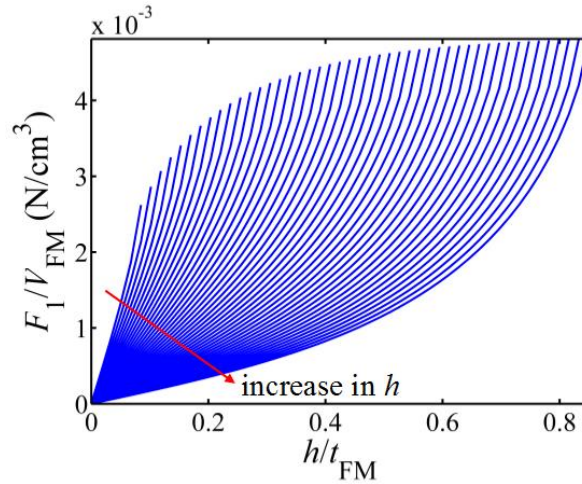


Figure 4.3. Variation of the normalized diamagnetic repulsive force (F_1/V_{FM}) vs h/t_{FM} .

For the parametric studies shown in Figure 4.2 and Figure 4.3, the objective was to find the FMs aspect ratio and the relative size of the DP that maximizes the force between them along with understanding its variation with distance, hence, the magnetic field of the LM was not included for calculating F_{DP} . Once the volume and aspect ratio of the LM is determined for achieving levitation along with an enhanced levitation gap (Figure 4.4 (a)-(d)), the magnetic field of the LM will be included for calculating F_{DP} for further discussion there forth (Figure 4.5 and Figure 4.6).

It can be seen from equation (4.1) that $|F_1|$ needs to be always greater than $|F_2|$ to maintain the stability of the FM. For this to be achieved, one needs a LM that balances the weight of the FM at a point and maintains a gradient of force smaller than that of F_1 between the DPs. A cylindrical magnet with a low aspect ratio provides a low force gradient at large axial distances [132] and hence are good candidates for LMs. This is shown in Figure 4.4(a, b), where the net gravity compensation by the LM per unit V_{LM} (F_2/V_{LM}) is plotted with respect to the ratio z/t_{FM} , for aspect ratio of the LM ($\beta_{LM} = t_{LM}/d_{LM}$, where t_{LM} is the thickness of the LM and d_{LM} is the diameter of the LM) varying from 0.05 to 0.2. Here $z = 0$ represents the stable levitation point of the FM. A fixed volume of the FM ($V_{FM} = 1 \text{ cm}^3$) and LM ($V_{LM} = 100 \text{ cm}^3$) are considered with equal magnetizations ($M_{FM} = M_{LM} = 1/\mu_0$). However, it should be noted that for low aspect ratios the demagnetization of the LM should be taken into account for calculating the residual magnetic flux density (Br) [99]. The slope of the force also decreases with increase in volume for a fixed β_{LM} with the drawback being L

increases as seen in Figure 4.4(c, d). In Figure 4.4(d) the volume ratio (η) is defined as V_{LM} / V_{FM} . For all further discussions from here forth β_{LM} is taken as 0.1 as this gives a considerably low slope of F_2 and any lower aspect ratios are generally difficult to manufacture.

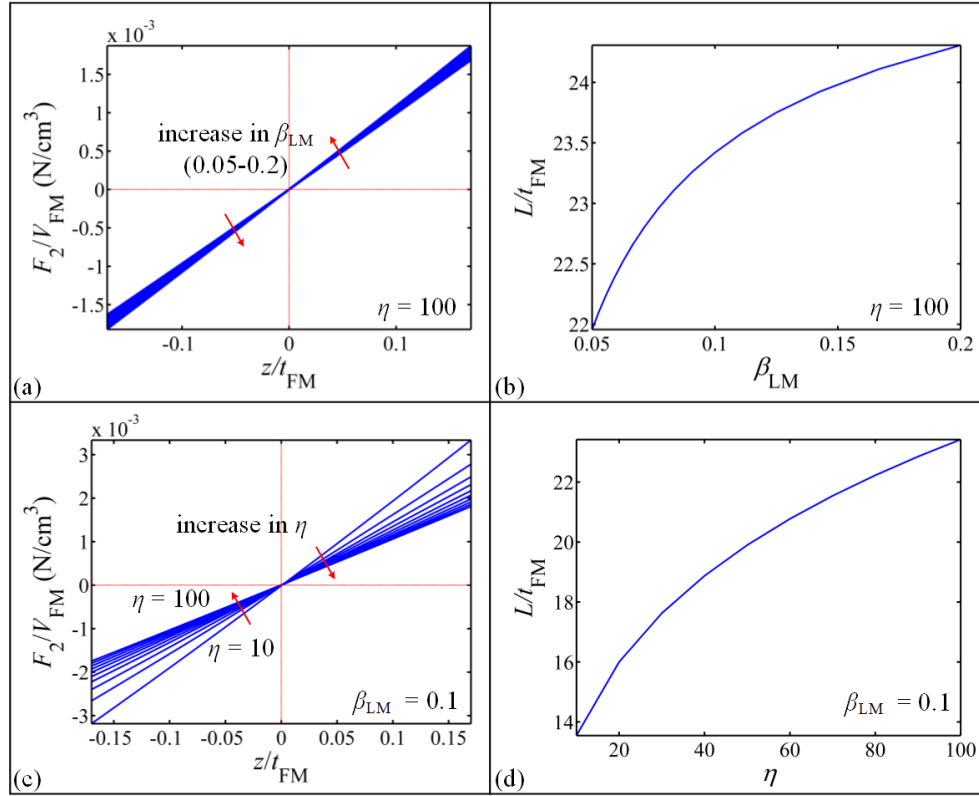


Figure 4.4. Force F_2 and L varies with β_{LM} (aspect ratio of the LM) in (a) and (b) for a fixed V_{LM} and V_{FM} , in (c) and (d) force F_2 and L varies with V_{LM} for a fixed V_{FM} and fixed β_{LM} ($\eta = V_{LM} / V_{FM}$).

$$\eta = V_{LM} / V_{FM}.$$

4.1.2 Design of the VDL system

With an understanding of the effect of the aspect ratios of the individual components on the restoring force and the levitation gap (h), the volume requirements of the LM for a given V_{FM} for levitation with the desired h can be determined. The VDL system can be designed in two ways, one is for the minimum weight and size of the harvester, for compactness, and the other is for a maximum h , to increase the maximum allowable amplitude of the vibrating mass which in turn unlocks the nonlinearity inherent in the system. For the minimum weight and size of the harvester for a given V_{FM} , the minimum V_{LM} is found by iteratively finding a volume that can stably levitate a FM with a minimal h , say 0.1 mm.

For a set of V_{FM} , from 0.1cm^3 to 1cm^3 , with $\beta_{FM} = 0.4$, $\beta_{DP}^d = 2$, $\beta_{DP}^l = 2$, a minimum V_{LM} with $\beta_{LM} = 0.1$ is calculated such that the mono-stable condition is met in Figure 4.5(a). The figure shows that as previously stated in literature the volume of the LM need not be bigger in size when compared to the FM, but it can in fact be much smaller in size. However, to achieve a h greater than 0.1 mm, V_{LM} needs to be increased beyond the minimum value as this would decrease the slope of F_2 according to Figure 4.4(c) on the tradeoff that this increases L (Figure 4.4(d)). It can be seen from Figure 4.5(b) that h in general increases for larger η . This case of designing the VDL system for a maximum h is preferred from a vibration energy harvesting perspective as the output power depends on the maximum amplitude of the vibrating mass [55], amplitude of the FM in this case. It should be noted that the magnetization of grade N52 magnets (K&J Magnetics, Inc.) were considered in Figure 4.5(a) and (b) along with accounting for their demagnetizations due to their aspect ratios.

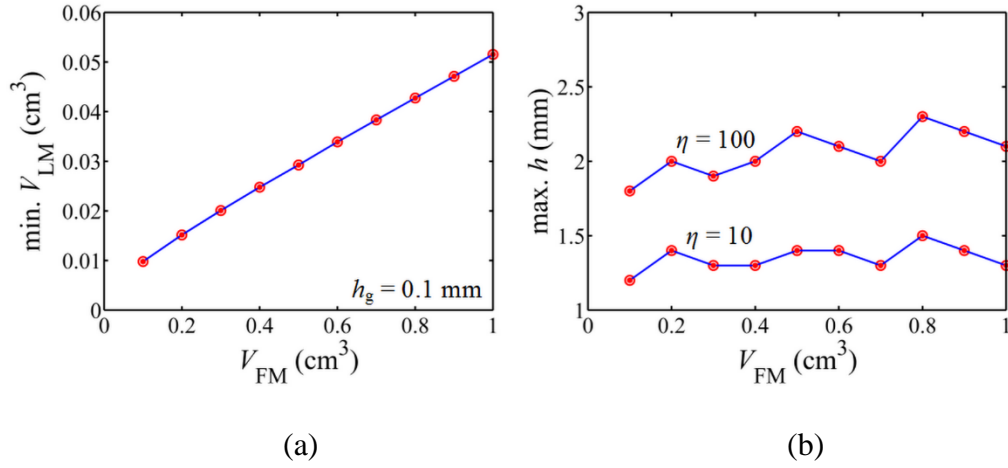


Figure 4.5. (a) Variation of minimum V_{LM} with V_{FM} and (b) variation of maximum h with V_{FM} .

With the dependence of the size of the harvester (L) and the levitation gap (h) on V_{LM} discussed, one important aspect that needs to be discussed is the factors that affect the resonant frequency of the system. For this two parametric sweeps were done, one considers the resonant frequency of a set of V_{FM} ranging from 0.1 cm^3 to 1 cm^3 with varying levitation gap from the minimal to the maximum possible h with a fixed volume ratio (η) of 100 (Figure 4.6(a)). The other parametric sweep considers the resonant frequency of a V_{FM} of 1 cm^3 with varying levitation gap and varying η from 10 to 100 (Figure 4.6(b)). It can be seen that there is a strong dependency of f_n with V_{FM} and h , from Figure 4.6(a), and it can be seen that there is not a significant change in f_n with η , from Figure 4.6(b). For these two figures the system is assumed to operate in the linear region and the magnetization of grade N52 magnets (K&J Magnetics,

Inc.) were considered for the numerical calculations along with accounting for their demagnetizations due to their the aspect ratios.

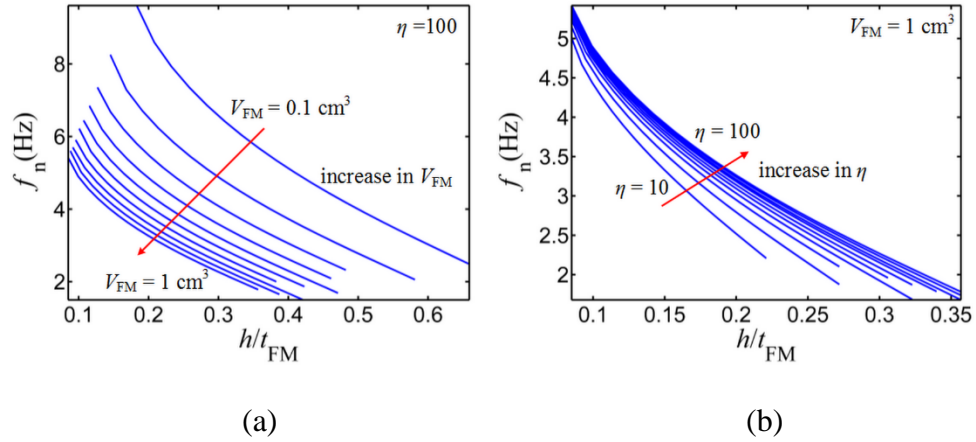


Figure 4.6. (a) Variation in f_n with normalized h for a fixed $\eta = 100$ with V_{FM} varying from 0.1 cm^3 to 1 cm^3 and (b) variation in f_n with normalized h for a fixed $V_{FM} = 1 \text{ cm}^3$ for η varying from 10 to 100.

A flowchart is shown in Figure 4.7 which summarizes the detailed design methodology discussed in this section. Here k represents the equivalent spring stiffness of the system, ρ represents the density of the FM and g represents a function. The flowchart includes the optimized aspect ratios of the FM and the DP to maximize the force between them, the selection of the volume and the aspect ratio of the LM for levitation to be achieved with the required levitation gap (with a certain maximum limit based on η) and the frequency tuning capability of the system. The next section will discuss about the damping due to eddy currents

in the DP of the VDL system, ways to mitigate it and a coil geometry for electromagnetic transduction.

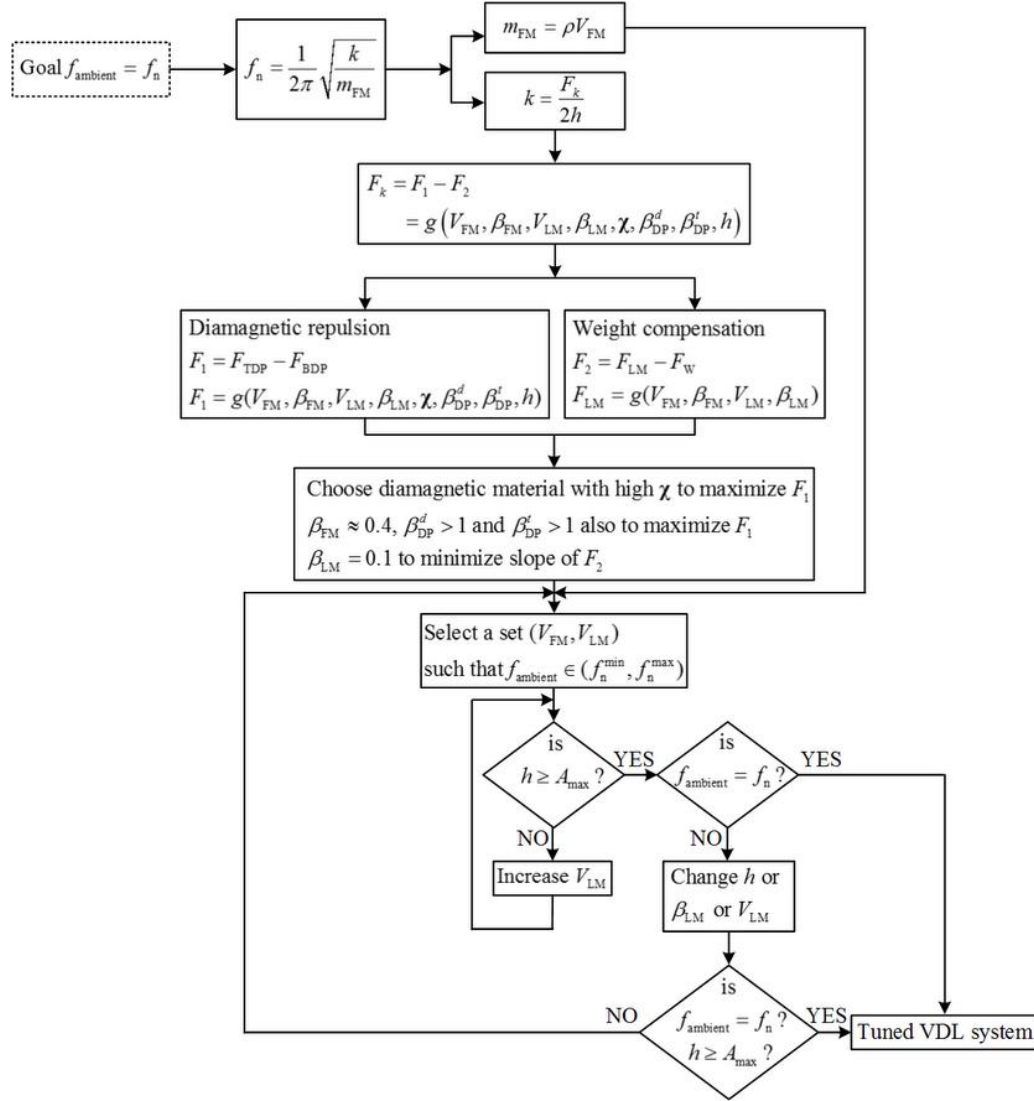


Figure 4.7. Flowchart for tuning f_n of a VDL system with the dominant f_{ambient}

4.2 Damping due to eddy currents in the DP and a copper coil for transduction

Current is induced in a conductor when a magnetic flux through it changes according to Faraday's law. In a VEH system like Figure 4.9, these can be either lost as heat due to eddy currents or be harnessed to power something. In either case they will produce a magnetic field of their own opposing the change in the magnetic field through it. This opposing magnetic field produces a force by Lorentz law which is proportional to the velocity and hence act like a viscous damping force to the motion of the object causing this magnetic flux change. In the present VDL system, when the FM moves relative to the DP and considering that DPs are usually made of pyrolytic graphite, which is a good conductor, eddy currents are generated in them which oppose the motion of the FM.

The estimation of the eddy current force presented in [133, 134] is used here. The angular component of the electric field at the edge of the DP should be zero; so the angular current density should be zero to maintain continuity at the boundary between the DP and air. Hence the damping force (F_z), by taking into account for the edge effects, is given by

$$F_z = 2\pi\sigma v \int_0^{h_{DP}} \int_0^{r_{DP}} r [B_r(r, a+z) - B_r(2r_{DP} - r, a+z)] dr dz \quad (4.2)$$

where σ is the conductivity of the DP, v is the velocity of the FM, r_{DP} is the radius of the DP ($d_{DP}/2$), a is the axial distance between the DP and the FM at which the force is being calculated and (r, z) are the radial and axial positions in the DP at which the magnetic field is being calculated.

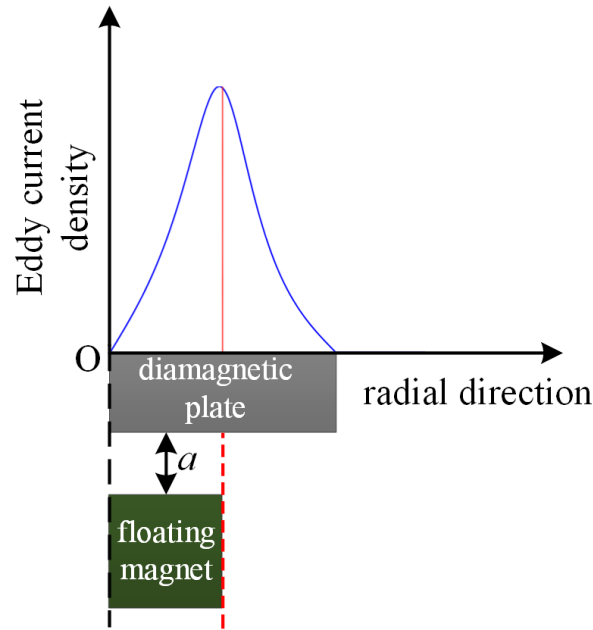


Figure 4.8. Cylindrically symmetric eddy current density profile in the DP.

With equation (4.2) and with the dimensions of the FM and the DP as given in Table 4.2, Figure 4.8 shows the eddy current density profile when the FM moves axially relative to the DP. This figure is cylindrically symmetric about O and hence only half of it is shown here. It can be seen that the eddy current density is maximum around the radius of the FM, this is expected because of the highest magnetic flux density around this region. The energy lost due to eddy currents can severely dampen the system at resonance. A possible solution to avoid the eddy currents would be to replace a part of the DP with coil for vibration energy harvesting as in the experimental setup of Chapter 3. Although it decreases the damping in the system it also decreases the stiffness which results in a smaller h .

Owing to the drawback of decrease in h , hence potential loss in achieving nonlinearity, a second topology is considered as shown in Figure 4.9(a). In this topology there is no loss in

h but the open-loop Q factor ($=0.5/\zeta_m$, where ζ_m is the mechanical damping ratio) is low owing to the stronger eddy currents as shown in Figure 4.8. Hence, a laminated pyrolytic graphite plate is made by cutting the pyrolytic graphite plate into slices of 2 mm and joining them back with an insulation in between them as shown in Figure 4.12(b), much similar to laminated iron cores generally used in transformers. The open-loop Q factor is found experimentally by measuring the ring-down of the FM after stopping the external vibration input (Figure 4.10(b)). As $Q = \pi(\ln(V_1/V_2))^{-1}$, where V_1 and V_2 are voltage amplitudes of successive cycles, it was measured to be 48 immediately after the vibration input was turned off and to be around 65 after ten second. However, the Q factor is not a constant but depends on the relative speed of the FM with the DP and hence this value is only an averaged approximate value.

A comparison is made with the damping due to eddy currents and the damping in conventional cantilever based energy harvesters in Table 4.1. The value of the damping coefficient (c_m) not only depends on the Q factor of the system but also on the natural frequency (f_n) of the system. The damping in this system can be engineered to decrease the damping further, say by laminating the DP with smaller thicknesses or using a DP material with higher resistance (e.g., silver) without a considerable difference in the stiffness of the system. Such equivalent design opportunity is not easily available for conventional cantilever based systems.

Table 4.1 Mechanical damping co-efficient for the fundamental vibration mode for different reported VEHs

| References | $c_m / m = 4\pi\zeta_m f_n = 2\pi f_n / Q (s^{-1})$ |
|--------------------------|---|
| Roundy and Wright [4] | 22.62 |
| Erturk and Inman [32] | 15.47 |
| Mann and Sims [61] | 9.743 |
| Glynee-Jones et al. [22] | 4.72 |
| Present study | 0.264 |

This section summarized the equivalent mechanical damping in the VDL system, ways to mitigate it and a coil geometry for electromagnetic transductions. As sections 4.1 and 4.2 covered the restoring force, damping force and electromagnetic transduction characteristics of the VDL system one is now in a position to design an experimental setup with an enhanced levitation gap and possibly a more efficient energy harvester than the previous study (Chapter 3). The following section will discuss about one such experimental setup along with discussing its frequency response characteristics.

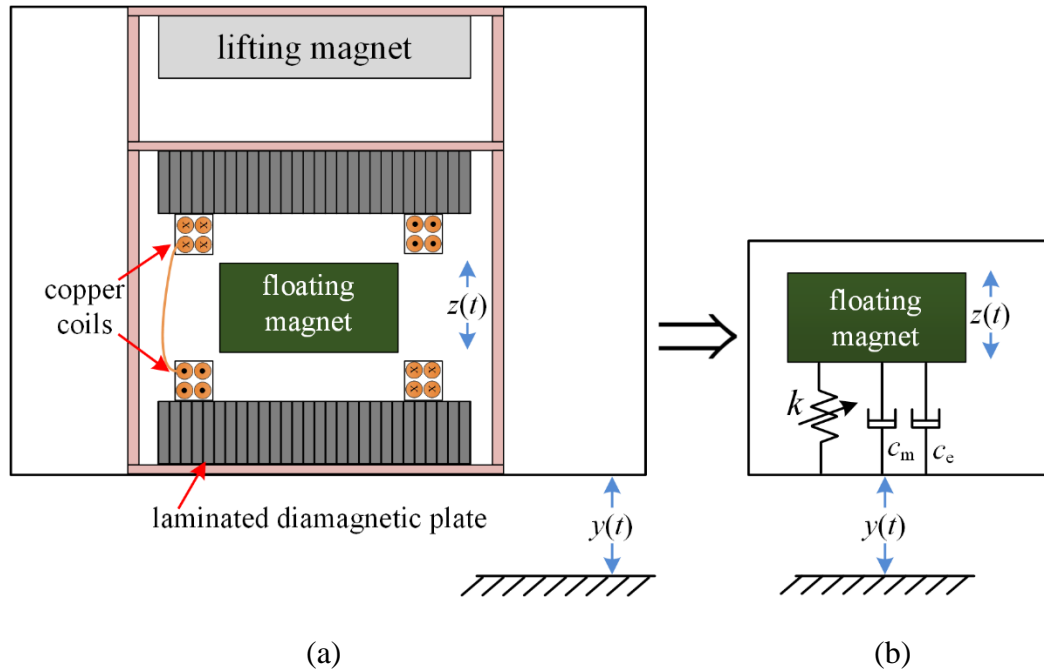


Figure 4.9. (a) A two dimensional model of the VDL energy harvester with the copper coils and (b) an equivalent 1 degree of freedom (1-DOF) model of the VDL energy harvester.

4.3 Experimental setup

An electromagnetic VEH like the one of the present study can be simply modeled as a one degree of freedom system consisting of a spring, a mass and a damper (Figure 4.9(b)) [135]. The total power that is absorbed from the ambient vibration by the energy harvester is the power consumed by the damper. The damper consists of two components, namely a mechanical and an electrical damper. The equivalent mechanical damper models the dissipated energy due to eddy currents (or due to internal friction for conventional cantilever based systems) and air damping whereas the electrical damper corresponds to the ohmic losses in the

induction coil and in the load resistance that is attached. The electromechanical equations of motion are given by

$$\begin{aligned} m_{\text{FM}}\ddot{z} + c_m\dot{z} + F_K(z) + F_L(i, z) &= m_{\text{FM}}\omega^2 A \sin \omega t \\ \dot{i}L_{\text{coil}} + iR_L + iR_{\text{coil}} &= V(z, \dot{z}) \end{aligned} \quad (4.3)$$

here z is the relative displacement of the FM, i is the current in the coil, A is the amplitude of the sinusoidal base displacement, $F_L(i, z)$ is the electromagnetic (Lorentz) force as a function of the relative displacement and the current in the coil, R_L is the resistance of the load, R_{coil} is the resistance of the coil, L_{coil} is the inductance of the coil, $V(z, \dot{z})$ is the voltage induced in the coil as a function of the relative displacement and velocity, c_m is the mechanical damping co-efficient and $F_K(z)$ is the restoring force as a function of relative displacement. The electromagnetic force, is defined by the product of the radial magnetic field of FM at every loop of the coil, the length of the loop and the current in the loop, that is

$$F_L(i, z) = 2\pi i \sum_{j=1}^N \bar{r} B_r(\bar{r}, \bar{z}) \quad (4.4)$$

where, N is the number of turns of the coil, (\bar{r}, \bar{z}) are the radial and axial distances of the position of the coil with respect to the center of the FM. The voltage induced (V) is defined by the product of the radial magnetic field of FM at every loop of the coil with the length of the loop and the velocity of the magnet, that is,

$$V(z, \dot{z}) = 2\pi \dot{z} \sum_{j=1}^N \bar{r} B_r(\bar{r}, \bar{z}) \quad (4.5)$$

To make a fair comparison with a previous study (Chapter 3) a similar experimental procedure of maintaining a constant mechanical input power to the harvester while doing a

frequency sweep is done here. For a harmonic base excitation $A \sin \omega t$ to the harvester, ω is the angular frequency of the base excitation and A is the amplitude of the base excitation, then the average mechanical input power to the energy harvester (\bar{P}_{input}) is approximated by integrating the product of the total mass of the harvester ($m_{\text{harvester}}$) with the velocity and acceleration over one-fourth of the cycle.

$$\begin{aligned}\bar{P}_{\text{input}} &\approx \frac{2\omega}{\pi} \int_0^{\pi/2\omega} m_{\text{harvester}} \left| (-A\omega^2 \sin \omega t)(A\omega \cos \omega t) \right| dt \\ &\approx \frac{\omega}{\pi} \int_0^{\pi/2\omega} m_{\text{harvester}} \omega^3 A^2 \sin 2\omega t dt \approx \frac{1}{\pi} m_{\text{harvester}} \omega^3 A^2\end{aligned}\quad (4.6)$$

As shown in equation (3.21), a constant mechanical input power to the energy harvester can be maintained by keeping $\omega^3 A^2$ constant. For this study the excitation frequency was varied from 0.5 Hz to 5.8 Hz and the input amplitude was varied from 4.01 mm to 0.1 mm in order to keep the product $\omega^3 A^2$ constant to $500 \text{ mm}^2/\text{s}^3$.

For the experimental setup a V_{FM} was selected based on availability from the vendors to be as close as possible to the previous study (Chapter 3) and an aspect ratio closest to the optimum ($V_{\text{FM}} = 0.8 \text{ cm}^3$, $\beta_{\text{FM}} = 0.5$). The choice of V_{LM} with an aspect ratio of 0.1 at large η ($\eta > 10$) were not easily available and hence a compromise was made by selecting a larger η and a larger β_{LM} ($\eta = 32$, $\beta_{\text{LM}} = 0.25$). The radius of the DP was around four times the radius of the FM but the thickness was only slightly greater than half the thickness of the FM, mainly due to the difficulty in the lamination process. Also it can be seen from Figure 4.2(b) and (c) that an aspect ratio of half for the FM and such relative ratios for the DP provide for a reasonably high repulsive force. The pyrolytic graphite plate, used as the DP here, was cut into

thin slices by using a wire EDM process and stuck back together with an insulation between them to reduce eddy currents. A coil-winding machine using step motors was built to wind two copper coils with an AWG 36 magnet wire. Axially thicker coils would provide a better electromagnetic transduction coefficient, but coils thicker than 1.5 mm would make the tracking of the motion of the FM difficult. Hence, a compromise was made in the transduction coefficient for the sake of demonstration. The full details of the present system are given in Table 4.2.

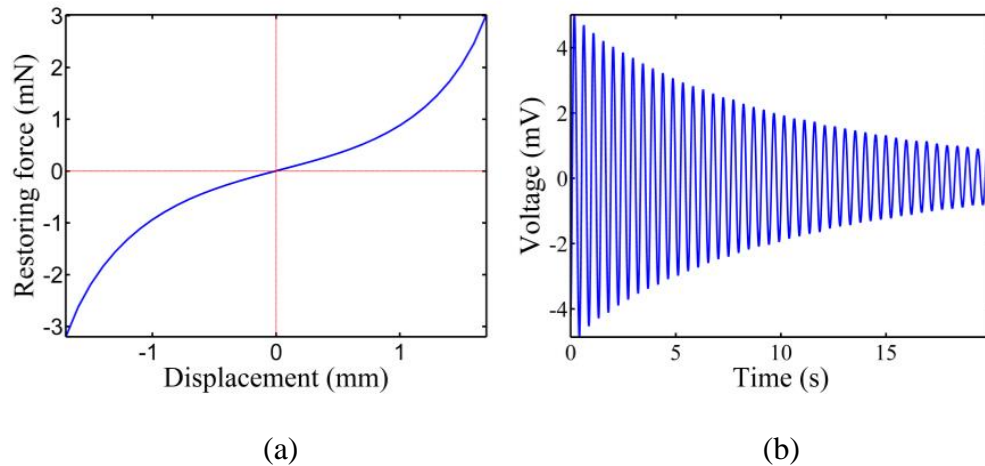


Figure 4.10. (a) Restoring force and (b) ring down of the FM, to determine open-loop Q factor.

The experimental setup is shown in Figure 4.12 and Figure 4.12, with the LM, the FM, the laminated pyrolytic graphite plate, copper coils, a high speed camera and an Instron test bed to carry out the low-frequency vibration tests. A green tape was used to cover the FM, which can be seen in Figure 4.12, to enhance its visibility while recording its motion with the high

speed camera. Figure 4.13(a)-(d) show the experimental results along with the theoretical predictions. The VDL based VEH system with parameters as given in Table 4.2 has a restoring force which varies nonlinearly with displacement as shown in Figure 4.10(a), a hardening type nonlinearity, due to which the resonance frequency shifted to the right in Figure 4.13 [136].

The experimental value of the voltage/displacement is lower than the theoretical value at some frequencies because of the shortened peak due to the impact of the FM with the DPs, especially near the jump-down frequency. This is mainly due to the extremely low mechanical damping in the system and one would require a significantly larger LM or a significantly smaller FM to increase the levitation gap to avoid the impacts between the FM and the DP. A larger V_{LM} or a smaller V_{FM} would further increase η which was already at 32 and was considered detrimental to the overall efficiency of the harvester in terms of either increasing the overall weight of the harvester (larger V_{LM}) or decreasing the induced voltage ($V \propto B_r \propto V_{FM}$). Also, to further reduce the impacts the load resistance value chosen was not optimum but varied to arrive at a value such that the hardening type nonlinearity was observed and there was not a considerable loss in the peak voltage/displacement near the jump-down frequency. Experimentally the jump-down frequency occurred at 2.1 Hz whereas theoretically it occurs at 2.2 Hz, this moderate discrepancy is because of the loss of stiffness from the DP due to the process of laminating the DP to reduce eddy currents. Figure 4.13(a) shows two unstable points at frequencies 2.2 Hz and 2.3 Hz (marked as \circ), which are achievable when the initial conditions of the FM are not set to zero. The other discrepancies can be due to the large input displacements of the harvester at low frequencies when compared to the levitation gap which

causes impact between the DP and FM, small differences between the given manufacturer magnetization value from the actual magnetization value of the magnets, inaccurate estimation of the open-loop Q factor and assumption of uniform magnetization in the theoretical analysis.

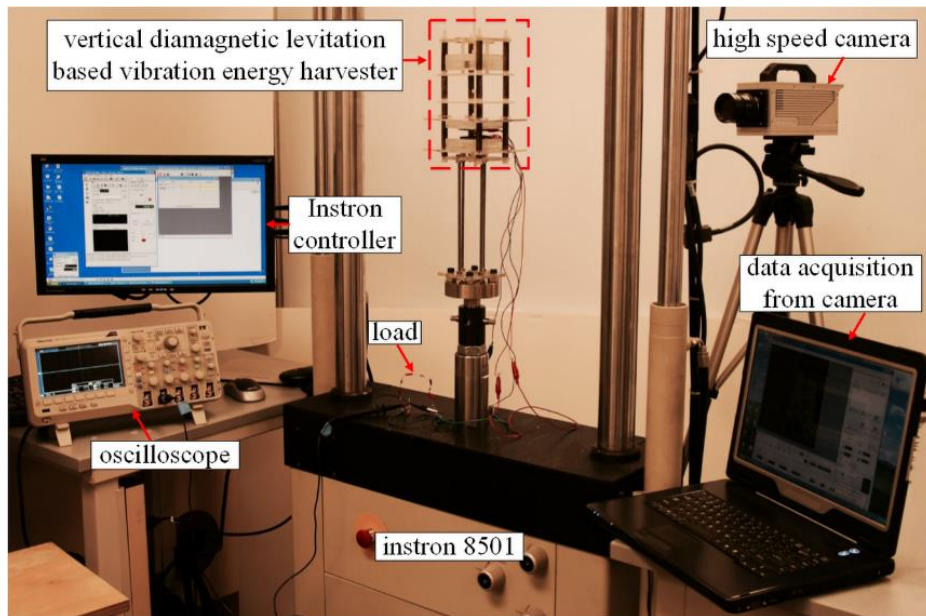


Figure 4.11. Experimental setup of the VDL based VEH

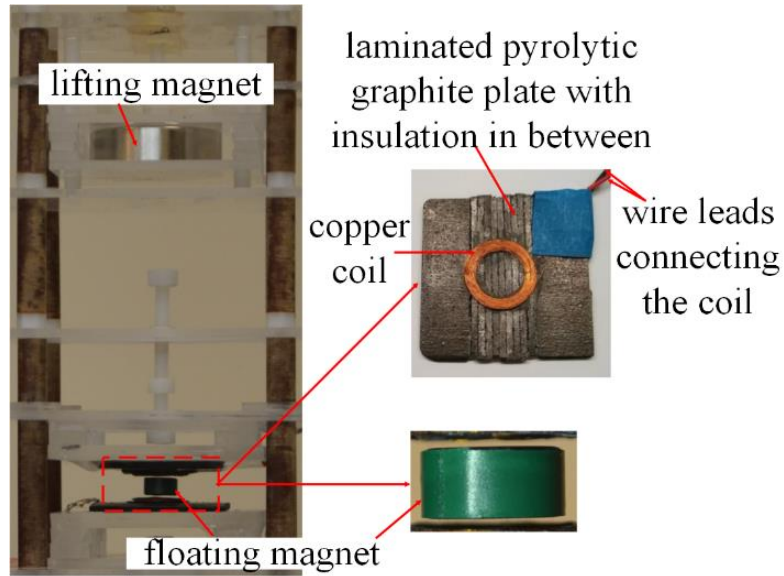


Figure 4.12. Close-up of the VDL based VEH.

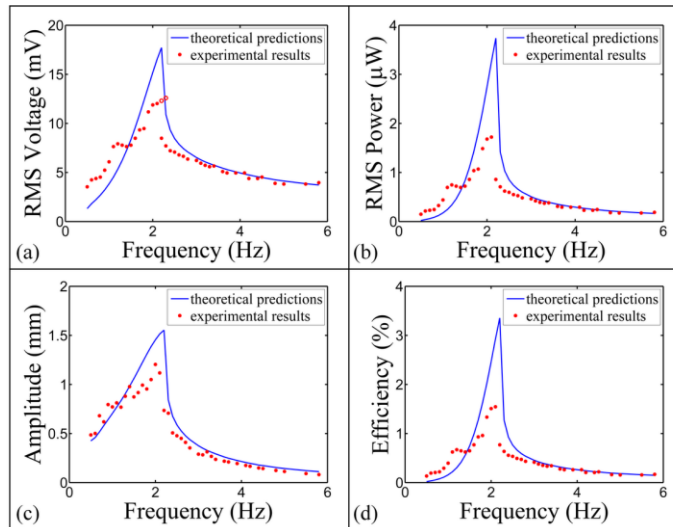


Figure 4.13. Experimental results and theoretical predictions of (a) RMS voltage across the load resistance, (b) RMS power in the load resistance, (c) peak relative displacement of the FM and (d) overall efficiency of the VDL based VEH system.

Table 4.2 Model parameters for experimental setup

| | | | | | | | | |
|-----------|-------------------------------|--------------------------------|-------------------|-----------------|------------------------|-----------------|--------------------------|--------------------------|
| Parameter | d_{FM} | t_{FM} | m_{FM} | d_{LM} | t_{LM} | d_{DP} | t_{DP} | r_{wire} |
| Value | 12.7 | 6.35 | 6 | 50.8 | 12.7 | 50 | 3.5 | 15.8 |
| Unit | mm | mm | g | mm | mm | mm | mm | μm |
| Parameter | $r_{\text{coil}}^{\text{in}}$ | $r_{\text{coil}}^{\text{out}}$ | t_{coil} | h | $m_{\text{harvester}}$ | N | $A^2\omega^3$ | \bar{P}_{input} |
| Value | 7.5 | 11 | 1.25 | 1.7 | 700 | 160 | 500 | 111.41 |
| Unit | mm | mm | mm | mm | g | - | mm^2/s^3 | μW |

4.4 Conclusions

An optimal mono-stable design of a VDL based VEH with a hardening-type nonlinearity has been investigated in this chapter. By using the semi-analytic techniques, parametric studies to quantify the geometric effects of its components on levitation gap, size of device and natural frequency are presented. An aspect ratio of around four-tenth for the FM, a DP of thickness greater than the thickness of the FM and a radius greater than the radius of the FM provide for a maximum force between the two, which is deemed essential for a greater levitation gap. An aspect ratio of one-tenth is considered ideal for the LM, subject to availability of smaller aspect ratios without considerable loss in the residual magnetic flux, for enhancing the levitation gap. If the size of the device possesses a greater priority in design than the levitation gap then the volume of the LM can in fact be much smaller than the volume of the FM, contrary to the popular notion for the VDL system. However, if larger levitation gaps are required larger volumes of LM are needed.

From a vibration energy harvesting aspect of the system, the open-circuit natural frequency of the system is primarily dependent on the volume of the FM and the levitation

gap. Damping due to eddy currents in the DP and ways to mitigate them are critically discussed along with the incorporation of a coil is considered such that it does not significantly affect the levitation gap or natural frequency of the system. Lastly, an experimental system is setup to validate the findings. The VDL based VEH due to the increased levitation gap showed hardening type nonlinearity and the jump-down phenomena was seen in the frequency response curves. The results show an overall efficiency of 1.54 %, a root mean square (RMS) power output of 1.72 μW when excited at a mechanical input power of 111.41 μW (corresponds to an acceleration of 0.081m/s^2) and at a frequency of 2.1 Hz. The open-loop Q factor of the system was measured to be around 48, however, the closed-loop Q factor was reduced by varying the load to decrease the loss in energy due to the impact of the FM with the DP. Further studies are needed to understand how the jump-down frequency and the peak output voltage vary with the levitation gap and the damping while trying to minimize the loss due to impact between the FM and the DP.

5 A horizontal diamagnetic levitation (HDL) based vibration energy harvester

This chapter is largely reprinted with permission from the recently accepted article S. Palagummi, J. Zou, F.G. Yuan A horizontal diamagnetic levitation based low frequency vibration energy harvester, *Journal of Vibration and Acoustics – Transactions of the ASME*, doi:10.1115/1.4030665.

This chapter investigates a horizontal diamagnetic levitation (HDL) system for vibration energy harvesting in contrast to the vertical diamagnetic levitation (VDL) system discussed in the previous chapters. In this configuration, two large magnets, alias lifting magnets (LMs), are arranged co-axially at a distance such that in between them a magnet, alias floating magnet (FM), is passively levitated at a laterally offset equilibrium position. The levitation is stabilized in the horizontal direction by two diamagnetic plates (DPs) made of pyrolytic graphite placed on each side of the FM. This HDL configuration mitigates the limitation on the amplitude of the FM imposed in the VDL configuration and exploits the ability to tailor the geometry to meet specific applications due to its frequency tuning capability. A simple circular coil geometry is designed to replace a portion of the pyrolytic graphite plate without sacrificing the stability of the levitation for transduction.

The force between axially offset magnets discussed in Chapter 3 cannot be extended for laterally and axially offset magnets present in this HDL system. For this reason, a semi-analytical technique using Bessel functions for the force between two laterally offset magnets

is discussed here. The modeling for the rest of the forces in the system are largely inherited from the VDL system analysis (presented in the earlier chapters). With an understanding of the theoretical modeling, an experimental system was setup. The experimental system validated the theoretical findings and the system exhibited a weak softening frequency response.

5.1 A HDL system

The VDL system served as a first mechanism in energy harvesting literature which can be designed to have natural frequencies from sub-Hertz to a couple of Hertz (Chapter 4). Additionally, due to the passive stable levitation of the vibrator (the FM) in the system, there was no mechanical friction. Even eddy currents which arose in the system could be engineered to be a minimum. However, several challenges still hindered the VDL system from becoming an efficient system. The main challenges faced were the strict stability conditions and the limitations of the maximum amplitude of the vibrating mass, which was inherently limited by the distance between the DPs which in turn was coupled back with the stabilization condition. To overcome these challenges, alternative configurations of the diamagnetic levitation mechanism needed to be investigated.

A HDL system is proposed for the use of vibration energy harvesting in this chapter. This configuration was first shown in a publication by Simon *et al* [110]. To be consistent with the literature on the levitation mechanisms using diamagnetism, this form of levitation should be actually referred to as the diamagnetically stabilized horizontal levitation rather than horizontal diamagnetic levitation as the latter may refer to the levitation of the diamagnetic

material as opposed to a magnet in the former. However, to shorten the lengthy reference to the levitation, here it will be referred to as horizontal diamagnetic levitation or simply as HDL.

In this HDL configuration, the weight of the FM is balanced by the attractive force of two LMs in the vertical direction and stability is realized by the repulsive force of the DPs, pyrolytic graphite plates are selected for this purpose in this chapter, in the horizontal direction (Figure 5.1). Due to the motion of the FM primarily in the vertical direction, its maximum amplitude is no longer limited by a physical constraint and the stabilization conditions are more relaxed, which is discussed later in the chapter, hence overcoming the limitations faced in the vertical configuration.

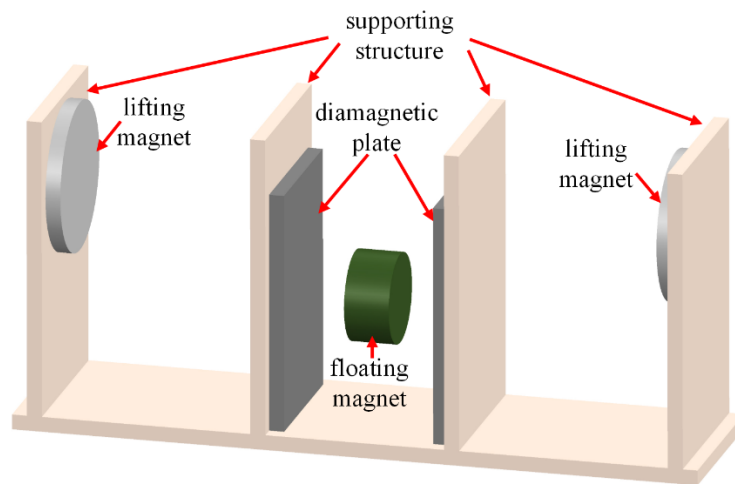


Figure 5.1 Schematic of a HDL system

The rest of this chapter is discussed as follows. Section 5.2 presents a theoretical analysis on the forces on the FM due to the DPs and the LMs in all three directions, the stability brought about by the DPs and the LMs and the frequency tuning capabilities. Section 5.3

discussed the eddy current damping, a simple coil geometry for transduction without sacrificing stability and the electromechanical equations of motion for the vibration energy harvester. The experimental validation is discussed in section 5.5. Section 5.6 put forwards a discussion on possible further studies need to improve the performance of the harvester and section 5.7 discusses the major conclusions of this work and future proposed work.

5.2 Theoretical modeling

A schematic of the HDL vibration energy harvester system is shown in Figure 5.2. A copper coil is shown which replaces a portion of each of the DP for transduction. One of the points of investigation in the chapter is to make a fair comparison of the HDL system with the VDL system discussed in chapter 3. Hence, the volume of the LM and FM have been nearly maintained to be the same. As two LMs are used in this setup, the total volume of the LM was split into two equal ones (LM_1 and LM_2) and used symmetrically on either side of the FM.

This section presents the theoretical modeling required to understand the static levitation and dynamic response characteristics unique to this HDL system. The discussion in this section will be divided into the static levitation conditions, stability conditions and characterization of the restoring forces.

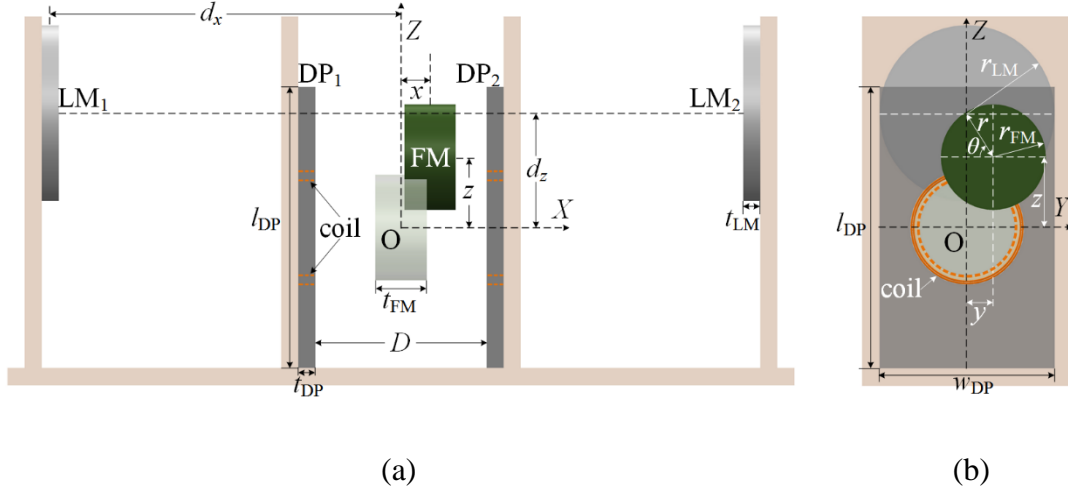


Figure 5.2 A schematic of the HDL based vibration energy harvester system (a) front view (b) side section view with the lifting magnets (LM_1 and LM_2), the diamagnetic plates (DP_1 and DP_2), the floating magnet (FM) and the copper coil. The lighter colored FM shows its static equilibrium position whereas the darker colored FM shows its perturbed dynamic position.

In order to statically levitate a magnet under this configuration one needs to estimate the forces from both the LMs and the DPs. Firstly, the forces acting on the FM due to the two LMs needs to be estimated to determine the axial and lateral positions (d_x and d_z , cf. Figure 5.2) where the weight of the FM is balanced.

The attractive forces between the LM and the FM can be estimated by modeling the magnets as a dipole or as a thin coil. The force between two magnetic dipoles of dipole strength m_{FM} and m_{LM} separated by a distance d (d_x in the x -direction, d_y in the y -direction and d_z in the z -direction, such that, $d^2 = d_x^2 + d_y^2 + d_z^2$) is given by

$$\begin{aligned}
F_x^D &= \frac{3\mu_0}{4\pi d^5} \left(3m_{\text{FM}}m_{\text{LM}}d_x - \frac{5m_{\text{FM}}m_{\text{LM}}d_x^3}{d^2} \right) \\
F_y^D &= \frac{3\mu_0}{4\pi d^5} \left(m_{\text{FM}}m_{\text{LM}}d_y - \frac{5m_{\text{FM}}m_{\text{LM}}d_x^2d_y}{d^2} \right) \\
F_z^D &= \frac{3\mu_0}{4\pi d^5} \left(m_{\text{FM}}m_{\text{LM}}d_z - \frac{5m_{\text{FM}}m_{\text{LM}}d_x^2d_z}{d^2} \right)
\end{aligned} \tag{5.1}$$

where F_x^D , F_y^D and F_z^D represent the dipole forces in the x , y and z directions.

Alternatively, a semi-analytical form which models the magnets as thin coils and estimates the force between individual coils of each magnet and integrates over the length of each magnet can be used to calculate the force between the magnets (*cf.* Figure 5.3). The modeling of the magnets is similar to what was done in Chapter 3 but here the force between laterally and axially offset magnets is calculated rather than just axially offset magnets as in the former. Assuming the FM and LM have magnetizations M_{FM} , M_{LM} with residual magnetic flux densities Br_{FM} , Br_{LM} and are equivalently modeled as thin coils with currents I_{FM} , I_{LM} , with turns N_{FM} , N_{LM} and have axial turn densities σ_{FM} , σ_{LM} . The relation between these terms are given by

$$\begin{aligned}
M_{\text{LM}} &= Br_{\text{LM}} / \mu_0, \\
M_{\text{FM}} &= Br_{\text{FM}} / \mu_0, \\
I_{\text{LM}} &= M_{\text{LM}}t_{\text{LM}} / N_{\text{LM}}, \\
I_{\text{FM}} &= M_{\text{FM}}t_{\text{FM}} / N_{\text{FM}}, \\
\sigma_{\text{LM}} &= \frac{N_{\text{LM}}}{t_{\text{LM}}}, \\
\sigma_{\text{FM}} &= \frac{N_{\text{FM}}}{t_{\text{FM}}}
\end{aligned} \tag{5.2}$$

where t_{LM} and t_{FM} are the thickness of LM and FM respectively

The geometry of the problem leads to the use of Bessel functions and upon simplification, the forces (F_x^{TC} , F_y^{TC} and F_z^{TC}) are given by [137]

$$\begin{aligned}
F_x^{\text{TC}} &= c \int_{d_x^-}^{d_x^+} \int_0^{t_{\text{FM}}} \int_0^\infty s J_0(sd_{yz}) J_1(sr_{\text{LM}}) J_1(sr_{\text{FM}}) \text{sgn}(x_2 - x_1) \exp(-s|x_2 - x_1|) ds dx_1 dx_2 \\
F_y^{\text{TC}} &= c \cos \theta \int_{d_x^-}^{d_x^+} \int_0^{t_{\text{FM}}} \int_0^\infty s J_1(sd_{yz}) J_1(sr_{\text{LM}}) J_1(sr_{\text{FM}}) \exp(-s|x_2 - x_1|) ds dx_1 dx_2 \\
F_z^{\text{TC}} &= c \sin \theta \int_{d_x^-}^{d_x^+} \int_0^{t_{\text{FM}}} \int_0^\infty s J_1(sd_{yz}) J_1(sr_{\text{LM}}) J_1(sr_{\text{FM}}) \exp(-s|x_2 - x_1|) ds dx_1 dx_2
\end{aligned} \tag{5.3}$$

where $d_x^+ = d_x + (t_{\text{FM}} + t_{\text{LM}})/2$, $d_x^- = d_x + (t_{\text{FM}} - t_{\text{LM}})/2$, d_x is the axial distance between the centers of LM and FM (*cf.* Figure 5.2), r_{LM} and r_{FM} are the radii of LM and FM respectively, $c = -\mu_0 \pi I_{\text{FM}} I_{\text{LM}} r_{\text{FM}} r_{\text{LM}} \sigma_{\text{FM}} \sigma_{\text{LM}}$, J_0 and J_1 are Bessel functions of the first kind of order zero and one respectively and d_{yz} ($d_{yz}^2 = d_y^2 + d_z^2$) is the lateral distance between the LM and FM.

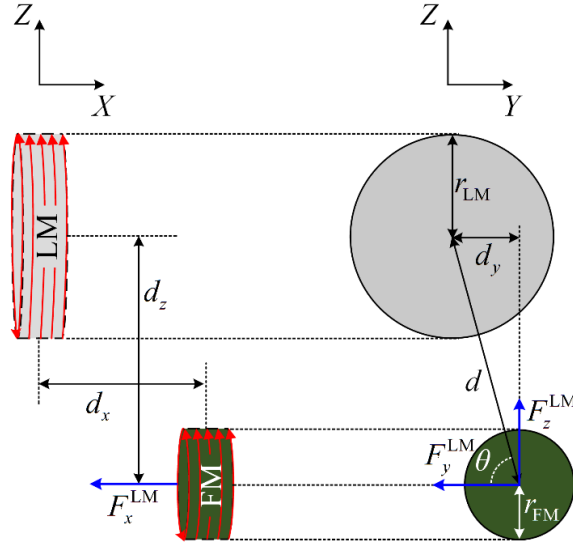


Figure 5.3 Thin coil (TC) model for estimating the force between laterally and axially offset magnets

Off the equations in (5.1) and (5.3), except in the y -direction there are competing forces in other directions. Hence, it is safe to assume that the levitation is sustained for small displacements in the y -direction without much further analysis. However, for large displacements in the y -direction, forces in the z -direction may not be able to balance w_{FM} and as a result FM may lose its stability in the z -direction. For this study, it is assumed that there are no large displacements of the FM in the y -direction as this issue can easily be averted by placing mechanical constraints.

To estimate the error between the two models for a certain range of axial and lateral distances between the magnets, equation (5.4) has been used to plot Figure 5.4. For this error analysis only forces in the x and z direction are considered as they are of primary importance and hence it is assumed $d_y = 0$ which leads to $F_y^D = F_y^{TC} = 0$. It can be seen from the figures

that the error percentages for axial forces can be significant for certain range of values. Although, for some distances the error percentages for the lateral force may be lower than 3%, which is generally acceptable. The thin coil model has been used for further analysis to avoid the ambiguity ($F_x^{\text{LM}} = F_x^{\text{TC}}, F_y^{\text{LM}} = F_y^{\text{TC}}, F_z^{\text{LM}} = F_z^{\text{TC}}$). Also, computationally, the calculations are not prohibitive.

$$e_z = \frac{|F_z^{\text{TC}} - F_z^{\text{D}}|}{F_z^{\text{TC}}}, e_x = \frac{|F_x^{\text{TC}} - F_x^{\text{D}}|}{F_x^{\text{TC}}} \quad (5.4)$$

As both the LMs are identical in this case and d_x is the same for both, the forces from both the LMs in the z -direction is the same ($F_z^{\text{LM}} = F_z^{\text{LM}_1} = F_z^{\text{LM}_2}$). Figure 5.5(a) shows the various positions of d_x and the corresponding d_z at which the attractive force from the LMs in the z -direction balances the weight of the FM ($2F_z^{\text{LM}} = F_w$, where F_w is the weight of FM). In this figure, the starting d_x value is chosen based on a minimum clearance between the surfaces of the LM and the FM as 50 mm, taking the support structure into consideration. It is seen that the weight is balanced up to a certain d_x (≈ 100.4 mm) after which the attractive force from the LMs cannot balance the weight of the FM (F_w).

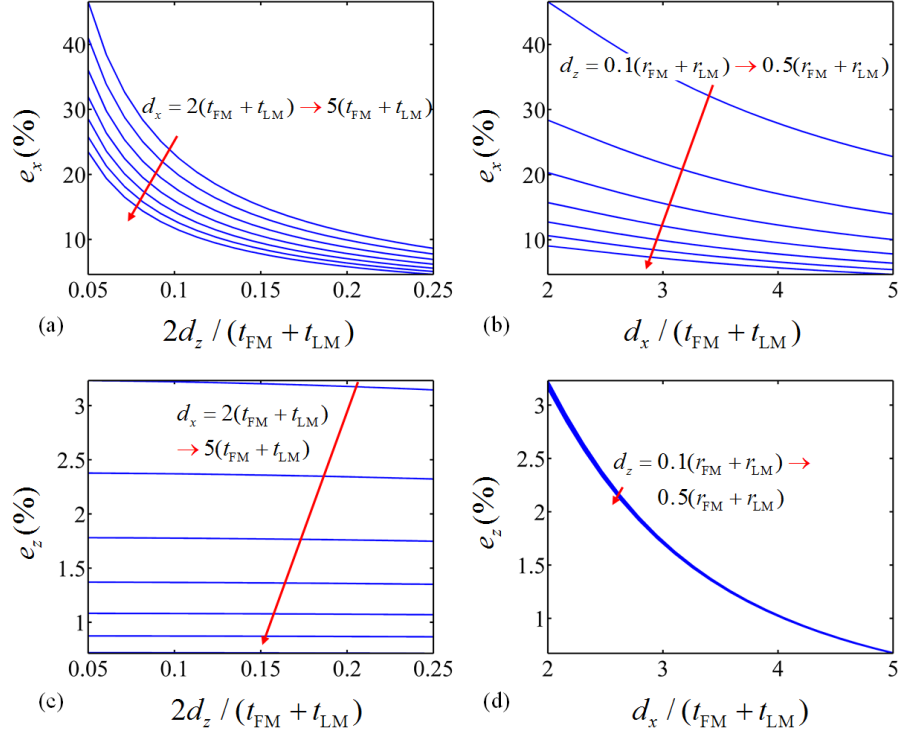


Figure 5.4 Error estimates between the thin coil model and the dipole model for estimating the lateral and axial force between two magnets.

The LMs not only attract the magnet in the z -direction, but also attract it in the x -direction which hinders the static levitation. The DP provides the repulsive force in the x -direction to nullify this axial attractive force from the LM and makes levitation possible. This repulsive force from the DP can be calculated by taking the negative gradient of the magnetic potential energy of the DP in that direction.

$$F_x^{\text{DP}} = -\int \nabla_x U \, dV = -\int \nabla_x (\mathbf{M} \cdot \mathbf{B}_{\text{FM}}) \, dV = -\int \mathbf{M} \cdot \nabla_x \mathbf{B}_{\text{FM}} \, dV \quad (5.5)$$

where \mathbf{M} is the magnetization due to the total magnetic field inside the DP (due to the FM and the LMs) and \mathbf{B}_{FM} is the magnetic field vector of the FM inside the DP. The magnetic field is

determined by modeling the magnet as a thin coil as described in Chapter 3 and in Ref. [127].

The magnetization \mathbf{M} is given by

$$\begin{aligned}\mathbf{M} &= (\chi_x B_x^T \hat{\mathbf{x}} + \chi_y B_y^T \hat{\mathbf{y}} + \chi_z B_z^T \hat{\mathbf{z}}) / \mu_0, \\ B_i^T &= B_i^{\text{FM}} + B_i^{\text{LM}_1} + B_i^{\text{LM}_2}, \quad (i = x, y, z) \\ \mathbf{B}_{\text{FM}} &= B_x^{\text{FM}} \hat{\mathbf{x}} + B_y^{\text{FM}} \hat{\mathbf{y}} + B_z^{\text{FM}} \hat{\mathbf{z}}\end{aligned}\quad (5.6)$$

where B_i^T represents the total magnetic field inside the DP due to the FM (B_i^{FM}) and the two LMs ($B_i^{\text{LM}_1}$ and $B_i^{\text{LM}_2}$) in one of the three directions, χ_x, χ_y and χ_z represent the magnetic susceptibilities of the DP in the three directions and $\hat{\mathbf{x}}, \hat{\mathbf{y}}$ and $\hat{\mathbf{z}}$ represent the unit vectors in the three directions. By discretizing the DP into a finite number of cuboids of size dl, dw and dt ($dV = dldw dt$) one can approximate the volume integral into summation of all the cuboids with $n_{\text{DP}}, m_{\text{DP}}$ and k_{DP} as the number of cuboids in the height, width and thickness dimension respectively.

$$F_x^{\text{DP}} \approx - \sum_i \sum_j \sum_{k=1}^{k=k_{\text{DP}}} \sum_{m=1}^{m=m_{\text{DP}}} \sum_{n=1}^{n=n_{\text{DP}}} \frac{\chi_i}{\mu_0} B_i^T B_{ij}^{\text{FM}} dl dw dt, \quad (i, j = x, y, z) \quad (5.7)$$

where $B_{ij}^{\text{FM}} = \Delta B_i^{\text{FM}} / \Delta j$, ($i, j = x, y, z$). The DPs do not provide any net diamagnetic forces for displacements of the FM in y and z directions.

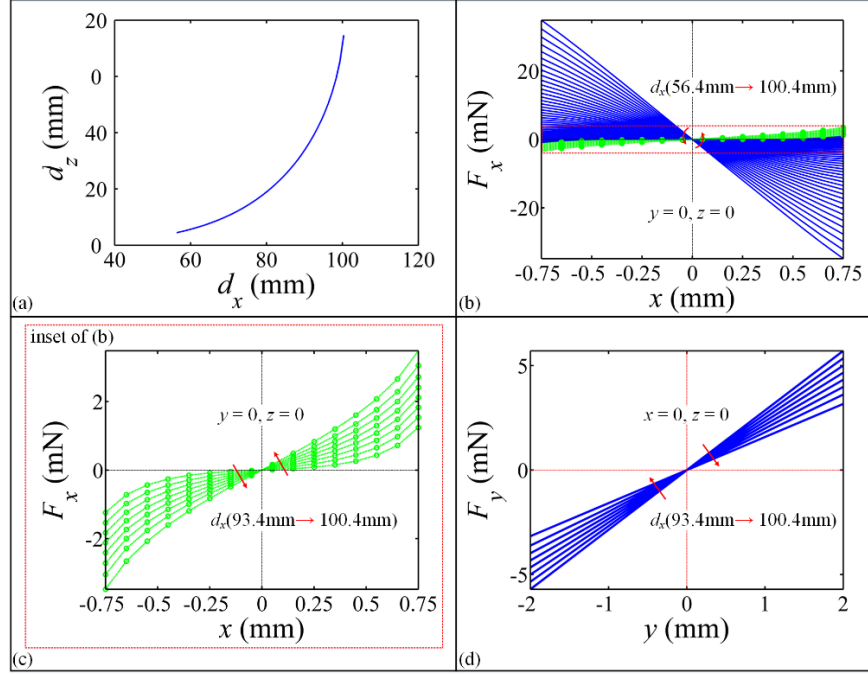


Figure 5.5 (a) Weight balance positions d_z of the FM with the LM at the respective d_x , (b) restoring force in the x -direction for the d_x values taken from (a), (c) zoomed section of (b) at which static levitation is permissible (d) restoring force in the y -direction for the d_x values taken from (c).

Now by taking the net force in the x -direction (F_x), that is, due to the DPs and the LMs ($F_x = F_x^{\text{DP}_2} + F_x^{\text{LM}_1} - F_x^{\text{LM}_2} - F_x^{\text{DP}_1}$), the numerically calculated values are plotted in Figure 5.5(b). The dimensions of the DP and D are taken from Table 5.1 and the d_x and d_z values are taken from Figure 5.5(a) at positions where the weight is balanced. In Figure 5.5(b), (c) and (d) the point $x = 0$, $y = 0$ and $z = 0$ represents the various d_x and d_z points at which the weight of the FM is balanced. It can be seen from Figure 5.5(b) that the net restoring force in

the x -direction reverses its direction and becomes positive, hence enabling static levitation, only for a small range of d_x , i.e., from 93.4 mm to 100.4 mm, this is shown in Figure 5.5(c). In Figure 5.5(d), the restoring force in the y -direction is plotted for small displacements (< 2 mm) to show that the force is directed towards the static equilibrium position for d_x ranging from 93.4 mm to 100.4 mm. Hence it can be seen that static stability exists in all three directions for a range of d_x from 93.4 mm to 100.4 mm and its corresponding d_z ranging from 20.7 mm to 37.33 mm. It should be noted that in Figure 5.5(c) and (d) only small displacements are considered, hence, it is safe to assume the stability in the z -direction for these displacements in the orthogonal directions.

Figure 5.6(a) shows the amplitude of the FM (z_{\max}) up to which the stability still prevails in the z -direction; that is, $2F_z^{\text{LM}} > F_w$. It can be seen that for larger d_x the z_{\max} decreases, this is expected as the region of influence of the magnetic field of the LM over the FM decreases as d_x increases. Figure 5.6(b) shows how the restoring force in the z -direction varies for different d_x , it can be seen that a softening characteristic is present below the stable point, however the restoring force keeps increasing with decreasing d_x . These figures show how d_x can regulate the maximum amplitude of the FM and the slope of the restoring force (or the natural frequency) which makes it an “effective” tuning parameter for this configuration.

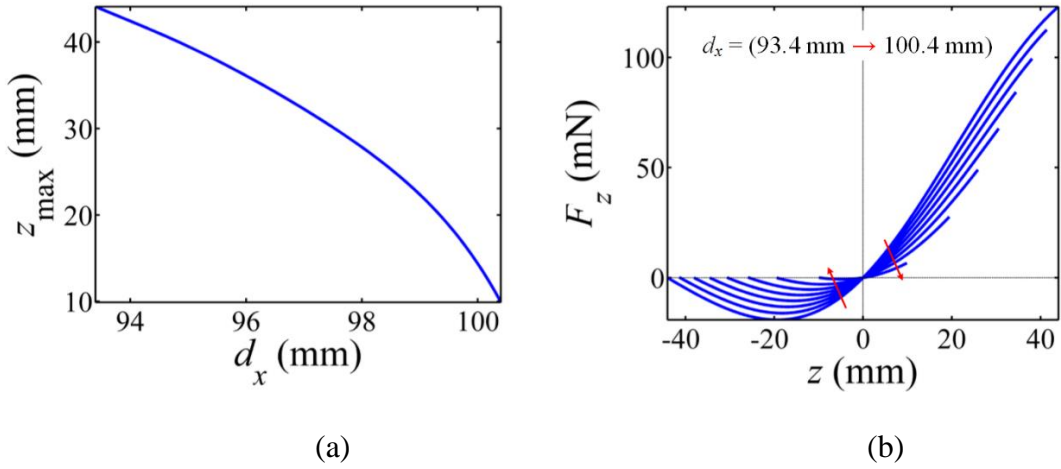


Figure 5.6 (a) Amplitude of FM in the z -direction (z_{\max}) for different d_x (b) Restoring force in the z -direction for varying d_x .

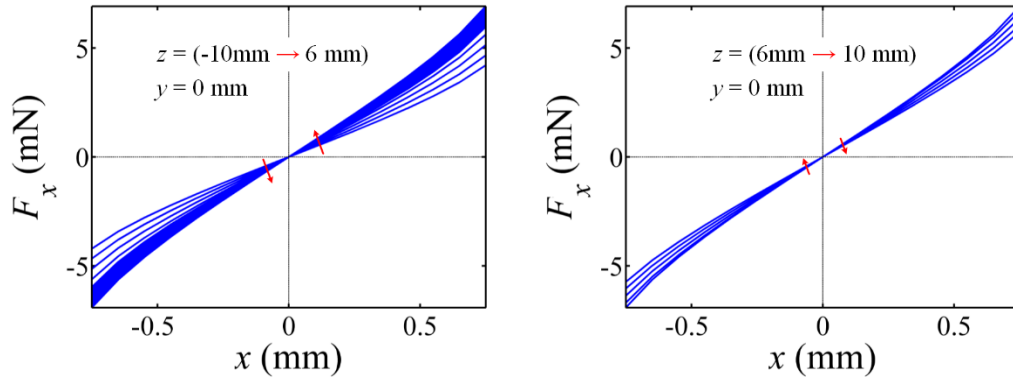


Figure 5.7 Restoring force in the x -direction at different z amplitudes.

As the axial attraction force F_x^{LM} changes with z , it would be necessary to check if the FM impacts the DP at larger amplitudes. This impact can happen if the net restoring force in the x -direction (F_x) is not directed towards $x = 0$ for small displacements in the x -direction.

However, this impact does not mean the FM will lose stability but may alter the dynamics of the FM. In this particular case for the d_x chosen (Table 5.1), Figure 5.7 implies that the FM doesn't impact the DP for z displacements from -10 mm to 10 mm which is the maximum range of displacement (z_{\max}) for the maximum d_x from Figure 5.6. Also, it can be seen in Figure 5.7 the trend of the change in the force in the x -direction at around $z = 6$ mm, this is because of the overlap case [137], that is, when the lateral distance between the two magnets is less than the sum of their radii. The stability in the y -direction is unperturbed as there are no competing forces in this direction. However, large displacements in y -direction can lead to loss of z -stability but such situations can be easily averted by using mechanical stoppers.

It should also be noted that the stability conditions discussed here are more relaxed than the ones discussed for the VDL system (Chapter 3 and 4). Firstly, in the VDL system the stability is strictly depended on a particular distance at which the weight of the FM is balanced whereas for the HDL system certain leeway has been provided in this regard. Secondly, after the weight of the FM is balanced stability is still depended on the maximum repulsive force from the DP for the VDL system. Although this is true even for the HDL system but because this stability condition is imposed in a different direction than the vertical direction it is partially uncoupled with the first stability condition and makes it easily achievable.

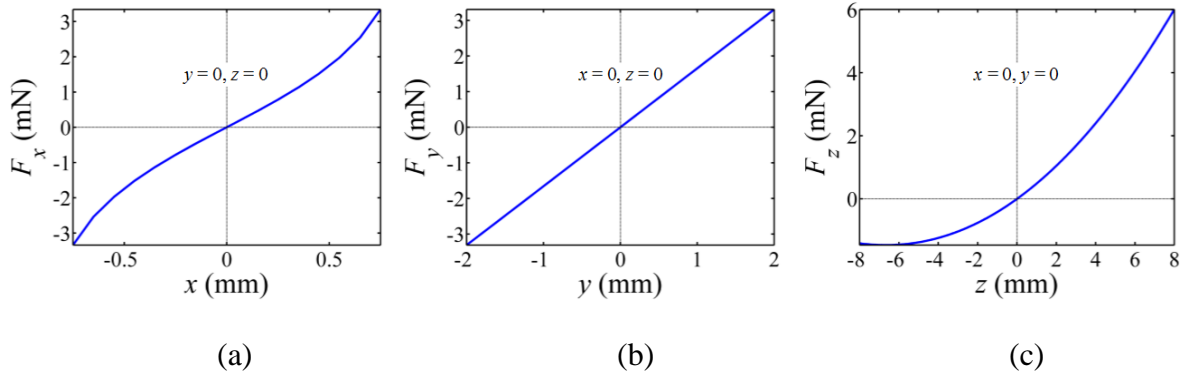


Figure 5.8 (a) Restoring force in the x -direction, (b) in the y -direction, (c) in the z -direction.

Finally, with the selected parameters from Table 5.1, Figure 5.8(a), (b) and (c) show the restoring forces in the x , y and z directions about the d_x and d_z position. Figure 5.8 (a) and (b) reassert the stability of the FM in these directions as discussed previously in this section and the dynamics of the system in the vertical direction, z -direction, only will be a subject of the current study in the following sections. The restoring force in the z -direction shows a softening and a weak hardening characteristics in different directions (Figure 5.8(c)), however it will be later shown that a net effect of softening is seen in the frequency response of the system. With the restoring forces of the HDL system discussed, now it is of interest to discuss the damping and vibration energy harvesting aspect of the HDL based vibration energy harvester.

5.3 Eddy current damping and coil geometry

In contrast to conventional cantilever based energy harvester systems [4, 32, 43, 138], no mechanical friction or internal damping is present in the system. However, as pyrolytic

graphite were used as DPs, eddy current forces arise due to its conductive property. These eddy currents are generated in the DP due to the motion of the FM relative to it and hence contribute to “equivalent” mechanical damping in the system. The damping factor can be analytically calculated using the methods discussed in [133] for better estimation but for simplicity reasons here the mechanical damping factor is estimated by measuring the open-loop Q factor experimentally by measuring the ring-down of the FM after perturbation. The ring-down amplitude of the FM is shown in Figure 5.9(a), measured with a high speed camera, the averaged open-loop Q factor is measured to be around 13.5. In the last chapter on the optimization of the VDL system (Chapter 4), a laminated DP, much similar to laminated cores used in transformers, was used to greatly decrease the eddy currents in the DP and the open-loop Q factors reached up to 50, similar effort is to be made in future studies on the HDL system.

A magnet-across coil architecture [59] is chosen for this energy harvester due to its simplicity in incorporating it in the HDL system by wrapping a coil around a circular shaped DP. In order to determine the geometry of the coil, it is necessary to estimate the maximum relative amplitude of the FM as the transduction factor is affected vastly by its range of motion. Using the open-loop Q factor, an estimate on the relative amplitude was made at resonance to be around six millimeters by plotting the frequency response of the open-loop system. Using this amplitude and fixing the coil thickness in both lateral and axial directions, a parametric sweep is conducted to find a suitable coil_{out} to increase the peak electromotive force (EMF), shown in Figure 5.9(b). It is seen from the figure that a coil_{out} to r_{FM} ratio of 1.25 manages the

highest EMF considering an axial thickness equal to thickness of the DP ($t_{\text{coil}} = t_{\text{DP}}$) and a lateral thickness of 2 mm. A circular coil with dimensions close to the optimum are experimentally made; however, it should be noted that Figure 5.9(b) does not infer that the output voltage needs to be as stated as the parametric study did not take into consideration the damping due to the coils at resonance.

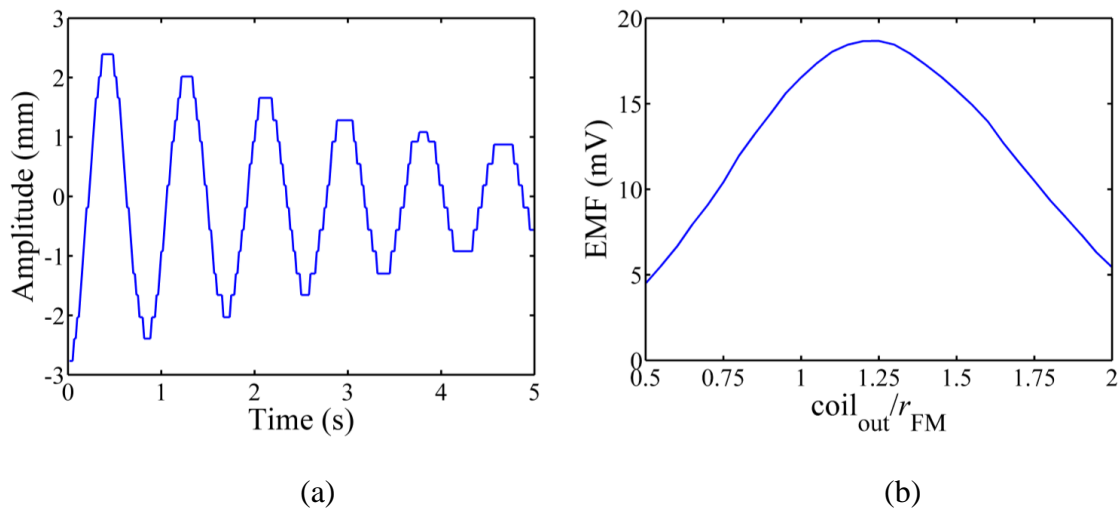


Figure 5.9 (a) Ring-down of the FM using a high speed camera. (b) Parametric sweep to determine coil_{out}

5.4 Equations of motion

In general, a vibration energy harvester can be modelled as a single degree-of-freedom (1-DOF) vibration system subjected to base excitations in the vertical direction (z -direction) by using a lumped-parameter model (Figure 5.10) [2]. The HDL vibration energy harvester is inherently nonlinear due to the nature of the damping and restoring force. The mechanical

damping is, however, simplified and is assumed to be an approximate value, from Figure 5.9(a), to make it independent of position. The electrical damping is however a function of the relative amplitude and the current in the coil, which is defined later in this section. Now, considering the mechanical and electrical equations of motions, one has:

$$\begin{aligned} m_{\text{FM}} \ddot{z} + c_m \dot{z} + F_{\text{K}}(z) + F_{\text{L}}(i, z) &= m_{\text{FM}} A \omega^2 \sin \omega t \\ \dot{i} L_{\text{coil}} + i(R_{\text{load}} + R_{\text{coil}}) &= V(z, \dot{z}) \end{aligned} \quad (5.8)$$

here z is the relative displacement of the FM, c_m is the mechanical damping factor (calculated from Figure 5.9(a)), $F_{\text{K}}(z)$ is the nonlinear restoring force (*cf.* Figure 5.8(c)), $F_{\text{L}}(i, z)$ is the electrical damping force, i is the current in the coil, m_{FM} is the mass of the FM, A is the amplitude of the sinusoidal base displacement, ω is the angular frequency of excitation, L_{coil} is the inductance of the coil, R_{load} is the resistance of the load, R_{coil} is the resistance of the coil, $V(z, \dot{z})$ is the voltage induced and the dot over a variable represents the derivative with time.

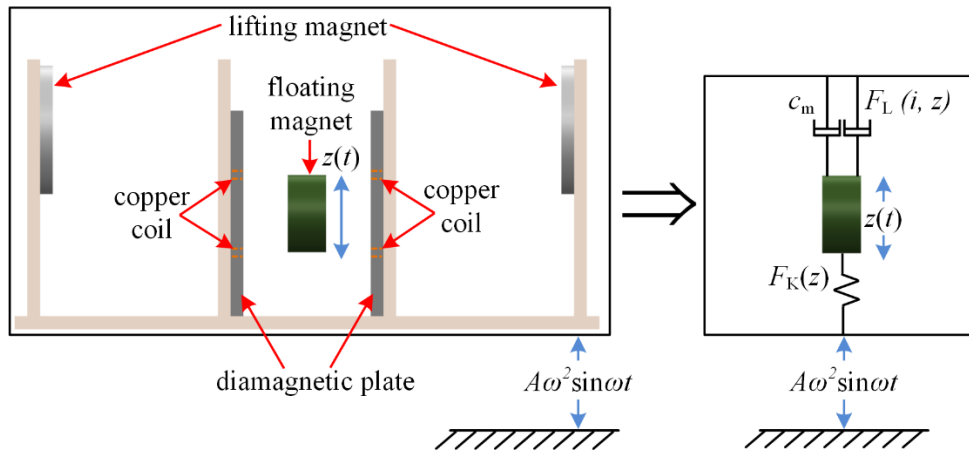


Figure 5.10 An equivalent one degree-of-freedom (1-DOF) model of the HDL based VEH.

The voltage function ($V(z, \dot{z})$) in equation (5.8) is determined by the Faraday's law of induction. By summing over the infinitesimal areas ($rd\theta dr$) as shown in Figure 5.11(a), one arrives at

$$V(z, \dot{z}) = 2\dot{z} \frac{d}{dz} \sum_{x_{\text{coil}}=D^-}^{x_{\text{coil}}=D^+} \sum_{\text{coil}_{\text{hor}}=\text{coil}_{\text{in}}}^{\text{coil}_{\text{hor}}=\text{coil}_{\text{out}}} \sum_{r=0}^{r=\text{coil}_{\text{hor}}} \sum_{\theta=0}^{\theta=\pi} B_x^{\text{FM}}(\rho, x_{\text{coil}}) r dr d\theta \quad (5.9)$$

where $\rho = \sqrt{(z - r \cos \theta)^2 + r \sin \theta^2}$, $D^- = (D - t_{\text{FM}}) / 2$, $D^+ = (D - t_{\text{FM}}) / 2 + t_{\text{coil}}$, coil_{in} is the inner radius of the coil and coil_{out} is the outer radius of the coil. The axial magnetic field component B_x^{FM} is written in terms of the cylindrical co-ordinates with respect to the center of the FM and is determined by modeling the magnet as a thin coil [127]. The variables mentioned in equation (5.9) are also shown in Figure 5.11(a).

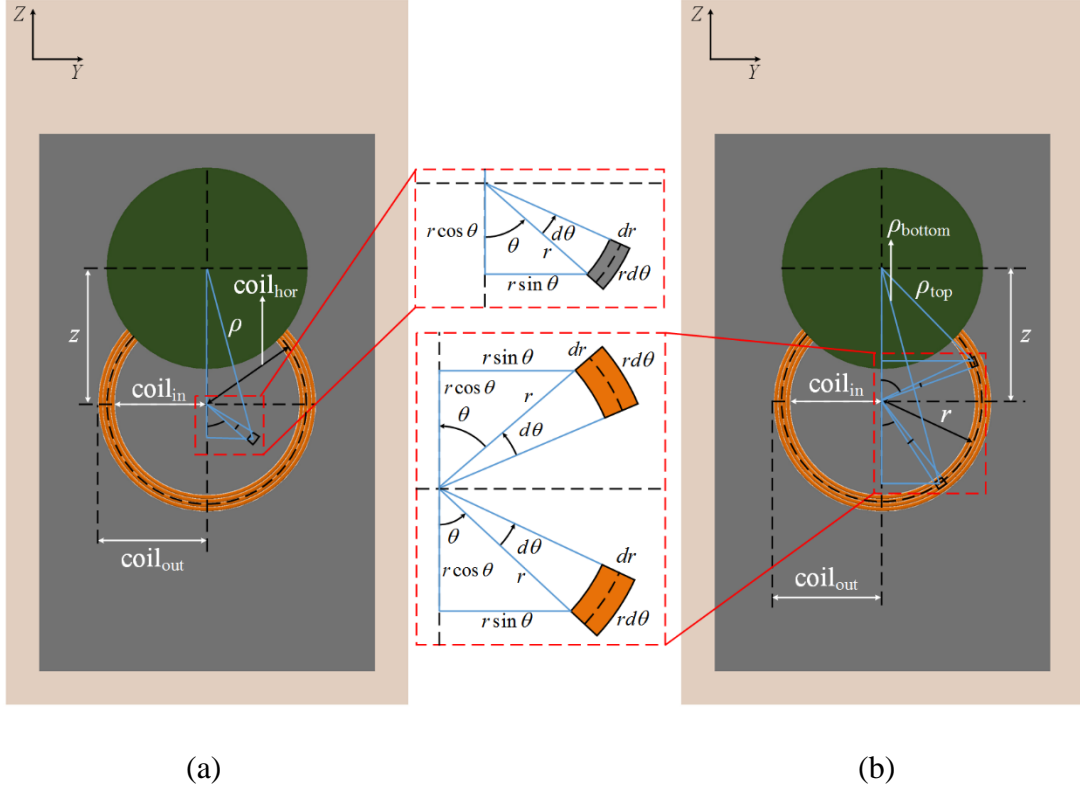


Figure 5.11 Schematic of the coil geometry for (a) voltage induced calculation for each loop of the coil ($V(z, \dot{z})$ in equation(5.9)) (b) Lorentz force calculation from each loop of the coil ($F_L(i, z)$ in equation (5.10)).

The electrical damping force ($F_L(i, z)$) is defined by Lorentz law. By summing the damping force due to each part of the conductor ($rd\theta$) as shown in Figure 5.11(b), one arrives at

$$F_L(i, z) = 2i \sum_{x_{\text{coil}}=D^-}^{x_{\text{coil}}=D^+} \sum_{r=\text{coil}_{\text{in}}}^{r=\text{coil}_{\text{out}}} \left\{ \begin{array}{l} \sum_{\theta=0}^{\theta=\pi/2} [B_x^{\text{FM}}(\rho_{\text{top}}, x_{\text{coil}})rd\theta] - \\ \sum_{\theta=0}^{\theta=\pi/2} [B_x^{\text{FM}}(\rho_{\text{bottom}}, x_{\text{coil}})rd\theta] \end{array} \right\} \quad (5.10)$$

where, $\rho_{\text{top}} = \sqrt{r^2 \sin^2 \theta + (z - r \cos \theta)^2}$, $\rho_{\text{bottom}} = \sqrt{r^2 \sin^2 \theta + (z + r \cos \theta)^2}$ and the subscripts ‘top’ and ‘bottom’ relate to the top and bottom part of the current carrying coils. The definition of D^- , D^+ and B_x^{FM} mean the same as defined for equation (5.9). The variables mentioned in equation (5.10) are also shown in Figure 5.11(b). The next section deals with the experimental validation of the theoretical modeling discussed in this section.

5.5 Experimental validation

This section discusses the experimental setup and the frequency response characteristics of the HDL system. The complete parameter list of the system is given in Table 5.1. For a system defined by equation(5.8), if the input mechanical power is held constant, it can absorb the maximum energy that will be generated around its resonance frequency. For a harmonic base excitation, if the mass of the vibrator (mass of the FM, m_{FM} , in this case) is much less than the mass of the energy harvester, the input mechanical power to the energy harvester is approximated by:

$$\begin{aligned} \bar{P}_{\text{input}} &\approx \frac{2\omega}{\pi} \int_0^{\pi/2\omega} m_{\text{harvester}} \left| (-A\omega^2 \sin \omega t)(A\omega \cos \omega t) \right| dt \\ &\approx \frac{\omega}{\pi} \int_0^{\pi/2\omega} m_{\text{harvester}} \omega^3 A^2 \sin 2\omega t dt \approx \frac{1}{\pi} m_{\text{harvester}} \omega^3 A^2 \end{aligned} \quad (5.11)$$

where $m_{\text{harvester}}$ is the mass of the energy harvester, \bar{P}_{input} is the average input mechanical power to the harvester. As shown in equation (5.11), a constant input mechanical power to the energy harvester is maintained by keeping $\omega^3 A^2$ constant. For this experimental study $\omega^3 A^2$ is

maintained at $500 \text{ mm}^2/\text{s}^3$ (same as in Chapter 3 and 4) which corresponds to a \bar{P}_{input} of $186.6 \mu\text{W}$.

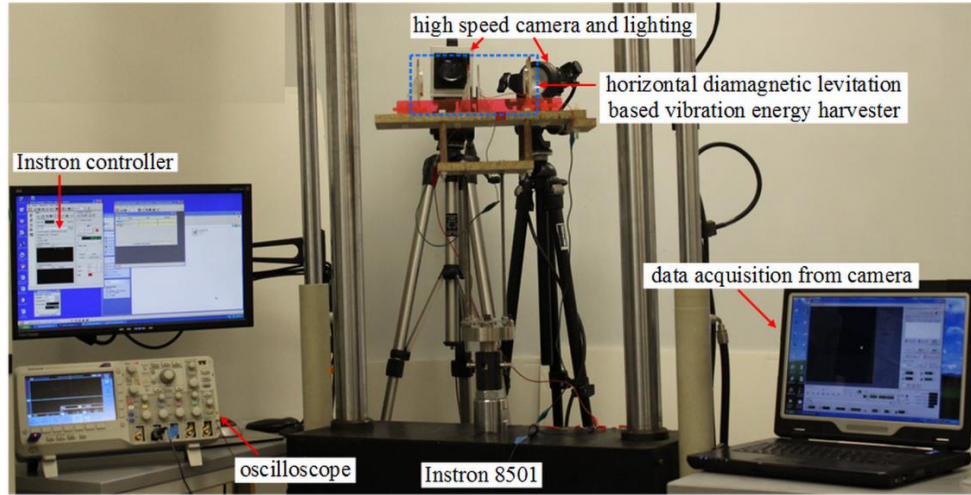


Figure 5.12 Experimental system for HDL based VEH.

Table 5.1 Model parameters for the experimental system

| Parameter | Value | Units |
|---|-------|-------|
| r_{FM} (radius of FM) | 6.35 | mm |
| t_{FM} (thickness of FM) | 6.35 | mm |
| Br_{FM} (residual magnetic flux of FM) | 1.43 | Tesla |
| r_{LM} (radius of LM) | 25.4 | mm |
| t_{LM} (thickness of LM) | 6.35 | mm |
| Br_{LM} (residual magnetic flux of LM) | 1.36 | Tesla |
| l_{DP} (length of DP) | 50 | mm |
| w_{DP} (width of DP) | 50 | mm |

Table 5.1 Continued

| Parameter | Value | Units |
|---|-----------------------|---------|
| t_{DP} (thickness of DP) | 3.25 | mm |
| χ_x (perpendicular magnetic susceptibility of DP) | -450×10^{-6} | - |
| χ_y, χ_z (parallel magnetic susceptibility of DP) | -85×10^{-6} | - |
| $coil_{in}$ (inner radius of copper coil) | 5.25 | mm |
| $coil_{out}$ (outer radius of copper coil) | 7 | mm |
| t_{coil} (thickness of copper coil) | 3.25 | mm |
| N (Number of turns of copper coil) | 150 | turns |
| R_{coil} (resistance of copper coil) | 9.5 | ohms |
| R_{load} (load resistance) | 45 | ohms |
| L_{coil} (inductance of copper coil) | 178 | μH |
| d_x (axial distance between LM and FM) | 100 | mm |
| D (distance between DP) | 7.85 | mm |
| d_z (lateral distance between LM and FM) | 35.8 | mm |
| $m_{harvester}$ (total mass of harvester) | 1172.5 | g |
| m_{FM} (mass of FM) | 6 | g |
| \bar{P}_{input} (normalized input mechanical power) | 186.6 | μW |

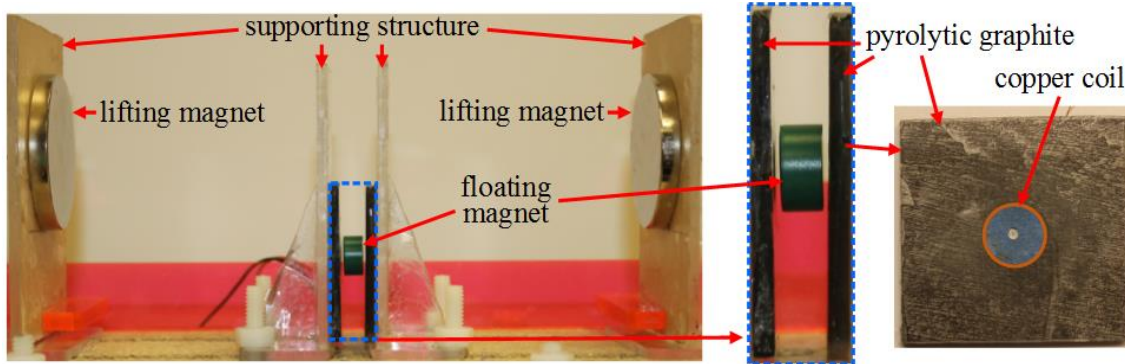


Figure 5.13 Close-up of the HDL based VEH showing the FM (covered with a green tape), the LMs and the pyrolytic graphite with the copper coil.

The HDL vibration energy harvester is shown in Figure 5.12 and Figure 5.13 along with a high speed camera, an oscilloscope and an Instron 8501 test bed to carry out the low-frequency tests. A green tape was used to cover the FM, which can be seen in Figure 5.13, to enhance its visibility while recording its motion with the high speed camera. A blue tape on the DP was used for initial alignment of the FM and the setup of the harvester. The experimental tests were performed by keeping the mechanical power input to the harvester constant at all frequencies. The excitation frequency was varied from 0.5 Hz to 3 Hz and the input amplitude was varied from 4.01 mm to 0.27 mm, which correlates to root mean square (RMS) acceleration levels varying from 0.028 m/s^2 (0.00285 grms) to 0.0678 m/s^2 (0.0069 grms) in order to keep the product $\omega^3 A^2$ a constant for constant mechanical power input (*cf.* equation (5.11)). Figure 5.14 (a), (b), (c) and (d) show the experimental results along with the theoretical predictions.

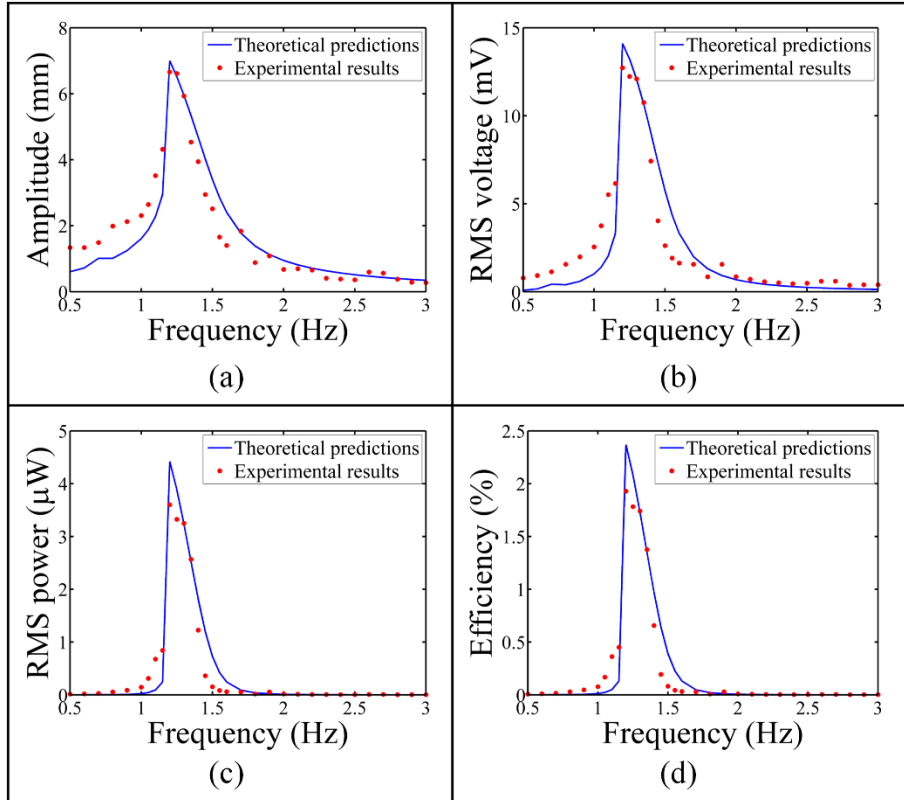


Figure 5.14 Experimental and theoretical predictions (a) relative amplitude of the FM (b) RMS voltage across the load (c) RMS power and (d) average efficiency of the system. (RMS excitation acceleration varied from 0.028 m/s^2 to 0.0678 m/s^2 as the frequency was varied from 0.5 Hz to 3 Hz)

Due to the nonlinearity of the restoring force (Figure 5.8(c)), the optimal load is different than the one derived for the linear model in [121]. The theoretical modelling discussed in the last section was used to simulate the frequency responses for different to select the one which achieves close to the maximum power output. At this (Table 5.1), at an average mechanical input power of $186.6 \mu\text{W}$ and at a frequency of 1.2 Hz, the harvester generated a

RMS power of $3.6 \mu\text{W}$ with an average system efficiency of 1.93%. Under similar excitation conditions the VDL energy harvester had an average system efficiency of 0.72% (Figure 3.12 of Chapter 3).

5.6 Discussion

It is worth noting three salient features of the system. Firstly, the system shows a weak softening response which is a result of the nonlinear restoring force (Figure 5.8(c) and Figure 5.14). Secondly, it is very sensitive to the small variations in the displacement and angular position of the LMs with respect to each other. Thirdly, while performing the experiments for some of the frequencies the motion of the FM is not entirely along the Z-axis and that some motion exists in the x -direction. The reasons for the two former characteristic are due to the nature of the forces and slopes of the forces from the LMs and the later characteristic is due to the small differences in the magnetization values of the two LMs and possible non-uniform magnetizations. It can also be seen in Figure 5.14 that for some of the frequencies there is a moderate discrepancy from the theoretical predictions, this can be mainly due to the difference in the manufactures magnetization value from its actual magnetization value (after taking into account each magnets shape effect, i.e. the permeance coefficient), inaccurate estimation of the open-loop Q factor and assumption of uniform magnetization in the theoretical analysis. The same reasons discussed in this paragraph lead to a small tilt in the stably levitating position of the magnet (Figure 5.13).

When compared to the VDL based vibration energy harvester (Chapter 3) there was a 168% increase in the average efficiency of the HDL based vibration energy harvester. This

was mainly due to the unrestricted motion of the FM in the z -direction. As the power harvested depends on the third power of the natural frequency of the harvester [139], it would be fair only to compare the present HDL system with energy harvesters in literature which work at this frequency range (< 2 Hz). However, there are only a handful of harvesters in literature that operate at this low frequency range. The most notable harvester that works at this frequency range was developed by Galchev et al. [140]. To compare with other harvesters in literature they use the volume figure of merit (FoM_v) introduced by Mitcheson et al. [7].

$$\text{FoM}_v(\%) = \frac{\text{Useful Power Output}}{\frac{1}{16} A \rho_{\text{AU}} \text{Vol}^{4/3} \omega^3} \times 100 \quad (5.12)$$

where ‘ Vol ’ represents the volume of the harvester, ρ_{AU} represents the density of gold, A represents the input excitation amplitude and ω represents the input excitation angular frequency. Now, if there is a hypothetical closure that can enclose the current prototype harvester it would have an internal volume of roughly 520 cm^3 . This corresponds to a $\text{FoM}_v(\%)$ of 0.0154 when computed at 1.2 Hz and Galchev et al. [140] harvester had a $\text{FoM}_v(\%)$ of 0.02 when computed at 2 Hz. Hence, it would be reasonable (accounting for the difference in the frequency of operation) to say this current prototype fairs well as an initial design when compared to other harvesters in literature.

Leveraging the knowledge that the authors have gained by working on optimizing the design of the VDL in Chapter 4, it seems evident that a similar characterization study can further greatly boost the efficiency of this HDL based vibration energy harvester. One of the important parameters that can be optimized is the volume of the LM. Since such a large volume of the LM, as the one used in this study, can provide stability to the FM for up to 45 mm amplitude (z_{max} in Figure 5.6(a)), which is much greater than the maximum amplitude of the FM in the experimental study, a smaller volume of the LM with stability range of 20 mm with

mechanical stoppers will suffice. This smaller volume of LM would also lead to a smaller d_x , hence a smaller device. Also, as an optimum LM would provide the least axial force (F_x^{LM}) and the maximum lateral force (F_z^{LM}) for its volume, future optimization studies on the relative volume of the LM to the volume of the FM along with the aspect ratio of the LM will be studied to achieve this. After optimizing the LM, the coil volume will be greatly increased by either replacing a large section of the DP (without sacrificing static stability) or will be designed around the FM with its axis along the Z-axis (isolated from the DP). Lastly, as mentioned previously, a laminated DP will be used for future studies which was seen to achieve Q-factors of around 50 (Chapter 4). All such improvements to the HDL system will greatly improve its energy harvesting characteristics.

There have been only a few studies in literature of systems with softening type nonlinearity [141, 142]. These studies have nevertheless shown superiority over the hardening type nonlinearity in being able to achieve higher orbit stable solutions for large accelerations and over a larger frequency bandwidth. In future studies, along with the optimization studies described above, superiority in large frequency bandwidth operation will be attempted by strengthening the softening nonlinearity in the system.

5.7 Conclusions

A HDL based VEH is discussed in detail in this chapter. This configuration carries the same attributes as the VDL system of being friction-free and having a low resonant frequency (less than a few hertz), however, some notable limitations of the later have been mitigated in

this configuration. For example, spatial constraint and the stability conditions in the vertical direction are uncoupled with the diamagnetic force which relaxed the constraints on the maximum amplitude of the FM, which was severely limited in the VDL system. As being the first demonstration of this system, the system parameters were maintained to be nearly the same as the ones of the previous study of the VDL system to make a fair comparison between them.

The theoretical modelling of the single degree-of-freedom HDL vibration energy harvester system is discussed in detailed pertaining to the stability conditions, the restoring forces, the damping due to the eddy currents, a simple coil geometry that replaces a portion of the pyrolytic graphite plate (diamagnetic plate) and the equation of motion with harmonic base excitation. Due to the nature of the attractive (lateral) forces from the LMs, the net restoring force showed a softening type characteristic. Also, the restoring forces in the system can easily be tuned to change the natural frequency of the system by changing the distance between the LMs. Experiments were setup to validate the theoretical findings. The system was excited with harmonic sinusoidal excitations and the frequency response characteristics were discussed. At an average mechanical input power of $186.6 \mu\text{W}$ (root mean square acceleration of 0.0434 m/s^2) and at a frequency of 1.2 Hz , the prototype generated a root mean square power of $3.6 \mu\text{W}$ with a system efficiency of 1.93% .

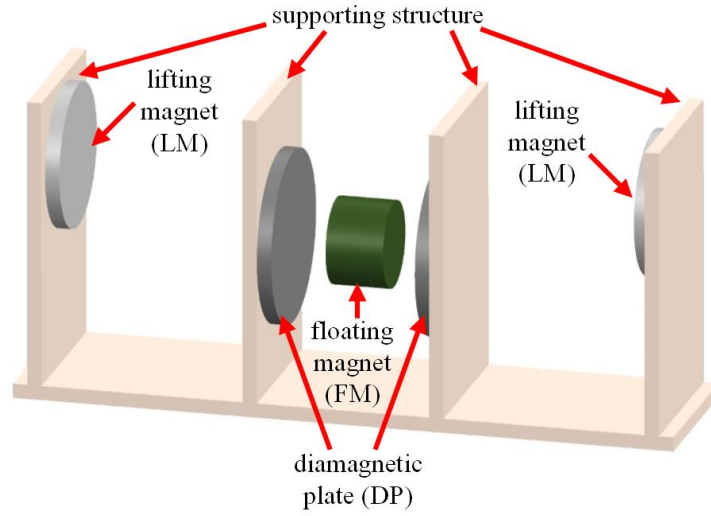
6 An efficient low resonant frequency horizontal diamagnetic levitation (HDL) based vibration energy harvester

In the last chapter (Chapter 5) a horizontal configuration of the diamagnetic levitation system was introduced to overcome the challenges of the vertical configuration described in Chapters 3 and 4. In Chapter 5, the horizontal diamagnetic levitation (HDL) based vibration energy harvester (VEH) was demonstrated to have potential benefits over the vertical diamagnetic levitation (VDL) based VEH. The system showed enhanced performance especially due to the relaxed constraints on the motion of the floating magnet in the vertical direction. In addition, a softening type response was witnessed in the frequency response curves. The aim of this chapter is to characterize the parameters of the HDL system and discuss the key factors that affect the static levitation, stability, frequency response, the power density and present an efficient low resonant frequency HDL based VEH. Firstly, some parametric studies are shown to understand the effects of the volume and aspect ratios of each of the components of the HDL system, namely, the lifting magnet (LM), the floating magnet (FM) and the diamagnetic plates (DPs) on the size of the system, the stability of the levitation and the resonant frequency of the system. Then, the electromagnetic coupling with a copper coil for transduction, the eddy current damping and the electromechanical equations of motion are discussed. For vibration energy harvesting using the HDL system, a coil geometry and eddy current damping are critically discussed. Based on the analysis, an efficient experimental

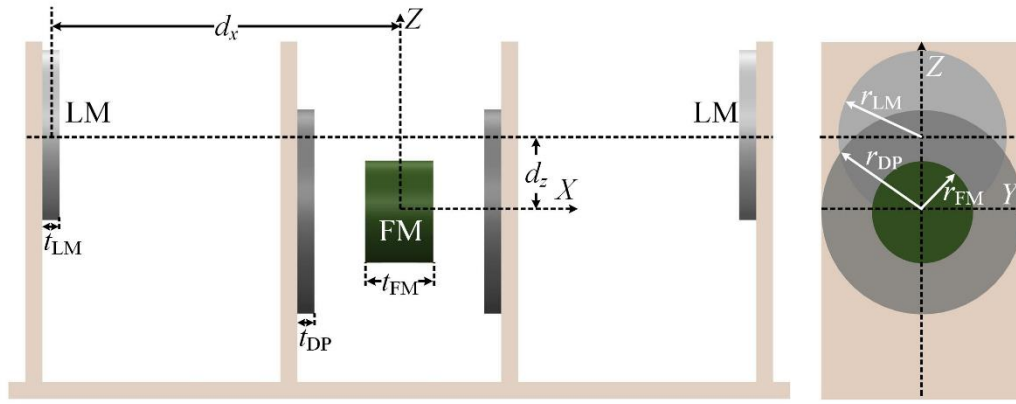
system is setup which achieved a system average efficiency of 25.8 % when excited at a RMS acceleration of 0.0546 m/s^2 and at a frequency of 1.9 Hz.

6.1 Parametric studies on the HDL system

The primary objective for a mass to levitate is its weight needs to be balanced. For this purpose, in a HDL system (Figure 6.1(a)) two large magnets, alias LMs, are arranged co-axially at a distance such that their lateral/vertical attractive force balances the weight of a magnet, alias FM, placed in between them. The LMs, however, also attract the magnet in the axial/horizontal direction which hinders static levitation. To counter this, the FM is flanked closely by two DPs made of pyrolytic graphite which provide weak repulsive force in the horizontal direction and hence stabilize the static levitation. A schematic of the HDL system is shown in Figure 6.1(b) and (c), where d_x is the axial distance between the centers of the LM and FM, d_z is the lateral distance between the centers of the LM and FM, r_{DP} is the radius of the DP, t_{DP} is the thickness of the DP, r_{FM} is the radius of the FM, t_{FM} is the thickness of the FM, r_{LM} is the radius of the LM, t_{LM} is the thickness of the LM.



(a)



(b)

(c)

Figure 6.1 Schematic of the HDL vibration energy harvester system with the floating magnet (FM), the lifting magnets (LMs) and the diamagnetic plates (DPs) (a) 3D view (b) front view (c) side view.

The stability conditions are usually discussed from the energy basins point of view [110] but due to the numerical form of these equations, which will be elaborated in the following paragraphs, we adopt a force perspective for stability. From this perspective, the stability conditions of the FM are such that the net forces acting on the FM be zero at the point of static equilibrium and any small perturbations will lead to the restoring forces directing it back to the initial static stable point. This condition directly corresponds to the stability condition in the energy perspective where the energy of the FM forms a basin around the equilibrium point. The restoring forces acting on the FM (F_x^{FM} , F_y^{FM} and F_z^{FM}) at a displaced position from the equilibrium point are given by

$$\begin{aligned} F_x^{\text{FM}} &= \Delta F_x^{\text{LM}} - \Delta F_x^{\text{DP}} \\ F_y^{\text{FM}} &= -2F_y^{\text{LM}} \\ F_z^{\text{FM}} &= 2F_z^{\text{LM}} - w_{\text{FM}} \end{aligned} \quad (6.1)$$

The terms F_x^{LM} , F_y^{LM} and F_z^{LM} represent the attractive force the LMs apply on the FM, F_x^{DP} represents the repulsive force from the DP in the X-axis direction, w_{FM} represents the weight of the FM and ΔF_x^{LM} , ΔF_x^{DP} represents the difference of the forces from the pair of LMs and the pair of DPs on either side of the FM respectively. The attractive forces from the LM are calculated by modeling the magnets as thin coils and using Lorentz force to estimate the force between as discussed in Chapter 5 (equation (5.3)). The repulsive force from the DP (F_x^{DP}) can be calculated by taking the negative gradient of the magnetic potential energy of the DP in that direction as discussed in Chapter 5 (equation (5.7)).

With this brief summary of the forces that are needed for analyzing the HDL system, the following subsections discuss parametric studies on how these forces vary with the geometries of the components of the system.

6.1.1 Aspect ratio of the FM (β_{FM})

The repulsive force from the DP is a critical component to achieve static levitation and its magnitude is limited by its magnetic susceptibility. Hence, firstly some parametric studies are done on the aspect ratio of the FM and the DP to determine what ratios maximize the force between them. For this, an appropriate aspect ratio of the FM ($\beta_{\text{FM}} = t_{\text{FM}} / (2r_{\text{FM}})$) is determined by estimating the force F_x^{DP} (shown in Figure 6.2(a) using equation (5.7)) between a DP and FM at a distance of 0.1mm. The size of the DP is taken to be much larger in size when compared to the FM. It can be seen from Figure 6.2(a) that for an aspect ratio of around four-tenth for different volumes of the FM (V_{FM}), the force F_x^{DP} has a maximum. For further parametric studies this aspect ratio of the FM is used.

6.1.2 Relative ratio of the DPs ($r_{\text{DP/FM}}, t_{\text{DP/FM}}$)

Instead of using an excessively large DP, one would want to use a sufficient size DP to achieve values of the force F_x^{DP} similar to the ones in Figure 6.2(a). For this reason a parametric sweep is done on the radius and thickness relative ratio of the DP to that of the FM ($r_{\text{DP/FM}}, t_{\text{DP/FM}}$). Figure 6.2(b) and (c) is plotted to estimate the variation of force F_x^{DP} with these relative ratios for an aspect ratio of four-tenth and with a volume of 1cm^3 of the FM (Figure

6.2(a)). It can be seen from the plots that the force F_x^{DP} increases drastically as the relative ratio of the DP reaches unity, this is mainly because the field of the magnet is strongest on the edges. Hence, for further discussion a $r_{\text{DP/FM}}$ and a $t_{\text{DP/FM}}$ of 1.5 are considered as they provide a reasonably high portion of the maximum repulsive force possible.

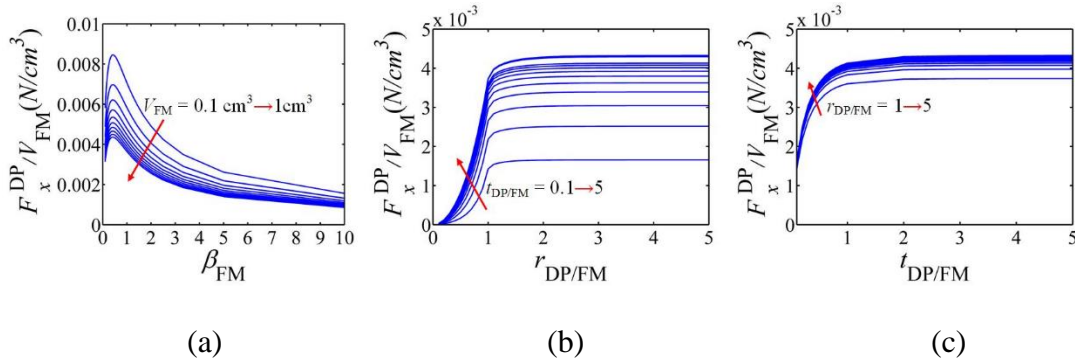


Figure 6.2 (a) Force per unit V_{FM} ($F_x^{\text{DP}} / V_{\text{FM}}$) versus β_{FM} (b) Force per unit V_{FM} ($F_x^{\text{DP}} / V_{\text{FM}}$) versus $r_{\text{DP/FM}} = r_{\text{DP}} / r_{\text{FM}}$ and (c) Force per unit volume ($F_x^{\text{DP}} / V_{\text{FM}}$) versus

$$t_{\text{DP/FM}} = t_{\text{DP}} / t_{\text{FM}}$$

6.1.3 Aspect ratio of the LMs (β_{LM})

The desirable properties of a LM are to provide maximum lateral force for its volume to counter the weight of the FM and to provide minimal destabilizing force in the axial direction. In order to analyze how the lateral force varies, a parametric sweep for different aspect ratios of the LM ($\beta_{\text{LM}} = t_{\text{LM}} / (2r_{\text{LM}})$) is plotted in Figure 6.3(a) with their maximum d_x at which the weight of the FM is balanced. Also, the stable minimum d_x is plotted in

Figure 6.3(b) for different β_{LM} for understanding the variation of the axial force. For these figures a V_{FM} of 1cm^3 and a V_{LM} of 10cm^3 is chosen along with the aspect ratio of the FM and the relative ratio of the DP that maximize F_x^{DP} chosen as discussed previously. From Figure 6.3(a) and (b) it can be seen that the axial and lateral forces follow a similar trend with the aspect ratio. As a low aspect ratio LM achieves the lowest d_x , choosing this value seems preferable for designing a higher power density VEH.

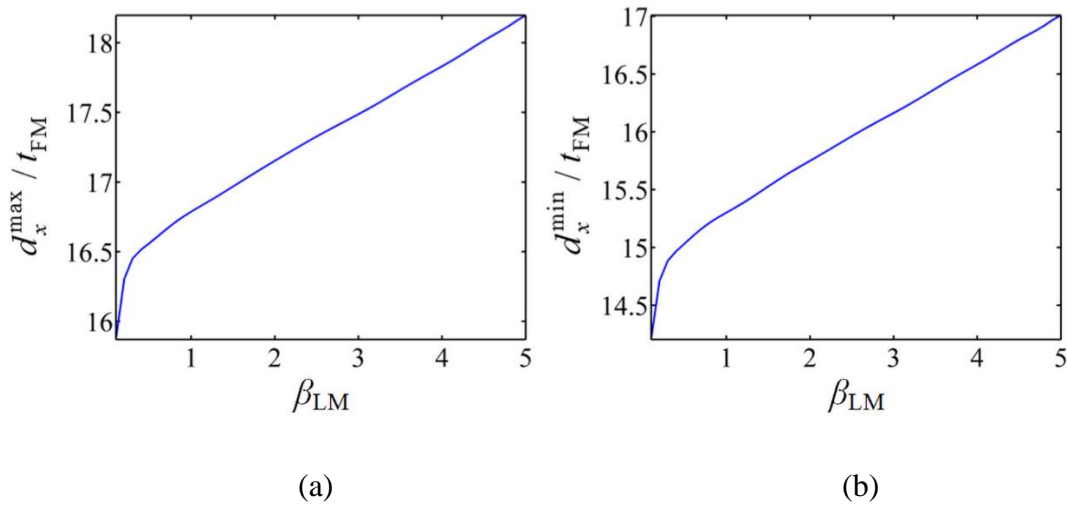


Figure 6.3 Normalized (a) maximum d_x (b) minimum d_x with β_{LM}

6.1.4 Stability of the FM

Now that the geometric parameters of the HDL system components are discussed, an important factor that needs to be considered is the limits of the stability of the FM in z -direction. As the FM moves along the negative z -direction, the weight of the FM overcomes the attractive force from the LM at a certain amplitude and the FM loses stability. The amplitude at which

this instability occurs depends on β_{LM} considering for a constant V_{LM} . Figure 6.4(a) shows the maximum range of displacement (z_{max}) for d_x^{min} , for which dynamic stability exists for the FM for each β_{LM} with the same set of parameters as used for Figure 6.3. The plot of this figure has been fitted to numerically calculated data. It can be seen from Figure 6.3 and Figure 6.4(a) that a low aspect ratio of LM is preferable as it provides a smaller size of the device and a larger range of displacement. Considering manufacturing constraints, an aspect ratio of 0.1 is chosen for further discussion in this section.

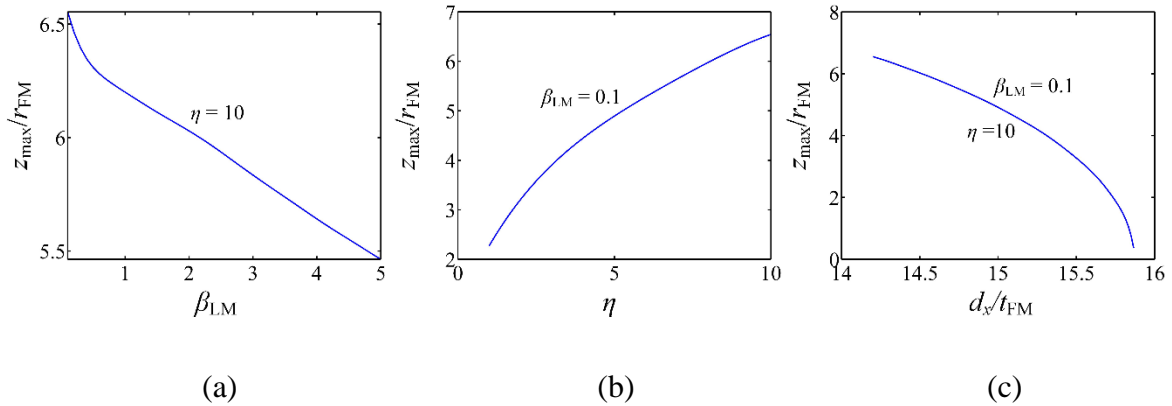


Figure 6.4 Normalized amplitude in the negative z -direction with the (a) aspect ratio of LM (β_{LM}) (b) volume ratio ($\eta = V_{LM} / V_{FM}$) and (c) normalized d_x .

Figure 6.4(b) shows the normalized amplitude with a constant aspect ratio ($\beta_{LM} = 0.1$) of the LM for varying volume ratio ($\eta = V_{LM} / V_{FM}$) which shows that larger η is required for larger displacement range of the FM. It is to be noted that increasing the size of the harvester

also has a negative impact of decreasing the maximum amplitude of the FM for a fixed η and β_{LM} as shown in Figure 6.4(c).

6.1.5 Volume of the LM and natural frequency (V_{LM}, f_n)

An algorithm is described in Figure 6.5 which discusses the design steps to tune the natural frequency of a HDL system to that of the ambient frequency ($f_n = f_{\text{ambient}}$) and with a maximum range of displacement in the z -direction (z_{max}) greater than the relative amplitude of the FM (A_{FM}) at resonance for the given excitation. The natural frequency of the HDL system can be tuned depending on the choice of V_{FM}, η and d_x . Figure 6.6(a) shows the variation of the natural frequency with the maximum d_x to the minimum d_x for a set of V_{FM} from 0.1 cm^3 to 1 cm^3 with a fixed η of 10. Figure 6.6(b) shows the variation of the natural frequency with the maximum d_x to the minimum d_x for each set of η for a fixed V_{FM} of 1 cm^3 . A parametric study on the minimum volume of LM needed to levitate for a V_{FM} of 1 cm^3 is done before plotting Figure 6.6(b). A minimum ratio of 0.5 is shown in the figure, however, smaller ratios are possible but would have considerably smaller dynamic stability in the z -direction (Figure 6.6(b)). It should be noted that β_{LM} was taken to be 0.1 for the numerical calculations in this figure.

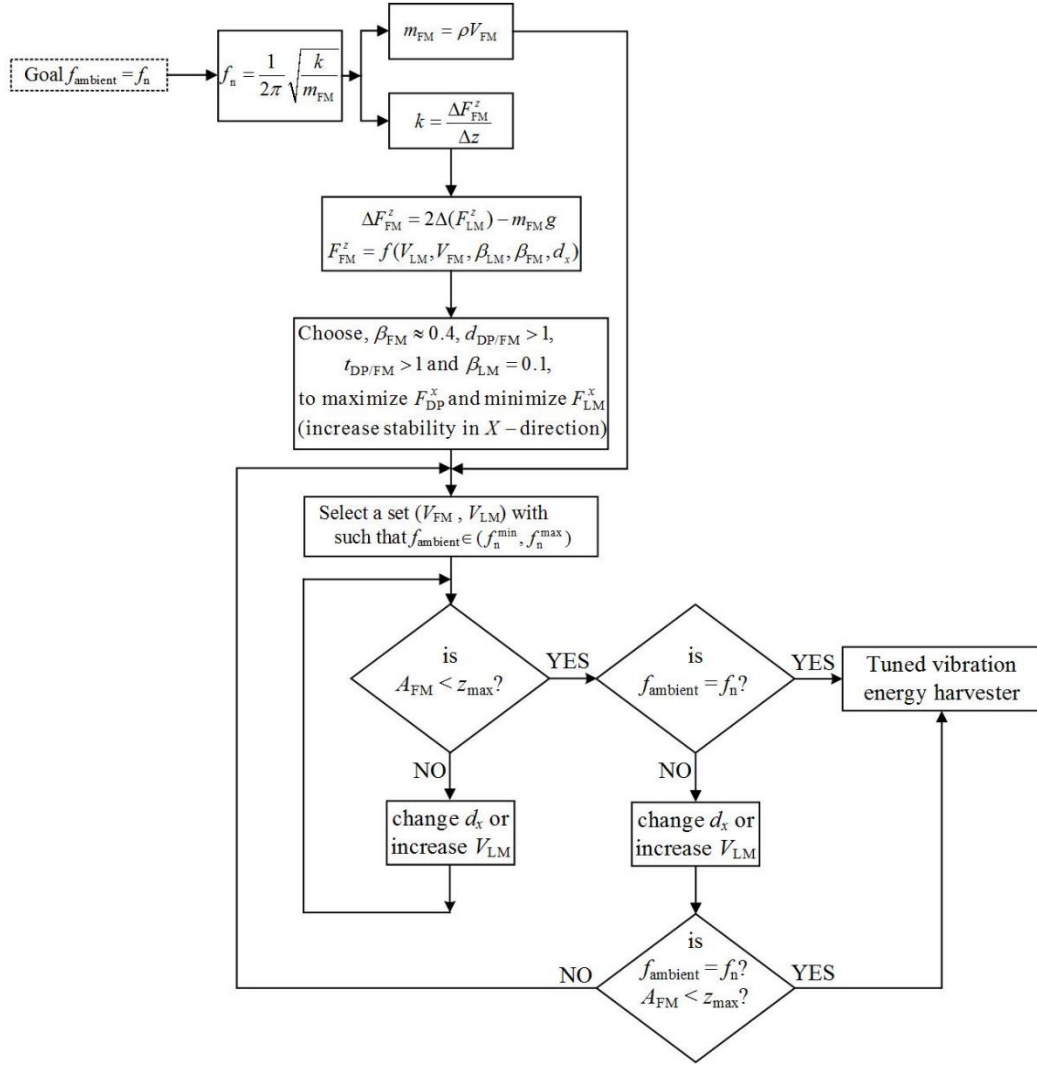


Figure 6.5 Flowchart for tuning f_n of a HDL system with the dominant f_{ambient} .

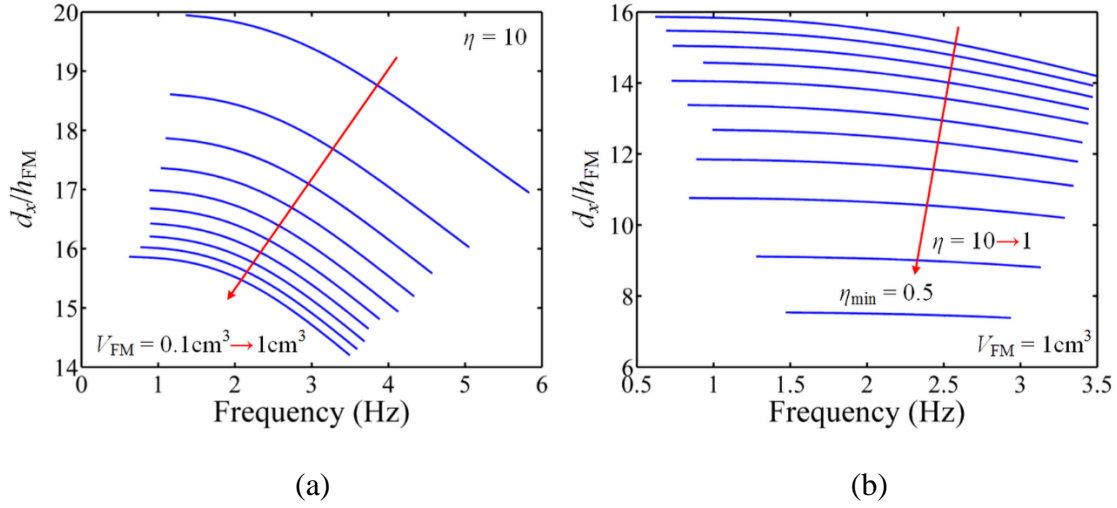


Figure 6.6 (a) Natural frequency range for V_{FM} ranging from 0.1 cm^3 to 1 cm^3 ($\eta = 10$)

(b) Natural frequency range for a fixed $V_{FM} = 1 \text{ cm}^3$ with η from 1 to 10.

To summarize, this section puts forward the modeling tools and parametric studies necessary to characterize a HDL system. The aspect ratio of the FM and the DP necessary to maximize the force between them, the volume and the aspect ratio of the V_{LM} for levitation to be achieved along with its stability constraints have been discussed. Also, a design strategy to tune the natural frequency of the HDL system to a given ambient natural frequency has been discussed. The next section will discuss about the electromagnetic coupling characteristics of the system by discussing damping due to eddy currents in the DP and a coil geometry for electromagnetic transduction.

6.2 Electromagnetic coupling characteristics

Current is induced in a conductor when a magnetic flux through it changes according to Faraday's law. In a vibration energy harvester system like Figure 6.1, these can be either lost as heat due to eddy currents or can be harnessed to power something. In either case they will produce a magnetic field of their own opposing the change in the magnetic field through it. This opposing magnetic field produces a force by Lorentz law which is proportional to the velocity and hence act like a viscous damping force to the motion of the object causing this magnetic flux change. In the present HDL system (Figure 6.1), the DP used for levitation is pyrolytic graphite, due to its strong diamagnetic properties, is incidentally also a good conductor of electricity. When the FM moves relative to the DP, currents are generated in them, aka eddy currents, which act a force to oppose the motion of the FM. It is possible to analytically (or semi-analytically) estimate these forces by using techniques described in [133]. However, it would be sufficient to approximate this damping force by an averaged value per unit velocity by experimentally measuring the ring down of the FM on perturbation. This averaged value from the experiments which includes the force due to eddy currents and the air resistance will discussed in a later paragraph.

For vibration energy harvesting using the HDL system a copper coil is incorporated into the design, shown in Figure 6.7. The copper coil geometry shown is placed around the DP with its axis along the X -axis. Alternate geometries such as placing the coil on the surface of the DP with its axis along the X -axis or a coil with its axis along the Z -axis around the FM would be difficult to integrate owing to the small levitation gaps that are generally the nature of diamagnetically stabilized magnet levitation systems.

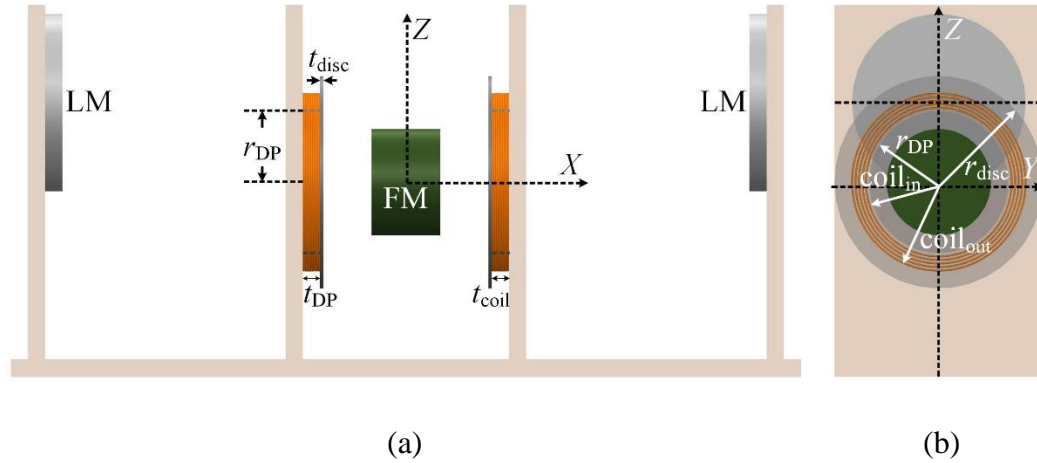


Figure 6.7 Schematic of the (a) front view and (b) side view showing the incorporation of a coil in the HDL system.

Although, Figure 6.2(b) shows the diametric relative ratio of the DPs $d_{DP/FM}$ that maximize F_x^{DP} to be around 1.5 but it is here of concern to limit the ratio to the value required to achieve static levitation as the remaining available space can be occupied by the copper coil. It should be noted that with increasing V_{LM} the destabilizing axial force is decreased and the required DP can be smaller, hence a slightly larger copper coil volume can be used, leading to possibly higher transductions, however at the cost of increasing d_x which may lead to overall smaller power densities. For these reasons and to allocate for sufficient dynamic stability in the z -direction for the system (Figure 6.4(b)) a η of two is chosen for this study. For these dimensions of LM and FM it is found that a DP of $r_{DP/FM} = 0.75$ ($r_{DP} \approx 4.75$ mm) and $t_{DP/FM} = 0.25$ ($t_{DP} \approx 1.6$ mm) is sufficient for levitating the FM. It was however found experimentally

that due to small gaps and tilts of the FM, a slightly larger DP of $r_{\text{DP/FM}} = 1.1$ ($r_{\text{DP}} \approx 7$ mm) and a $t_{\text{DP/FM}} = 0.6$ ($t_{\text{DP}} \approx 4$ mm) is chosen for better visual clarity of the levitation.

Using the minimum size of the DP required for static levitation and the parameters of LM and FM given in Table 6.1, the open-loop Q factor is found experimentally by measuring the ring-down of the FM after stopping the external vibration input. As $Q = \pi(\ln(A_1 / A_2))^{-1}$, where A_1 and A_2 are relative displacement amplitudes of the FM of successive cycles. A Q factor value of 25 was calculated after averaging over a set of 5 readings. However, the Q factor is not a constant but depends on the relative speed of the FM with the DP and hence this value is only an averaged approximate value which will be used in determining the frequency response of the system (equation (6.4)). The open-loop Q factor can reach to higher values on lamination of the pyrolytic graphite plate. This lamination process of the pyrolytic graphite has been done in Chapter 4 for the VDL system, quality factors of close to fifty were reached. It is expected that similar quality factor values can be reached with the HDL system, however, this task will be done for future research work.

With the estimation of the minimum size of the DP for static levitation, the rest of the volume available can be occupied by the copper coil. In this regard, one would want to estimate the outer radius copper coil as well as the thickness of the coil that can maximize the voltage. The voltage generated in the copper coil can be estimated by numerically calculating the differential of the net flux using Faraday's law. The equation for $V(z, \dot{z})$ is given by

$$V(z, \dot{z}) = -2\dot{z} \frac{d}{dz} \sum_{x_{\text{coil}}=D^-}^{x_{\text{coil}}=D^+} \sum_{\text{coil}_{\text{hor}}=\text{coil}_{\text{in}}}^{\text{coil}_{\text{hor}}=\text{coil}_{\text{out}}} \sum_{r=0}^{r=\text{coil}_{\text{hor}}} \sum_{\theta=0}^{\theta=\pi} B_x^{\text{FM}}(\rho, x_{\text{coil}}) r dr d\theta \quad (6.2)$$

where $\rho = \sqrt{(z - r \cos \theta)^2 + r \sin \theta^2}$, $D^+ = (D - t_{\text{FM}}) / 2 + t_{\text{coil}}$, $D^- = (D - t_{\text{FM}}) / 2$. The terms used in equation (6.2) are also shown in Figure 6.9(a).

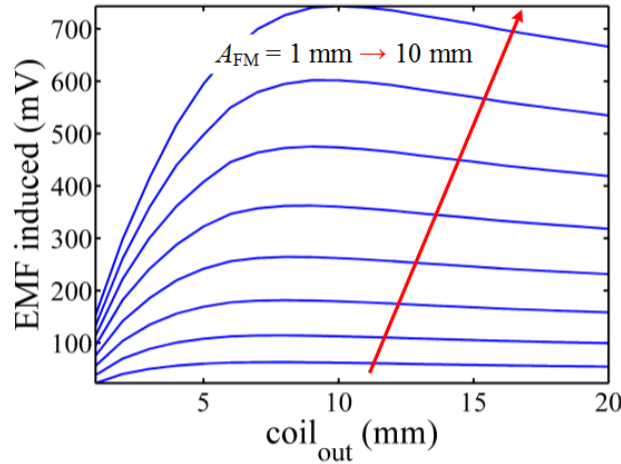


Figure 6.8 Voltage induced variation with coil_{out} of the copper coil for different A_{FM}

The rate of change of flux or the transduction factor in an electromagnetic vibration energy harvester with the magnet-across coil architecture is maximum at the point where the velocity of the magnet is maximum, that is, at the static equilibrium position of the magnet. For this position the coils closest to the magnet edge have a high transduction factor. Due to the static levitation constraints, as discussed earlier, the closest coil to the FM from the center is at a radius of 7 mm. The outer radius of the copper coil (coil_{out}) that maximizes the voltage induced depends on the amplitude of the FM (A_{FM}) as shown in Figure 6.8. It should be noted that for this study the thickness of the coil in the lateral direction (t_{coil}) has been fixed to the

thickness of the DP (t_{DP}) used. An estimate on the maximum achievable A_{FM} was made by simulating the open-loop frequency response of the system using the estimated Q factor in equation (6.4) to be around 6 mm. Based on this estimate, a $coil_{out}$ radius of 7 mm has been used for the experimental setup (Table 6.1).

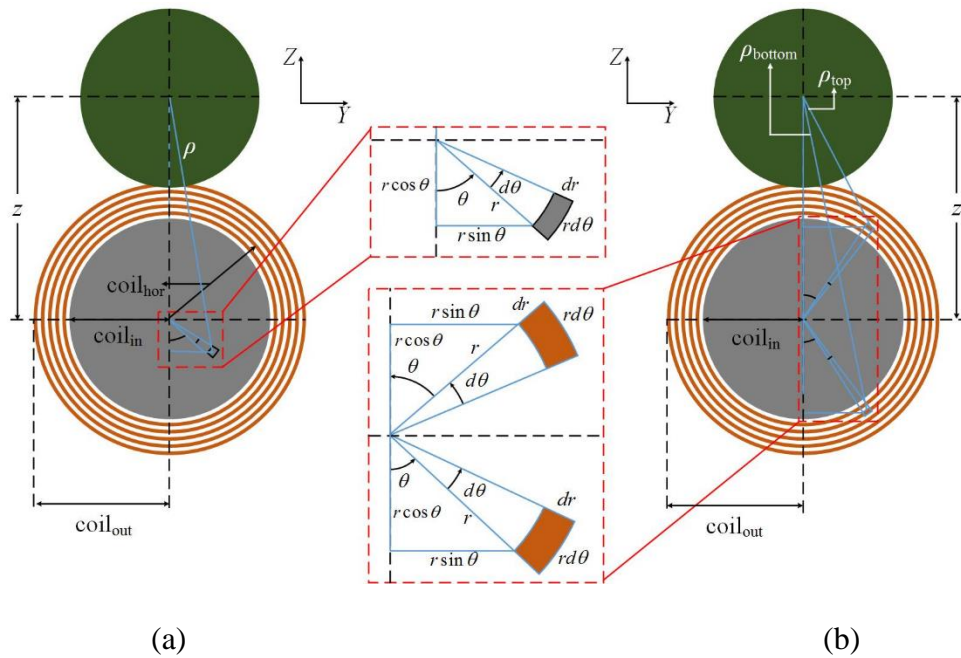


Figure 6.9 Schematic of coil geometry along with representation of terms used for calculation of (a) voltage in equation (6.2) and (b) the electromechanical coupling coefficient for equation (6.3).

Similar to how eddy currents in the DP act a force on the FM to restrict its motion, currents in the coil act a force on the FM which can be calculated by Lorentz law. This force (

$F_L(i, z)$ needs to be calculated to estimate the dynamics of the FM as will be discussed in equation (6.4).

$$F_L(i, z) = 2i \sum_{x_{\text{coil}}=D^+}^{x_{\text{coil}}=D^-} \sum_{r=\text{coil}_{\text{in}}}^{r=\text{coil}_{\text{out}}} \left\{ \begin{array}{l} \sum_{\theta=0}^{\theta=\pi/2} [B_x^{\text{FM}}(\rho_{\text{top}}, x_{\text{coil}})rd\theta] - \\ \sum_{\theta=0}^{\theta=\pi/2} [B_x^{\text{FM}}(\rho_{\text{bottom}}, x_{\text{coil}})rd\theta] \end{array} \right\} \quad (6.3)$$

where, $\rho_{\text{top}} = \sqrt{r^2 \sin^2 \theta + (z - r \cos \theta)^2}$, $\rho_{\text{bottom}} = \sqrt{r^2 \sin^2 \theta + (z + r \cos \theta)^2}$, coil_{in} is the inner radius of the coil, coil_{out} is the outer radius of the coil and the subscripts ‘top’ and ‘bottom’ relate to the top and bottom part of the current carrying coils due to the use of symmetry of the coils. The terms used in equation (6.3) are also shown in Figure 6.9(b) for a better understanding.

Due to the selection of a small DP to favor larger electromagnetic transduction, the axial repulsive force from the DP has been compromised especially for large amplitudes of the FM (such as near resonance). Also as the axial attraction force F_x^{LM} changes with z , it would be necessary to check if the FM impacts the DP at amplitudes near resonance. This impact can happen if the net restoring force in the x -direction (F_x^{FM}) is not directed towards $x = 0$ for small displacements in the x -direction. However, this impact does not mean the FM will lose stability but may alter the dynamics of the FM. For the d_x chosen (Table 6.1), Figure 6.10 shows that the force on the FM changes directions and would impact the DP for displacements from 4 mm to 6 mm.

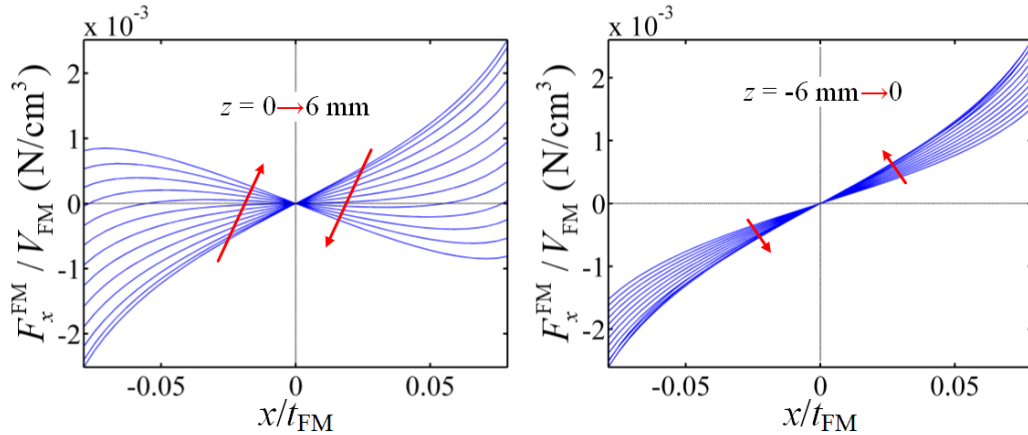


Figure 6.10 Normalized force F_x^{FM} between the DP and the FM for varying z - displacement of the FM.

Hence, this section summarizes the electromagnetic coupling factors that affect the dynamics of the FM that is damping due to eddy currents and copper coils. Also a copper coil geometry, for electromagnetic transduction, with conflicting constraints on stability are discussed that need to be considered while designing a HDL vibration energy harvester. The next section will discuss the equations of motion taking into consideration the factors discussed in Section 6.1 and Section 6.2 along with experimentally validating the frequency response characteristics of the vibration energy harvester.

6.3 Experimental validation

In general, a vibration energy harvester can be modeled as a single degree-of-freedom (1-DOF) vibration system subjected to base excitations by using a lumped-parameter model

[2]. The constituent elements of the model such as the restoring forces, the damping elements that have been discussed in previous sections are now used in equation (6.4) to understand its frequency response. The mechanical and electrical equations of motions are

$$\begin{aligned} m_{\text{FM}}\ddot{z} + c_m\dot{z} + F_{\text{K}}(z) + F_{\text{L}}(i, z) &= m_{\text{FM}}\omega^2 A \sin \omega t \\ iL_{\text{coil}} + i(R_{\text{load}} + R_{\text{coil}}) &= V(z, \dot{z}) \end{aligned} \quad (6.4)$$

here z is the relative displacement of the FM, i is the current in the coil, A is the amplitude of the sinusoidal base displacement, $F_{\text{K}}(z)$ is the restoring force (which is the same as $F_{\text{K}}(z)$ in equation (6.1)), c_m is the mechanical damping factor, $F_{\text{L}}(i, z)$ is the electrical damping force and $V(z, \dot{z})$ is the voltage induced, R_{load} is the resistance of the load, R_{coil} is the resistance of the coil, L_{coil} is the inductance of the coil. The restoring forces of the present experimental system (Table 6.1) is given in Figure 6.11. The values x , y and $z = 0$ represent the static levitation point of the FM.

For a system defined by equation (6.4), if the input power is held constant, it can absorb the maximum energy that will be generated around its resonance frequency. For a harmonic base excitation, if the mass of the vibrator (mass of the FM in this case, m_{FM}) is much less than the mass of the energy harvester (m_{H}), the input power to the energy harvester is approximated by:

$$\begin{aligned} \bar{P}_{\text{input}} &\approx \frac{2\omega}{\pi} \int_0^{\pi/2\omega} m_{\text{H}} \left| (-A\omega^2 \sin \omega t)(A\omega \cos \omega t) \right| dt \\ &\approx \frac{\omega}{\pi} \int_0^{\pi/2\omega} m_{\text{H}} \omega^3 A^2 \sin 2\omega t dt \approx \frac{1}{\pi} m_{\text{H}} \omega^3 A^2 \end{aligned} \quad (6.5)$$

where ω is the angular frequency of the base excitation, A is the amplitude of the base excitation, \bar{P}_{input} is the average input power to the harvester. As shown in equation (6.5), a constant input power to the energy harvester is maintained by keeping $\omega^3 A^2$ constant.

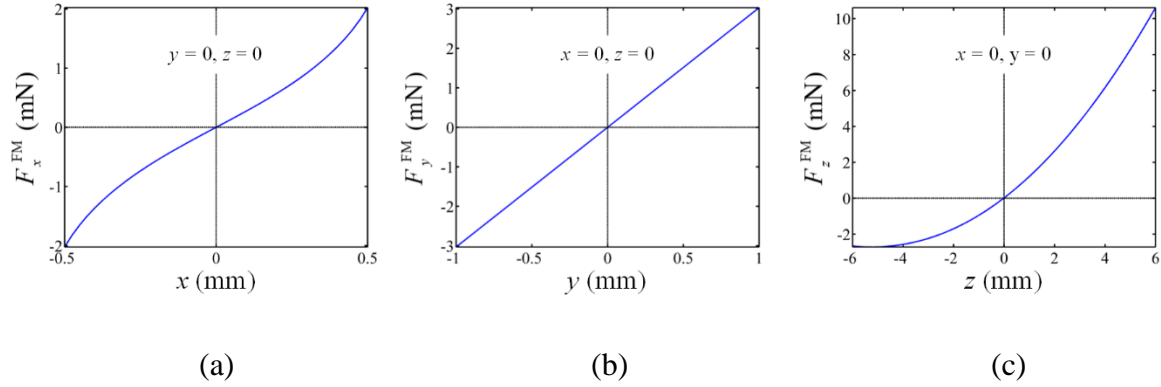


Figure 6.11 Restoring forces for the HDL system in the (a) x -direction (b) y -direction and (c) z -direction with system parameters given in Table 6.1.

The experimental system of the HDL vibration energy harvester is shown in Figure 6.12 along with a close up of the HDL vibration energy harvester system in Figure 6.13. The figure shows the energy harvester along with a high speed camera, a light source, an oscilloscope, an amplifier, a laser vibrometer and an APS 113 shaker to carry out the low-frequency tests. The vibration response of the system for various frequencies has been tested by measuring the voltage output of the harvester along with measuring the amplitude response of the FM. The experimental tests were performed by keeping the mechanical power input to the harvester constant at all frequencies (equation (6.5)). The excitation frequency was varied from 0.5 Hz to 4 Hz and the input amplitude was varied from 4 mm to 0.18 mm, which

correlates to RMS acceleration levels varying from 0.028 ms^{-2} to 0.079 ms^{-2} in order to keep the product $\omega^3 A^2$ a constant for constant mechanical input power.

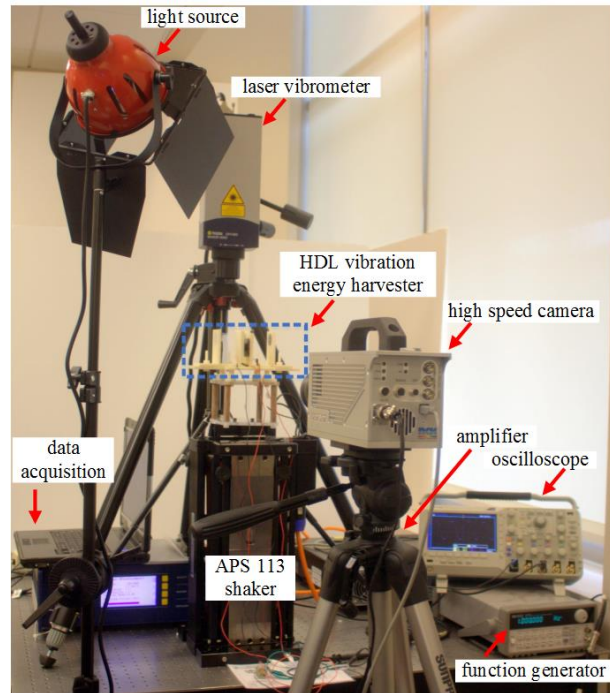


Figure 6.12 Experimental setup of the HDL vibration energy harvester

Figure 6.14 (a) – (d) show the experimental results along with the theoretical predictions. At a mechanical input power of $36.6 \mu\text{W}$ and at a frequency of 1.9 Hz , the harvester generated an average power of $9.47 \mu\text{W}$ with an average system efficiency of 25.8% . The system shows a weak softening response which is a result of the nonlinear restoring force (Figure 6.11(c)). Due to the unsymmetrical nature of the restoring force in the z -direction, unequal amplitudes of the FM are seen on either side of the equilibrium position. The

theoretical and experimental relative displacement values shown in Figure 6.14(a) are the average of the unequal amplitudes. Due to the compromise on the size of the DP as discussed previously, some motion exists in the x -direction as predicted theoretically in Figure 6.10 and also impacts with the DP are observed, however, no considerable change in the dynamics of the FM is observed as majority of the dynamics of the FM correlate well with the theoretical predictions (Figure 6.14). One way in which such impacts can be avoided is by increasing the levitation gap between the DP and the FM. This can be done by introducing repelling magnets below the static stable position of the FM, more details on such configurations are discussed in section 6.4.

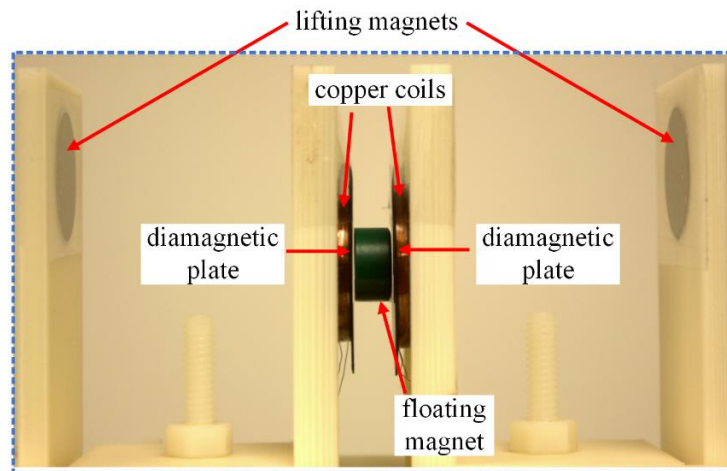


Figure 6.13 Close up of the HDL vibration energy harvester

It can also be seen in Figure 6.14 that for some of the frequencies there is a moderate discrepancy from the theoretical predictions, this can be mainly due to the difference in the manufactures magnetization value from its actual magnetization value (after taking into

account each magnets shape effect, i.e. the permeance coefficient), inaccurate estimation of the open-loop Q factor and assumption of uniform magnetization in the theoretical analysis. The same reasons discussed in this paragraph lead to a small tilt in the stably levitating position of the magnet (Figure 6.13).

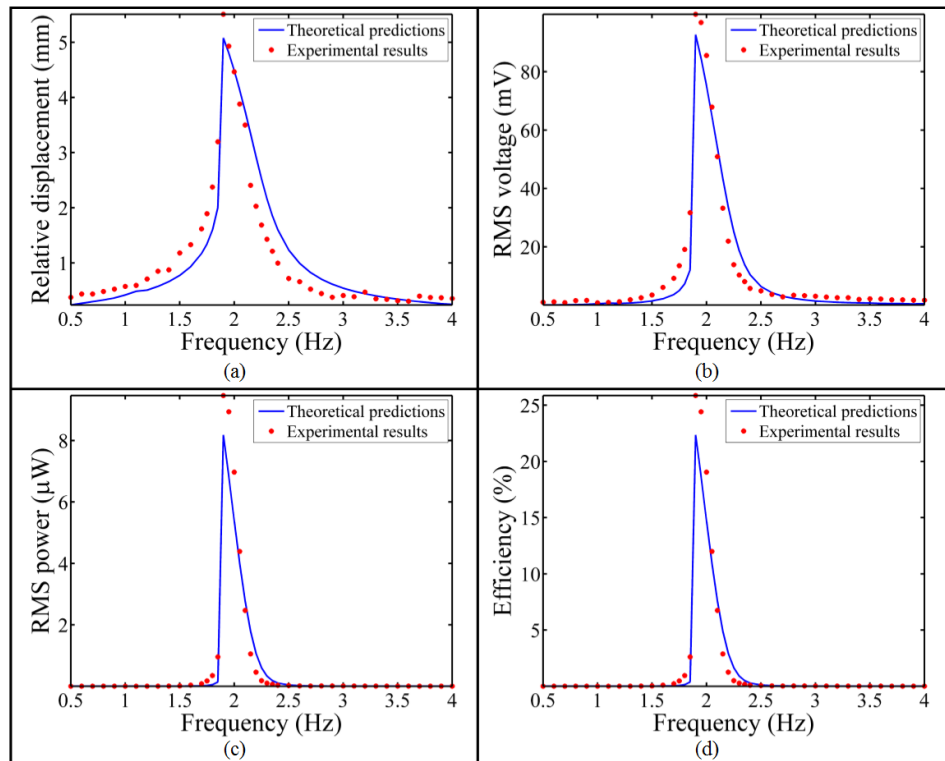


Figure 6.14 Theoretical predictions and experimental measurements of the (a) average amplitude of the FM (b) the RMS voltage (c) the RMS power and (d) the efficiency

Table 6.1 Model parameters for the experimental system

| | | | | | | | | |
|-----------|----------|------------|--------------------|---------------------|------------|----------|-----------------------|----------------------|
| Parameter | r_{FM} | t_{FM} | r_{LM} | t_{LM} | r_{DP} | t_{DP} | χ_x | χ_y, χ_z |
| Value | 6.35 | 6.35 | 12.7 | 3.175 | 7 | 3.5 | -4.5×10^{-4} | -85×10^{-6} |
| Unit | mm | mm | mm | mm | mm | mm | - | - |
| Parameter | d_x | r_{wire} | coil _{in} | coil _{out} | t_{coil} | N | m_H | \bar{P}_{input} |
| Value | 59.5 | 15.8 | 7 | 14 | 3.5 | 2000 | 230 | 36.6 |
| Unit | mm | μm | mm | mm | mm | - | g | μW |

A useful metric to compare the relative performance of the proposed energy harvesters in literature was introduced by Mitcheson et al.[7]. This metric is called the volume figure of merit (FoM_v) and is given by

$$FoM_v = \frac{\text{Useful Power Output}}{\frac{1}{16} A \rho_{AU} Vol^{4/3} \omega^3} \quad (6.6)$$

where ‘Vol’ represents the volume of the harvester, ρ_{AU} represents the density of gold, A represents the input excitation amplitude and ω represents the input excitation angular frequency. Now, if there is a hypothetical closure that can enclose the current prototype harvester it would have an internal volume of roughly 85 cm³. This corresponds to a FoM_v (%) of 0.23 computed at 1.9 Hz. With respect to the current state of the art vibration energy harvesters that work at this frequency range (≈ 2 Hz) it measures competitively ([140], FoM_v (%) at 2 Hz is 0.02; [143], FoM_v (%) at 2 Hz is 0.16). However, this prototype does not fare well with the bandwidth figure of merit, which is a performance metric which takes into consideration frequency range of operation as well [7]. This bandwidth figure of merit will be

the focus of future studies to design a bi-stable levitating system which inherently has a wider frequency bandwidth of operation.

6.4 Improving stability of diamagnetically stabilized magnet levitation systems

In the vertical and horizontal configurations discussed till now there have been one or two LMs which balance the weight of a magnet (FM) and the stability in either the same or orthogonal directions is balanced by the diamagnetic repulsive force. In this chapter, the idea of using repelling magnets into the design of the horizontal and vertical configurations is discussed on how they increase the stability region of the FM by decreasing the apparent weight of it seen by the LMs. Additionally, the inclusion of repelling magnets gives more design space to alter the frequency response characteristics of the system.

As discussed previously, the LM introduces destabilizing forces in the axial direction in the HDL system which are stabilized by the DPs. However, if one introduces repelling magnets at a distance below the stable levitation position of the FM and at a particular axial distance depending on its magnetization, the repelling force decreases the net weight seen by the LMs and also decreases the destabilizing attractive force in the axial direction and hence contributes to larger levitation gaps (Figure 6.15). This larger levitation gaps could avoid the FM from impacting the DP as was seen in the experimental investigation of this chapter. Equation (6.7) shows the adjusted restoring forces on introduction of the repelling magnets that need to be considered, the superscripts RM indicate the forces due to the repelling LMs. There is a small net decrease in the repulsive force from the DP due to the decrease in the induced magnetization as a result of some field cancellation due to the repulsive magnets,

however, this change is insignificant when compared to the decrease in the destabilizing axial force from the same magnets. Care should be taken that there would be a limit on the strength of the repelling force that can be exerted from these repelling magnets as they can destabilize the forces in the y -direction. This destabilization can lead to the magnet tilting about the Y -axis.

$$\begin{aligned}
 F_x^{\text{FM}} &= \Delta F_x^{\text{LM}} - \Delta F_x^{\text{RM}} - \Delta F_x^{\text{DP}} \\
 F_z^{\text{FM}} &= 2F_z^{\text{LM}} - 2F_z^{\text{RM}} - w_{\text{FM}} \\
 F_y^{\text{FM}} &= -2F_y^{\text{LM}} + 2F_y^{\text{RM}}
 \end{aligned}
 \tag{6.7}$$

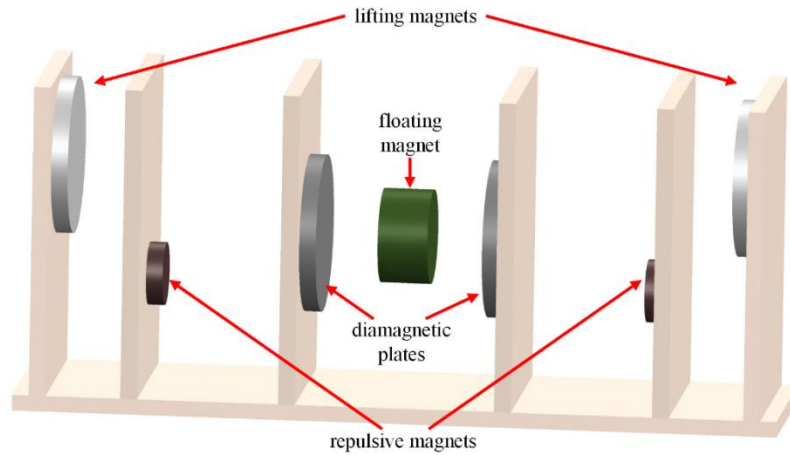


Figure 6.15 Schematic of HDL system with repulsive magnet for enhanced levitation gap.

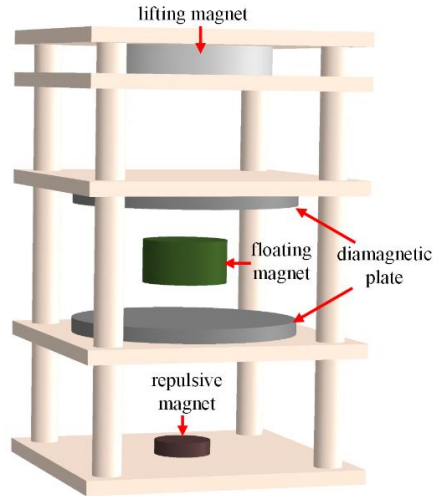


Figure 6.16 Schematic of VDL system with repulsive magnets for enhanced levitation gap.

Figure 6.16 shows the schematic of the VDL system discussed in Chapters 3 and 4 with the inclusion of a repelling magnet axially below the FM. The introduction of the repelling magnet at a distance below the stable levitation position of the FM and at a particular axial distance depending on its magnetization, the repelling force decreases the net weight seen by the LMs and also decreases the destabilizing attractive force in the axial direction and hence contributes to larger levitation gaps. Equation (6.8) shows the adjusted restoring forces on introduction of the repelling magnets that need to be considered, the superscripts RM indicate the forces due to the repelling magnet. Care should be taken that there would be a limit on the strength of the repelling force that can be exerted as they can destabilize the forces in the x or y -direction. This destabilization can lead to the magnet tilting about one of the axes (x or y).

$$\begin{aligned}
F_z^{\text{FM}} &= F_z^{\text{LM}} + F_z^{\text{RM}} - \Delta F_z^{\text{DP}} - w_{\text{FM}} \\
F_y^{\text{FM}} &= -F_y^{\text{LM}} + F_y^{\text{RM}} \\
F_x^{\text{FM}} &= -F_x^{\text{LM}} + F_x^{\text{RM}}
\end{aligned} \tag{6.8}$$

6.5 Conclusions

A characterization study on a HDL system has been detailed in this chapter for its design as a vibration energy harvester. Parametric studies on the different components of the HDL system are carried out to quantify their influence on stability, size and frequency characteristics. An aspect ratio of around four-tenth for the FM provide for a maximum force from the diamagnetic material which is essential for stabilization of levitation for a given volume of the FM. A low aspect ratio of the LM for a volume that can provide enough lateral force to overcome the weight of the FM provide for the least size of the device. Also, a low aspect ratio allows for larger maximum amplitude of the FM for a given volume of the LM. The stability of the FM in the lateral and axial direction has been discussed for large amplitudes. The incorporation of a copper coil is considered for electromagnetic transduction, its design is discussed with conflicting constraints of stability as it replaces a part of the diamagnetic material. Finally, an experimental system is setup to demonstrate the HDL based vibration energy harvester. Experimental results and theoretical predictions show a softening frequency response with an average power output of 9.47 μW with an average mechanical input power of 36.6 μW (which corresponds to an RMS acceleration of 0.0546 m/s^2) at a frequency of 1.9 Hz. The volume figure of merit of 0.23% is achieved at 1.9 Hz, which is an improvement to the state of the art in the field when considering very low frequency (< 5 Hz)

by an order of magnitude. Additionally, the inclusion of repelling magnets into diamagnetic levitation systems is discussed to improve stability and to give more design space to alter the frequency characteristics of the system.

7 A bi-stable horizontal diamagnetic levitation (BHDL) based low frequency wideband vibration energy harvester

A bi-stable system based on horizontal diamagnetic levitation is proposed in this chapter to take advantage of the broad bandwidth frequency response inherent in a bi-stable system (Chapter 1). From initial conceptual design which includes multiple lifting magnets (LMs) to a final robust frequency tunable design involving multiple LMs and repelling magnets (RMs) are discussed. The theoretical modelling discussed involved the superposition of the magnetic fields and forces from the LMs and RMs on the diamagnetic plate (DP) and the floating magnet (FM) respectively. While discussing the different designs, conflicting constraints on achieving equal potential well bi-stability, maintaining stable levitation during intra-well and inter-well motion, and design flexibility were addressed. An experimental prototype with four LMs and eight RMs placed around the floating magnet (FM) is setup in which priority was given to stability over equality of potential energy wells. Frequency response characteristics of the bi-stable system were experimentally and theoretically validated for input sinusoidal excitation with three different input amplitudes, 0.5mm, 1mm and 1.5mm for varying frequency.

Once the dynamics of the bi-stable system were validated, a copper coil geometry is discussed to be incorporated in the DP. For this, a part of the DP is replaced with a copper coil for transduction at a location, between the two stably levitating positions of the FM, where it does not affect the stability at either of the static levitations positions. Voltage-frequency

response characteristics of the bi-stable system were validated experimentally and theoretically by measuring the voltage across a resistive load attached to the copper coils. The FM underwent chaotic and interwell motions for a range of input excitation frequencies (5.8Hz – 8Hz) at a constant input displacement of 1.5 mm. Hence, the bi-stable system showed broader frequency bandwidth operation over the mono-stable HDL systems discussed in the previous chapters. Finally, conclusions are presented with suggestions on directions of future studies that can improve the performance of the BHDL system for efficient low frequency vibration energy harvesting.

7.1 Conceptual design of a BHDL system

Intuitively, the starting point of designing a bi-stable system based on HDL would be the use of a set of four LMs as shown in Figure 7.1(a). The top two LMs (LM_1, LM_2 , *cf.* Figure 7.1(a)) on either side of the FM sustain the levitation of the FM at the top stable position (marked as ‘1’) and the bottom two LMs (LM_3, LM_4 , *cf.* Figure 7.1(a)) sustain the levitation of the FM at the bottom stable positions (marked as ‘2’). However, the distance between the two sets of LMs laterally (z_{LM} , *cf.* Figure 7.1(a)) should be large enough to avoid any significant influence of one set of LMs over the other stable position of the FM, that is, the influence of the top set of LMs over the bottom stable position and vice versa. Especially, the top stable position would be rather difficult to achieve because the lateral force from the top set of LMs have to not only compensate the weight of the FM but have to compensate for the downward pull of the bottom set of LMs.

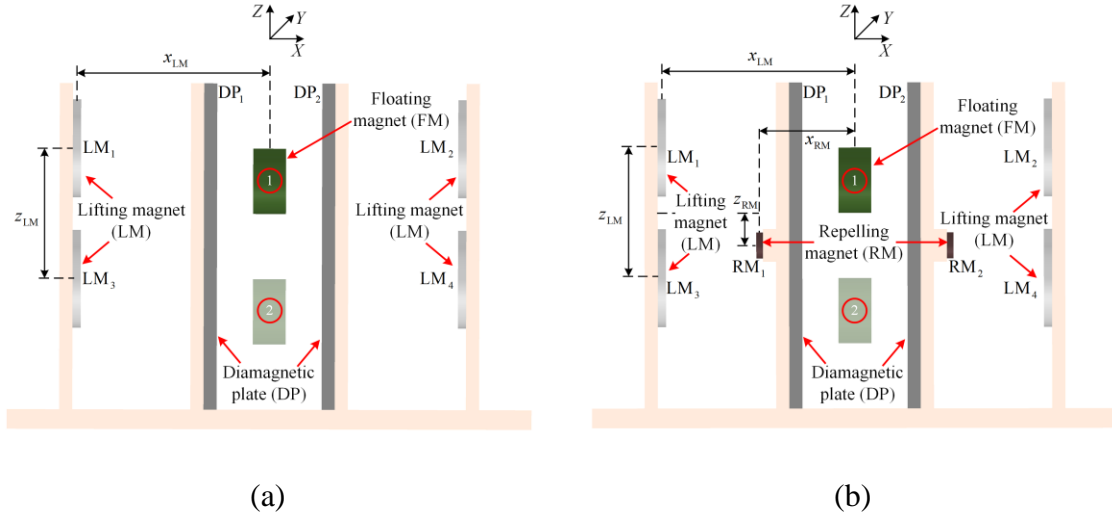


Figure 7.1 Possible BHDL system with (a) four LMs (LM_4) (b) four LMs and two RMs (LM_4RM_2)

Before one can make a judgement on the possibility of bi-stability of the design shown in Figure 7.1(a), some mathematical modelling is described and later numerical simulations are run to test and identify candidate system parameters that can achieve bi-stability in the next section.

7.2 Theoretical modeling of the BHDL

Firstly, the repulsive force from the DP, discussed in Chapter 5 (Equation (5.5)), will be used in this chapter and is reproduced below,

$$F_x^{DP} = -\int \nabla_x U dV = -\int \nabla_x (\mathbf{M} \cdot \mathbf{B}_{FM}) dV = -\int \mathbf{M} \cdot \nabla_x \mathbf{B}_{FM} dV \quad (7.1)$$

where \mathbf{M} is the magnetization due to the total magnetic field inside the DP (due to the FM and the LMs) and \mathbf{B}_{FM} is the magnetic field vector of the FM inside the DP. The magnetic field of a magnet whenever mentioned in this chapter is determined by modeling the magnet as a thin coil as described in Chapter 3. The magnetization \mathbf{M} is given by

$$\begin{aligned}\mathbf{M} &= (\chi_x B_x^T \hat{\mathbf{x}} + \chi_y B_y^T \hat{\mathbf{y}} + \chi_z B_z^T \hat{\mathbf{z}}) / \mu_0, \\ B_i^T &= B_i^{\text{FM}} + \sum_{j=1}^4 B_i^{\text{LM}_j}, \quad (i = x, y, z) \\ \mathbf{B}_{\text{FM}} &= B_x^{\text{FM}} \hat{\mathbf{x}} + B_y^{\text{FM}} \hat{\mathbf{y}} + B_z^{\text{FM}} \hat{\mathbf{z}}\end{aligned}\tag{7.2}$$

where B_i^T represents the total magnetic field inside the DP due to the FM (B_i^{FM}) and the LMs in one of the three directions, $B_i^{\text{LM}_j}$ represents the magnetic field due to the j th LM in one of the three directions inside the DP, χ_x , χ_y and χ_z represent the magnetic susceptibilities of the DP in the three directions and $\hat{\mathbf{x}}$, $\hat{\mathbf{y}}$ and $\hat{\mathbf{z}}$ represent the unit vectors in the three directions. By discretizing the DP into a finite number of cuboids of size dl , dw and dt one can approximate the volume integral into summation of all the cuboids with n_{DP} , m_{DP} and k_{DP} as the number of cuboids in the length, width and thickness dimension respectively.

$$F_x^{\text{DP}} \approx - \sum_i \sum_j \sum_{k=1}^{k_{\text{DP}}} \sum_{m=1}^{m_{\text{DP}}} \sum_{n=1}^{n_{\text{DP}}} \frac{\chi_i}{\mu_0} B_i^T B_{ij}^{\text{FM}} dl dw dt, \quad (i, j = x, y, z)\tag{7.3}$$

where $B_{ij}^{\text{FM}} = \Delta B_i^{\text{FM}} / \Delta j$, ($i, j = x, y, z$).

As a starting point to investigate the possibility of bi-stability in the LM_4 configuration (Figure 7.1(a)), the volume of the LM (V_{LM}) and the volume of the FM (V_{FM}) used in Chapter 6 were used here. The necessary conditions for the system to have bi-stability

is for the force on the FM in the z -direction (F_z^{FM}) to be zero at two points along the z -direction and for the repulsive force from the DP (F_x^{DP}) to be greater than the net of the attractive forces from the LM at the equilibrium points in the x -direction. That is,

$$\begin{aligned}
 F_z^{\text{FM}^1} &= \sum_{j=1}^2 F_z^{\text{LM}^1_j} - \sum_{j=3}^4 F_z^{\text{LM}^1_j} - w_{\text{FM}} = 0 \\
 F_z^{\text{FM}^2} &= \sum_{j=1}^4 F_z^{\text{LM}^2_j} - w_{\text{FM}} = 0
 \end{aligned}
 \tag{7.4}$$

where the super-superscript ‘1’ and ‘2’ refer to the equilibrium points shown in Figure 7.1(a), super-subscript ‘1’, ‘2’, ‘3’ and ‘4’ represent the LMs shown in Figure 7.1(a) and w_{FM} represents the weight of the FM. The semi-analytical equations which models the magnets as thin coils and estimates the force by integrating the force between individual coils of each magnet, which were discussed in detail in Chapter 5 (equation (5.3)), are used in this chapter as well. For example, in equation (7.4) they are used to estimate the forces $F_z^{\text{LM}^1_j}$ and $F_z^{\text{LM}^2_j}$.

In the x -direction, the restoring forces on the FM are

$$\begin{aligned}
 F_x^{\text{FM}^1} &= \sum_{j=1}^2 (-1)^j F_x^{\text{DP}^1_j} + \sum_{j=1}^4 (-1)^{j+1} F_x^{\text{LM}^1_j} \\
 F_x^{\text{FM}^2} &= \sum_{j=1}^2 (-1)^j F_x^{\text{DP}^2_j} + \sum_{j=1}^4 (-1)^{j+1} F_x^{\text{LM}^1_j}
 \end{aligned}
 \tag{7.5}$$

$F_x^{\text{FM}^1}, F_x^{\text{FM}^2}$ need to be positive for $x > 0$ and $F_x^{\text{FM}^1}, F_x^{\text{FM}^2}$ need to be negative for $x < 0$ in equation (7.5) for stability in this direction. The super-superscript and super-subscripts have the same meaning as in equation (7.4).

For different sets of x_{LM} and z_{LM} (*cf.* Figure 7.1(a)), simulations were run to meet conditions mentioned in equations (7.4) and (7.5). The results showed that z_{LM} needs to be unrealistically high (two orders greater at the least) when compared to the dimensions of the magnets to satisfy equation (7.4). Consequently, simulations were also run with different V_{LM} , V_{FM} and with varying ratios of the two which resulted in similar unrealistic results.

In Chapter 6, RMs were introduced to discuss about improving stability conditions in diamagnetic levitation systems. Here, it is explored how the inclusion of RMs can promote bi-stability. Figure 7.1(b) shows a schematic of a possible bi-stable system with one RM on each side of the FM. This RM mitigates the effect of the lateral and axial attractive forces of the bottom set of LMs (LM_3 and LM_4) at the top stable position of the FM. It also mitigates the influence of the top set of LMs (LM_1 and LM_2) at the bottom stable position of the FM which pushes the bottom stable position further away from the top stable position.

As introduced previously the necessary conditions for the system to be stably levitating and to have bi-stability is to satisfy equations (7.4) and (7.5). With the inclusion of RMs, equation (7.2) becomes

$$\begin{aligned} \mathbf{M} &= (\chi_x B_x^T \hat{\mathbf{x}} + \chi_y B_y^T \hat{\mathbf{y}} + \chi_z B_z^T \hat{\mathbf{z}}) / \mu_0, \\ B_i^T &= B_i^{\text{FM}} + \sum_{j=1}^4 B_i^{\text{LM}_j} + \sum_{j=1}^2 B_i^{\text{RM}_j}, \quad (i = x, y, z) \\ \mathbf{B}_{\text{FM}} &= B_x^{\text{FM}} \hat{\mathbf{x}} + B_y^{\text{FM}} \hat{\mathbf{y}} + B_z^{\text{FM}} \hat{\mathbf{z}} \end{aligned} \quad (7.6)$$

where $B_i^{\text{RM}_j}$ represents the magnetic field due to the j th RM in one of the three directions inside the DP. Also, equations (7.4) and (7.5) are updated to include the influence of RMs,

$$\begin{aligned}
F_z^{\text{FM}^1} &= \sum_{j=1}^2 F_z^{\text{LM}_j^1} - \sum_{j=3}^4 F_z^{\text{LM}_j^1} + \sum_{j=1}^2 F_z^{\text{RM}_j^1} - w_{\text{FM}} = 0 \\
F_z^{\text{FM}^2} &= \sum_{j=1}^4 F_z^{\text{LM}_j^2} - \sum_{j=1}^2 F_z^{\text{RM}_j^2} - w_{\text{FM}} = 0
\end{aligned} \tag{7.7}$$

and,

$$\begin{aligned}
F_x^{\text{FM}^1} &= \sum_{j=1}^2 (-1)^j F_x^{\text{DP}_j^1} + \sum_{j=1}^4 (-1)^{j+1} F_x^{\text{LM}_j^1} + \sum_{j=1}^2 (-1)^j F_x^{\text{RM}_j^1} \\
F_x^{\text{FM}^2} &= \sum_{j=1}^2 (-1)^j F_x^{\text{DP}_j^2} + \sum_{j=1}^4 (-1)^{j+1} F_x^{\text{LM}_j^2} + \sum_{j=1}^2 (-1)^j F_x^{\text{RM}_j^2}
\end{aligned} \tag{7.8}$$

where $F_x^{\text{FM}^1}, F_x^{\text{FM}^2}$ need to be positive for $x > 0$ and $F_x^{\text{FM}^1}, F_x^{\text{FM}^2}$ need to be negative for $x < 0$.

Additionally, stability in the y -direction also needs to be considered as there are now competing forces in this direction due to the inclusion of RMs. The condition of stability in y -direction is,

$$\begin{aligned}
F_y^{\text{FM}^1} &= -\sum_{j=1}^4 F_y^{\text{LM}_j^1} + \sum_{j=1}^2 F_x^{\text{RM}_j^1} \\
F_y^{\text{FM}^2} &= -\sum_{j=1}^4 F_y^{\text{LM}_j^2} + \sum_{j=1}^2 F_x^{\text{RM}_j^2}
\end{aligned} \tag{7.9}$$

where $F_y^{\text{FM}^1}, F_y^{\text{FM}^2}$ need to be positive for $y > 0$ and $F_y^{\text{FM}^1}, F_y^{\text{FM}^2}$ need to be negative for $y < 0$.

To investigate the possibility of bi-stability in the LM_4RM_2 configuration (Figure 7.1(b)), several V_{LM} , V_{FM} , and different ratios of the two were used in simulations. Also, as mentioned in Chapter 6, the volume of the RM (V_{RM}) needs to be considerably smaller than V_{FM} to avoid instability along the y -direction (Section 6.5). Hence, the volume of the RM were selected from a set of volumes which were at least twenty times smaller than the volume of the FM. Also, to minimize the volume and increase the axial and lateral force from the RM, based

on Figure 6.3 in Chapter 6, a high aspect ratio of the RM is chosen. Simulations were carried out with different set of volumes (V_{FM} , V_{LM} and V_{RM}) at different set of distances (x_{LM} , z_{LM} , x_{RM} and z_{RM} , cf. Figure 7.1(b)) to find candidate set of parameters that satisfy the conditions of equations (7.7)-(7.9). Several candidate sets were found and on setting up the experimental system with these parameters, it was observed that there was a significant tilt in the FM about the Y -axis in each of them and the FM could not be levitated as it was in contact with the DP as a result of the tilt. Hence, experimentally equation (7.8) was not satisfied. It is believed that although the equation (5.3) of Chapter 5 used for calculating equations (7.7) and (7.8) were accurate, the assumption of the net force to act at the center of mass of the magnet might not be valid for all distances between two magnets. This is especially true when the distance between the magnets is small enough such that there is considerable magnetic field gradient over the surface of the FM. Hence, to overcome the problem with the tilt of the magnet, first the RM with high aspect ratio was replaced with a low aspect ratio one and the ratio of LM to FM ($\eta = V_{LM} / V_{FM}$) was increased, both of which reduce the magnetic field gradient seen by surface of the FM.

On making these changes, simulations were carried out and several candidate volumes of the LM and RM were found that could achieve bi-stability of the FM. A few of them were experimentally validated to show the bi-stability of the FM. In order to select the best candidate among the bi-stable system parameters found, firstly, the various parameters involved in a potential energy plot of a generic double well BHDL system need to be discussed. An example of such a potential energy plot is shown in Figure 7.2. In this figure, it is shown that the energy

of the bottom stable position represents the lowest potential energy of the FM in the bi-stable system, that is $U_2 = 0$, U_1 represents the potential energy of the FM at the top stable position, U_{barrier} represents the minimum gain in potential energy required for the FM to jump from the bottom stable position (shown as “2” in Figure 7.2) to top stable position (shown as “1” in Figure 7.2) and $U_{\text{stability}}$ is the maximum gain in potential energy of the FM below the stable position “2” which would make it lose z -stability. Hence, one another important stability condition that arises for the BHDL system is

$$U_{\text{stability}} > U_{\text{barrier}} \quad (7.10)$$

This is required so that the FM doesn't lose stability while undergoing interwell motion. Secondly, an ideal case would be to design a system close to $U_2 = U_1 = 0$ to reap the maximum frequency bandwidth benefits of the double well system [73].

Only a very small set of the experimental setups of the candidate solutions found from the simulations satisfied equation (7.10) but an additional challenge appeared in most of the setup experiments. During the translation of the FM from one stable point to the other instability in the y -direction existed due to which the motion was not primarily in the z -direction. This additional challenge further narrowed to only a tiny fraction of the experimental setups of the BHDL design presented in Figure 7.1(b) which satisfied all the conditions. Although few experimental setups satisfied all the conditions, there was little design control over the potential energy of the wells and a considerable difference between the potential energy of the wells was seen. This is disadvantageous as it is known that a bi-stable system need to be maintained closed to $U_2 = U_1 = 0$ to reap the maximum frequency bandwidth

benefits of the double well system [73]. These reasons motivated to explore other designs to achieve bi-stability in the HDL system.

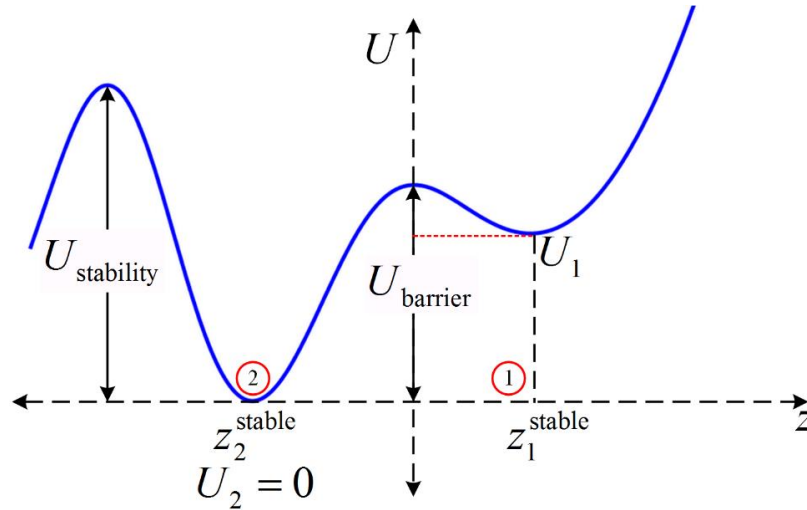


Figure 7.2 A general double-well potential system using HDL

7.3 Proposed BHDL system

Taking note of the challenges of the previous design, a schematic of a proposed BHDL design with two major changes is shown in Figure 7.3. The first change involved splitting the RMs into two by volume and placing them at equal distances apart in the y -direction. They are placed such that they provide the necessary repulsive force in the x -direction and nearly cancel out their respective forces in the y -direction. This solves the problem of y -stability in the previous design (Figure 7.1(b)). The second change involved introducing another set of RMs below the bottom set of LMs which would help in meeting the condition of equation (7.10). This also helps in achieving an equal potential well system ($U_1 = U_2 = 0$, cf. Figure 7.2), as

the bottom set of RMs raise the potential energy of the bottom stable point which was generally seen to be much lower than the potential energy of the top stable point in designs of Figure 7.1(b) type. A schematic of the side view and cut section view are shown in Figure 7.4. The LM_4RM_8 configuration provides a large design flexibility in achieving all the stability conditions for the system due to the various sets of magnets each serving a particular design parameter for stability and energy of the potential wells. For example, the top set of RMs stabilize the top levitating position and the bottom RMs increase the energy of the bottom potential well along with increasing $U_{\text{stability}}$. Additionally, it also provides frequency tunable parameters of the individual wells in terms of the position and volume of the RMs.

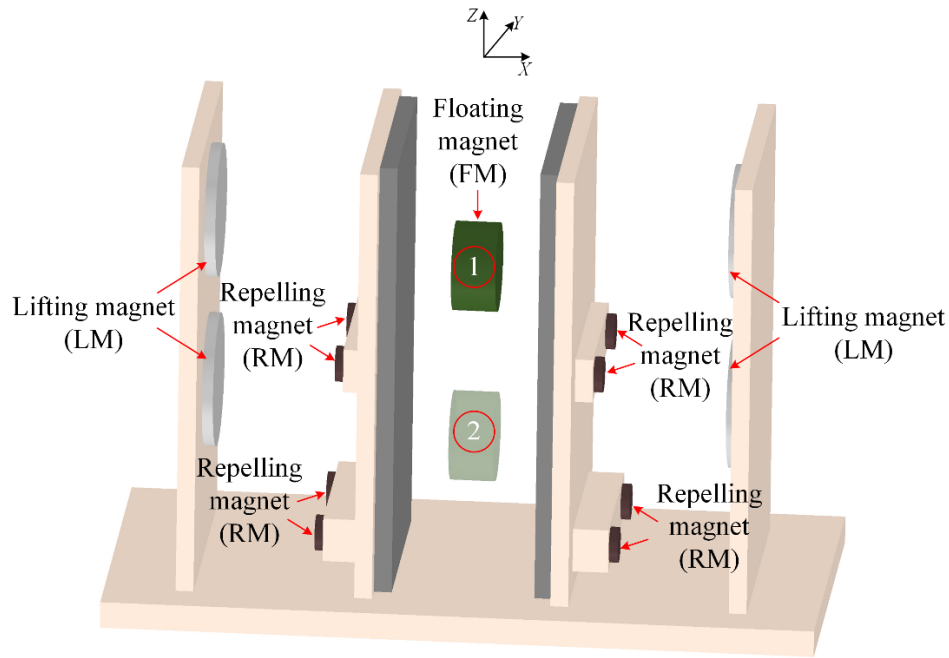


Figure 7.3 Proposed BHDL design with four LMs and eight RMs (LM_4RM_8)

The conditions of stability mentioned in equations (7.7)-(7.9) are updated to include the influence of the additional RMs in the z -direction,

$$\begin{aligned}
F_z^{\text{FM}^1} &= \sum_{j=1}^2 F_z^{\text{LM}_j^1} - \sum_{j=3}^4 F_z^{\text{LM}_j^1} + \sum_{j=1}^8 F_z^{\text{RM}_j^1} - w_{\text{FM}} = 0 \\
F_z^{\text{FM}^2} &= \sum_{j=1}^4 F_z^{\text{LM}_j^2} - \sum_{j=1}^4 F_z^{\text{RM}_j^2} + \sum_{j=5}^8 F_z^{\text{RM}_j^2} - w_{\text{FM}} = 0
\end{aligned} \tag{7.11}$$

in the x -direction,

$$\begin{aligned}
F_x^{\text{FM}^1} &= \sum_{j=1}^2 (-1)^j F_x^{\text{DP}_j^1} + \sum_{j=1}^4 (-1)^{j+1} F_x^{\text{LM}_j^1} - \sum_{j=1}^2 F_x^{\text{RM}_j^1} \\
&\quad - \sum_{j=5}^6 F_x^{\text{RM}_j^1} + \sum_{j=3}^4 F_x^{\text{RM}_j^1} + \sum_{j=7}^8 F_x^{\text{RM}_j^1} \\
F_x^{\text{FM}^2} &= \sum_{j=1}^2 (-1)^j F_x^{\text{DP}_j^2} + \sum_{j=1}^4 (-1)^{j+1} F_x^{\text{LM}_j^2} - \sum_{j=1}^2 F_x^{\text{RM}_j^1} \\
&\quad - \sum_{j=5}^6 F_x^{\text{RM}_j^1} + \sum_{j=3}^4 F_x^{\text{RM}_j^1} + \sum_{j=7}^8 F_x^{\text{RM}_j^1}
\end{aligned} \tag{7.12}$$

where $F_x^{\text{FM}^1}, F_x^{\text{FM}^2} > 0$, for $x > 0$ and $F_x^{\text{FM}^1}, F_x^{\text{FM}^2} < 0$, for $x < 0$

and in the y -direction,

$$\begin{aligned}
F_y^{\text{FM}^1} &= -\sum_{j=1}^4 F_y^{\text{LM}_j^1} - \sum_{j=1}^4 F_x^{\text{RM}_{2j}^1} + \sum_{j=1}^4 F_x^{\text{RM}_{2j-1}^1} \\
F_y^{\text{FM}^2} &= -\sum_{j=1}^4 F_y^{\text{LM}_j^2} - \sum_{j=1}^4 F_x^{\text{RM}_{2j}^2} + \sum_{j=1}^4 F_x^{\text{RM}_{2j-1}^2}
\end{aligned} \tag{7.13}$$

where $F_y^{\text{FM}^1}, F_y^{\text{FM}^2} > 0$, for $y > 0$ and $F_y^{\text{FM}^1}, F_y^{\text{FM}^2} < 0$, for $y < 0$

Simulations were run with different parameters of $z_{\text{LM}}, x_{\text{LM}}, z_{\text{RM}}^{\text{top}}, z_{\text{RM}}^{\text{bottom}}, x_{\text{RM}}^{\text{top}}$ and $x_{\text{RM}}^{\text{bottom}}$ with a set of volumes ($V_{\text{LM}}, V_{\text{FM}}$, and V_{RM}) and aspect ratios (β_{LM} and β_{RM}) to select candidate sets. The candidate set of parameters selected which met the conditions of equations (7.10) - (7.13) are given in Table 7.1. The negative sign for some of the values along the Z -

axis indicate that they are below the set origin (O-O), that is, the midpoint between the two sets of LMs as shown in Figure 7.4. An experimental prototype with these parameters was setup as shown in Figure 7.9.

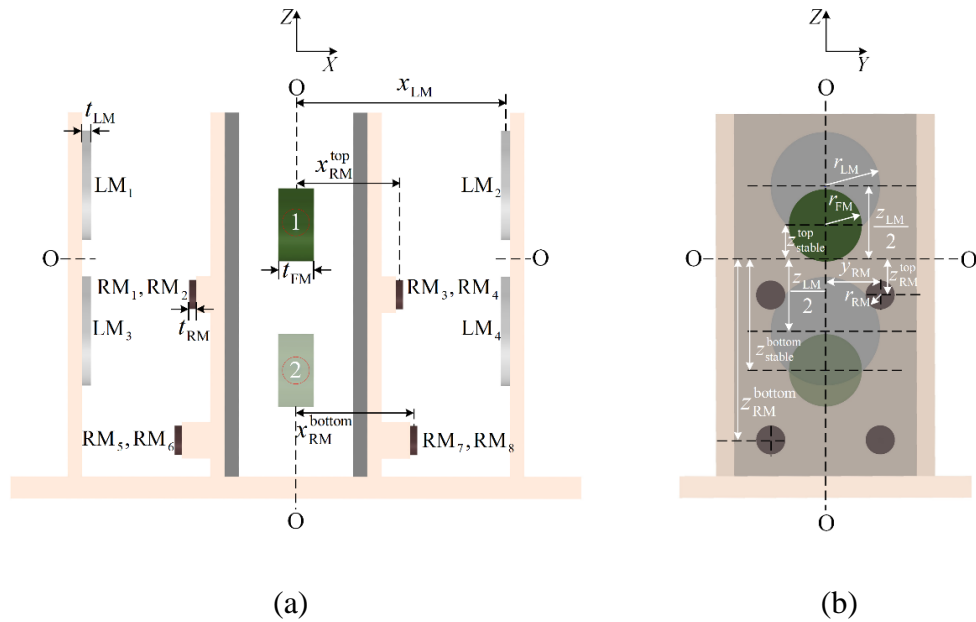


Figure 7.4 (a) Side view and (b) cut-section view of the proposed BHDL system

Table 7.1 Parameters of the experimental setup of the BHDL system

| | | | | | | | | |
|-----------|----------------|-------------------|----------------|-------------------|----------|--------------------|-----------------------|----------|
| Parameter | r_{FM} | t_{FM} | r_{LM} | t_{LM} | r_{RM} | t_{RM} | z_{LM} | x_{LM} |
| Value | 3.175 | 3.175 | 7.14 | 3.175 | 2.38 | 0.03 | 36.5 | 42.2 |
| Unit | mm | mm | mm | mm | mm | mm | mm | mm |
| Parameter | z_{RM}^{top} | z_{RM}^{bottom} | x_{RM}^{top} | x_{RM}^{bottom} | y_{RM} | z_{stable}^{top} | z_{stable}^{bottom} | m_H |
| Value | -12.3 | -30.3 | 19 | 14 | 8 | -2.4 | -17.4 | 175 |
| Unit | mm | mm | mm | mm | mm | mm | mm | g |

The equation of the restoring force in the z -direction is given by,

$$\begin{aligned}
 F_z^{FM} &= -\sum_{j=1}^2 F_z^{LM_j} - \sum_{j=3}^4 F_z^{LM_j} + \sum_{j=1}^8 F_z^{RM_j} - w_{FM}, \text{ for } z > \frac{z_{LM}}{2} \\
 F_z^{FM} &= \sum_{j=1}^2 F_z^{LM_j} - \sum_{j=3}^4 F_z^{LM_j} + \sum_{j=1}^8 F_z^{RM_j} - w_{FM}, \text{ for } z_{RM}^{top} < z < \frac{z_{LM}}{2} \\
 F_z^{FM} &= \sum_{j=1}^2 F_z^{LM_j} - \sum_{j=3}^4 F_z^{LM_j} - \sum_{j=1}^4 F_z^{RM_j} + \sum_{j=5}^8 F_z^{RM_j} - w_{FM}, \text{ for } -\frac{z_{LM}}{2} < z < z_{RM}^{top} \\
 F_z^{FM} &= \sum_{j=1}^4 F_z^{LM_j} - \sum_{j=1}^4 F_z^{RM_j} + \sum_{j=5}^8 F_z^{RM_j} - w_{FM}, \text{ for } z_{RM}^{bottom} < z < -\frac{z_{LM}}{2} \\
 F_z^{FM} &= \sum_{j=1}^4 F_z^{LM_j} - \sum_{j=1}^8 F_z^{RM_j} - w_{FM}, \text{ for } z < z_{RM}^{bottom}
 \end{aligned} \tag{7.14}$$

The associated potential energy is found by integrating the fitted function of the plot of the restoring force shown in Figure 7.5(a). A plot of this potential energy resulting from the integration with respect to the z -displacement is shown in Figure 7.5(b). As it can be noticed from the plots that a compromise is made on the equality of the potential energy of the wells.

The next section will discuss the vibration energy harvesting aspects of the BHDL system in terms of the eddy current damping, design of a copper coil for electromagnetic

transduction, voltage estimation by Lenz's law due to the relative motion of the FM and the force due to Lorentz's law on the FM due to the current in the copper coils.

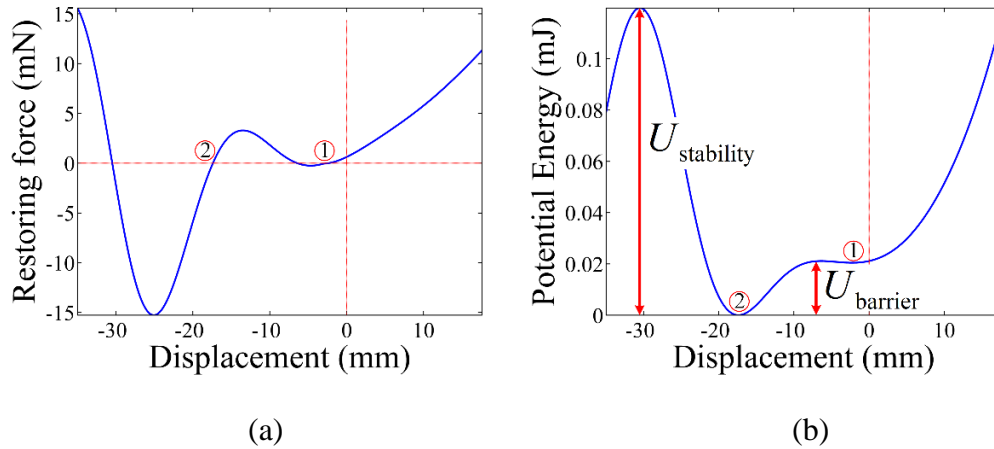


Figure 7.5 (a) Restoring force and (b) potential energy plot of the BHDL system

7.4 Electromagnetic coupling characteristics

Current is induced in a conductor when a magnetic flux through it changes according to Faraday's law. In a VEH system like Figure 7.3, where changing magnetic flux due to the motion of the FM can be either lost as heat due to eddy currents or can be harnessed to power something. In either case they will produce a magnetic field of their own opposing the change in the magnetic field through it. This opposing magnetic field produces a force by Lorentz law which is proportional to the velocity and hence act like a viscous damping force to the motion of the object causing this magnetic flux change. One such force, the eddy current force in the BHDL system is discussed in the following sub-section.

7.4.1 Equivalent mechanical damping

In the present BHDL system, the DP used for levitation is pyrolytic graphite, due to its strong diamagnetic properties, which is incidentally also a good conductor of electricity. When the FM moves relative to the DP, currents are generated in them, aka eddy currents, which act a force to oppose the motion of the FM. These eddy current forces can be approximated by an averaged value per unit velocity by experimentally measuring the ring down of the FM after perturbation. The Q factor, which is estimated from measuring the ring down of the FM, is related to the mechanical damping (c_m) by $c_m = 2\pi f_n m_{FM} / Q$, where f_n is the resonant frequency of the potential well about which the damping is being measured and m_{FM} is the mass of the FM. As $Q = \pi(\ln(A_1 / A_2))^{-1}$, where A_1 and A_2 are relative displacement amplitudes of the FM of successive cycles. A Q factor value of 24.8 was calculated after averaging over a set of 5 readings. However, the Q factor is not a constant but depends on the relative speed of the FM with the DP and hence this value is only an averaged approximate value which will be used in determining the frequency response of the system (equation (7.17)). The Q factor can reach to higher values on lamination of the pyrolytic graphite plate. This lamination process of the pyrolytic graphite has been done in a previous demonstration in Chapter 4 for the VDL system, quality factors of close to fifty were reached. It is expected that similar quality factor values can be reached with the BHDL system, however, this task will be done for future research work.

For vibration energy harvesting using the BHDL system a copper coil needs to be incorporated into the design. The position of the coil is chosen between the top and bottom

stably levitating positions for two reasons. The first reason being to maximize the gain in harvested energy when the FM undergoes interwell motion and the second reason being to avoid static stability issues of the FM at the already determined stable points. The second reason arises because the coil replaces a part of the DP and this decreases F_x^{FM} at that location, as copper is less diamagnetic than pyrolytic graphite (which is used as DP in this setup). Hence, the inclusion of the coil at locations overlapping with the stable points is avoided as it may lead to unsatisfying equation (7.12) which is critical for stability. Hence, to avoid this complication in this study the coil has been placed such that it doesn't affect the axial force at both the levitating points. Based on this discussion the coil inner radius (coil_{in}) is selected to be 3.12 mm and its outer radius (coil_{out}) to be around 4.25 mm. The inner radius is chosen based on the difficulty in handling spools smaller than that radius and the outer radius is chosen such that the sum of the diameter of the FM and twice this radius is almost equal to $\left| z_{\text{stable}}^{\text{bottom}} - z_{\text{stable}}^{\text{top}} \right|$, which is consistent with the discussion to avoid stability issues. The schematic of the assembled DP alongside with the actual assembled DP is shown in Figure 7.6. Alternate geometries such as placing the coil on the surface of the DP with its axis along the x -direction or with its axis along the z -direction around the FM would be difficult to integrate owing to the small levitation gaps that are generally the nature of diamagnetically stabilized magnet levitation systems.

The Q factor value is again measured experimentally now with the DP assembled with the copper coil in open-loop. The value was measured to be around 30.6 by averaging over a set of 5 readings. This slight increase in value, when compared to the one measured with the

standalone DP, is possibly due to the replacement of a part of the DP with the copper coil, which led to decrease in the eddy current force. The reason the Q factor is being measured twice, one with the standalone DP and one with the assembled DP, is because of the two step experimental validation process that will be discussed in the next section. With the equivalent mechanical damping due to the electromagnetic coupling between the FM and the conductive DP discussed, the voltage generated in the copper coil and the electrical damping it acts on the FM need to be discussed.

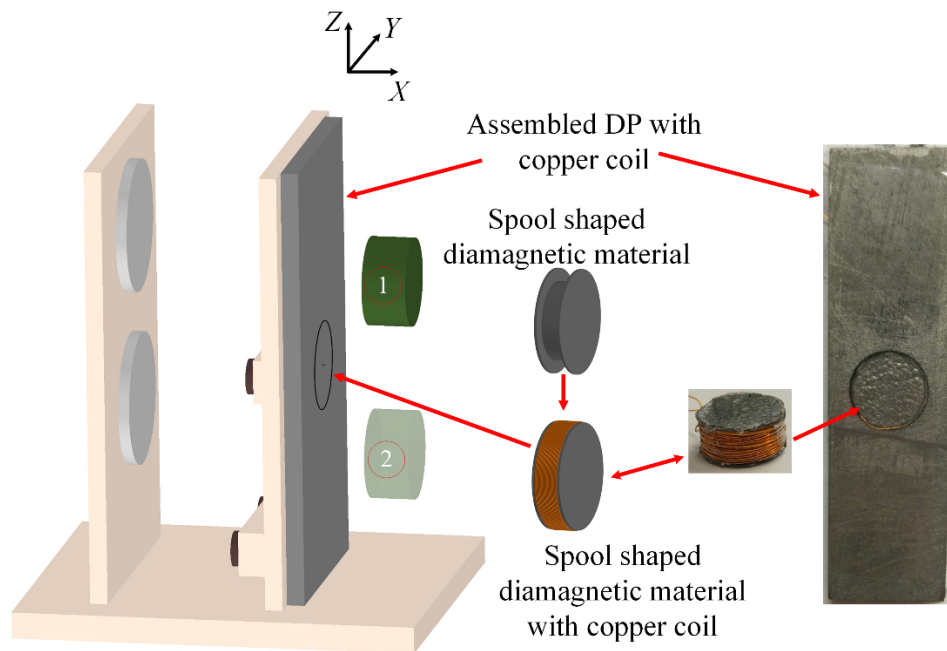


Figure 7.6 Schematic showing a cut-section (view along Y -axis) of the BHDL based VEH alongside with the actual copper coil assembled DP

7.4.2 Electromagnetic transduction and electrical damping

Based on the geometry of the coil discussed in section 7.4.1 the voltage ($V(z, \dot{z})$) induced in the copper coil due to the relative motion of the FM can be determined by using Faraday's law. On approximating the voltage generated to a summing over the infinitesimal areas ($rd\theta dr$) as shown in Figure 7.7(a), one arrives at

$$V(z, \dot{z}) = 2\dot{z} \frac{d}{dz} \sum_{x_{\text{coil}}=D^-}^{x_{\text{coil}}=D^+} \sum_{\text{coil}_{\text{hor}}=\text{coil}_{\text{in}}}^{\text{coil}_{\text{hor}}=\text{coil}_{\text{out}}} \sum_{r=0}^{r=\text{coil}_{\text{hor}}} \sum_{\theta=0}^{\theta=\pi} B_x^{\text{FM}}(\rho, x_{\text{coil}}) r dr d\theta \quad (7.15)$$

where

$$\rho = \sqrt{((z_{\text{coil}} - z) + r \cos \theta)^2 + r \sin^2 \theta} \quad \text{for } z < z_{\text{coil}}, \quad \rho = \sqrt{(-(z_{\text{coil}} - z) + r \cos \theta)^2 + r \sin^2 \theta} \quad \text{for } z > z_{\text{coil}}$$

$D^- = (D - t_{\text{FM}}) / 2$, $D^+ = (D - t_{\text{FM}}) / 2 + t_{\text{coil}}$, z_{coil} is half the distance between the potential wells, coil_{in} is the inner radius of the coil and coil_{out} is the outer radius of the coil.

The magnetic field B_x^{FM} is written in terms of the cylindrical co-ordinates with respect to the center of the FM.

The electrical damping force ($F_L(i, z)$) acting on the FM due to the currents induced in the copper coil can be calculated by using Lorentz law. On approximating it as a summation of the damping force due to each part of the conductor ($rd\theta$) as shown in Figure 7.7(b), one arrives at

$$F_L(i, z) = 2i \sum_{x_{\text{coil}}=D^-}^{x_{\text{coil}}=D^+} \sum_{r=\text{coil}_{\text{in}}}^{r=\text{coil}_{\text{out}}} \left\{ \begin{array}{l} \sum_{\theta=0}^{\theta=\pi/2} [B_x^{\text{FM}}(\rho_{\text{top}}, x_{\text{coil}}) r d\theta] - \\ \sum_{\theta=0}^{\theta=\pi/2} [B_x^{\text{FM}}(\rho_{\text{bottom}}, x_{\text{coil}}) r d\theta] \end{array} \right\} \quad (7.16)$$

where, $\rho_{\text{top}} = \sqrt{r^2 \sin^2 \theta + (z_{\text{coil}} - z - r \cos \theta)^2}$, $\rho_{\text{bottom}} = \sqrt{r^2 \sin^2 \theta + (z_{\text{coil}} - z + r \cos \theta)^2}$ for $z < z_{\text{coil}}$, $\rho_{\text{top}} = \sqrt{r^2 \sin^2 \theta + (-z_{\text{coil}} + z - r \cos \theta)^2}$, $\rho_{\text{bottom}} = \sqrt{r^2 \sin^2 \theta + (-z_{\text{coil}} + z + r \cos \theta)^2}$ for $z > z_{\text{coil}}$ and the subscripts ‘top’ and ‘bottom’ relate to the top and bottom part of the current carrying coils. The definition of D^- , D^+ and B_x^{FM} mean the same as defined for equation (7.15). The variables mentioned in equation (7.16) are also shown in Figure 7.7(b).

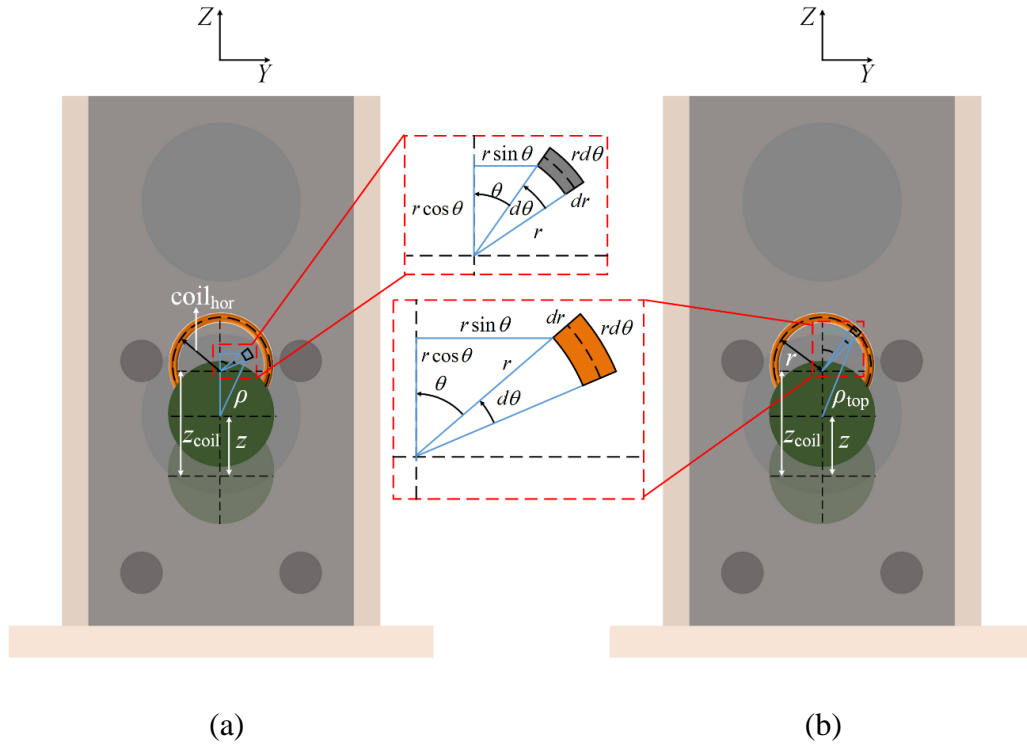


Figure 7.7 Schematic of the VEH with the coil geometry (cut-section view along X-axis) for (a) voltage induced calculation for each loop of the coil ($V(z, \dot{z})$ in equation (7.15)) (b) Lorentz force calculation from each loop of the coil ($F_L(i, z)$ in equation (7.16)).

The discussion in this section summarized the damping forces that are present in the BHDL based VEH system. The next section will put together the restoring forces and damping forces discussed till now to make some theoretical predictions of the amplitude-frequency response, voltage-frequency response of the system and validate it experimentally.

7.5 Experimental validation

In sections 7.3 and 7.4 the equivalent mechanical stiffness and damping (mechanical and electrical) elements of the BHDL based VEH have been discussed. The dynamics of the FM will now be studied for understanding the amplitude-frequency characteristics of this bi-stable system. The experimental validation will be done in two steps. Firstly, the bi-stable system with the standalone DP (without the copper coil) will be used to measure the amplitude-frequency response of the system under various excitation amplitudes. Secondly, once the dynamics of the bi-stable system are validated, the voltage-frequency response curves will be validated by using the assembled DP (DP with the copper coil as discussed in section 7.4.2).

The BHDL system will be simplified to a single degree-of-freedom (1-DOF) vibration system which will be subjected to base excitations in the vertical direction (z -direction) by using a lumped-parameter model [2]. For the BHDL system the initial condition for the FM is considered as the lower stable levitating position, unless mentioned otherwise. Hence, the mechanical equation of motion with the bottom stable point as the origin is:

$$m_{\text{FM}}\ddot{z} + c_m\dot{z} + F_K(z) = m_{\text{FM}}A\omega^2 \sin \omega t \quad (7.17)$$

here z is the relative displacement of the FM from the bottom stable position, c_m is the mechanical damping factor, $F_K(z)$ is the nonlinear restoring force function fitted from Figure 7.5(a) (with origin shifted to the bottom stable position), m_{FM} is the mass of the FM, A is the amplitude of the sinusoidal base displacement and ω is the angular frequency of excitation. Equation (7.17) will be integrated for different input excitations to determine the amplitude-frequency response and these theoretical predictions will be tested with the experiments.

The complete experimental system which includes, in addition to the BHDL based VEH, an oscilloscope, a function generator, an amplifier (not shown), two laser vibrometers and an APS 113 shaker to carry out the low-frequency tests is shown in Figure 7.8. A close up of the BHDL based VEH is shown in Figure 7.9. For the first set of experimental validation, the standalone DP (without the copper coil) is used.

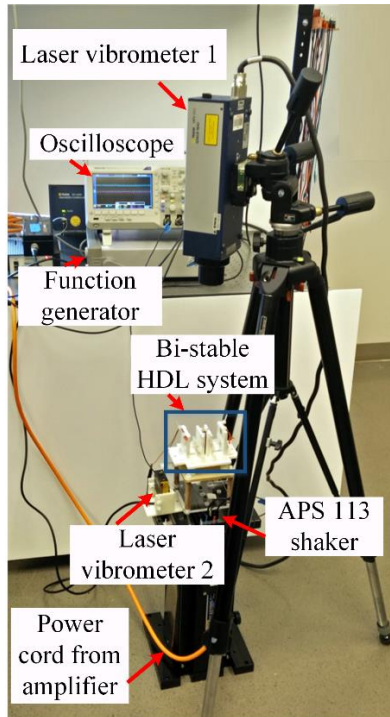


Figure 7.8 Experimental setup of the BHDL based VEH

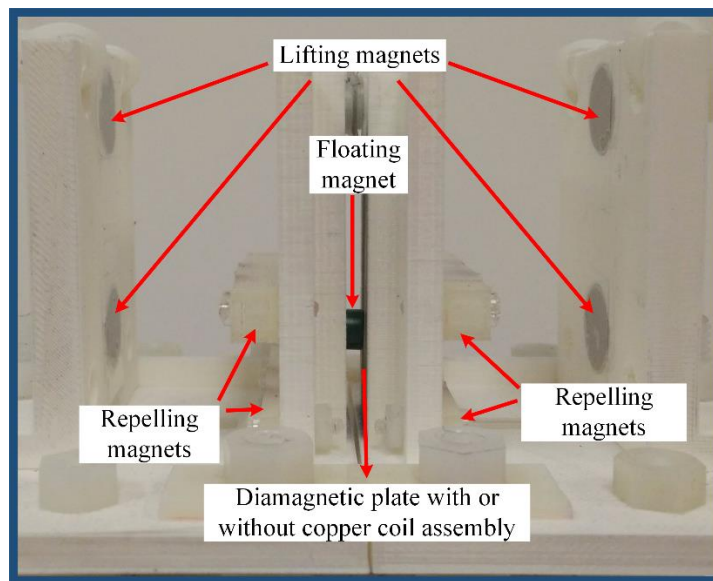


Figure 7.9 Close-up of the BHDL based VEH

Now, this experimental system is given base excitations with frequencies varying from 3 Hz to 10 Hz with a constant input amplitude of 0.5mm, 1mm and 1.5mm respectively. Firstly, Figure 7.10(a) shows the theoretical and experimental amplitude-frequency response curve for a constant input amplitude of 0.5mm. The softening type behavior about the lower stable point with its peak amplitude at a frequency of 6.8 Hz is seen in this figure. Secondly, Figure 7.10(b) shows the frequency response curve for a constant input amplitude of 1 mm. It can be seen that for input frequencies from 6.2Hz to 6.6Hz the FM goes into chaotic motion. Thirdly, Figure 7.10(c) shows the frequency response curve for a constant input amplitude of 1.5 mm, it can be seen that the FM goes into chaotic and interwell motion for frequencies ranging from 6.2Hz to 8Hz. The black dots seen in the plots of Figure 7.10(b) and (c) are the measured amplitude of the FM after a small disturbance was given to the FM to make it escape from the top potential wells, after which the consistent chaotic motion was seen for the FM. The disturbance can be as small as a gust of wind from one's mouth.

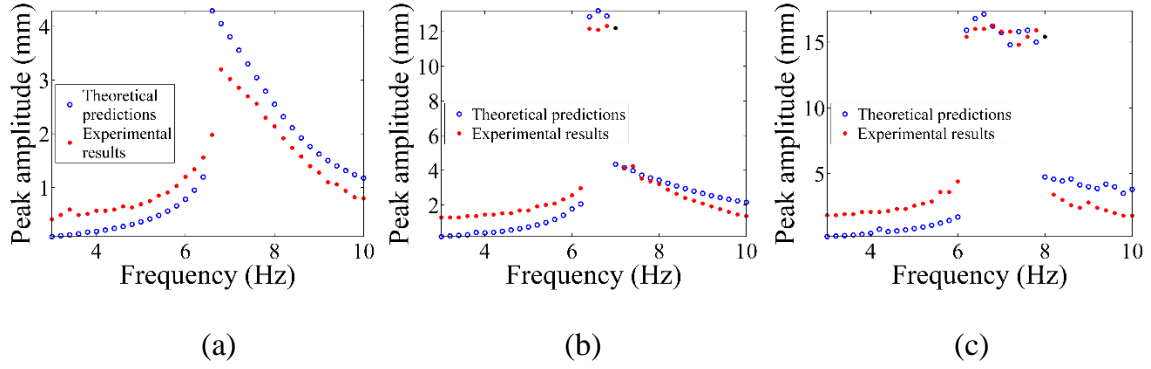


Figure 7.10 Amplitude-frequency response curves with excitation amplitudes (a) of 0.5 mm, (b) 1 mm and (c) 1.5 mm

Now, with the dynamics of the FM in the BHDL system validated. The standalone DP is now replaced with the copper coil assembled DP (Figure 7.6) for the second step of the experimental validation. A resistive load is attached across the coil and the voltage across it is recorded for varying frequency with a constant input excitation of 1.5mm to the VEH. The theoretical predictions of the voltage are made by updating equation (7.17) to include the electrical equation of motion. The voltage induced and the electrical damping force which were described in section 7.4.2 are used to write the combined mechanical and electrical equations of motion

$$\begin{aligned}
 m_{\text{FM}}\ddot{z} + c_m\dot{z} + F_K(z) + F_L(i, z) &= m_{\text{FM}}A\omega^2 \sin \omega t \\
 iL_{\text{coil}} + i(R_{\text{coil}} + R_{\text{load}}) &= V(z, \dot{z})
 \end{aligned}
 \tag{7.18}$$

where $F_L(i, z)$ is the electrical damping force (equation (7.16)), i is the current in the coil, L_{coil} is the inductance of the coil (in this case 187 μH), R_{load} is the resistance of the load (35 Ω in

this case), R_{coil} is the resistance of the coil (12.4Ω in this case), $V(z, \dot{z})$ is the voltage induced (equation (7.15)) and the dot over a variable represents the derivative with time.

Figure 7.11(a) shows the peak voltage response of the system when excited at frequencies ranging from 3Hz to 10Hz at a constant input amplitude of 1.5 mm. Chaotic and interwell response is seen in a slightly larger frequency range (5.8Hz -8Hz) when compared to the amplitude-frequency response curve of Figure 7.10(c), most likely due to the different mechanical damping factors in both the cases. The black dots seen in the plot are the measured voltage after a small disturbance given to the FM, to make it escape the top potential well, after which consistent chaotic motion was seen for the FM. To determine the efficiency of a system defined by equation (7.18), which when excited by a harmonic base excitation and if the mass of the vibrator (mass of the FM, m_{FM} , in this case) is much less than the mass of the energy harvester, then the input mechanical power to the energy harvester is approximated by:

$$\begin{aligned}\bar{P}_{\text{input}} &\approx \frac{2\omega}{\pi} \int_0^{\pi/2\omega} m_{\text{H}} \left| (-A\omega^2 \sin \omega t)(A\omega \cos \omega t) \right| dt \\ &\approx \frac{\omega}{\pi} \int_0^{\pi/2\omega} m_{\text{H}} \omega^3 A^2 \sin 2\omega t dt \approx \frac{1}{\pi} m_{\text{H}} \omega^3 A^2\end{aligned}\quad (7.19)$$

where m_{H} is the mass of the energy harvester, \bar{P}_{input} is the average input mechanical power to the harvester. Using the value of m_{H} and using the voltage response from Figure 7.11(a), the peak efficiency of the BHDL based vibration energy harvester is estimated in Figure 7.11(b) to be around 2.5%.

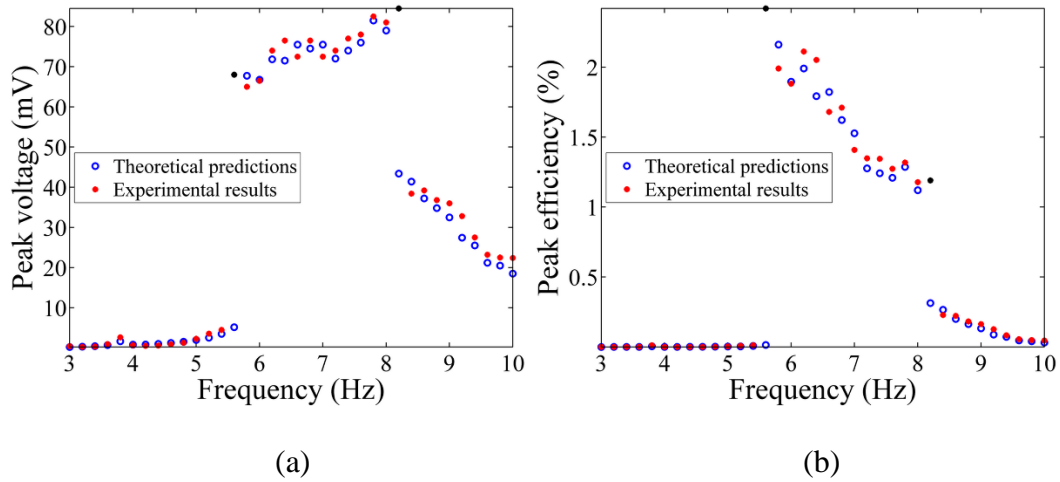


Figure 7.11 (a) Peak voltage frequency response curves with excitation amplitude of 1.5 mm
 (b) Peak efficiency of the BHDL based vibration energy harvester

Thus this section validated the amplitude and voltage frequency response curves of the BHDL based VEH. Further studies are underway to improve the efficiency and the frequency bandwidth of operation of the system. One essential improvement needed is the increase in the volume ratio of the FM to the LM, but as mentioned earlier this increased volume ratio brings in a tilt in the FM. To mitigate this tilt, efforts need to be directed to derive semi-analytical equations to understand and reduce the gradient of the disturbed magnetic force on the FM due to the LMs and the RMs. Also, a laminated DP needs to be used in future studies (as used in VDL based VEH, Chapter 4) to increase the Q factor and ways to increase copper coil volume without affecting stability or by other coil geometries need to be explored.

7.6 Conclusions

A bi-stable system based on HDL is proposed in this chapter to take advantage of the broad bandwidth frequency response inherent in a bi-stable system. From initial conceptual design which involves multiple LMs to a final robust frequency tunable design involving multiple LMs and RMs are discussed. An experimental prototype is discussed with four LMs and eight RMs placed around the FM to achieve bi-stability in this HDL system. Conflicting design constraints on achieving equal potential well bi-stability, maintaining stable levitation during interwell motion and designing a copper coil for transduction are critically discussed. An experimental system is setup with priority given to stability and with a compromise on equal potential energy wells. A part of the diamagnetic plate is replaced with a copper coil for transduction at a location, between the two stably levitating positions of the FM, where it does not affect the stability at either of the stably levitations positions.

The FM underwent chaotic and interwell motions for a range of input excitation frequencies (5.8Hz – 8Hz) at a constant input displacement of 1.5 mm, hence, the bi-stable system showed enhanced frequency bandwidth operation over mono-stable HDL systems discussed in the previous chapters. Peak efficiencies of close to 2.5% were recorded by measuring the power dissipated across a resistive load which was connected to the copper coils. Future studies that need to be undertaken to improve the performance of the BHDL based VEH in terms of power density and in terms of broadening the frequency bandwidth are suggested.

8 Conclusions and future work

8.1 Conclusions

In this dissertation, firstly the state of the art in vibration energy harvesting is briefly reviewed. The progression of literature from linear systems to nonlinear systems is discussed along with challenges that face the state of the art in vibration energy harvesting. Then, the physics of diamagnetic levitation and diamagnetically stabilized magnet levitation are introduced which form the core subject of this dissertation. A working prototype of a linear and hardening type vertical diamagnetic levitation (VDL) based vibration energy harvester (VEH), a softening type horizontal diamagnetic levitation (HDL) system and a bi-stable horizontal diamagnetic levitation (BHDL) system are theoretically and experimentally validated. In summary, it has been shown that the diamagnetically stabilized magnet levitation systems hold promise as an efficient way to harvest low frequency vibrational energy.

Specific contributions of this study to vibration energy harvesting and diamagnetically stabilized magnet levitation systems are summarized as follows:

- i) A VDL based VEH are discussed from a conceptual design to a final experimental prototype. The amplitude-frequency response of the system was validated by the theoretical analysis which showed that the VEH works in a low frequency range (resonant frequency ≈ 2.7 Hz). Then, an optimal design strategy for a VDL system is detailed for understanding the effects of the geometry of the components on the levitation gap, size of the system and the natural frequency of the system. The VDL based VEH due to the increased levitation gap showed hardening type nonlinearity and the jump-down

phenomena was seen in the frequency response curves. The results showed an overall efficiency of 1.54 %, a root mean square (RMS) power output of 1.72 μW when excited at a mechanical input power of 111.41 μW (corresponds to an acceleration of 0.081m/s^2) and at a frequency of 2.1 Hz. More details about these results and conclusions can be found in Chapters 3 and 4.

ii) A first prototype of a HDL based VEH is discussed in Chapter 5. This configuration carries the same attributes as the VDL system of being friction-free and having a low resonant frequency (less than a few hertz), however, some notable limitations of the later have been mitigated in this configuration. For example, spatial constraint and the stability conditions in the vertical direction are uncoupled with the diamagnetic force which relaxed the constraints on the maximum amplitude of the FM, which was severely limited in the VDL system. Then, the influence of the geometry of the floating magnet, the lifting magnet and the diamagnetic plate are parametrically studied to quantify their effects on the size of the system, the stability of the levitation and the resonant frequency of the system. Experimental results and theoretical predictions of an optimized prototype showed a softening frequency response with an average power output of 9.47 μW with an average mechanical input power of 36.6 μW (which corresponds to an RMS acceleration of 0.0546m/s^2) at a frequency of 1.9 Hz. The volume figure of merit of 0.23% is achieved at 1.9 Hz, which is an improvement to the state of the art in the field when considering very low frequency ($< 5\text{ Hz}$) by an order of magnitude. More details about these results and conclusions can be found in Chapter 6.

iii) A BHDL based VEH is proposed to take advantage of the broad bandwidth frequency response inherent in a bi-stable system. From initial conceptual design which involves multiple lifting magnets to a final robust frequency tunable design involving multiple lifting magnets and repelling magnets are discussed. The final proposed prototype which consisted of four LMs and eight RMs placed around the FM to achieve bi-stability in this HDL system is discussed. Conflicting design constraints on achieving equal potential well bi-stability, maintaining stable levitation during interwell motion and designing a copper coil for transduction are critically discussed. An experimental system is setup with priority given to stability and a compromise on equal potential energy wells. The floating magnet underwent chaotic and interwell motions for a range of input excitation frequencies (5.8Hz – 8Hz) at a constant input displacement of 1.5 mm, hence, the bi-stable system showed enhanced frequency bandwidth operation over mono-stable HDL system. Peak efficiencies of close to 2.5% were recorded by measuring the power dissipated across a resistive load. More details about these results and conclusions can be found in Chapter 7.

8.2 Future Work

Further work can be focused on the following issues to improve the performance of the current VEHs based on diamagnetic levitation and diamagnetically stabilized magnet levitation systems.

i) Modeling efforts need to be developed to avoid the tilt in the floating magnet (FM) in the BHDL system when the ratio of the volumes of the FM and the lifting magnet (LM) are similar. This will improve the efficiency greatly and will also provide for new semi-

analytical techniques which can calculate disturbed forces on the surface of magnets. Along with these, an optimization strategy, similar to what was developed for the VDL based VEH in Chapter 4 and for the HDL based VEH in Chapter 6, needs to be developed to assess the geometric components effects on the natural frequency of the wells, potential energy of the wells, bandwidth operation of wells and stability of the FM.

ii) The response of the BHDL system based VEH needs to be tested under actual ambient excitations (colored noise excitation) collected from a civil infrastructure and discuss design parameters most ideal for these category of excitations.

iii) Efforts can be directed towards integrating the BHDL based VEH with appropriate conditioning circuit that can be built over COTS ultra-low voltage DC-DC converter ICs such as BQ25504, TPS65290 (Texas Instruments) and LT3108 (Linear Technologies) along with connecting to a super capacitor or a rechargeable battery to demonstrate full functionality of the harvester. A recent review on power conditioning circuits by Szarka et al. [144] discusses the state of the art in literature in this area.

iv) Efforts can be directed to investigate a bi-stable VDL based VEH and compare its performance with the BHDL based VEH discussed in this dissertation in terms of power density, frequency bandwidth operation and frequency tunability. The bi-stability can be realized in a VDL system with minimal changes to the design of the mono-stable system discussed in Chapters 3 and 4. These changes involve, for example, increasing the distance

between the DPs (discussed briefly in Simon et al.[110]), adjusting the distance between the LM and the FM or adding an additional LM below the FM. These possibilities have been dealt theoretically by Liu and Yuan [131]. However, several challenges such as limitation of amplitude of the FM between the two DPs, impact effects on the DPs and determining the parameters to design an equal double well potential system still need to be addressed before experimental setups can be tested.

v) Efforts can be directed to investigate a diamagnetic levitation based VEH possibly by the use of two-dimensional magnet arrays [145, 146] as they have the potential of having a smaller foot print. The main limitation that currently challenges this approach is the low ratio of the weight to the height of levitation that can be achieved.

9 References

- [1] J.M. Rabaey, J. Ammer, T. Karalar, S. Li, B. Otis, M. Sheets, T. Tuan, PicoRadios for Wireless Sensor Networks: The Next Challenge in Ultra-Low Power Design, *IEEE Intl. Solid-State Circuits Conf. Digest of Technical Papers*, Piscataway, NJ, 2002 45, pp. 200-201.
- [2] S.P. Beeby, M.J. Tudor, N.M. White, Energy harvesting vibration sources for microsystems applications. *Measurement Science & Technology* 17 (12) (2006) R175.
- [3] J.A. Paradiso, T. Starner, Energy scavenging for mobile and wireless electronics. *IEEE Pervasive Computing* 4 (1) (2005).
- [4] S. Roundy, P.K. Wright, A piezoelectric vibration based generator for wireless electronics. *Smart Materials & Structures* 13 (5) (2004) 1131-1142.
- [5] X. Jiang, J. Polastre, D. Culler, Perpetual environmentally powered sensor networks, Fourth International Symposium on Information Processing in Sensor Networks (IPSN), 2005, pp. 463-468.
- [6] C. Park, P.H. Chou, Ambimax: Autonomous energy harvesting platform for multi-supply wireless sensor nodes, 3rd Annual IEEE Communications Society on Sensor and Ad Hoc Communications and Networks (SECON), 2006 1, pp. 168-177.
- [7] P.D. Mitcheson, E.M. Yeatman, G.K. Rao, A.S. Holmes, T.C. Green, Energy harvesting from human and machine motion for wireless electronic devices. *Proceedings of the IEEE* 96 (9) (2008) 1457-1486.
- [8] S. Roundy, E. Leland, J. Baker, E. Carleton, E. Reilly, E. Lai, B. Otis, J. Rabaey, P. Wright, V. Sundararajan, Improving power output for vibration-based energy scavengers. *Pervasive Computing, IEEE* 4 (1) (2005) 28-36.
- [9] S. Roundy, P.K. Wright, J. Rabaey, A study of low level vibrations as a power source for wireless sensor nodes. *Computer Communications* 26 (11) (2003) 1131-1144.

- [10] J.S. Roundy, Energy Scavenging for Wireless Sensor Nodes with a Focus on Vibration to Electricity Conversion, Ph.D. Thesis, The University of California, Berkeley, 2003.
- [11] S.R. Anton, H.A. Sodano, A review of power harvesting using piezoelectric materials (2003–2006). *Smart Materials and Structures* 16 (3) (2007) R1.
- [12] K.A. Cook-Chennault, N. Thambi, A.M. Sastry, Powering MEMS portable devices - a review of non-regenerative and regenerative power supply systems with special emphasis on piezoelectric energy harvesting systems. *Smart Materials and Structures* 17 (4) (2008) 043001.
- [13] F.C. Moon, *Chaotic and Fractal Dynamics: Introduction for Applied Scientists and Engineers*, John Wiley & Sons, 2008.
- [14] A.H. Nayfeh, D.T. Mook, *Nonlinear Oscillations*, John Wiley & Sons, 2008.
- [15] C.B. Williams, C. Shearwood, M.A. Harradine, P.H. Mellor, T.S. Birch, R.B. Yates, Development of an electromagnetic micro-generator. *IEEE Proceedings - Circuits Devices and Systems* 148 (6) (2001) 337-342.
- [16] R. Amirtharajah, A.P. Chandrakasan, Self-powered signal processing using vibration-based power generation. *IEEE Journal of Solid-State Circuits* 33 (5) (1998) 687-695.
- [17] M. Mizuno, D.G. Chetwynd, Investigation of a resonance microgenerator. *Journal of Micromechanics and Microengineering* 13 (2) (2003) 209-216.
- [18] S. Scherrer, D.G. Plumlee, A.J. Moll, Energy scavenging device in LTCC materials, *IEEE Workshop on Microelectronics and Electron Devices (WMED)*, 2005, pp. 77-78.
- [19] S.P. Beeby, M.J. Tudor, E. Koukharenko, N.M. White, T. O'Donnell, C. Saha, S. Kulkarni, S. Roy, Micromachined silicon generator for harvesting power from vibrations. *Proceedings of Transducers*, Seoul, Korea, 2005, pp. 780-781,782,783.
- [20] D.P. Arnold, Review of microscale magnetic power generation. *IEEE Transactions on Magnetics* 43 (11) (2007) 3940-3951.

- [21] M. El-hami, P. Glynne-Jones, N.M. White, M. Hill, S. Beeby, E. James, A.D. Brown, J.N. Ross, Design and fabrication of a new vibration-based electromechanical power generator. *Sensors and Actuators A: Physical* 92 (1-3) (2001) 335-342.
- [22] P. Glynne-Jones, M.J. Tudor, S.P. Beeby, N.M. White, An electromagnetic, vibration-powered generator for intelligent sensor systems. *Sensors and Actuators A-Physical* 110 (1-3) (2004) 344-349.
- [23] A. Marin, S. Bressers, S. Priya, Multiple cell configuration electromagnetic vibration energy harvester. *Journal of Physics D-Applied Physics* 44 (29) (2011) 295501.
- [24] S. Cheng, N. Wang, D.P. Arnold, Modeling of magnetic vibrational energy harvesters using equivalent circuit representations. *Journal of Micromechanics and Microengineering* 17 (11) (2007) 2328-2335.
- [25] S. Kwon, J. Park, K. Law, Electromagnetic energy harvester with repulsively stacked multilayer magnets for low frequency vibrations. *Smart Materials and Structures* 22 (5) (2013) 055007.
- [26] S.D. Moss, O.R. Payne, G.A. Hart, C. Ung, Scaling and power density metrics of electromagnetic vibration energy harvesting devices. *Smart Materials and Structures* 24 (2) (2015) 023001.
- [27] C. Cepnik, R. Lausecker, U. Wallrabe, Review on Electrodynamic Energy Harvesters-A Classification Approach. *Micromachines* 4 (2) (2013) 168-196.
- [28] N.M. White, P. Glynne-Jones, S.P. Beeby, A novel thick-film piezoelectric micro-generator. *Smart Materials & Structures* 10 (4) (2001) 850-852.
- [29] A. Erturk, D.J. Inman, Issues in mathematical modeling of piezoelectric energy harvesters. *Smart Materials & Structures* 17 (6) (2008) 065016.
- [30] A. Erturk, D.J. Inman, On Mechanical Modeling of Cantilevered Piezoelectric Vibration Energy Harvesters. *Journal of Intelligent Material Systems and Structures* 19 (11) (2008) 1311-1325.

- [31] A. Erturk, D.J. Inman, A distributed parameter electromechanical model for cantilevered piezoelectric energy harvesters. *Journal of Vibration and Acoustics - Transactions of the ASME* 130 (4) (2008) 041002.
- [32] A. Erturk, D.J. Inman, An experimentally validated bimorph cantilever model for piezoelectric energy harvesting from base excitations. *Smart Materials & Structures* 18 (2) (2009) 025009.
- [33] X. Jiang, W. Huang, S. Zhang, Flexoelectric nano-generator: Materials, structures and devices. *Nano Energy* 2 (6) (2013) 1079-1092.
- [34] Q. Deng, M. Kammoun, A. Erturk, P. Sharma, Nanoscale flexoelectric energy harvesting. *International Journal of Solids and Structures* 51 (18) (2014) 3218-3225.
- [35] R. Amirtharajah, S. Meninger, J.O. Mur-Miranda, A. Chandrakasan, J. Lang, A micropower programmable DSP powered using a MEMS-based vibration-to-electric energy converter, *Solid-State Circuits Conference, 2000. Digest of Technical Papers. ISSCC. 2000 IEEE International*, 2000, pp. 362-363.
- [36] S. Meninger, J.O. Mur-Miranda, R. Amirtharajah, A.P. Chandrakasan, J.H. Lang, Vibration-to-electric energy conversion. *Very Large Scale Integration (VLSI) Systems*, *IEEE Transactions on* 9 (1) (2001) 64-76.
- [37] S. Roundy, P.K. Wright, K.S.J. Pister, Micro-electrostatic vibration-to-electricity converters, *ASME International Mechanical Engineering Congress and Exposition*, 2002, pp. 487-496.
- [38] T. Sterken, P. Fiorini, G. Altena, C. Van Hoof, R. Puers, *Harvesting Energy from Vibrations by a Micromachined Electret Generator*, 2007.
- [39] S. Boisseau, G. Despesse, B. Ahmed Seddik, *Electrostatic Conversion for Vibration Energy Harvesting*, in: *Anonymous*, 2012.
- [40] Y. Suzuki, *Recent Progress in MEMS Electret Generator for Energy Harvesting*. *Ieej Transactions on Electrical and Electronic Engineering* 6 (2) (2011) 101-111.

- [41] Z.L. Wang, Triboelectric nanogenerators as new energy technology and self-powered sensors - Principles, problems and perspectives. *Faraday discussions* 176 (2014) 447-458.
- [42] F. Fan, Z. Tian, Z.L. Wang, Flexible triboelectric generator! *Nano Energy* 1 (2) (2012) 328-334.
- [43] L. Wang, F.G. Yuan, Vibration energy harvesting by magnetostrictive material. *Smart Materials & Structures* 17 (4) (2008) 045009.
- [44] S.D. Moss, J.E. McLeod, I.G. Powlesland, S.C. Galea, A bi-axial magnetoelectric vibration energy harvester. *Sensors and Actuators A-Physical* 175 (2012) 165-168.
- [45] A. Lundgren, H. Tiberg, L. Kvarnsjo, A. Bergqvist, G. Engdahl, A Magnetostrictive Electric Generator. *IEEE Transactions on Magnetics* 29 (6) (1993) 3150-3152.
- [46] J.K. Huang, R.C. O'Handley, D. Bono, New, high-sensitivity, hybrid magnetostrictive/electroactive magnetic field sensors. *Proc. of SPIE, Smart Structures and Materials: Smart Sensor Technology and Measurement Systems* 5050 (2003) 229-237.
- [47] A. Bayrashev, W.P. Robbins, B. Ziaie, Low frequency wireless powering of microsystems using piezoelectric-magnetostrictive laminate composites. *Sensors and Actuators A-Physical* 114 (2-3) (2004) 244-249.
- [48] M.E. Staley, A.B. Flatau, Characterization of energy harvesting potential of Terfenol-D and Galfenol. *Proc. of SPIE, Smart Structures and Materials: Smart Structures and Integrated Systems* 5764 (2005) 630-640.
- [49] X. Zhao, D.G. Lord, Application of the Villari effect to electric power harvesting. *Journal of Applied Physics* 99 (8) (2006) 08M703.
- [50] J. Hu, F. Xu, A.Q. Huang, F.G. Yuan, Optimal design of a vibration-based energy harvester using magnetostrictive material (MsM). *Smart Materials & Structures* 20 (1) (2011) 015021.
- [51] J. Yang, Y. Wen, P. Li, X. Dai, M. Li, A Broadband Vibration Energy Harvester Using Magnetoelectric Transducer. *IEEE Sensors Conference* (2010) 1905-1909.

- [52] J. Yang, Y. Wen, P. Li, X. Dai, A magnetoelectric, broadband vibration-powered generator for intelligent sensor systems. *Sensors and Actuators A-Physical* 168 (2) (2011) 358-364.
- [53] C.L. Zhang, W.Q. Chen, A wideband magnetic energy harvester. *Applied Physics Letters* 96 (12) (2010) 123507.
- [54] T. Onuta, Y. Wang, C.J. Long, I. Takeuchi, Energy harvesting properties of all-thin-film multiferroic cantilevers. *Applied Physics Letters* 99 (20) (2011) 203506.
- [55] P.D. Mitcheson, T.C. Green, E.M. Yeatman, A.S. Holmes, Architectures for vibration-driven micropower generators. *Journal of Microelectromechanical Systems* 13 (3) (2004) 429-440.
- [56] S. Roundy, On the effectiveness of vibration-based energy harvesting. *Journal of Intelligent Material Systems and Structures* 16 (10) (2005) 809-823.
- [57] A. Erturk, D.J. Inman, *Piezoelectric Energy Harvesting*, Wiley, 2011.
- [58] S. Beeby, N. White, *Energy Harvesting for Autonomous Systems*, Artech House, 2010.
- [59] D. Spreemann, Y. Manoli, *Electromagnetic Vibration Energy Harvesting Devices: Architectures, Design, Modeling and Optimization*, Springer Series in Advanced Microelectronics, New York, 2012.
- [60] S.G. Burrow, L.R. Clare, A Resonant Generator with Non-Linear Compliance for Energy Harvesting in High Vibrational Environments, *Electric Machines & Drives Conference, 2007. IEMDC '07. IEEE International*, 2007 1, pp. 715-720.
- [61] B.P. Mann, N.D. Sims, Energy harvesting from the nonlinear oscillations of magnetic levitation. *Journal of Sound and Vibration* 319 (1-2) (2009) 515-530.
- [62] D.A.W. Barton, S.G. Burrow, L.R. Clare, Energy Harvesting From Vibrations With a Nonlinear Oscillator. *Journal of Vibration and Acoustics - Transactions of the ASME* 132 (2) (2010) 021009.

- [63] Y. Zhu, J.W. Zu, A Magnetolectric Generator for Energy Harvesting From the Vibration of Magnetic Levitation. *IEEE Transactions on Magnetics* 48 (11) (2012) 3344-3347.
- [64] X. Dai, Y. Wen, P. Li, J. Yang, G. Zhang, Modeling, characterization and fabrication of vibration energy harvester using Terfenol-D/PZT/Terfenol-D composite transducer. *Sensors and Actuators A-Physical* 156 (2) (2009) 350-358.
- [65] X. Dai, Y. Wen, P. Li, J. Yang, M. Li, Energy harvesting from mechanical vibrations using multiple magnetostrictive/piezoelectric composite transducers. *Sensors and Actuators A-Physical* 166 (1) (2011) 94-101.
- [66] J. Baker, S. Roundy, P.K. Wright, Alternative Geometries for Increasing Power Density in Vibration Energy Scavenging for Wireless Sensor Networks, 2005 5617.
- [67] F. Cottone, H. Vocca, L. Gammaitoni, Nonlinear energy harvesting. *Physical Review Letters* 102 (8) (2009) 080601.
- [68] A. Erturk, J. Hoffmann, D.J. Inman, A piezomagnetoelastic structure for broadband vibration energy harvesting. *Applied Physics Letters* 94 (25) (2009) 254102.
- [69] R. Masana, M.F. Daqaq, Energy harvesting in the super-harmonic frequency region of a twin-well oscillator. *Journal of Applied Physics* 111 (4) (2012) 044501.
- [70] B.P. Mann, B.A. Owens, Investigations of a nonlinear energy harvester with a bistable potential well. *Journal of Sound and Vibration* 329 (9) (2010).
- [71] R. Ramlan, M.J. Brennan, B.R. Mace, S.G. Burrow, On the performance of a dual-mode non-linear vibration energy harvesting device. *Journal of Intelligent Material Systems and Structures* 23 (13) (2012) 1423-1432.
- [72] S.D. Nguyen, E. Halvorsen, I. Paprotny, Bistable springs for wideband microelectromechanical energy harvesters. *Applied Physics Letters* 102 (2) (2013) 023904.
- [73] M.F. Daqaq, R. Masana, A. Erturk, D.D. Quinn, On the role of nonlinearities in vibratory energy harvesting: A critical review and discussion. *Applied Mechanics Reviews* 66 (4) (2014) 040801.

- [74] R.L. Harne, K.W. Wang, A review of the recent research on vibration energy harvesting via bistable systems. *Smart Materials and Structures* 22 (2) (2013) 023001.
- [75] H. Kulah, K. Najafi, An electromagnetic micro power generator for low-frequency environmental vibrations, *Proceedings of 17th IEEE International Conference on MEMS, Maastricht, The Netherlands, 2004*, pp. 237-240.
- [76] T. Galchev, E.E. Aktakka, K. Najafi, A Piezoelectric Parametric Frequency Increased Generator for Harvesting Low-Frequency Vibrations. *Journal of Microelectromechanical Systems* 21 (6) (2012) 1311-1320.
- [77] T. Galchev, H. Kim, K. Najafi, Micro power generator for harvesting low-frequency and nonperiodic vibrations. *Journal of Microelectromechanical Systems* 20 (4) (2011) 852-866.
- [78] L. Gu, C. Livermore, Impact-driven, frequency up-converting coupled vibration energy harvesting device for low frequency operation. *Smart Materials and Structures* 20 (4) (2011) 045004.
- [79] S. Jung, K. Yun, Energy-harvesting device with mechanical frequency-up conversion mechanism for increased power efficiency and wideband operation. *Applied Physics Letters* 96 (11) (2010) 111906.
- [80] H. Kuelah, K. Najafi, Energy scavenging from low-frequency vibrations by using frequency up-conversion for wireless sensor applications. *IEEE Sensors Journal* 8 (3-4) (2008) 261-268.
- [81] S.D. Moss, J.E. McLeod, S.C. Galea, Wideband vibro-impacting vibration energy harvesting using magnetoelectric transduction. *Journal of Intelligent Material Systems and Structures* 24 (11) (2013) 1313-1323.
- [82] M. Umeda, K. Nakamura, S. Ueha, Analysis of the transformation of mechanical impact energy to electric energy using piezoelectric vibrator. *Japanese Journal of Applied Physics Part 1-Regular Papers Short Notes & Review Papers* 35 (5B) (1996).
- [83] M. Umeda, K. Nakamura, S. Ueha, Energy storage characteristics of a piezo-generator using impact induced vibration. *Japanese Journal of Applied Physics Part 1-Regular Papers Short Notes & Review Papers* 36 (5B) (1997) 3146-3151.

- [84] M. Renaud, P. Fiorini, C. van Hoof, Optimization of a piezoelectric unimorph for shock and impact energy harvesting. *Smart Materials & Structures* 16 (4) (2007) 1125-1135.
- [85] E. Jacquelin, S. Adhikari, M.I. Friswell, A piezoelectric device for impact energy harvesting. *Smart Materials & Structures* 20 (10) (2011) 105008.
- [86] M.J. Ramsay, W.W. Clark, Piezoelectric energy harvesting for bio MEMS applications. *Proc. of SPIE, Smart Structures and Materials: Industrial and Commercial Applications of Smart Structures Technologies* 4332 (2001) 429-438.
- [87] J.M. Donelan, Q. Li, V. Naing, J.A. Hoffer, D.J. Weber, A.D. Kuo, Biomechanical energy harvesting: Generating electricity during walking with minimal user effort. *Science* 319 (5864) (2008) 807-810.
- [88] E. Romero, R.O. Warrington, M.R. Neuman, Energy scavenging sources for biomedical sensors. *Physiological Measurement* 30 (9) (2009) R35-R62.
- [89] P.L. Green, E. Papatheou, N.D. Sims, Energy harvesting from human motion and bridge vibrations: An evaluation of current nonlinear energy harvesting solutions. *Journal of Intelligent Material Systems and Structures* 24 (12) (2013) 1494-1505.
- [90] Y. Fujino, Vibration, control and monitoring of long-span bridges - recent research, developments and practice in Japan. *Journal of Constructional Steel Research* 58 (1) (2002).
- [91] C. C. Chang, T. Y. P. Chang, and Q. W. Zhang, Ambient vibration of Long-Span Cable-Stayed Bridge. *Journal of Bridge Engineering* 6 (2001) 46-53.
- [92] K. Tanida, Progress in the application of active vibration control technologies to long-span bridges in Japan. *Progress in Structural Engineering and Materials* 4 (4) (2002) 363-371.
- [93] R. Betti, R.B. Testa, Vibration and damage control for long-span bridges. *Smart Materials and Structures* 4 (1) (1995) 91.
- [94] Y.B. Yang, C.W. Lin, Vehicle-bridge interaction dynamics and potential applications. *Journal of Sound and Vibration* 284 (1-2) (2005) 205-226.

- [95] C.B. Williams, A. Pavic, R.S. Crouch, R.C. Woods, Feasibility study of vibration-electric generator for bridge vibration sensors, Proceedings of the Society of Photo-Optical Instrumentation Engineers (SPIE), Santa Barbara, CA, 1998 3243, pp. 1111-1117.
- [96] M. Ferrari, V. Ferrari, M. Guizzetti, B. Ando, S. Baglio, C. Trigona, Improved energy harvesting from wideband vibrations by nonlinear piezoelectric converters. Sensors and Actuators A-Physical 162 (2) (2010).
- [97] C.R. McInnes, D.G. Gorman, M.P. Cartmell, Enhanced vibrational energy harvesting using nonlinear stochastic resonance. Journal of Sound and Vibration 318 (4-5) (2008).
- [98] S.C. Stanton, C.C. McGehee, B.P. Mann, Nonlinear dynamics for broadband energy harvesting: Investigation of a bistable piezoelectric inertial generator. Physica D-Nonlinear Phenomena 239 (10) (2010) 640-653.
- [99] D. Jiles, Introduction to Magnetism and Magnetic Materials, Chapman & Hall, 1998.
- [100] J.M.D. Coey, Magnetism and Magnetic Materials, Cambridge University Press, 2010.
- [101] E.T. LaCheisserie, D. Gignoux, M. Schlenker, Magnetism: Fundamentals, Materials and Applications, Springer, 2002.
- [102] R.E. Hummel, Electronic Properties of Materials, Springer, 2011.
- [103] S. Earnshaw, On the nature of the molecular forces which regulate the constitution of the luminiferous ether. Transactions of the Cambridge Philosophical Society 7 (1842) 97-112.
- [104] W. Thomson, On the Forces Experienced by Small Spheres Under Magnetic Influence; and on some of the Phenomena Presented by Diamagnetic Substances; Reprint of Papers on Electrostatics and Magnetism, Cambridge University Press, 1872.
- [105] W. Braunbeck, Freies Schweben diamagnetischer Körper im Magnetfeld. Zeitschrift für Physik 112 (1939) 764-769.
- [106] A. Boerdijk, Technical aspects of levitation. Philips Research Report 11 (1956) 45-46.

- [107] A. Boerdijk, Levitation by static magnetic fields. *Philips Technical Review* 18 (1956) 57.
- [108] M.V. Berry, A.K. Geim, Of flying frogs and levitrons. *European Journal of Physics* 18 (4) (1997) 307-313.
- [109] A.K. Geim, M.D. Simon, M.I. Boamfa, L.O. Heflinger, Magnet levitation at your fingertips. *Nature* 400 (6742) (1999) 323-324.
- [110] M.D. Simon, L.O. Heflinger, A.K. Geim, Diamagnetically stabilized magnet levitation. *American Journal of Physics* 69 (6) (2001) 702-713.
- [111] C.B. Coleman, R.A. Gonzalez-Villalobos, P.L. Allen, K. Johanson, K. Guevorkian, J.M. Valles, T.G. Hammond, Diamagnetic levitation changes growth, cell cycle, and gene expression of *Saccharomyces cerevisiae*. *Biotechnology and bioengineering* 98 (4) (2007) 854-863.
- [112] R. Herranz, R. Anken, J. Boonstra, M. Braun, P.C.M. Christianen, M. de Geest, J. Hauslage, R. Hilbig, R.J.A. Hill, M. Lebert, F. Javier Medina, N. Vagt, O. Ullrich, J.J.W.A. van Loon, R. Hemmersbach, Ground-Based Facilities for Simulation of Microgravity: Organism-Specific Recommendations for Their Use, and Recommended Terminology. *Astrobiology* 13 (1) (2013) 1-17.
- [113] J.S. Brooks, J.A. Reavis, R.A. Medwood, T.F. Stalcup, M.W. Meisel, E. Steinberg, L. Arnowitz, C.C. Stover, J.A.A.J. Perenboom, New opportunities in science, materials, and biological systems in the low-gravity (magnetic levitation) environment (invited). *Journal of Applied Physics* 87 (9) (2000) 6194-6199.
- [114] S.A. Peyman, E.Y. Iwan, O. Margaron, A. Iles, N. Pamme, Diamagnetic repulsion-A versatile tool for label-free particle handling in microfluidic devices. *Journal of Chromatography A* 1216 (52) (2009) 9055-9062.
- [115] H. Chetouani, C. Jeandey, V. Haguet, H. Rostaing, C. Dieppedale, G. Reyne, Diamagnetic levitation with permanent magnets for contactless guiding and trapping of microdroplets and particles in air and liquids. *IEEE Transactions on Magnetics* 42 (10) (2006) 3557-3559.

- [116] C. Pigot, H. Chetouani, G. Poulin, G. Reyne, Diamagnetic Levitation of Solids at Microscale. *IEEE Transactions on Magnetics* 44 (11) (2008) 4521-4524.
- [117] J. Chen, J. Zhou, G. Meng, Diamagnetic bearings for MEMS: Performance and stability analysis. *Mechanics Research Communications* 35 (8) (2008) 546-552.
- [118] A. Cansiz, Static and dynamic analysis of a diamagnetic bearing system. *Journal of Applied Physics* 103 (3) (2008) 034510.
- [119] R. Pelrine, A. Wong-Foy, B. McCoy, D. Holeman, R. Mahoney, G. Myers, J. Herson, T. Low, Diamagnetically Levitated Robots: An Approach to Massively Parallel Robotic Systems with Unusual Motion Properties. *IEEE International Conference on Robotics and Automation (ICRA)* (2012) 739-744.
- [120] <http://spectrum.ieee.org/automaton/robotics/industrial-robots/watch-sris-nimble-microrobots-cooperate-to-build-structures>, (Accessed 6/18/2015).
- [121] Q. Li, K. Kim, A. Rydberg, Lateral force calibration of an atomic force microscope with a diamagnetic levitation spring system. *Review of Scientific Instruments* 77 (6) (2006) 065105.
- [122] J. Abadie, E. Piat, S. Oster, M. Boukallel, Modeling and experimentation of a passive low frequency nanoforce sensor based on diamagnetic levitation. *Sensors and Actuators A-Physical* 173 (1) (2012) 227-237.
- [123] I. Simon, Diamagnetic accelerometer, Patent No. US 3465598, 1969.
- [124] F. Barrot, J. Sandtner, H. Bleuler, Acceleration Sensor Based on Diamagnetic Levitation, 2005.
- [125] L. Liu, F.G. Yuan, Nonlinear vibration energy harvester using diamagnetic levitation. *Applied Physics Letters* 98 (20) (2011) 203507.
- [126] R. Ravaud, G. Lemarquand, S. Babic, V. Lemarquand, C. Akyel, Cylindrical magnets and coils: Fields, forces, and inductances. *IEEE Transactions on Magnetics* 46 (9) (2010) 3585-3590.

[127] N. Derby, S. Olbert, Cylindrical magnets and ideal solenoids. *American Journal of Physics* 78 (3) (2010) 229-235.

[128] W. Robertson, B. Cazzolato, A. Zander, A Simplified Force Equation for Coaxial Cylindrical Magnets and Thin Coils. *IEEE Transactions on Magnetics* 47 (8) (2011) 2045-2049.

[129] <http://dlmf.nist.gov/>, (Accessed 30 May/2013).

[130] M. Boukallel, J. Abadie, E. Piat, Levitated micro-nano force sensor using diamagnetic materials, *IEEE International Conference on Robotics and Automation*, Taipei, Taiwan, September 2003, pp. 3219-3224.

[131] L. Liu, F.G. Yuan, Diamagnetic levitation for nonlinear vibration energy harvesting: Theoretical modeling and analysis. *Journal of Sound and Vibration* 332 (2) (2013) 455-464.

[132] J.S. Agashe, D.P. Arnold, A study of scaling and geometry effects on the forces between cuboidal and cylindrical magnets using analytical force solutions. *Journal of Physics D-Applied Physics* 41 (10) (2008) 105001.

[133] K. Lee, K. Park, Modeling eddy currents with boundary conditions by using Coulomb's law and the method of images. *IEEE Transactions on Magnetics* 38 (2) (2002) 1333-1340.

[134] H.A. Sodano, J.S. Bae, D.J. Inman, W.K. Belvin, Improved concept and model of current damper. *Journal of Vibration and Acoustics - Transactions of the ASME* 128 (3) (2006) 294-302.

[135] C.B. Williams, R.B. Yates, Analysis of a micro-electric generator for microsystems. *Sensors and Actuators A-Physical* 52 (1-3) (1996) 8-11.

[136] W.T. Thomson, M.D. Dahleh, *Theory of Vibration with Applications*, Prentice Hall, 1997.

[137] J.T. Conway, Forces between thin coils with parallel axes using Bessel functions. *IEEE Transactions on Magnetics* 49 (9) (2013) 5028-5034.

- [138] S.P. Beeby, R.N. Torah, M.J. Tudor, P. Glynn-Jones, T. O'Donnell, C.R. Saha, S. Roy, A micro electromagnetic generator for vibration energy harvesting. *Journal of Micromechanics and Microengineering* 17 (7) (2007) 1257-1265.
- [139] N.G. Stephen, On energy harvesting from ambient vibration. *Journal of Sound and Vibration* 293 (1-2) (2006) 409-425.
- [140] T.V. Galchev, J. McCullagh, R.L. Peterson, K. Najafi, Harvesting traffic-induced vibrations for structural health monitoring of bridges. *Journal of Micromechanics and Microengineering* 21 (10) (2011) 104005.
- [141] D.S. Nguyen, E. Halvorsen, G.U. Jensen, A. Vogl, Fabrication and characterization of a wideband MEMS energy harvester utilizing nonlinear springs. *Journal of Micromechanics and Microengineering* 20 (12) (2010) 125009.
- [142] S.D. Nguyen, E. Halvorsen, Nonlinear springs for bandwidth-tolerant vibration energy harvesting. *Journal of Microelectromechanical Systems* 20 (6) (2011) 1225-1227.
- [143] J.J. McCullagh, T. Galchev, R.L. Peterson, R. Gordenker, Y. Zhang, J. Lynch, K. Najafi, Long-term testing of a vibration harvesting system for the structural health monitoring of bridges. *Sensors and Actuators A-Physical* 217 (2014) 139-150.
- [144] G.D. Szarka, B.H. Stark, S.G. Burrow, Review of power conditioning for kinetic energy harvesting systems. *IEEE Transactions on Power Electronics* 27 (2) (2012) 803-815.
- [145] R. Moser, F. Barrot, J. Sandtner, H. Bleuler, Optimization of two-dimensional permanent magnet arrays for diamagnetic levitation, *Maglev'2002 The 17th International Conference on Magnetically Levitated Systems and Linear drives*, Lausanne, Switzerland, 2002.
- [146] G. Kuestler, Diamagnetic levitation of pyrolytic graphite over monolithic NdFeB magnet. *Electronics Letters* 50 (18) (2014) 1289-U132.